

Yale University

EliScholar – A Digital Platform for Scholarly Publishing at Yale

Yale Graduate School of Arts and Sciences Dissertations

Spring 2022

T Cell Regulation of Antibody Responses to Infection and Immunization

Jennifer Shuen Chen

Yale University Graduate School of Arts and Sciences, jennifer101@gmail.com

Follow this and additional works at: https://elischolar.library.yale.edu/gsas_dissertations

Recommended Citation

Chen, Jennifer Shuen, "T Cell Regulation of Antibody Responses to Infection and Immunization" (2022). *Yale Graduate School of Arts and Sciences Dissertations*. 573.
https://elischolar.library.yale.edu/gsas_dissertations/573

This Dissertation is brought to you for free and open access by EliScholar – A Digital Platform for Scholarly Publishing at Yale. It has been accepted for inclusion in Yale Graduate School of Arts and Sciences Dissertations by an authorized administrator of EliScholar – A Digital Platform for Scholarly Publishing at Yale. For more information, please contact elischolar@yale.edu.

Abstract

T Cell Regulation of Antibody Responses to Infection and Immunization

Jennifer Shuen Chen

2022

T follicular helper (Tfh) cells are the conventional drivers of protective, germinal center (GC)-based antiviral antibody responses. However, loss of Tfh cells and GCs has been observed in patients with severe COVID-19. As T cell-B cell interactions and immunoglobulin class switching still occur in these patients, non-canonical pathways of antibody production may be operative during SARS-CoV-2 infection. We found that both Tfh-dependent and -independent antibodies were induced against SARS-CoV-2 infection, SARS-CoV-2 vaccination, and influenza A virus infection. Even though Tfh-independent antibodies to SARS-CoV-2 had evidence of reduced somatic hypermutation, they were still high-affinity, durable, and reactive against diverse spike-derived epitopes and were capable of neutralizing both homologous SARS-CoV-2 and the B.1.351 (beta) variant of concern. Indeed, we found by epitope mapping and BCR sequencing that Tfh cells focused the B cell response and therefore, in the absence of Tfh cells, a more diverse clonal repertoire was maintained. These data support a new paradigm for the induction of B cell responses during viral infection that enables effective, neutralizing antibody production to complement traditional GC-derived antibodies that might compensate for GCs damaged by viral inflammation.

Furthermore, we sought to reconcile the roles of Tfh cell-derived IL-4 as both a pro-survival factor for highly proliferative GC B cells as well as a switch factor for IgE and IgG1. Due to its potent effects on B cell proliferation and differentiation, IL-4 is considered a canonical Tfh cell cytokine, produced even during antimicrobial responses that elicit little IgG1 and no IgE. However, given that IL-4 is also a switch factor that is sufficient for IgE induction, this raises the

question of how Tfh cells produce IL-4 during type 1 immune responses without aberrantly inducing IgE. We first clarified the role of Tfh cell-derived IL-4 during type 1 immune responses, finding that it was required for IgG1 switching in response to immunization with lipopolysaccharide and haptened protein antigen as well as influenza A virus infection; however, GC B cell formation and plasmablast differentiation were unaffected by the loss of IL-4 from Tfh cells. In addition, we found that Tfh cells during type 1 immune responses generated minimal IL-4 protein, with levels of IL-4 tightly regulated by both transcriptional and post-transcriptional mechanisms. These data support the role of Tfh cell-derived IL-4 as a rheostat for the appropriate induction of IgG1 versus IgE antibodies during type 1 and type 2 immune responses, rather than as a pro-survival factor for GC B cells.

Finally, when public health officials raised concerns about the use of nonsteroidal anti-inflammatory drugs (NSAIDs) for treating COVID-19 at the start of the pandemic, we sought to determine whether and how NSAIDs could affect COVID-19 pathogenesis. NSAIDs affect the production of prostaglandins, which play diverse biological roles in homeostasis and inflammatory responses. Thus, it is plausible that NSAIDs could affect COVID-19 pathogenesis in multiple ways, including modifying expression of angiotensin-converting enzyme 2 (*ACE2*), the cell entry receptor for SARS-CoV-2; regulating replication of SARS-CoV-2 in host cells; and modulating the immune response to SARS-CoV-2. We found that NSAID treatment had no effect on *ACE2* expression, viral entry, or viral replication. However, NSAIDs did affect the immune response to SARS-CoV-2 by impairing the production of proinflammatory cytokines as well as early neutralizing antibodies. Our findings therefore indicate that NSAID treatment may affect COVID-19 outcomes by dampening the inflammatory response and the production of protective antibodies, which also has implications for NSAID use during SARS-CoV-2 vaccination.

T Cell Regulation of Antibody Responses to Infection and Immunization

A Dissertation
Presented to the Faculty of the Graduate School
Of
Yale University
In Candidacy for the Degree of
Doctor of Philosophy

By
Jennifer Shuen Chen

Dissertation Directors: Stephanie Eisenbarth and Craig Wilen

May 2022

© 2022 by Jennifer Shuen Chen

All rights reserved.

TABLE OF CONTENTS

CONTENT ATTRIBUTION	1
ACKNOWLEDGEMENTS	2
§ CHAPTER 1: Introduction	4
Antibodies enable tailored responses to diverse targets	4
T follicular helper cells are the conventional drivers of antibody responses	6
Tfh-independent responses may also generate protective antibodies	8
Goals of thesis	9
§ CHAPTER 2: High-affinity, neutralizing antibodies to SARS-CoV-2 can be made in the absence of T follicular helper cells	11
SARS-CoV-2 infection and vaccination induce Tfh-dependent and -independent antibodies ..	11
Influenza virus infection induces Tfh-dependent and -independent antibodies	21
Durable, high-affinity antibodies to SARS-CoV-2 can be made in the absence of Tfh cells ...	21
Tfh-deficient mice demonstrate similar V gene usage but impaired mutation selection compared to Tfh-sufficient mice	27
Tfh cells focus the antibody repertoire but are dispensable for broad coverage of SARS-CoV-2 epitopes	34
RBD-specific antibodies are generated in the absence of Tfh cells	39
Tfh-dependent and -independent antibodies demonstrate similar neutralization potency against homologous SARS-CoV-2 as well as the B.1.351 variant of concern	40
Th1 cells express Tfh effector molecules and co-localize with IgG2c ⁺ B cells following viral infection	45
Discussion	53
Future directions	58
§ CHAPTER 3: IL-4 regulation in T follicular helper cells dictates appropriate antibody class switching during type 1 versus type 2 immune responses	62
IL-4 is necessary and sufficient for high-affinity IgE production <i>in vivo</i>	62
IL-4 from Tfh cells is required for IgG1 switching but not germinal center formation or plasmablast differentiation during type 1 immune responses	64
Transcriptional and post-transcriptional regulation limit IL-4 protein production by Tfh cells during type 1 immune responses	67
Subcellular localization and ribosomal association of <i>Il4</i> mRNA may provide further insight into mechanisms of post-transcriptional regulation	70
Discussion and future directions	74

§ CHAPTER 4: Nonsteroidal anti-inflammatory drugs dampen the cytokine and antibody response to SARS-CoV-2 infection	78
§ CHAPTER 5: Conclusion and Implications	95
MATERIALS AND METHODS.....	99
REFERENCES	131

CONTENT ATTRIBUTION

This dissertation includes work that first appeared in the following publications:

- Chen JS, Chow RD, Song E, Mao T, Israelow B, Kamath K, Bozekowski J, Haynes WA, Filler RB, Menasche BL, Wei J, Alfajaro MM, Song W, Peng L, Carter L, Weinstein JS, Gowthaman U, Chen S, Craft J, Shon JC, Iwasaki A, Wilen CB, Eisenbarth SC. High-affinity, neutralizing antibodies to SARS-CoV-2 can be made without T follicular helper cells. *Sci Immunol*. 2022 Feb 4;7(68):eabl5652.
- Gowthaman U, Chen JS, Eisenbarth SC. Regulation of IgE by T follicular helper cells. *J Leukoc Biol*. 2020 Mar;107(3):409-418.
- Chen JS, Alfajaro MM, Chow RD, Wei J, Filler RB, Eisenbarth SC, Wilen CB. Non-steroidal anti-inflammatory drugs dampen the cytokine and antibody response to SARS-CoV-2 infection. *J Virol*. 2021 Jan 13;95(7):e00014-21.
- Chen JS*, Grassmann JDS*, Gowthaman U*, Olyha SJ, Simoneau T, Berin MC, Eisenbarth SC, Williams A. Flow cytometric identification of Tfh13 cells in mouse and human. *J Allergy Clin Immunol*. 2021 Feb;147(2):470-483.

* denotes equal contribution

These publications are reproduced with full permissions from the respective publishers.

ACKNOWLEDGEMENTS

I would first like to thank Dr. Stephanie Eisenbarth for her many years of support and guidance, molding me from a clueless first-year graduate student into a curious and resilient scientist. You have been a role model for me in so many ways, including as a physician-scientist, a leader, and a mentor. Thank you for always being generous with your time and showing me how rewarding a career in science can be.

I am also grateful to Dr. Craig Wilen for being a thoughtful mentor and always a source of incisive advice. In a short amount of time, you have taught me so much, including how to be efficient with experiments while keeping my eye on the big picture, and that virology is pretty cool too. Thank you also for providing me with the support when I needed it and the autonomy when I wanted it.

I would also like to thank my thesis committee members, Dr. Carrie Lucas, Dr. Joseph Craft, Dr. Joao Pereira, and Dr. Keith Choate. It has been a privilege to learn from your wisdom and expertise. Thank you for challenging me to think more critically about my science and also for providing encouragement when I faced setbacks. Thank you also to Dr. Amanda Poholek for reading this thesis.

I am indebted to my two wonderful lab families, all past and present members of the Eisenbarth and Wilen labs. Thank you for making lab feel like a home away from home. I especially want to thank Dr. Gowthaman Uthaman for his endless supply of patience. Thank you for teaching me how to be a scientist, an immunologist, and a good labmate. Special thanks also to Biyan Zhang, who showed me the ropes of being a graduate student and always had a well-stocked stash of snacks for when I got hungry. I would also like to thank Dr. Jin Wei and Dr. Mia Madel Alfajaro for being patient and generous with their time as they taught me how to be a

virologist. And finally thank you to the incredible lab moms Lan Xu and Renata Filler for doing pretty much everything and taking care of all of us.

I am so lucky to have been a part of the Yale Immunobiology community. I have made countless friends here during my graduate training and been fortunate enough to collaborate with many of them. They have shown me that science is better (and more fun) when done together.

I am also thankful for everyone in the Yale MD/PhD program, including Dr. Barbara Kazmierczak, Dr. Reiko Fitzsimonds, Susan Sansone, Cheryl DeFilippo, Alex Mauzerall, and Dr. Tamar Taddei. Thank you for making Yale the best place to train to become a physician-scientist. Thank you also to my MD/PhD classmates for their unwavering friendship from the very beginning.

Finally, thank you to my parents Chun-Nan Chen and Sharon Lue, and my partner Ryan Chow. I am grateful every day to have your unconditional love and support, and I dedicate this work to you.

§ CHAPTER 1: Introduction

Antibodies enable tailored responses to diverse targets

Tasked with protecting the body from a diverse array of pathogens, the immune system mobilizes a tailored response best suited to each one. In general, the immune response to pathogens and other immunological insults can be categorized into type 1, type 2, and type 3 immunity (1). While type 1 immunity protects against intracellular microbes, type 2 immunity is directed against helminths, allergens, and toxins, and type 3 immunity combats extracellular bacteria and fungi (1). Each type of immunity begins with recognition of the pathogen by innate immune sensors, leading to the production of cytokines that instruct lymphocyte differentiation appropriate to the intruder (2). These lymphocytes then produce cytokines that stimulate effector responses, which are responsible for ultimately expelling or extinguishing the invading pathogen (2).

Antibodies are a powerful component of the effector response during type 1, 2, and 3 immunity. Comprised of two functional domains, antibodies recognize specific targets via their antigen-binding fragment (Fab) and then mediate specific functions through their crystallizable fragment (Fc) (3). Within the Fab domain, the variable (V) region confers specific antigen binding (4). The V region is encoded by recombined heavy chain V, D, and J gene segments and light chain V and J gene segments (5). Multiple copies of the V, D, and J gene segments as well as pairing of the heavy and light chains enables combinatorial diversity on the order of millions (5). Further amplifying the potential number of unique antibodies that can be formed, junctional diversity arises from the addition and subtraction of nucleotides at the ends of gene segments during recombination (5). Thus, the diversity of the naïve antibody repertoire ensures that any potential pathogen will be recognized.

Fc domain variants then direct effector functions tailored to the recognized pathogen. Depending on the choice of antibody isotype, subclass, and post-translational glycosylation, antibodies may simply neutralize their targets with little recruitment of immune cells, or they may mobilize innate immune cells with phagocytic, cytotoxic, or degranulatory activity (3). The main antibody isotypes are IgM, IgD, IgG, IgA, and IgE, with additional subclasses in mice (IgG1, IgG2a/c, IgG2b, IgG3) and humans (IgG1, IgG2, IgG3, IgG4, IgA1, IgA2) (3). The effector functions dictated by these isotypes and subclasses depend on both the Fc receptors (FcRs) that they bind and the expression of those receptors across immune cells (6). For example, mouse IgG2a/c, the predominant IgG subclass induced during type 1 immunity, is the main ligand for monocyte- and macrophage-expressed Fc γ RI (7). While mice deficient for Fc γ RI develop normal levels of IgG2a antibodies, they exhibit impaired clearance of bacterial infection (7), demonstrating the importance of IgG2a-Fc γ RI interactions for full-fledged effector responses. Similarly, recent work with severe acute respiratory syndrome coronavirus 2 (SARS-CoV-2) has shown that neutralizing antibodies with and without a functional Fc domain equivalently inhibit viral replication *in vitro*; however, optimal protection *in vivo* relies on Fc engagement of monocytes, neutrophils, and natural killer cells (8–10). In the case of type 2 immune responses, IgE antibodies are bound by Fc ϵ RI on mast cells. Upon IgE recognition of antigen, Fc ϵ RI crosslinking precipitates the release of mast cell mediators that stimulate increased vascular permeability, airway smooth muscle contraction, and mucus secretion (11). Fc glycosylation of each isotype and subclass further fine-tunes antibody activity by modulating FcR binding affinity, localization, and stability (3).

Though antibodies are small – only about 10 nm in size (12) – their ability to recognize specific targets and trigger precise effector responses makes them a powerful component of the

immune response. For instance, antibodies against SARS-CoV-2 work both prophylactically and therapeutically to prevent severe disease (13). When instead directed against innocuous or self-antigens, antibodies can promote life-threatening pathology such as anaphylaxis in a peanut-allergic child or systemic autoimmunity in patients with lupus (11, 14). Therefore, identifying the cellular and molecular pathways that regulate antibody production is critical for developing strategies to induce protective antibodies and prevent the production of pathogenic antibodies.

T follicular helper cells are the conventional drivers of antibody responses

With the exception of T-independent antibody responses induced by certain microbial antigens, most antibody responses rely on the collaboration between B cells and CD4⁺ T cells (15). CD4⁺ T cells that recognize the same antigen as a B cell license its activation through the provision of contact-dependent CD40L and secreted cytokines such as IL-21 (16, 17). T cell-derived CD40L and cytokines also direct isotype switching and formation of the germinal center (GC), the predominant site at which B cells undergo sequential rounds of somatic hypermutation and selection leading to affinity maturation of their B cell receptor (BCR) (18). Thus, CD4⁺ T cells instruct the generation of highly specific antibody responses with pathogen-appropriate Fc effector functions.

Work over the past two decades has identified T follicular helper (Tfh) cells as the particular CD4⁺ T cell subset specialized for helping B cells (19). Tfh cells can be distinguished from other CD4⁺ T cell subsets by their expression of lineage-defining transcription factor BCL6 as well as receptors CXCR5 and PD-1 that regulate their positioning and function in B cell follicles (20–24). Highlighting the importance of Tfh cell help for GC formation, T cell-specific deletion of *Bcl6* completely abrogates GCs (20–22, 25). Additionally, Tfh cells have been found to regulate

the antibody response to diverse immune stimuli, from infection to immunization during type 1 and type 2 immune responses.

Mouse models of Tfh cell deficiency or dysfunction have elucidated the critical role of Tfh cells during viral infection. For example, mice lacking Tfh cells due to *Bcl6*, *Stat3*, or *Ascl2* deletion demonstrate impaired IgG responses to Zika virus, acute lymphocytic choriomeningitis virus (LCMV), and influenza virus infection (26–28). In mice with CD4⁺ T cell-specific loss of CXCR5, lower IgG antibody titers in response to chronic LCMV infection result in a failure to control the virus (29, 30). Furthermore, SAP deficiency disrupts the formation of stable cognate Tfh cell-B cell conjugates, leading to defective antibody responses to acute LCMV and influenza virus (31–33). Defects in the antibody response are especially pronounced at later timepoints, consistent with the inability of these mice to generate long-lived plasma cells (32, 33). Similar to viral infection, protective IgG antibody responses to bacterial infection also rely on Tfh cells (34, 35). In addition, though certain vaccine strategies have been found to induce Tfh-independent class-switched antibody responses, these antibodies are of lower affinity (36, 37). Thus, during type 1 immune responses, high-affinity, class-switched, long-lived humoral immunity is largely thought to be Tfh-dependent.

Tfh cells also promote antibody production during type 2 immune responses. Helminth infections with *Nippostrongylus brasiliensis* and *Heligmosomoides polygyrus bakeri* have demonstrated that Tfh cells are required for pathogen-specific IgE and IgG1 (38, 39). Similarly, IgE and IgG1 antibody production against allergens, including house dust mite, *Alternaria alternata*, and peanut flour, is abrogated in mice lacking Tfh cells (40–42). Tfh cell-derived cytokines are also crucial for these antibody responses and cannot be compensated by cytokine production in other CD4⁺ T cell compartments (43). Specifically, Tfh cell-derived IL-4 is required

for antigen-specific IgE antibodies, and Tfh cell-derived IL-13 is necessary for the production of high-affinity IgE antibodies that mediate anaphylaxis (39, 44). Taken together, Tfh cells are the major, if not obligate, drivers of antibody responses to a diverse array of immune stimuli.

Tfh-independent responses may also generate protective antibodies

Given that many antibody responses rely on Tfh cell help, this raises the question of what happens to antibody production when Tfh cells and GCs are disrupted. Several infections are known to impair Tfh cells and GCs, including recent observations of Tfh cell and GC loss in patients with severe coronavirus disease 2019 (COVID-19) (45–47). Furthermore, normal aging is accompanied by reductions in the naïve T cell population, T cell receptor (TCR) repertoire, T cell activation, and Tfh cell differentiation and function, all of which contribute to decreased GC and antibody responses in older individuals (48). It is therefore important to understand whether antibodies can be generated through complementary pathways in the setting of Tfh/GC impairment, which would inform the development of vaccine strategies that can work more effectively under such circumstances.

Despite a loss of Tfh cells and GC structures in severe COVID-19, T cell-B cell interactions and antibody class switching still occur in the secondary lymphoid organs of these patients (46). Findings of enhanced extrafollicular B cell responses associated with severe disease further suggest that non-canonical pathways of antibody production may be operative in these individuals (46, 49). However, a causal relationship between antibody provenance and disease severity cannot be established by existing human studies. Thus, it remains unclear whether antibodies produced through non-canonical pathways without Tfh cell help are also protective against SARS-CoV-2.

In the setting of vaccination, certain vaccine strategies have been found to induce robust Tfh-independent antibody or B cell responses (36, 50). For example, vaccination of Tfh-deficient mice with inactivated influenza virus in aluminum hydroxide leads to the generation of IgG2 antibodies that are less mutated and of lower avidity, but still neutralize influenza *in vitro* and protect from lethal challenge *in vivo* (36). Furthermore, the induction of class-switched antigen-specific plasmablasts following immunization with 2W-PE in complete Freund's adjuvant relies on T cell help but no particular subset (e.g. Tfh, Th1, Th17) (50), indicating that multiple CD4⁺ T cell subsets may have the ability to help B cells in response to certain immune stimuli (51). Yet, other vaccine strategies fail to induce durable or class-switched antibodies in mice with Tfh cell deficiency or dysfunction (25, 33, 37, 52). In humans, circulating Tfh cell populations in the blood also correlate with the response to vaccination (53–55). Taken together, while non-Tfh CD4⁺ T cells can promote effective antibodies in certain contexts, protective anti-pathogen humoral immunity is largely thought to be Tfh-dependent.

Goals of thesis

The overarching goals of my thesis were to elucidate how CD4⁺ T cells and the cytokines they produce regulate the production of antibodies to infection and immunization. In Chapter 2, I studied the Tfh-dependent and -independent antibody responses to SARS-CoV-2 infection, SARS-CoV-2 vaccination, and influenza A virus infection, finding that Tfh cells are required for antibody quantity but not quality. In Chapter 3, I investigated the role of Tfh cell-derived IL-4 during type 1 immune responses, clarifying its requirement for IgG1 switching and dispensability for GC B cell formation and plasmablast differentiation. The motivation for Chapter 4, which I began working on at the start of the pandemic, was to interrogate the effect that nonsteroidal anti-

inflammatory drugs (NSAIDs) could have on COVID-19 pathogenesis. Our findings that NSAIDs impaired the early antibody response to SARS-CoV-2 are a reminder that commonly used medications can have unanticipated effects on the antiviral immune response. Collectively, the work in this thesis broadens our understanding of the diverse mechanisms that regulate the development of humoral immunity.

§ CHAPTER 2: High-affinity, neutralizing antibodies to SARS-CoV-2 can be made in the absence of T follicular helper cells

SARS-CoV-2 infection and vaccination induce Tfh-dependent and -independent antibodies

To study the cellular pathways that promote antibody production to SARS-CoV-2, we used mice that lack different CD4⁺ T cell subsets. *Bcl6*^{fl/fl}*Cd4*^{Cre} mice are a well-established model of Tfh cell deficiency due to deletion of the Tfh lineage-defining transcription factor BCL6 (25, 26, 41). *Ciita*^{-/-} mice lack all CD4⁺ T cells due to loss of MHC class II expression (56). As SARS-CoV-2 is unable to efficiently interact with mouse ACE2, we utilized two models of human ACE2 (hACE2) overexpression: adeno-associated virus (AAV)-mediated expression of hACE2 (AAV-hACE2) in the respiratory tract, and K18-hACE2 transgenic mice, which express hACE2 in epithelial cells (57–59).

For the AAV-hACE2 model, AAV9 expressing hACE2 from a CMV promoter was administered into the respiratory tract by intratracheal injection, and two weeks later the mice were infected intranasally with SARS-CoV-2 (58). This model allowed us to quickly use our mice lacking different CD4⁺ T cell subsets, without having to wait to cross them to hACE2-expressing mice. However, it is possible that pre-exposing mice to AAV could affect their subsequent immune response to SARS-CoV-2. Furthermore, AAV transduction may lead to hACE2 expression by cell types that normally would not express ACE2. To complement our findings with the AAV-hACE2 model, we crossed our Tfh cell-deficient mice to K18-hACE2 transgenic mice (59). Though K18-hACE2 mice circumvent the issue of AAV pre-exposure and also ensure epithelial cell-specific hACE2 expression, a caveat of both of these hACE2-expressing models is that hACE2 expression is driven by non-*ACE2* promoters, which may lead to non-physiological regulation of ACE2

expression. However, at the time that we began our studies, alternative mouse models of SARS-CoV-2 infection in which ACE2 expression is physiologically regulated were not available to us.

We first assessed the cellular responses to SARS-CoV-2 infection in AAV-hACE2 mice. Two weeks after AAV-hACE2 transduction, we infected mice intranasally with SARS-CoV-2 (isolate USA-WA1/2020). At 14 days post infection (dpi), PD-1^{hi}CXCR5^{hi} Tfh cells were efficiently deleted in the mediastinal LN (medLN) of AAV-hACE2 *Bcl6*^{fl/fl}*Cd4*^{Cre} mice (Fig. S1, A to C). Consistent with the loss of Tfh cells, GC B cells were severely impaired, and plasmablast formation was reduced (Fig. S1, D to H). Yet viral burden in the lungs of AAV-hACE2 *Bcl6*^{fl/fl} and *Bcl6*^{fl/fl}*Cd4*^{Cre} mice was similar at 7 dpi (Fig. S1I). To examine the cellular architecture of the medLN in mice lacking Tfh cells, we performed immunofluorescence on K18-hACE2 *Bcl6*^{fl/fl} and *Bcl6*^{fl/fl}*Cd4*^{Cre} mice at 14 dpi. K18-hACE2 *Bcl6*^{fl/fl} medLN exhibited robust GC formation, with large clusters of activated (GL7⁺) B cells colocalizing with CD35⁺ follicular dendritic cell (FDC) networks and infiltrated by T cells (Fig. S2A), presumably Tfh cells. In contrast, K18-hACE2 *Bcl6*^{fl/fl}*Cd4*^{Cre} medLN displayed a few small clusters of GL7⁺ cells that co-localized with sparse FDC networks but lacked T cells (Fig. S2B), congruent with the absence of Tfh cells. As GL7 is a marker of activated lymphocytes, including those outside of GCs, these rare cellular aggregates lacking T cells could represent sites of T-independent antigen-driven B cell stimulation.

We next determined the humoral responses to SARS-CoV-2 infection in AAV-hACE2 mice at 14 dpi (Fig. 1A). *Bcl6*^{fl/fl} mice produced high levels of spike (S)-specific IgG antibodies (Fig. 1B). While *Bcl6*^{fl/fl}*Cd4*^{Cre} mice had reduced levels of S-specific IgG, they still produced substantially more compared to *Ciita*^{-/-} mice. Among IgG subclasses, S-specific IgG1 and IgG3 were completely Tfh-dependent, while S-specific IgG2b and IgG2c were promoted by both Tfh and non-Tfh CD4⁺ T cells (Fig. 1B). Consistent with their divergent requirement for Tfh cell help,

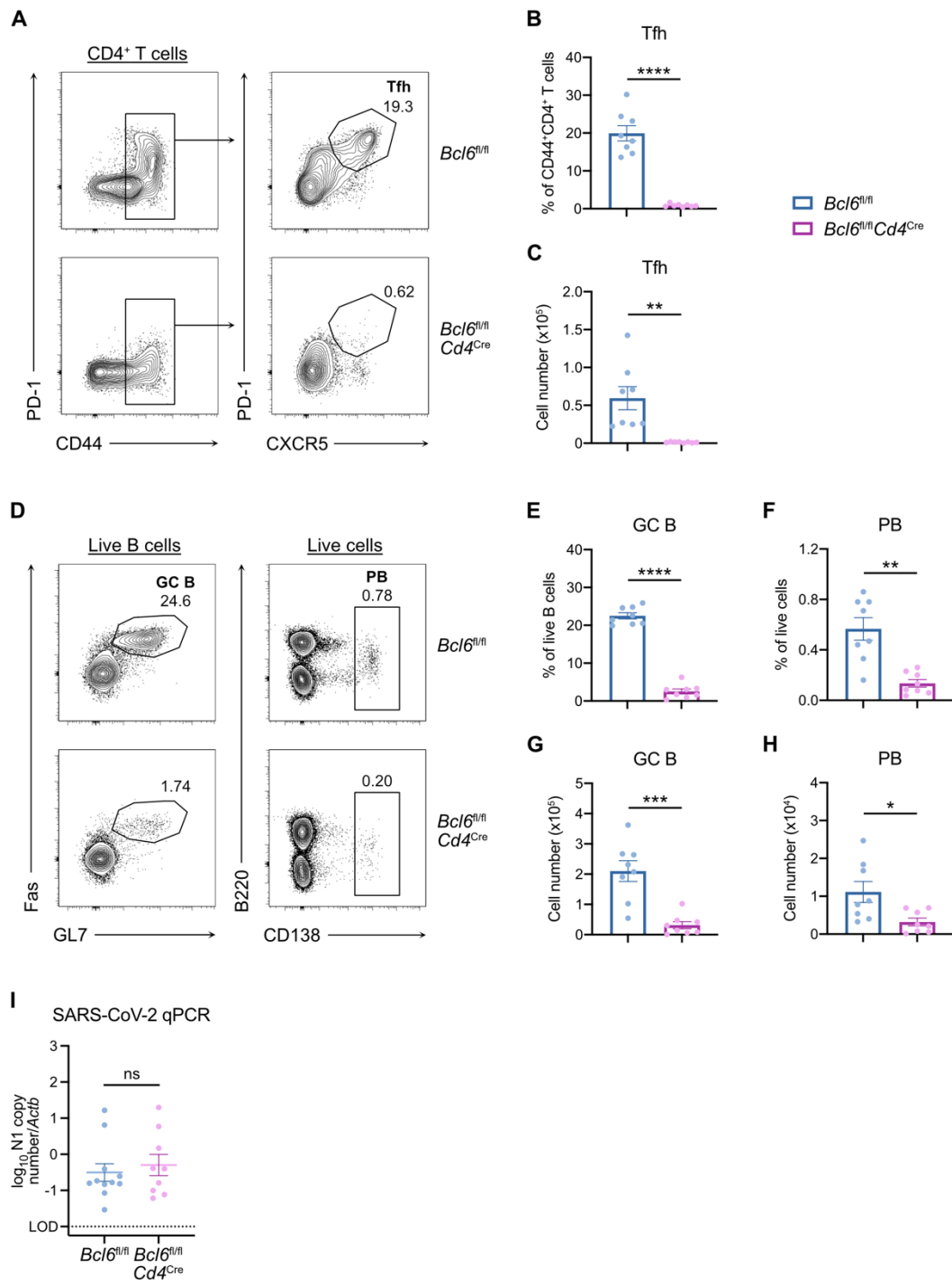
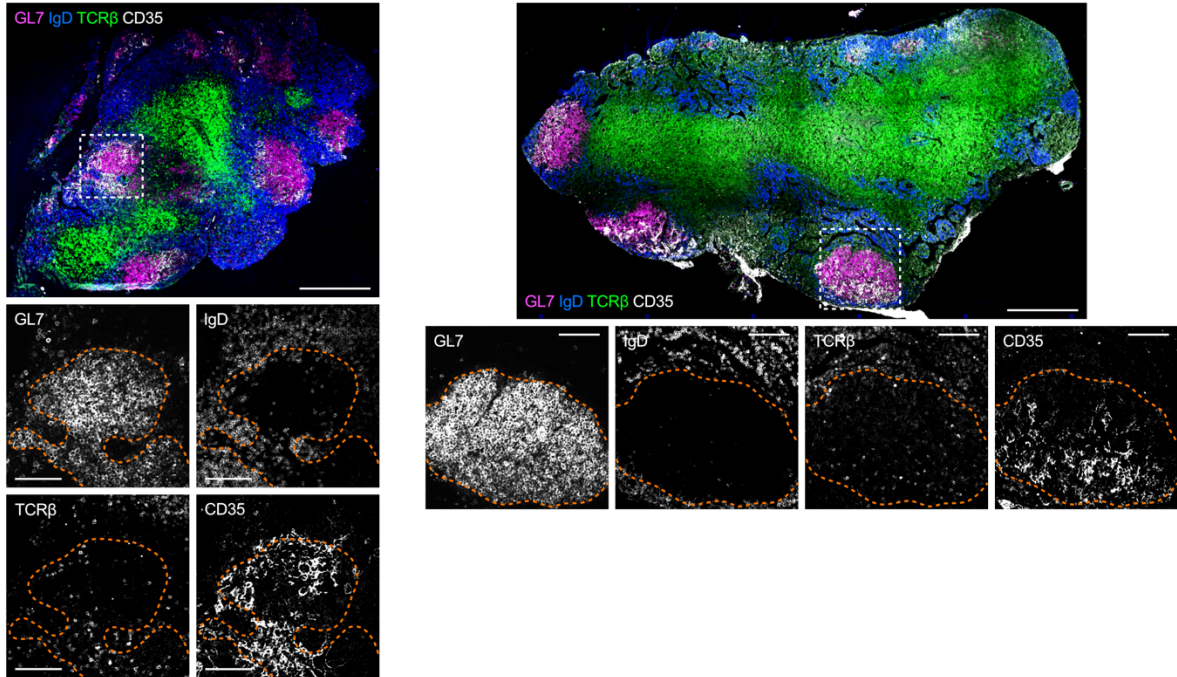


Figure S1: Cellular response to SARS-CoV-2 in Tfh-sufficient and -deficient mice
 (A to H) Flow cytometric analysis of mediastinal lymph nodes (medLN) from SARS-CoV-2-infected AAV-hACE2 mice at 14 dpi.

(A) Representative gating strategy to identify Tfh cells from total CD4⁺ T cells.
(B and C) Frequency among CD44⁺CD4⁺ T cells (B) and total number (C) of Tfh cells in *Bcl6*^{fl/fl} (blue) or *Bcl6*^{fl/fl}*Cd4*^{Cre} (magenta) mice.
(D) Representative gating strategy to identify germinal center (GC) B cells and plasmablasts (PB).
(E and F) Frequencies of GC B cells (E) and PB (F) in *Bcl6*^{fl/fl} (blue) or *Bcl6*^{fl/fl}*Cd4*^{Cre} (magenta) mice.
(G and H) Total number of GC B cells (G) and PB (H) in *Bcl6*^{fl/fl} (blue) or *Bcl6*^{fl/fl}*Cd4*^{Cre} (magenta) mice.
(I) Viral burden in lungs from AAV-hACE2 *Bcl6*^{fl/fl} mice or *Bcl6*^{fl/fl}*Cd4*^{Cre} mice infected with SARS-CoV-2 at 7 dpi. Data are expressed as log₁₀ N1 gene copy number by qPCR, normalized to *Actb*.
LOD, limit of detection of the assay. Statistical significance was assessed by either two-tailed unpaired t-test or Welch's t-test, based on the F test for unequal variance (B and C, E to I). **P* < 0.05; ***P* < 0.01; ****P* < 0.001; *****P* < 0.0001. ns, not significant. Data are expressed as mean ± standard error of mean (SEM). Each symbol in (B and C, E to I) represents an individual mouse. Data are aggregated from at least two independent experiments.

A *K18-hACE2 Bcl6^{fl/fl}*



B *K18-hACE2 Bcl6^{fl/fl} Cd4^{Cre}*

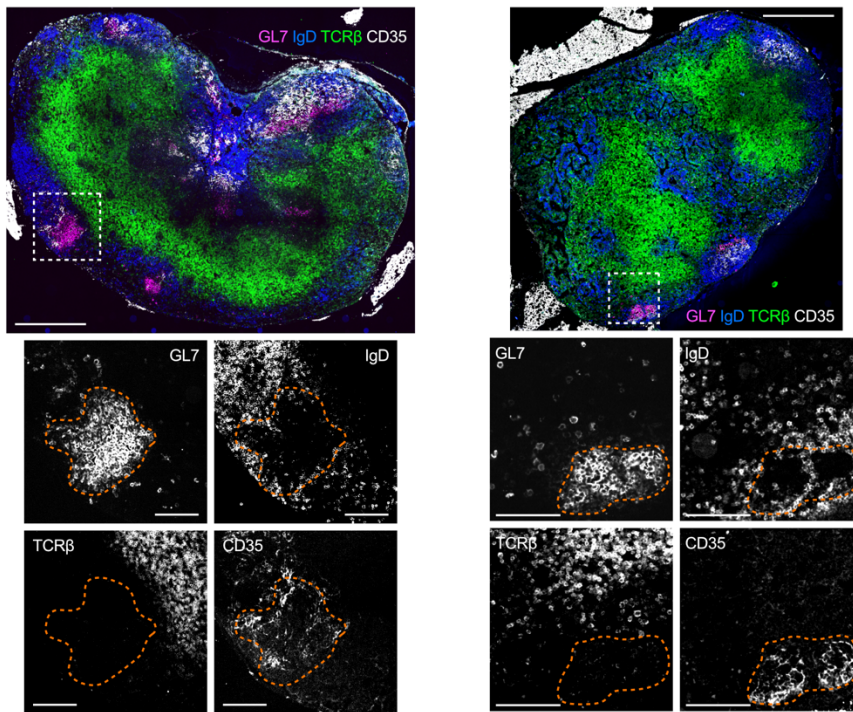


Figure S2: Lymph node structures of Tfh-sufficient and -deficient mice following SARS-CoV-2 infection

(A and B) Immunofluorescence of medLN from K18-hACE2 *Bcl6^{fl/fl}* (A) or K18-hACE2 *Bcl6^{fl/fl}Cd4^{Cre}* (B) mice infected with SARS-CoV-2 at 14 dpi. GL7 (magenta), IgD (blue), TCR β (green), CD35 (white). White dashed line demarcates region shown below at higher magnification. Orange dashed line demarcates GL7⁺ areas. Representative images from three mice per condition; scale bars, 400 μ m and 100 μ m (higher magnification).

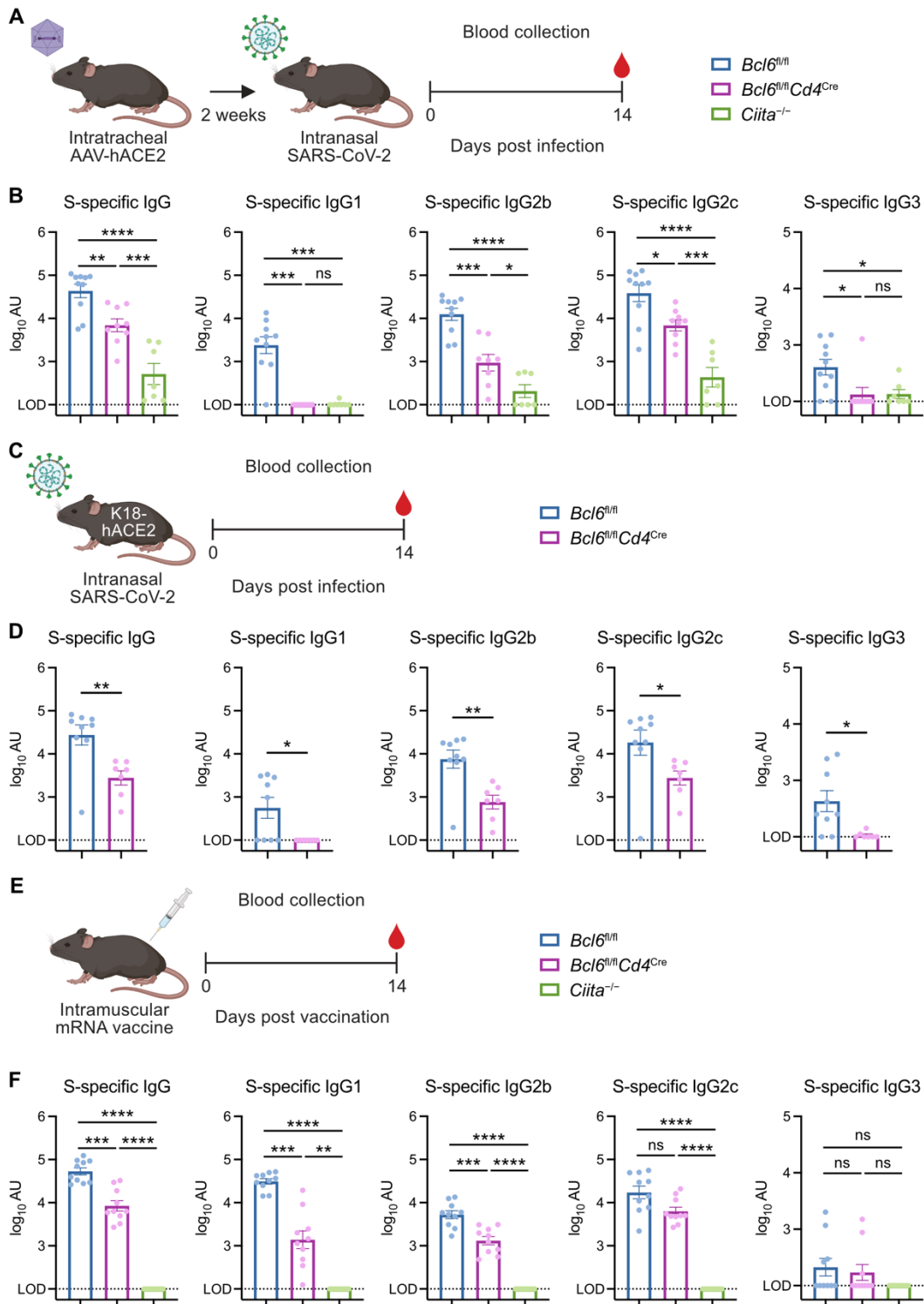


Figure 1: SARS-CoV-2 infection and vaccination induce Tfh-dependent and -independent antibodies

(A) Schematic of experimental design for assessing serum antibody responses against SARS-CoV-2 in AAV-hACE2 mice. Mice were infected intranasally with SARS-CoV-2 (isolate USA-WA1/2020) two weeks following intratracheal administration of AAV-hACE2. Sera were collected 14 days post infection (dpi) for quantification of antibody titers by ELISA.

(B) Spike (S)-specific total IgG, IgG1, IgG2b, IgG2c, and IgG3 antibody titers in sera from control (*Bcl6^{fl/fl}*; blue symbol), Tfh-deficient (*Bcl6^{fl/fl}Cd4^{Cre}*; magenta symbol), or CD4⁺ T cell-deficient (*Ciita^{-/-}*; green symbol) mice at 14 dpi with SARS-CoV-2.

(C) Schematic of experimental design for assessing serum antibody responses against SARS-CoV-2 in K18-hACE2 mice. Mice were infected with SARS-CoV-2 (isolate USA-WA1/2020) by intranasal administration. Sera were collected at 14 dpi for quantification of antibody titers by ELISA.

(D) S-specific total IgG, IgG1, IgG2b, IgG2c, and IgG3 antibody titers in sera from K18-hACE2 *Bcl6^{fl/fl}* (blue) or K18-hACE2 *Bcl6^{fl/fl}Cd4^{Cre}* (magenta) mice at 14 dpi with SARS-CoV-2.

(E) Schematic of experimental design for assessing serum antibody responses against SARS-CoV-2 mRNA vaccination. Mice were vaccinated intramuscularly with Moderna mRNA-1273 or Pfizer-BioNTech BNT162b2 mRNA vaccine. Sera were collected 14 days post vaccination (dpv) for quantification of antibody titers by ELISA.

(F) S-specific total IgG, IgG1, IgG2b, IgG2c, and IgG3 antibody titers in sera from *Bcl6^{fl/fl}* (blue), *Bcl6^{fl/fl}Cd4^{Cre}* (magenta), or *Ciita^{-/-}* (green) mice at 14 dpv with mRNA vaccine.

LOD, limit of detection of the assay. Statistical significance was assessed by one-way ANOVA with Tukey's test, or Welch's t-test with Bonferroni multiple hypothesis correction when sample variances were 0 (B and F); two-tailed unpaired t-test or Welch's t-test, based on the F test for unequal variance (D). * $P < 0.05$; ** $P < 0.01$; *** $P < 0.001$; **** $P < 0.0001$. ns, not significant. Data are expressed as mean \pm standard error of mean (SEM) \log_{10} arbitrary units (AU). Each symbol represents an individual mouse. Data are aggregated from at least two independent experiments.

S-specific IgG2c was induced earlier than S-specific IgG1 (Fig. S3A). S-specific IgM was unaffected by the absence of Tfh cells (Fig. S3B). Together, these results suggest that both Tfh cells and non-Tfh CD4⁺ T cells promote the production of class-switched antibodies to SARS-CoV-2, though Tfh cells are uniquely able to induce certain subclasses.

To corroborate these findings with a model that does not require AAV pre-transduction, we measured serum antibody titers of K18-hACE2 *Bcl6*^{fl/fl} and *Bcl6*^{fl/fl}*Cd4*^{Cre} mice at 14 dpi with SARS-CoV-2 (Fig. 1C). K18-hACE2 *Bcl6*^{fl/fl}*Cd4*^{Cre} mice produced substantial levels of S-specific IgG antibodies, though reduced compared to K18-hACE2 *Bcl6*^{fl/fl} mice (Fig. 1D). K18-hACE2 *Bcl6*^{fl/fl}*Cd4*^{Cre} mice also demonstrated similar patterns of IgG subclass production to AAV-hACE2 *Bcl6*^{fl/fl}*Cd4*^{Cre} mice. While S-specific IgG1 and IgG3 were completely abrogated in the absence of Tfh cells, S-specific IgG2b, IgG2c, and IgM were only partially reduced (Fig. 1D and S3C). This alternative model of SARS-CoV-2 infection therefore confirmed that certain IgG subclasses could be generated through Tfh-independent mechanisms.

Having observed Tfh-independent class-switched antibody production to SARS-CoV-2 infection, we asked whether this could also happen during non-live pathogen-driven immune stimulation such as vaccination. We hypothesized that while the strong and prolonged inflammatory response caused by infection might overcome the requirement for Tfh cell help, antibodies to vaccination would still be fully Tfh-dependent. We therefore vaccinated mice intramuscularly with a single dose of Moderna mRNA-1273 or Pfizer-BioNTech BNT162b2 mRNA vaccine and evaluated antibody responses at 14 days post vaccination (Fig. 1E). As with SARS-CoV-2 infection, mRNA vaccination induced both Tfh- and non-Tfh CD4⁺ T cell-dependent S-specific IgG antibodies (Fig. 1F). mRNA vaccination promoted higher levels of S-specific IgG1 compared to infection, and some IgG1 could even be made in the absence of Tfh

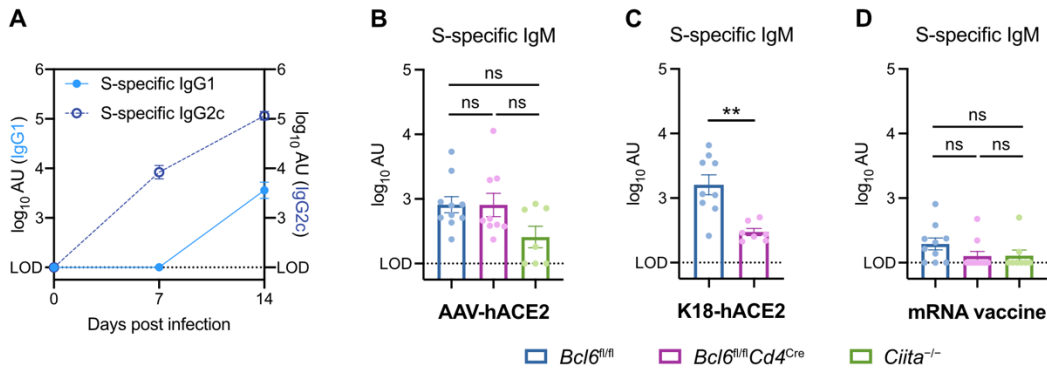


Figure S3: Humoral response to SARS-CoV-2 in Tfh-sufficient and -deficient mice

(A) Time course of S-specific IgG1 and IgG2c serum antibody titers from AAV-hACE2 *Bcl6^{fl/fl}* mice infected with SARS-CoV-2.

(B) S-specific IgM titers in sera from AAV-hACE2 *Bcl6^{fl/fl}* (blue), *Bcl6^{fl/fl}Cd4^{Cre}* (magenta), or *Ciita^{-/-}* (green) mice at 14 dpi with SARS-CoV-2.

(C) S-specific IgM titers in sera from K18-hACE2 *Bcl6^{fl/fl}* (blue) or K18-hACE2 *Bcl6^{fl/fl}Cd4^{Cre}* (magenta) mice at 14 dpi with SARS-CoV-2.

(D) S-specific IgM titers in sera from *Bcl6^{fl/fl}* (blue), *Bcl6^{fl/fl}Cd4^{Cre}* (magenta), or *Ciita^{-/-}* (green) mice at 14 dpv with mRNA vaccine.

LOD, limit of detection of the assay. Statistical significance was assessed by one-way ANOVA with Tukey's test (B and D) or two-tailed Welch's t-test (C). ** $P < 0.01$. ns, not significant. Data are expressed as mean \pm SEM. Each symbol in (A) represents the mean of six mice. Each symbol in (B to D) represents an individual mouse. Data are aggregated from at least two independent experiments.

cells, contrasting with the complete Tfh cell dependence of infection-induced IgG1. S-specific IgG2b and IgG2c could similarly be made without Tfh cell help. S-specific IgG3 and IgM were minimally induced by mRNA vaccination (Fig. 1F and S3D). Therefore, class-switched antibodies to SARS-CoV-2 infection and vaccination are generated through both Tfh-dependent and -independent mechanisms.

Influenza virus infection induces Tfh-dependent and -independent antibodies

We next determined whether our findings with SARS-CoV-2 infection were generalizable to other models of respiratory viral infection. To this end, we infected mice with mouse-adapted influenza virus A/PR/8/34 H1N1 (PR8) and assessed antibody production at 14 dpi (Fig. 2A). Similar to SARS-CoV-2 infection, PR8 infection induced both Tfh-dependent and non-Tfh CD4⁺ T cell-dependent IgG antibodies, while IgM was largely CD4⁺ T cell-independent (Fig. 2, B and C). Again, PR8-specific IgG1 demonstrated a complete dependence on Tfh cell help, while PR8-specific IgG2b and IgG2c were promoted by both Tfh-dependent and -independent pathways (Fig. 2D). PR8-specific IgG3 was only partially dependent on Tfh and CD4⁺ T cell help (Fig. 2D). Thus, both Tfh and non-Tfh CD4⁺ T cells contribute to antibody production in two distinct models of respiratory viral infection.

Durable, high-affinity antibodies to SARS-CoV-2 can be made in the absence of Tfh cells

We then measured the affinity of the antibodies generated during SARS-CoV-2 and PR8 infection using a modified ELISA that incorporates a urea wash step to dissociate low-affinity antibodies. As GCs are the conventional site of somatic hypermutation and affinity maturation (19), we expected that *Bcl6*^{fl/fl} mice would generate high-affinity antibodies while *Bcl6*^{fl/fl}*Cd4*^{Cre} mice

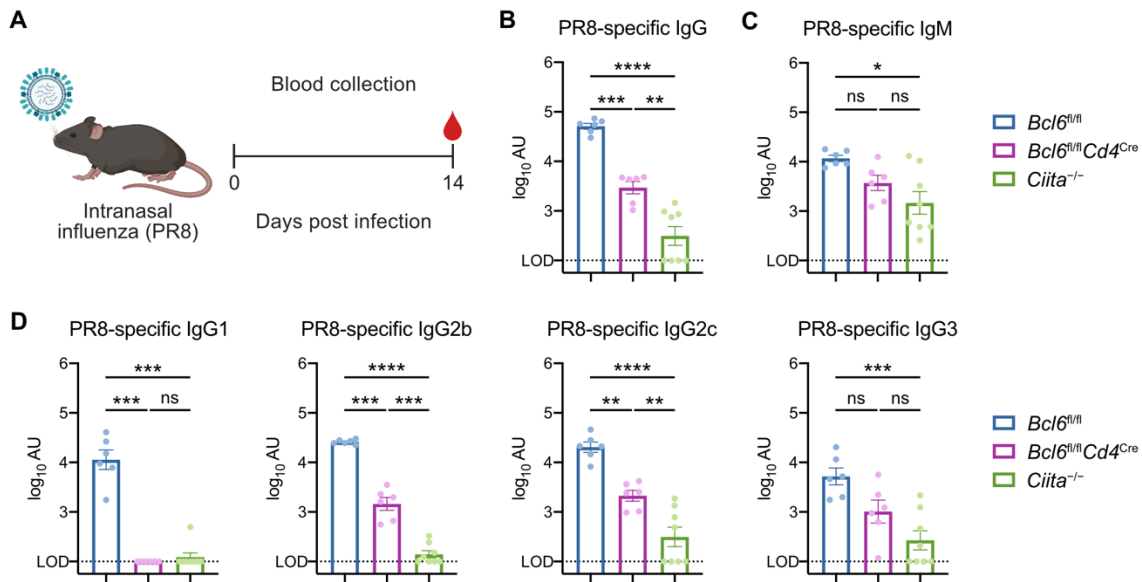


Figure 2: Influenza virus infection induces Tfh-dependent and -independent antibodies

(A) Schematic of experimental design for assessing serum antibody responses against influenza virus. Mice were infected with mouse-adapted influenza virus (PR8) by intranasal administration. Sera were collected at 14 dpi for quantification of antibody titers by ELISA.

(B and C) PR8-specific total IgG (B) and IgM (C) antibody titers in sera from $Bcl6^{fl/fl}$ (blue), $Bcl6^{fl/fl}Cd4^{Cre}$ (magenta), or $Ciita^{-/-}$ (green) mice at 14 dpi with PR8.

(D) PR8-specific IgG1, IgG2b, IgG2c, and IgG3 antibody titers at 14 dpi with PR8.

LOD, limit of detection of the assay. Statistical significance was assessed by one-way ANOVA with Tukey's test or Dunnett's test, or Welch's t-test with Bonferroni multiple hypothesis correction when sample variances were 0 (B to D). * $P < 0.05$; ** $P < 0.01$; *** $P < 0.001$; **** $P < 0.0001$. ns, not significant. Data are expressed as mean \pm SEM \log_{10} arbitrary units (AU). Each symbol represents an individual mouse. Data are aggregated from two independent experiments.

would generate low-affinity antibodies. Using the AAV-hACE2 model, we observed that *Bcl6*^{fl/fl} mice produced high-affinity IgG antibodies to S as well as the spike receptor-binding domain (RBD) (Fig. 3A), a major target of neutralizing antibodies (60). In contrast, S- and RBD-specific IgG antibodies from *Ciita*^{-/-} mice displayed minimal affinity. However, we discovered that antibodies from *Bcl6*^{fl/fl}*Cd4*^{Cre} mice still demonstrated substantial affinity toward S and RBD, suggesting that non-Tfh CD4⁺ T cells could also promote high-affinity antibody production.

Similarly, both K18-hACE2 *Bcl6*^{fl/fl} and *Bcl6*^{fl/fl}*Cd4*^{Cre} mice produced high-affinity antibodies to S and RBD (Fig. 3B), indicating that non-Tfh cells can support high-affinity antibody production in two separate models of SARS-CoV-2 infection. However, this was not the case with PR8 infection, as *Bcl6*^{fl/fl}*Cd4*^{Cre} mice produced IgG antibodies of minimal affinity to both PR8 and PR8 surface glycoprotein hemagglutinin (HA) (Fig. 3C). Therefore, the ability of non-Tfh cells to promote high-affinity antibodies may depend on the nature of the viral infection and the antigenic target.

We also evaluated the durability of S-specific IgG antibodies produced by K18-hACE2 *Bcl6*^{fl/fl} and *Bcl6*^{fl/fl}*Cd4*^{Cre} mice following SARS-CoV-2 infection. Previous studies of viral infection have shown that antibody titers in Tfh-impaired mice are especially reduced at later timepoints (26, 32, 33). In SARS-CoV-2-infected K18-hACE2 *Bcl6*^{fl/fl} mice, S-specific IgG levels peaked at 28 dpi and were stable through 84 dpi (Fig. 3, D and E). In K18-hACE2 *Bcl6*^{fl/fl}*Cd4*^{Cre} mice, S-specific IgG antibodies slowly declined after 28 dpi, but at 84 dpi still retained 50% of the antibody titer of 28 dpi (Fig. 3E and S4A). AAV-hACE2 *Bcl6*^{fl/fl} and *Bcl6*^{fl/fl}*Cd4*^{Cre} mice displayed a similar pattern of antibody kinetics (Fig. S4, B and C).

Given that both *Bcl6*^{fl/fl} and *Bcl6*^{fl/fl}*Cd4*^{Cre} mice demonstrated persistent S-specific IgG antibodies several months after infection, we investigated whether they had developed a virus-

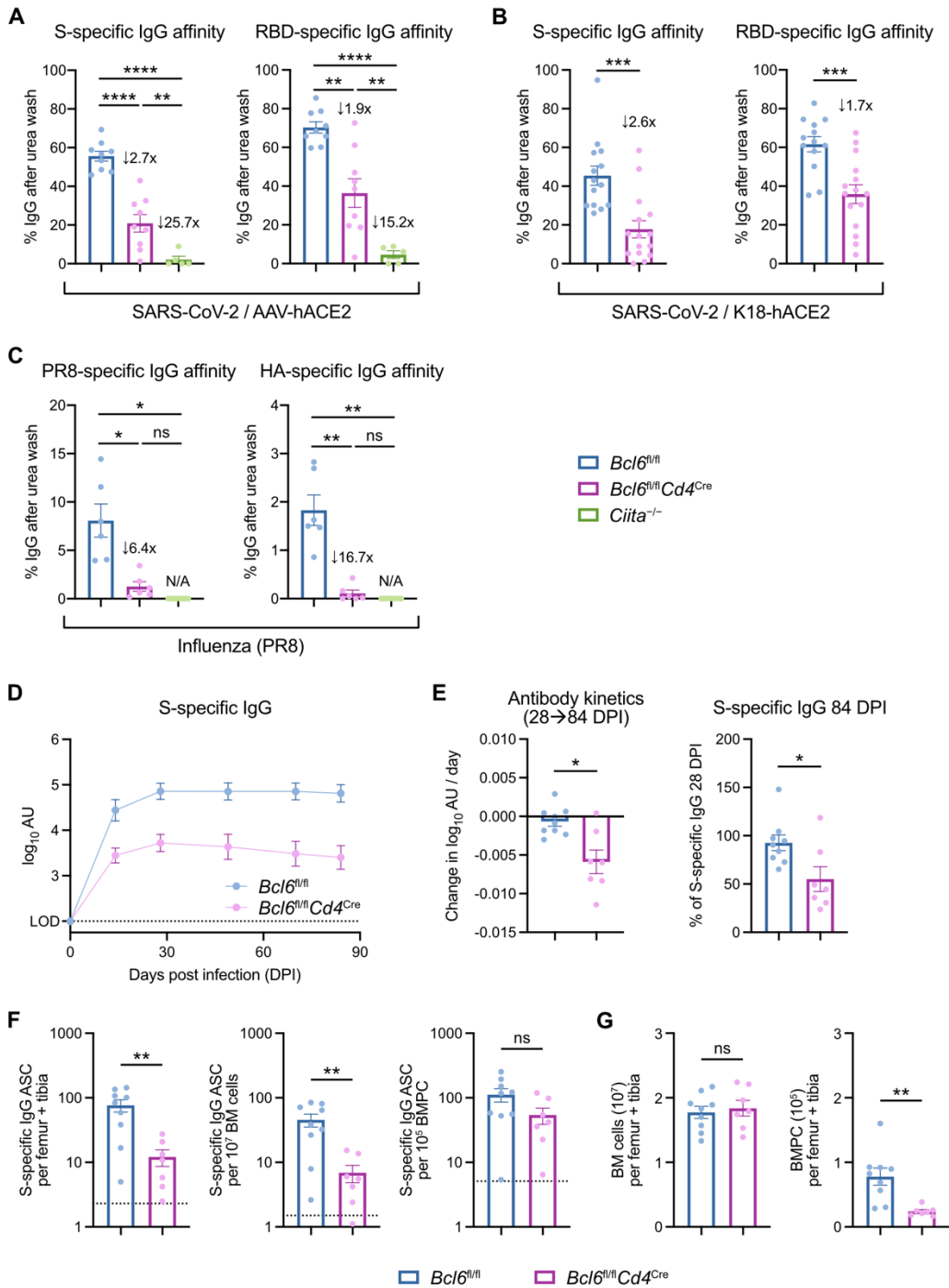


Figure 3: Durable, high-affinity antibodies to SARS-CoV-2 can be made in the absence of Tfh cells

(A) Affinity index of serum IgG antibodies against SARS-CoV-2 S (left) or RBD (right), calculated as relative ELISA signal after urea wash. Sera are from AAV-hACE2 *Bcl6^{fl/fl}* (blue),

Bcl6^{fl/fl}Cd4^{Cre} (magenta), or *Ciita^{-/-}* (green) mice infected with SARS-CoV-2 at 14 dpi. Fold changes relative to *Bcl6^{fl/fl}* mice are annotated.

(B) Affinity index of serum IgG antibodies against SARS-CoV-2 S (left) or RBD (right). Sera are from K18-hACE2 *Bcl6^{fl/fl}* (blue) or K18-hACE2 *Bcl6^{fl/fl}Cd4^{Cre}* (magenta) mice infected with SARS-CoV-2 at 14 dpi. Fold changes relative to K18-hACE2 *Bcl6^{fl/fl}* mice are annotated.

(C) Affinity index of serum IgG antibodies against PR8 (left) or HA (right), calculated as relative ELISA signal after urea wash. Sera are from *Bcl6^{fl/fl}* (blue), *Bcl6^{fl/fl}Cd4^{Cre}* (magenta), or *Ciita^{-/-}* (green) mice infected with PR8 at 14 dpi. Fold changes relative to *Bcl6^{fl/fl}* mice are annotated.

(D) Longitudinal dynamics of S-specific IgG antibodies up to 84 dpi, in sera from K18-hACE2 *Bcl6^{fl/fl}* or K18-hACE2 *Bcl6^{fl/fl}Cd4^{Cre}* mice infected with SARS-CoV-2.

(E) Change in S-specific IgG antibody titer per day between 28 and 84 dpi, as determined by linear regression (left). Relative titers of S-specific IgG at 84 dpi, compared to S-specific IgG at 28 dpi (right).

(F) ELISpot quantification of S-specific IgG antibody-secreting cells (ASC) in the bone marrow of K18-hACE2 *Bcl6^{fl/fl}* or K18-hACE2 *Bcl6^{fl/fl}Cd4^{Cre}* mice at 85 dpi with SARS-CoV-2. S-specific IgG ASC per femur + tibia (left), per 10⁷ bone marrow (BM) cells (middle), or per 10⁵ CD138⁺ bone marrow plasma cells (BMPC) (right). Dotted line indicates background signal from naïve mice.

(G) Total number of BM cells (left) and CD138⁺ BMPC (right) in femur + tibia of K18-hACE2 *Bcl6^{fl/fl}* or K18-hACE2 *Bcl6^{fl/fl}Cd4^{Cre}* mice at 85 dpi with SARS-CoV-2.

Statistical significance was assessed by one-way ANOVA with Dunnett's test, or Welch's t-test with Bonferroni multiple hypothesis correction when sample variances were 0 (A and C); two-tailed unpaired t-test or Welch's t-test, based on the F test for unequal variance (B, E, G); two-tailed Mann-Whitney test (F). **P* < 0.05; ***P* < 0.01; ****P* < 0.001; *****P* < 0.0001. ns, not significant. Data are expressed as mean ± SEM. Each symbol in (A to C and E to G) represents an individual mouse. Each symbol in (D) represents the mean of nine (*Bcl6^{fl/fl}*) and seven (*Bcl6^{fl/fl}Cd4^{Cre}*) mice. Data are aggregated from at least two independent experiments.

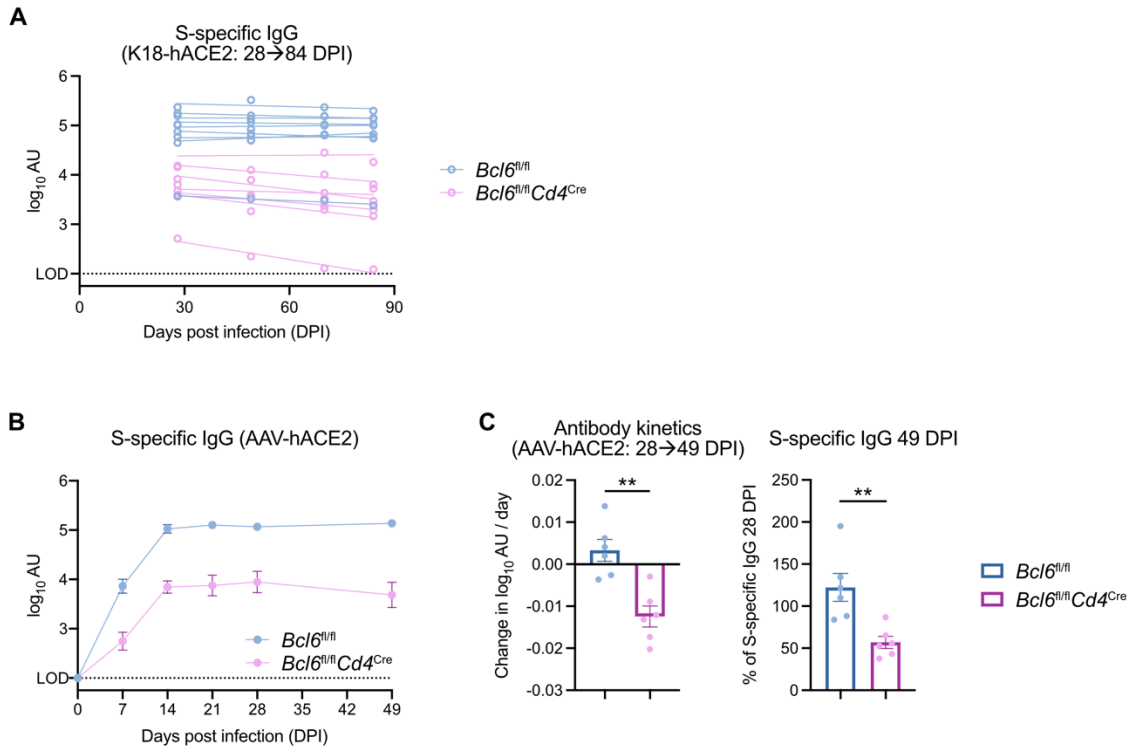


Figure S4: Long-term antibody production in Tfh-sufficient and -deficient mice infected with SARS-CoV-2

(A) S-specific IgG antibody titers between 28 and 84 dpi in sera from K18-hACE2 *Bcl6^{fl/fl}* (blue) or K18-hACE2 *Bcl6^{fl/fl}Cd4^{Cre}* (magenta) mice infected with SARS-CoV-2. Linear regression analyses for each mouse at 28, 49, 70, and 84 dpi are shown.

(B) Longitudinal dynamics of S-specific IgG antibodies up to 49 dpi, in sera from AAV-hACE2 *Bcl6^{fl/fl}* or *Bcl6^{fl/fl}Cd4^{Cre}* mice infected with SARS-CoV-2.

(C) Change in S-specific IgG antibody titer per day between 28 and 49 dpi for AAV-hACE2 mice, as determined by linear regression (left). Relative titers of S-specific IgG at 49 dpi, compared to S-specific IgG at 28 dpi (right).

Statistical significance was assessed by two-tailed unpaired t-test (C). ***P* < 0.01. Data are expressed as mean ± SEM. Each symbol in (A and C) represents an individual mouse. Each symbol in (B) represents the mean of six mice. Data are aggregated from two independent experiments.

specific long-lived plasma cell compartment. We quantified S-specific IgG antibody-secreting cells (ASCs) in the bone marrow of K18-hACE2 *Bcl6^{fl/fl}* and *Bcl6^{fl/fl}Cd4^{Cre}* mice at 85 dpi by ELISpot. S-specific IgG ASCs were detected in both groups of mice, though they were reduced tenfold in Tfh-deficient mice (Fig. 3F). However, Tfh-deficient mice also had fewer total bone marrow plasma cells (BMPCs), so the number of S-specific IgG ASCs per BMPC was similar between *Bcl6^{fl/fl}* and *Bcl6^{fl/fl}Cd4^{Cre}* mice (Fig. 3, F and G). Taken together, these results indicate that Tfh-independent antibodies to SARS-CoV-2 can still be high-affinity and durable – two important qualities usually attributed to Tfh-dependent responses.

Tfh-deficient mice demonstrate similar V gene usage but impaired mutation selection compared to Tfh-sufficient mice

To ascertain how Tfh-deficient mice generate high-affinity antibodies to S and RBD, we considered two non-mutually exclusive hypotheses: 1) unmutated, germline-encoded B cell receptors (BCRs) in the murine V(D)J repertoire may already possess high affinity for S and/or RBD, and 2) S-specific B cells may undergo somatic hypermutation (SHM) even in the absence of Tfh cells and GCs. The former possibility has already been observed for patient-derived SARS-CoV-2-specific antibodies, which demonstrate high potency with minimal SHM (61–65). The latter possibility is supported by prior reports of SHM occurring at extrafollicular sites during chronic autoimmunity and bacterial infection (66–68).

To investigate these two possibilities, we isolated S-specific plasmablasts from K18-hACE2 *Bcl6^{fl/fl}* and *Bcl6^{fl/fl}Cd4^{Cre}* mice at 14 dpi and performed BCR sequencing (Fig. S5, A to B). After read preprocessing and V(D)J gene annotation, we clustered the resulting BCR sequences into clonal families, identifying a range of 131 to 694 distinct clones in each sample (Fig. 4A and

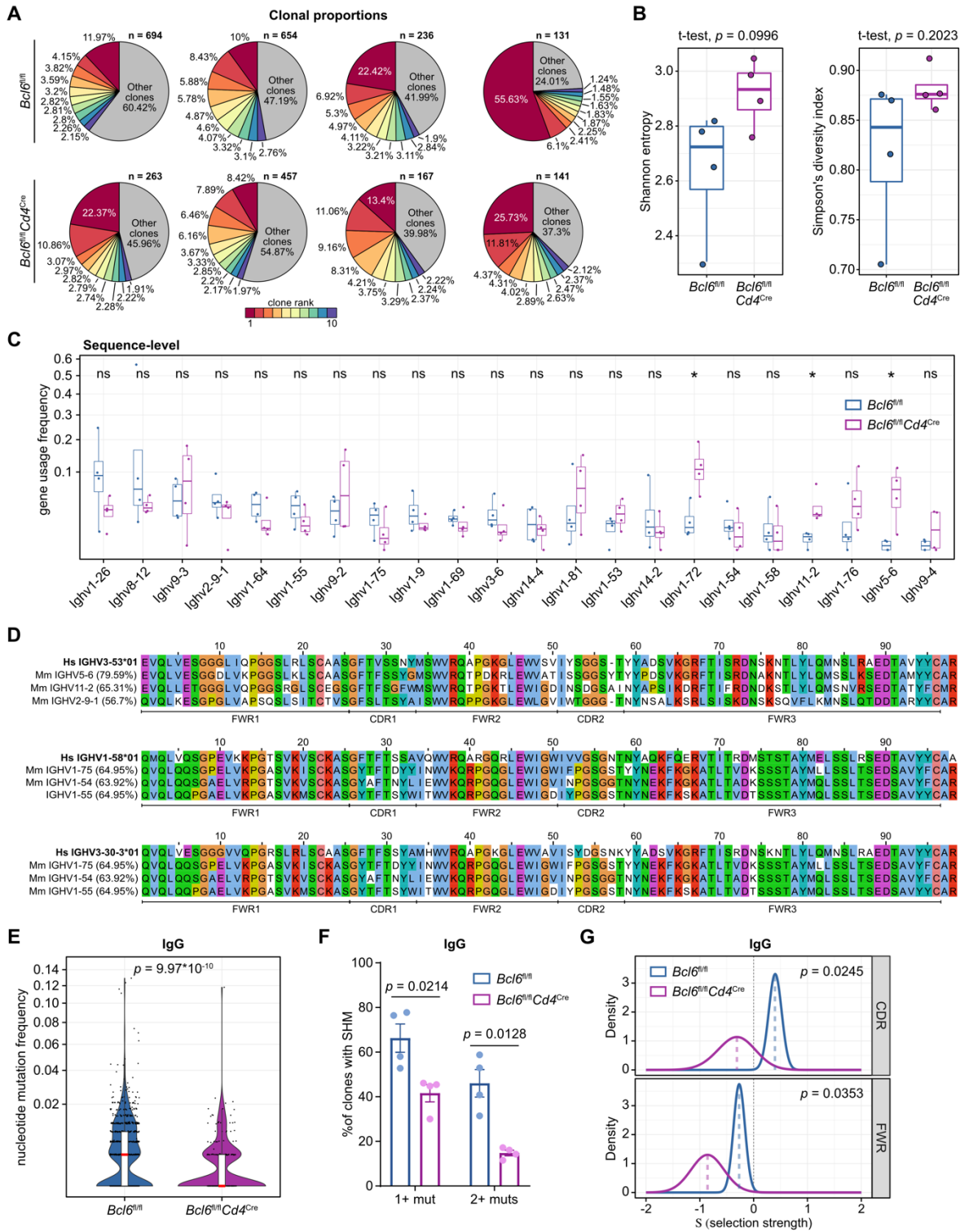


Figure 4: Tfh-deficient mice demonstrate similar V gene usage but impaired mutation selection compared to Tfh-sufficient mice

(A) Pie charts detailing the relative proportions of B cell clones identified in K18-hACE2 *Bcl6*^{fl/fl} (top row) or K18-hACE2 *Bcl6*^{fl/fl}*Cd4*^{Cre} (bottom row) mice infected with SARS-CoV-2 ($n = 4$ mice per condition from one experiment). The 10 largest clones in each sample are shown individually, with all other clones grouped together. The total number of clones in each sample is annotated above each pie chart.

(B) Tukey boxplots detailing Shannon entropy (left) and Simpson's diversity index (right) in *Bcl6*^{fl/fl} or *Bcl6*^{fl/fl}*Cd4*^{Cre} mice. Statistical significance was assessed by two-tailed unpaired Welch's t-test. Each symbol represents an individual mouse BCR repertoire.

(C) Tukey boxplots detailing V gene usage frequencies, calculated on the level of total BCR sequences in each sample. V genes with ≥ 0.02 usage frequency in ≥ 2 samples are shown here. Statistical significance was assessed by two-tailed unpaired Mann-Whitney test. * $P < 0.05$. ns, not significant.

(D) Alignment of human IGHV3-53, IGHV1-58, IGHV3-30-3 segments to the 3 murine V segments shown in (C) with the highest homology to each of the human V segments. The percentage sequence identity relative to the corresponding human V gene (bolded) is indicated on the left. The FWR and CDR regions within the V segments are annotated below.

(E) Violin plots of nucleotide mutation frequencies in IgG-predominant B cell clones from *Bcl6*^{fl/fl} or *Bcl6*^{fl/fl}*Cd4*^{Cre} mice. Red lines indicate median nucleotide mutation frequency. Statistical significance was assessed by two-tailed unpaired Mann-Whitney test.

(F) Quantification of the percentage of IgG-predominant B cell clones with either 1+ or 2+ mutations in *Bcl6*^{fl/fl} or *Bcl6*^{fl/fl}*Cd4*^{Cre} mice. Statistical significance was assessed by two-tailed unpaired Welch's t-test. Data are expressed as mean \pm SEM.

(G) Probability density function curves of selection strength in IgG-predominant B cell clones from *Bcl6*^{fl/fl} or *Bcl6*^{fl/fl}*Cd4*^{Cre} mice, as determined by BASELINE analysis. The density curves are separated by region within the V segment: CDRs (top) or FWRs (bottom). Selection was estimated using BASELINE focused test. Statistical differences between the probability density functions were assessed by a two-sample significance test with numerical integration.

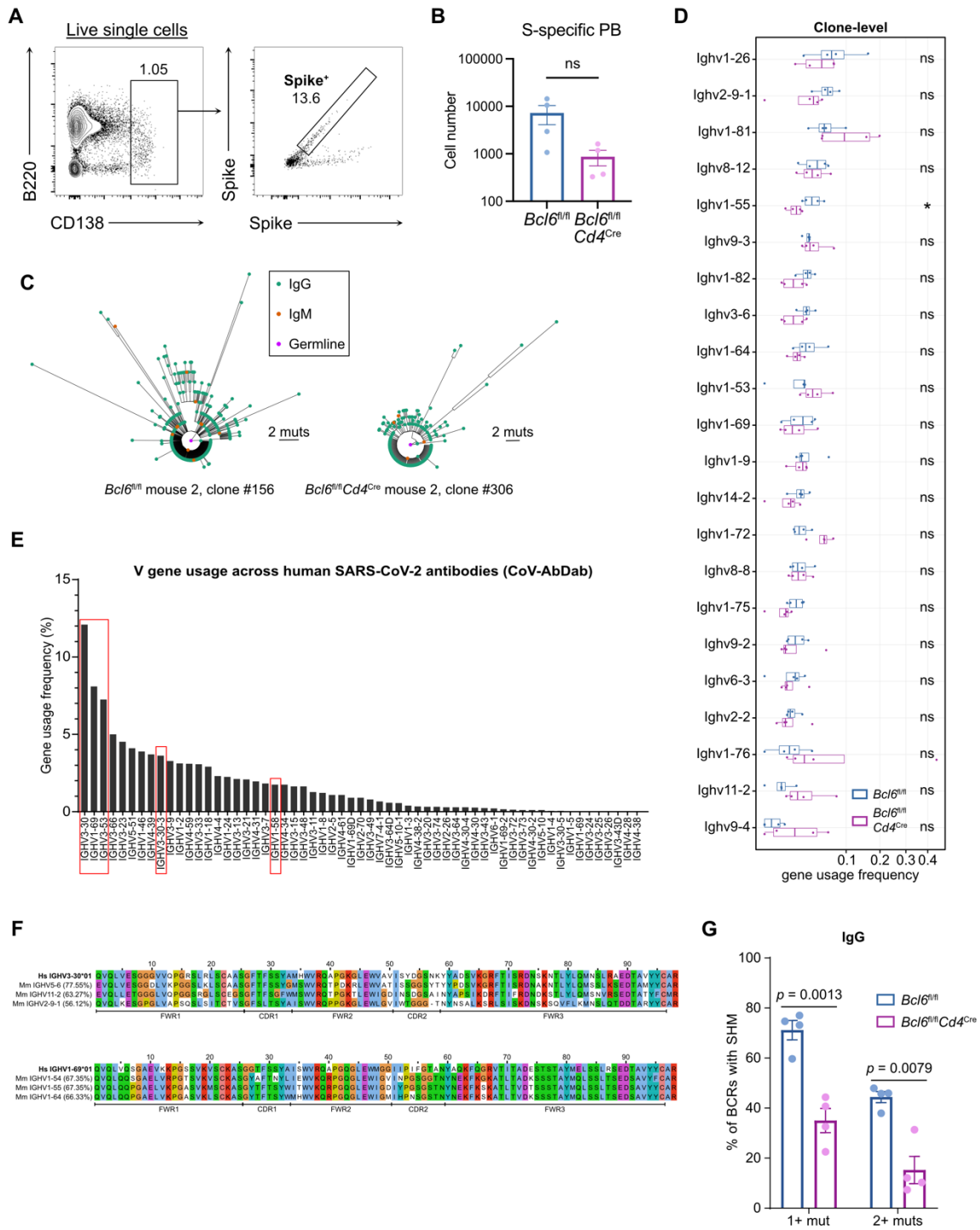


Figure S5: Analysis of SARS-CoV-2-reactive BCRs from mice and humans

(A) Representative sorting strategy to isolate spike-specific plasmablasts from live single cells from K18-hACE2 *Bcl6*^{fl/fl} and *Bcl6*^{fl/fl} *Cd4*^{Cre} medLN at 14 dpi with SARS-CoV-2.

(B) Quantification of spike-specific plasmablasts sorted from K18-hACE2 *Bcl6^{fl/fl}* and *Bcl6^{fl/fl}Cd4^{Cre}* medLN. Each symbol represents an individual mouse. Statistical significance was assessed by two-tailed unpaired Mann-Whitney test. ns, not significant.

(C) BCR lineage trees for the largest clone in a *Bcl6^{fl/fl}* mouse (left) or a *Bcl6^{fl/fl}Cd4^{Cre}* mouse (right). These mice were chosen for visualization because the total number of clones and the size of the largest clone were more similar than all other pairs of *Bcl6^{fl/fl}* and *Bcl6^{fl/fl}Cd4^{Cre}* mice. Branch lengths correspond to the number of mutations between nodes, with the scale bars on the bottom right of each plot. Nodes indicate one unique BCR sequence within the clone. Nodes are color-coded by the BCR isotype or germline status.

(D) Tukey boxplots detailing V gene usage frequencies, calculated on the level of B cell clones in each sample. V genes with ≥ 0.02 usage frequency in ≥ 2 samples are shown here. Statistical significance was assessed by two-tailed unpaired Mann-Whitney test. * $P < 0.05$. ns, not significant.

(E) Bar plot detailing the frequency of human V gene usage in SARS-CoV-2-specific antibodies isolated from patients, from analysis of the CoV-AbDab database (94). Alignments are shown for V genes boxed in red.

(F) Alignment of human IGHV3-30 and IGHV1-69 to the 3 murine V segments shown in Fig. 4C with the highest homology to each of the human V segments. The percentage sequence identity relative to the corresponding human V gene (bolded) is indicated on the left. The FWR and CDR regions within the V segments are annotated below.

(G) Quantification of the percentage of IgG-isotype BCRs with either 1+ or 2+ mutations in *Bcl6^{fl/fl}* or *Bcl6^{fl/fl}Cd4^{Cre}* mice. Statistical significance was assessed by two-tailed unpaired Welch's t-test. Data are expressed as mean \pm SEM.

S5C). We assessed the relative proportions of the 10 largest clones in each sample, finding that the top-ranked clone in each sample comprised 8% to 56% of total BCR sequences recovered, while the top 10 clones accounted for 40% to 76% of total BCR sequences (Fig. 4A). These findings indicate that clonal expansion had occurred in both *Bcl6^{fl/fl}* and *Bcl6^{fl/fl}Cd4^{Cre}* mice. To further characterize the clonal architecture of the BCR repertoires, we calculated the diversity of each BCR repertoire using the Shannon entropy score and Simpson's diversity index. These two metrics quantify the relative evenness of B cell clonal sizes across the entire repertoire, such that repertoires with limited clonal expansion will have higher diversity scores. The diversity of BCR repertoires in *Bcl6^{fl/fl}* and *Bcl6^{fl/fl}Cd4^{Cre}* mice was not statistically different by either metric, though we noted a trend towards increased diversity in the *Bcl6^{fl/fl}Cd4^{Cre}* mice (Fig. 4B).

Analysis of immunoglobulin heavy-chain variable (V) gene usage frequencies revealed that out of all candidate V genes, 22 were utilized at $\geq 2\%$ frequency in ≥ 2 samples. Usage of most V genes was not significantly different between *Bcl6^{fl/fl}* and *Bcl6^{fl/fl}Cd4^{Cre}* mice (Fig. 4C). However, we observed that *Ighv1-72*, *Ighv11-2*, and *Ighv5-6* were used more frequently in BCRs from *Bcl6^{fl/fl}Cd4^{Cre}* mice compared to *Bcl6^{fl/fl}* mice. Examining the median usage frequencies, *Ighv1-26* was the most frequently used V gene in *Bcl6^{fl/fl}* mice, while BCRs from *Bcl6^{fl/fl}Cd4^{Cre}* mice most frequently used *Ighv1-72*. Repeating this analysis on the clone-level, rather than the individual BCR sequence-level, similarly revealed that usage of most V genes was not significantly different in the absence of Tfh cells (Fig. S5D). Thus, while Tfh-deficient mice did not exhibit overt changes in V gene usage, there were nevertheless differences that could reflect the distinct nature of the T cell help in these mice.

COVID-19 patient studies have identified potent RBD-specific antibodies with recurrent V gene usage and minimal SHM (61–65). To explore whether there are murine V genes that can

similarly contribute to high-affinity S- or RBD-specific antibodies, we identified the murine V genes expressed in our dataset ($\geq 2\%$ frequency in ≥ 2 samples) with the greatest homology to frequently used and minimally mutated human V genes (Fig. 4D and S5, E and F) (61–65). Human IGHV3-53 and IGHV3-30 demonstrated the highest homology to murine *Ighv5-6* and *Ighv11-2*, which were utilized more frequently in BCRs from *Bcl6^{fl/fl}Cd4^{Cre}* compared to *Bcl6^{fl/fl}* mice (Fig. 4C). Murine V genes most similar to human IGHV1-58, IGHV3-30-3, and IGHV1-69 were used at comparable frequencies between BCRs from *Bcl6^{fl/fl}* and *Bcl6^{fl/fl}Cd4^{Cre}* mice. Taken together, these data suggest that homologous human and murine V genes may contribute to potent SARS-CoV-2-specific antibodies. Furthermore, preferential usage of these V genes in Tfh-deficient mice may enable the production of high-affinity antibodies with minimal SHM.

To investigate whether SHM could still occur in Tfh-deficient mice, we determined the mutational profiles of each clonal consensus sequence compared to the mouse germline using the Immcantation analysis pipeline (69). We found evidence of SHM in S-specific IgG plasmablasts from *Bcl6^{fl/fl}Cd4^{Cre}* mice, albeit at significantly lower frequency compared to plasmablasts from *Bcl6^{fl/fl}* mice (Fig. 4E). Overall, $66.28\% \pm 6.36\%$ (mean \pm s.e.m.) of clones from *Bcl6^{fl/fl}* mice had somatic mutations, compared to $41.61\% \pm 3.88\%$ of clones from *Bcl6^{fl/fl}Cd4^{Cre}* mice (Fig. 4F). This contrast was especially pronounced when considering the percentage of clones with two or more somatic mutations: $46.04\% \pm 6.13\%$ of *Bcl6^{fl/fl}* clones and $14.81\% \pm 1.25\%$ of *Bcl6^{fl/fl}Cd4^{Cre}* clones (Fig. 4F). Similar results were obtained by comparing individual BCR sequences (Fig. S5G).

We further compared mutation selection strength in *Bcl6^{fl/fl}* and *Bcl6^{fl/fl}Cd4^{Cre}* BCR repertoires using BASELINE, which determines the ratio of non-synonymous to synonymous mutations compared to a reference model (70, 71). Validating the BASELINE analytical approach, selection strength was positive in the complementarity determining regions (CDRs) of BCRs from

Bcl6^{fl/fl} mice and negative in the framework regions (FWRs) (Fig. 4G). This is consistent with the fact that CDRs are the main determinants of antigen specificity and thus enriched in non-synonymous mutations, while FWRs generally serve as structural scaffolds, making them less tolerant of residue-altering mutations. Across both CDRs and FWRs, we found that the ratio of non-synonymous to synonymous mutations was significantly lower in S-specific IgG plasmablasts from *Bcl6*^{fl/fl}*Cd4*^{Cre} mice compared to *Bcl6*^{fl/fl} mice (Fig. 4G), indicating that Tfh cells are required for positive selection of mutated B cell clones against SARS-CoV-2. Collectively, our analysis of the BCR repertoire after SARS-CoV-2 infection suggests that both V gene usage patterns and low levels of SHM, though without mutation selection, may contribute to the production of high-affinity Tfh-independent antibodies.

Tfh cells focus the antibody repertoire but are dispensable for broad coverage of SARS-CoV-2 epitopes

We next characterized the antibody epitope repertoire of Tfh-dependent versus -independent responses to SARS-CoV-2. Sera from AAV-hACE2 *Bcl6*^{fl/fl} and *Bcl6*^{fl/fl}*Cd4*^{Cre} mice at 14 dpi were profiled using a bacterial display library of 2410 linear peptides tiling the entire SARS-CoV-2 proteome (Fig. 5A). We first compared the diversity of antibody epitope reactivity, calculating the Shannon entropy, Simpson's diversity index, and the repertoire focusing index within each sample (Methods). We observed that antibody diversity assessed by Shannon entropy and Simpson's diversity index was significantly decreased in *Bcl6*^{fl/fl} mice compared to *Bcl6*^{fl/fl}*Cd4*^{Cre} mice, while the degree of repertoire focusing was increased (Fig. 5B). These findings were robust to variations in read counts (Fig. S6A). These results suggest that Tfh cells help focus the antibody response to particular viral epitopes while non-Tfh cells promote antibodies to a wider array of targets.

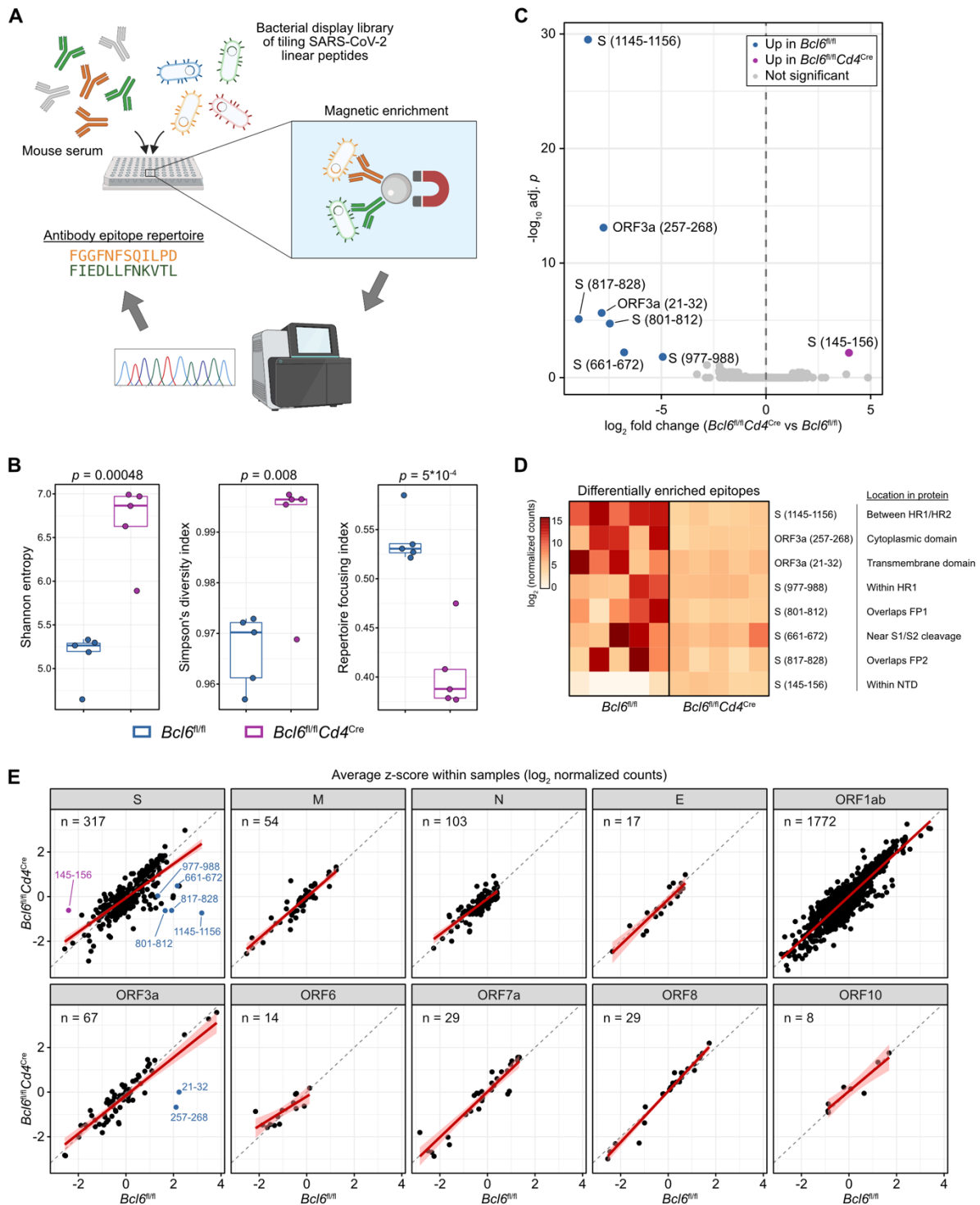


Figure 5: Tfh cells focus the antibody repertoire but are dispensable for broad coverage of SARS-CoV-2 epitopes

(A) Sera from infected AAV-hACE2 *Bcl6^{fl/fl}* or *Bcl6^{fl/fl}Cd4^{Cre}* mice ($n = 5$ mice per condition from two independent experiments) were assayed for reactivity against a bacterial display library of overlapping linear epitopes tiling the SARS-CoV-2 proteome.

(B) Tukey boxplots detailing Shannon entropy (left), Simpson's diversity index (middle), and repertoire focusing index (right) in *Bcl6^{fl/fl}* or *Bcl6^{fl/fl}Cd4^{Cre}* mice. Statistical significance was assessed by two-tailed unpaired Welch's t-test. Each symbol represents an individual mouse.

(C) Volcano plot of differentially enriched linear epitopes in *Bcl6^{fl/fl}* vs *Bcl6^{fl/fl}Cd4^{Cre}* mice. Epitopes that are significantly enriched in *Bcl6^{fl/fl}* sera are colored in blue, while epitopes that are enriched in *Bcl6^{fl/fl}Cd4^{Cre}* sera are colored in magenta. Point labels describe the amino acids within the indicated SARS-CoV-2 protein from which the epitope was derived. Statistical significance was assessed by two-tailed DESeq2 Wald test, with Benjamini-Hochberg multiple hypothesis correction (adjusted $p < 0.05$).

(D) Heatmap of differentially enriched linear epitopes in *Bcl6^{fl/fl}* vs *Bcl6^{fl/fl}Cd4^{Cre}* mice, from (C). Data are expressed as \log_2 -transformed normalized counts. The position of each epitope in relation to known protein domains is annotated.

(E) Scatter plots of relative enrichment scores for linear epitopes derived from each SARS-CoV-2 protein, comparing *Bcl6^{fl/fl}* vs *Bcl6^{fl/fl}Cd4^{Cre}* sera. Data are expressed as average z -scores (\log_2 normalized counts were scaled to z -scores within each sample, then averaged across *Bcl6^{fl/fl}* or *Bcl6^{fl/fl}Cd4^{Cre}* mice). The gray dashed line demarcates equivalence between *Bcl6^{fl/fl}* and *Bcl6^{fl/fl}Cd4^{Cre}*, while the red line denotes the linear regression model with 95% confidence intervals shaded in pink. Epitopes that were identified as differentially enriched are annotated as in (C). The number of epitopes derived from each SARS-CoV-2 protein is annotated in the top left.

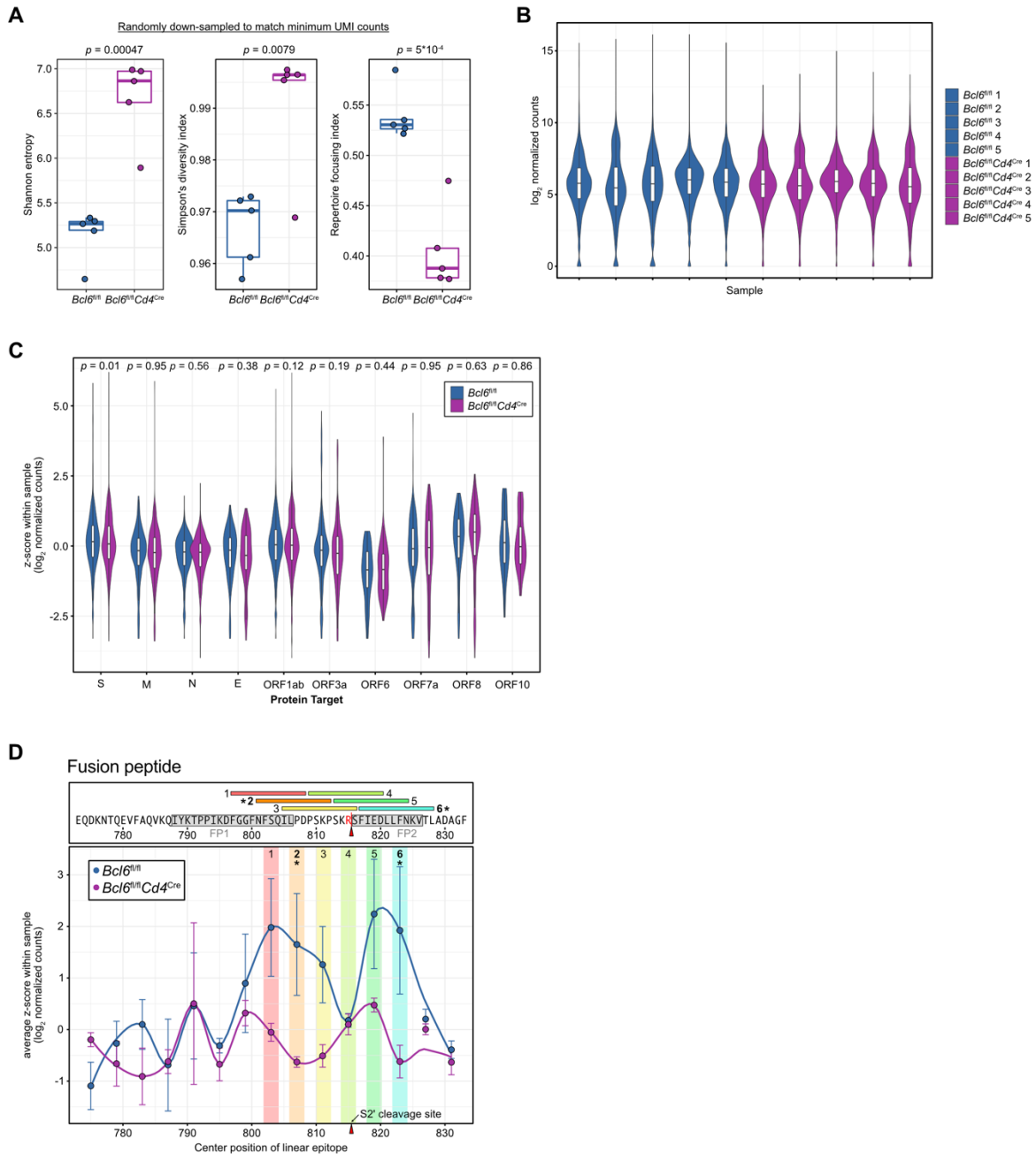


Figure S6: Analysis of SARS-CoV-2 linear epitopes recognized by antibodies from AAV-hACE2 $Bcl6^{fl/fl}$ or $Bcl6^{fl/fl}Cd4^{Cre}$ mice

(A) Boxplots detailing Shannon entropy (left), Simpson's diversity index (middle), and repertoire focusing index (right), after random down-sampling to match the sample with the lowest UMI counts. Statistical significance was assessed by two-tailed unpaired Welch's t-test. Each symbol represents an individual mouse.

(B) Violin plot of \log_2 normalized counts for all 2410 epitopes in each sample. Higher values indicate relative enrichment of antibodies that are reactive against a particular epitope.

(C) Violin plot detailing the relative enrichment of antibodies against different SARS-CoV-2 proteins, such that linear epitopes derived from the same protein are grouped together. Data are expressed as z -scores, scaled from \log_2 normalized counts within each sample; data are aggregated together by experimental group. Statistical significance was assessed by two-tailed unpaired Welch's t -test.

(D) Linear epitopes surrounding the S2' site (R815, red arrowhead), cleavage of which triggers fusion, are color-coded and numbered with their corresponding amino acid sequences annotated above. Epitopes that are differentially enriched in $Bcl6^{fl/fl}$ vs $Bcl6^{fl/fl}Cd4^{Cre}$ at a library-wide scale (from Figure 4C) are bolded and labeled with an asterisk. Putative fusion peptides are labeled in gray boxes above (FP1, 788-806; FP2, 816-826). Data are expressed as average z -scores in $Bcl6^{fl/fl}$ or $Bcl6^{fl/fl}Cd4^{Cre}$ mice, with SEM error bars and loess regression lines.

Given these changes in antibody diversity, we next explored whether there were differences in antibody reactivity at the level of individual linear epitopes. After normalizing for read count variations using the median of ratios method (Fig. S6B) (72, 73), we identified epitopes that were comparatively enriched or depleted in *Bcl6^{fl/fl}* versus *Bcl6^{fl/fl}Cd4^{Cre}* mice (Fig. 5C). We found that seven epitopes were enriched in *Bcl6^{fl/fl}* mice, while one epitope was depleted (Fig. 5D). Five of the seven enriched epitopes were derived from S: aa661-672 (proximal to S1/S2 cleavage site), aa801-812 (fusion peptide [FP] 1), aa817-828 (FP2), aa977-988 (heptad repeat [HR] 1), and aa1145-1156 (between HR1/HR2). On the other hand, aa145-156 (N-terminal domain) from S was comparatively depleted in *Bcl6^{fl/fl}* mice.

To further investigate alterations in epitope reactivity, we converted the normalized counts to z-scores on a sample-by-sample basis, such that the z-scores would denote the relative rank of a specific epitope within a particular sample (Fig. S6C). Consistent with our prior analyses, the average z-scores in *Bcl6^{fl/fl}* versus *Bcl6^{fl/fl}Cd4^{Cre}* mice were similar across most SARS-CoV-2 proteins, with the exception of regions within the S and ORF3a proteins (Fig. 5E). In particular, the regression lines for non-S proteins all closely followed the line of identity, indicating that the relative ranks of epitopes from non-S proteins were largely similar in the presence or absence of Tfh cells. These analyses therefore indicate that, while Tfh cells are dispensable for antibody production against most SARS-CoV-2 epitopes, they are required to focus the antibody response against certain S-derived epitopes.

RBD-specific antibodies are generated in the absence of Tfh cells

Analyzing antibody epitope reactivity along the length of S, we observed that the majority of epitopes enriched in *Bcl6^{fl/fl}* mice (17/21 epitopes with differential average z-score > 1) were found

in the S2 domain (aa686-1273; Fisher's exact test $p = 0.0012$) (Fig. 6A), which mediates fusion of viral and target cell membranes (74). These included most of the aforementioned S-derived epitopes that were significantly enriched (Fig. 5C), as well as contiguous epitopes whose enrichment did not reach statistical significance in the epitope-level analysis. For example, several epitopes in the fusion peptide were enriched adjacent to the significantly enriched epitopes aa801-812 and aa817-828 (Fig. S6D). Many of these epitopes are highly conserved across human coronaviruses (hCoVs) as well as the emerging variants of concern (Fig. 6A). Interestingly, the enriched epitopes spanning FP1/FP2 and preceding HR2 have also been identified in numerous studies profiling the antibody epitope repertoire of COVID-19 patients (75, 76). Given their immunodominance and conservation across hCoVs, these epitopes have been proposed as targets for a pan-coronavirus vaccine.

In contrast, *Bcl6^{fl/fl}* and *Bcl6^{fl/fl}Cd4^{Cre}* mice demonstrated similar antibody reactivity to most epitopes within the RBD (Fig. 6B), the target of most neutralizing antibodies (60). However, as most antibodies to RBD likely recognize conformational epitopes (75, 76), we also measured RBD-specific antibodies by ELISA using full-length RBD. RBD-specific IgG titers normalized by total S-specific IgG were similar between *Bcl6^{fl/fl}* and *Bcl6^{fl/fl}Cd4^{Cre}* mice (Fig. 6C). Thus, while Tfh cells focus the antibody response against immunodominant S2 epitopes, non-Tfh cells still promote antibodies against the primary target of neutralization, RBD.

Tfh-dependent and -independent antibodies demonstrate similar neutralization potency against homologous SARS-CoV-2 as well as the B.1.351 variant of concern

We next evaluated the function of antibodies from *Bcl6^{fl/fl}* and *Bcl6^{fl/fl}Cd4^{Cre}* mice following SARS-CoV-2 infection. While we had observed that Tfh-independent antibody responses to the

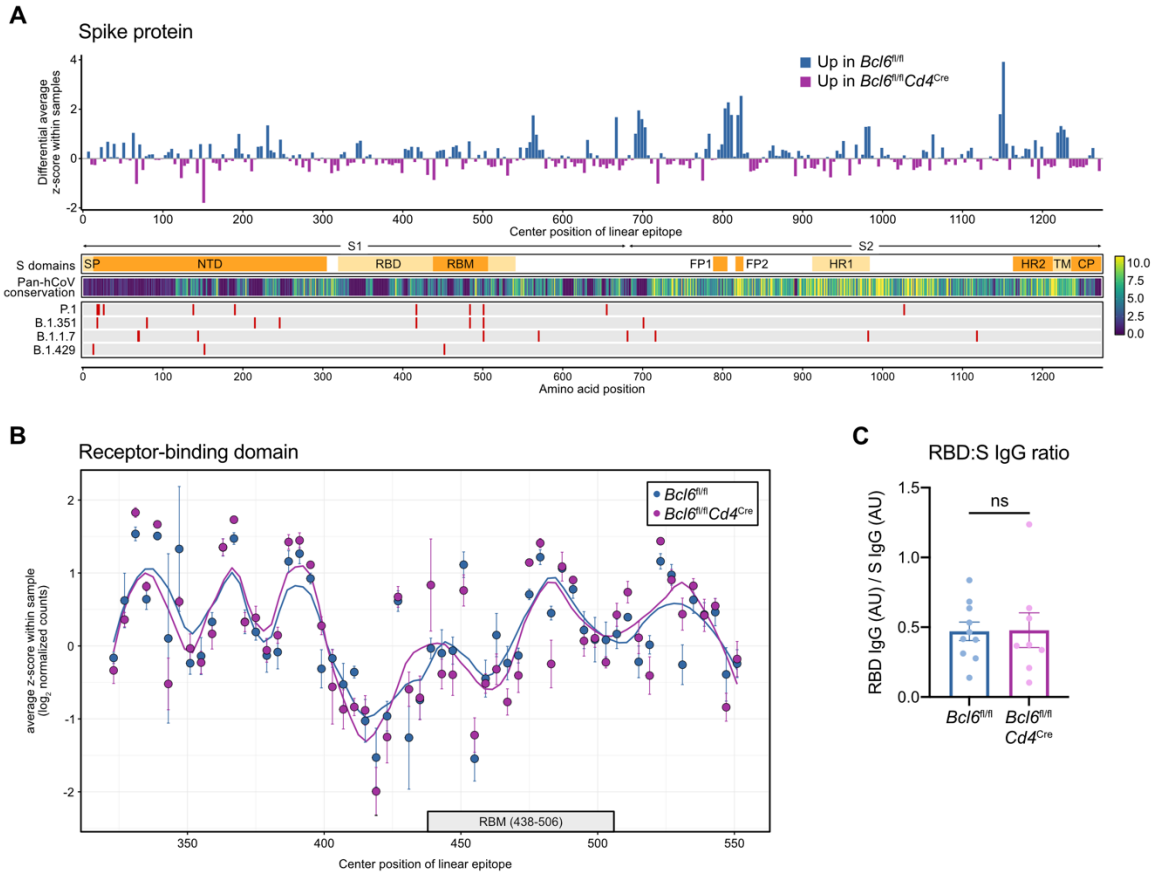


Figure 6: RBD-specific antibodies are generated in the absence of Tfh cells

(A) Top: differential enrichment scores for spike (S)-derived linear epitopes, such that epitopes that are comparatively enriched in $Bcl6^{fl/fl}$ mice are represented by positive values (blue), whereas epitopes that are relatively enriched in $Bcl6^{fl/fl}Cd4^{Cre}$ mice are indicated by negative values (magenta). Linear epitopes are each indicated by their center position within the S protein. Bottom: annotation tracks detailing S protein domains, pan-human coronavirus (hCoV) conservation scores, and mutations found in select SARS-CoV-2 variants of concern. SP, signal peptide. NTD, N-terminal domain. RBD, receptor-binding domain. RBM, receptor-binding motif. FP1, fusion peptide 1. FP2, fusion peptide 2. HR1, heptad repeat 1. HR2, heptad repeat 2. TM, transmembrane domain. CP, cytoplasmic domain.

(B) Relative enrichment scores for linear epitopes derived from RBD, comparing $Bcl6^{fl/fl}$ vs $Bcl6^{fl/fl}Cd4^{Cre}$ sera. Data are expressed as average z-scores in $Bcl6^{fl/fl}$ or $Bcl6^{fl/fl}Cd4^{Cre}$ mice, with SEM error bars and loess regression lines. The RBM is annotated below with a gray box.

(C) Ratio of RBD-specific to S-specific IgG antibodies in sera from $Bcl6^{fl/fl}$ or $Bcl6^{fl/fl}Cd4^{Cre}$ mice at 14 dpi with SARS-CoV-2. Statistical significance was assessed by two-tailed unpaired t-test. ns, not significant. Data are expressed as mean \pm SEM. Each symbol represents an individual mouse. Data are aggregated from three independent experiments.

virus lacked IgG1/IgG3 subclasses (Fig. 1, B and D) and S2 epitope focusing (Fig. 6A), these antibodies were still high-affinity (Fig. 3, A and B) and could target the RBD (Fig. 6C). We therefore predicted that Tfh-independent antibodies would demonstrate similar neutralizing function against homologous SARS-CoV-2 (USA-WA1/2020) as those generated with Tfh cell help. Using vesicular stomatitis virus (VSV) pseudotyped with USA-WA1/2020 S protein, we measured the neutralization titer (the reciprocal serum dilution achieving 50% neutralization of pseudovirus infection, NT50) of sera from AAV-hACE2 *Bcl6*^{fl/fl} and *Bcl6*^{fl/fl}*Cd4*^{Cre} mice. *Bcl6*^{fl/fl} sera exhibited increased NT50 (Fig. 7A), which was expected given their higher levels of S-specific IgG antibodies (Fig. 1B). However, by normalizing NT50 to S-specific IgG levels in each sample, we observed that the neutralization potency indices of *Bcl6*^{fl/fl} and *Bcl6*^{fl/fl}*Cd4*^{Cre} sera were similar and actually trended higher for *Bcl6*^{fl/fl}*Cd4*^{Cre} sera (Fig. 7A).

We next tested the same sera against VSV pseudotyped with S protein from the B.1.351 variant of concern. Multiple studies have shown that B.1.351 S mutations, particularly those in the RBD, disrupt binding by neutralizing antibodies and facilitate immune escape (77, 78). We therefore hypothesized that increased focusing of Tfh-dependent antibodies against conserved S2 epitopes would enable *Bcl6*^{fl/fl} sera to better neutralize B.1.351 pseudovirus than *Bcl6*^{fl/fl}*Cd4*^{Cre} sera. While *Bcl6*^{fl/fl} sera exhibited greater NT50 than *Bcl6*^{fl/fl}*Cd4*^{Cre} sera, we found that the neutralization potency index of *Bcl6*^{fl/fl}*Cd4*^{Cre} sera again trended higher than that of *Bcl6*^{fl/fl} sera (Fig. 7B). Nevertheless, both *Bcl6*^{fl/fl} and *Bcl6*^{fl/fl}*Cd4*^{Cre} sera demonstrated an approximately 10-fold reduction in NT50 against the B.1.351 variant compared to USA-WA1/2020 (Fig. 7C), consistent with previous studies (77, 78). Our findings therefore indicate that Tfh-independent antibodies exhibit similar, if not increased, neutralization potency to Tfh-dependent antibodies *in*

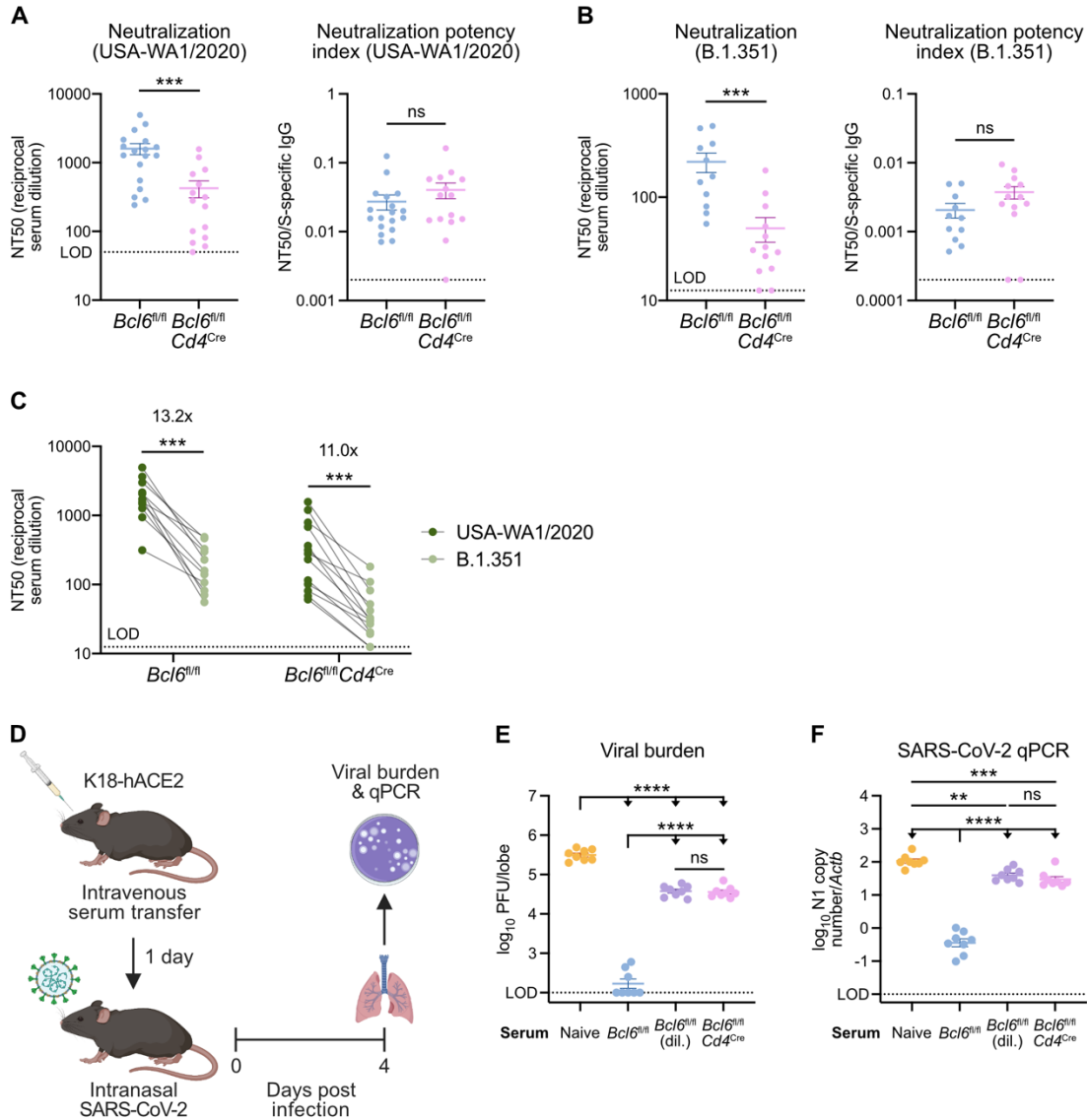


Figure 7: Tfh-dependent and -independent antibodies demonstrate similar neutralization potency against homologous SARS-CoV-2 as well as the B.1.351 variant of concern

(A) Left: neutralizing titers (inverse of half maximal inhibitory concentration; NT50) of sera from AAV-hACE2 $Bcl6^{fl/fl}$ (blue) or $Bcl6^{fl/fl}Cd4^{Cre}$ (magenta) mice against VSV particles pseudotyped with homologous S protein (USA-WA1/2020, the same isolate used to infect the mice). Right: neutralization potency indices (NT50 divided by S-specific total IgG) of sera from $Bcl6^{fl/fl}$ or $Bcl6^{fl/fl}Cd4^{Cre}$ mice against USA-WA1/2020 pseudovirus. Samples with NT50 at the limit of detection (LOD) were assigned a neutralization potency index of 0.002.

(B) Left: neutralizing titers of sera from AAV-hACE2 $Bcl6^{fl/fl}$ (blue) or $Bcl6^{fl/fl}Cd4^{Cre}$ (magenta) mice against VSV particles pseudotyped with variant S protein (B.1.351). Right: neutralization potency indices of sera from $Bcl6^{fl/fl}$ or $Bcl6^{fl/fl}Cd4^{Cre}$ mice against B.1.351 pseudovirus. Samples with NT50 at the LOD were assigned a neutralization potency index of 0.0002.

(C) Matched comparison of neutralizing titers against homologous (USA-WA1/2020) vs variant (B.1.351) pseudovirus. Fold changes are indicated above each group.

(D) Schematic of experimental design for assessing *in vivo* neutralization potency of sera.

(E and F) Viral burden in lungs from K18-hACE2 mice infected with SARS-CoV-2 at 4 dpi. Mice were treated with serum from naïve, infected AAV-hACE2 $Bcl6^{fl/fl}$, or infected AAV-hACE2 $Bcl6^{fl/fl}Cd4^{Cre}$ mice. $Bcl6^{fl/fl}$ sera was given undiluted or diluted (dil.) 7- to 9-fold to match the S-specific IgG titer of $Bcl6^{fl/fl}Cd4^{Cre}$ sera in each experiment. Data are expressed as \log_{10} plaque forming units (PFU) per lung lobe by plaque assay (E) or \log_{10} N1 gene copy number by qPCR, normalized to *Actb* (F).

Statistical significance was assessed by two-tailed Mann–Whitney test (A and B), two-tailed Wilcoxon signed-rank test (C), or one-way ANOVA with Tukey’s test (E and F). ** $P < 0.01$; *** $P < 0.001$; **** $P < 0.0001$. ns, not significant. Data are expressed as mean \pm SEM. Each symbol represents an individual mouse. Data are aggregated from at least two independent experiments.

in vitro and that S2 epitope focusing does not improve neutralization activity against the B.1.351 variant of concern.

Finally, we assessed the function of *Bcl6*^{fl/fl} and *Bcl6*^{fl/fl}*Cd4*^{Cre} sera against SARS-CoV-2 *in vivo*. To this end, we transferred sera from AAV-hACE2 *Bcl6*^{fl/fl} or *Bcl6*^{fl/fl}*Cd4*^{Cre} mice infected with SARS-CoV-2 (USA-WA1/2020) into naïve K18-hACE2 mice (Fig. 7D). *Bcl6*^{fl/fl} sera was given undiluted or diluted 7- to 9-fold to match the S-specific IgG titer of *Bcl6*^{fl/fl}*Cd4*^{Cre} sera in a given experiment. One day later, we infected the K18-hACE2 recipients with homologous SARS-CoV-2 and then measured viral burden in the lungs at 4 dpi. Undiluted *Bcl6*^{fl/fl} sera led to the greatest reduction in viral burden (Fig. 7, E and F), indicating that, as expected, antibody titer is an important determinant of protection against viral challenge. However, once matched for S-specific IgG titer, *Bcl6*^{fl/fl} and *Bcl6*^{fl/fl}*Cd4*^{Cre} sera provided a similar degree of protection (Fig. 7, E and F), corroborating our *in vitro* findings that Tfh-dependent and -independent antibodies exhibit similar neutralization potency. Taken together, these results demonstrate that Tfh-independent antibodies efficiently neutralize both homologous SARS-CoV-2 and the B.1.351 variant of concern but that optimal protection *in vivo* still relies on Tfh cells to generate high antibody titers.

Th1 cells express Tfh effector molecules and co-localize with IgG2c⁺ B cells following viral infection

To determine which non-Tfh CD4⁺ T cell populations promote antibody production, we analyzed CD4⁺ T cell populations in the medLN at 7 dpi with SARS-CoV-2. While total CD4⁺ T cell counts were unaffected in *Bcl6*^{fl/fl}*Cd4*^{Cre} mice, activated CD44⁺CD4⁺ T cell counts were reduced, consistent with the loss of Tfh cells (Fig. S7, A and B). We classified PD-1^{lo}CXCR5^{lo}CD44⁺CD4⁺ T cells by their expression of PSGL-1 and Ly6C (Fig. S7C). These markers have previously been

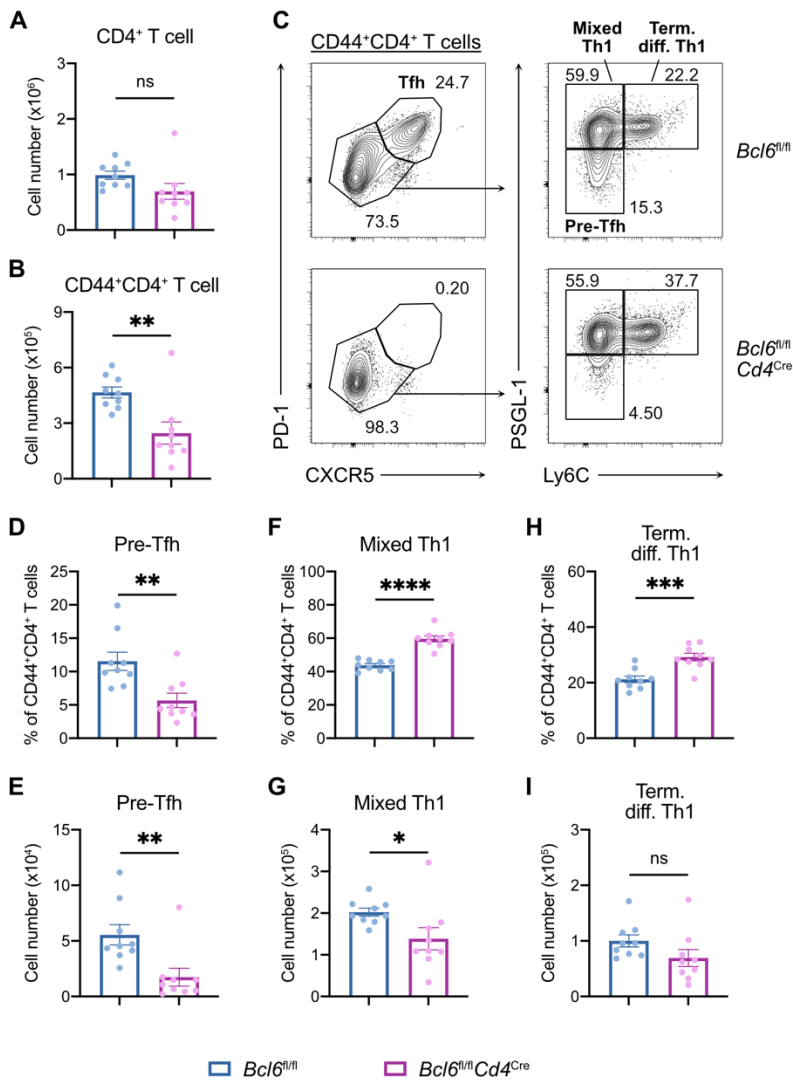


Figure S7: Characterization of CD4⁺ T cell subsets induced by SARS-CoV-2 infection

(A to I) Flow cytometric analysis of medLN from SARS-CoV-2-infected mice at 7 dpi.

(A and B) Total number of CD4⁺ T cells (A) and CD44⁺CD4⁺ T cells (B) in *Bcl6*^{fl/fl} (blue) or *Bcl6*^{fl/fl}*Cd4*^{Cre} (magenta) mice.

(C) Representative gating strategy to define Tfh cells, pre-Tfh cells, mixed Th1 cells, and terminally differentiated Th1 cells from CD44⁺CD4⁺ T cells.

(D to I) Frequency among CD44⁺CD4⁺ T cells and total number of pre-Tfh cells (D and E), mixed Th1 cells (F and G), and terminally differentiated Th1 cells (H and I) in *Bcl6*^{fl/fl} (blue) or *Bcl6*^{fl/fl}*Cd4*^{Cre} (magenta) mice.

Statistical significance was assessed by either two-tailed unpaired t-test or Welch's t-test, based on the F test for unequal variance. **P* < 0.05; ***P* < 0.01; ****P* < 0.001; *****P* < 0.0001. ns, not significant. Data are expressed as mean ± SEM. Each symbol represents an individual mouse. Data are aggregated from three independent experiments.

used in acute LCMV and influenza virus infection to distinguish terminally differentiated PSGL-1^{hi}Ly6C^{hi} Th1 cells from a heterogeneous PSGL-1^{hi}Ly6C^{lo} Th1 compartment containing memory precursors along with other Th1-related functional subsets (79–81). We therefore defined PSGL-1^{hi}Ly6C^{hi} cells as terminally differentiated Th1 cells and PSGL-1^{hi}Ly6C^{lo} cells as mixed Th1 cells. We also observed a BCL6-dependent PSGL-1^{lo}Ly6C^{lo} population within the PD-1^{lo}CXCR5^{lo} gate, which has previously been described as pre-Tfh cells (Fig. S7, D and E) (82). Mixed Th1 and terminally differentiated Th1 cells increased in relative frequency among activated CD4⁺ T cells in *Bcl6*^{fl/fl}*Cd4*^{Cre} mice, consistent with the loss of Tfh and pre-Tfh cells; however, their absolute numbers were similar between *Bcl6*^{fl/fl} and *Bcl6*^{fl/fl}*Cd4*^{Cre} mice, indicating that BCL6 deficiency did not lead to an aberrant increase in Th1 populations (Fig. S7, F to I).

We next evaluated whether these Th1 populations produce CD40L and IL-21, effector molecules usually ascribed to Tfh cells (19). CD40L and IL-21 act at multiple stages to support B cell activation, proliferation, differentiation, and antibody production (19). While Tfh cells produced the highest levels of CD40L, mixed Th1 cells also produced substantial levels of this effector molecule (Fig. 8, A and B). Tfh cells and mixed Th1 cells comprised the majority of CD40L-expressing CD4⁺ T cells in the medLN of *Bcl6*^{fl/fl} mice, while mixed Th1 cells became the main CD40L-expressing cells in *Bcl6*^{fl/fl}*Cd4*^{Cre} mice (Fig. 8C). In *Bcl6*^{fl/fl}*Cd4*^{Cre} mice, the frequency of CD40L⁺ cells among CD4⁺ T cells was decreased (Fig. S8A), likely owing to the loss of CD40L-expressing Tfh cells. However, mixed Th1 and terminally differentiated Th1 cells expressed higher levels of CD40L in *Bcl6*^{fl/fl}*Cd4*^{Cre} mice compared to *Bcl6*^{fl/fl} mice (Fig. S8, B and C). In the absence of Tfh cells, Th1 subsets may have more opportunities to interact with antigen-presenting cells and experience T cell receptor signaling, which promotes CD40L expression (83). In *Bcl6*^{fl/fl} mice infected with PR8, mixed Th1 cells also expressed substantial levels of CD40L

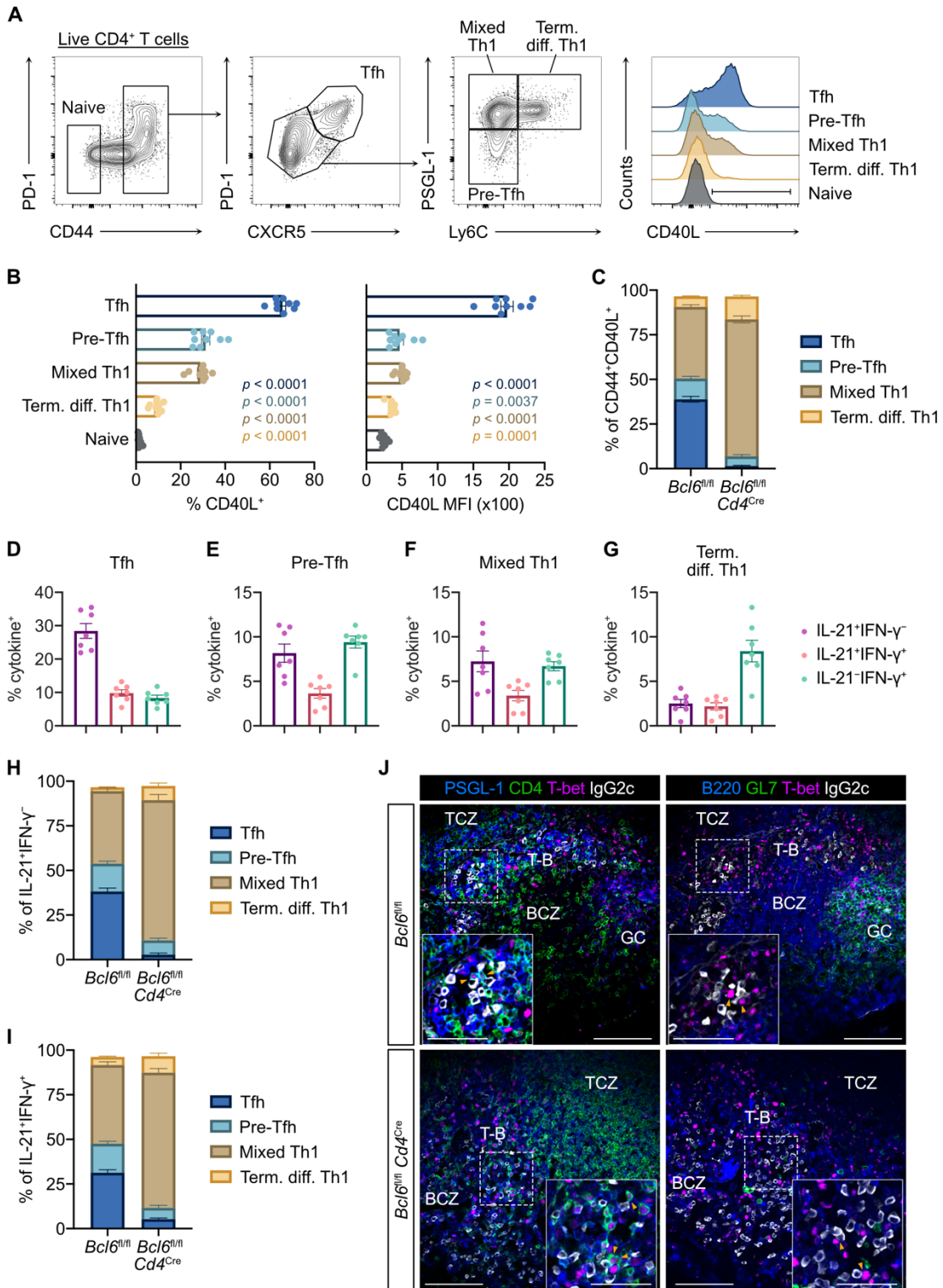


Figure 8: Th1 cells express Tfh effector molecules and co-localize with IgG2c⁺ B cells following viral infection

(A to I) Flow cytometric analysis of CD4⁺ T cells in mediastinal lymph nodes (medLN) from SARS-CoV-2-infected mice at 7 dpi.

(A) Representative gating strategy for quantifying CD40L expression in distinct CD4⁺ T cell subsets. Pre-Tfh cells express a low amount of PD-1 and CXCR5 but are BCL6-dependent (82). Mixed Th1 cells classically include Th1 effectors and memory precursors. Terminally differentiated Th1 cells have been shown to express high levels of T-bet, IFN- γ , and GzmB (79).

(B) Frequency (left) and median fluorescence intensity (MFI) (right) of CD40L expression within CD4⁺ T cell subsets from control *Bcl6*^{fl/fl} mice. Statistical significance was assessed by two-tailed unpaired Welch's t-test. *P* values for each subset relative to naive CD4⁺ T cells are color-coded.

(C) Relative proportions of CD4⁺ T cell subsets among CD44⁺CD40L⁺ cells from *Bcl6*^{fl/fl} or *Bcl6*^{fl/fl}*Cd4*^{Cre} mice.

(D to G) Frequency of IL-21⁺IFN- γ ⁻ (purple), IL-21⁺IFN- γ ⁺ (red), and IL-21⁻IFN- γ ⁺ (teal) expression by intracellular cytokine staining in Tfh cells (D), pre-Tfh cells (E), mixed Th1 cells (F), and terminally differentiated Th1 cells (G) cells from control *Bcl6*^{fl/fl} mice.

(H and I) Relative proportions of CD4⁺ T cell subsets among IL-21⁺IFN- γ ⁻ (H) and IL-21⁺IFN- γ ⁺ (I) cells from *Bcl6*^{fl/fl} or *Bcl6*^{fl/fl}*Cd4*^{Cre} mice.

Data are expressed as mean \pm SEM. Each symbol represents an individual mouse. Data are aggregated from at least two independent experiments.

(J) Immunofluorescence of serial sections of medLN from *Bcl6*^{fl/fl} (top row) or *Bcl6*^{fl/fl}*Cd4*^{Cre} (bottom row) mice infected with PR8 at 14 dpi. Left column: PSGL-1 (blue), CD4 (green), T-bet (magenta), and IgG2c (white). Right column: B220 (blue), GL7 (green), T-bet (magenta), and IgG2c (white). Dashed line demarcates region shown in inset. Orange arrowheads denote Th1 cells interacting with IgG2c⁺ B cells. BCZ, B cell zone. TCZ, T cell zone. T-B, T cell–B cell border. GC, germinal center. Representative images from 3 mice; scale bars, 100 μ m and 50 μ m (inset).

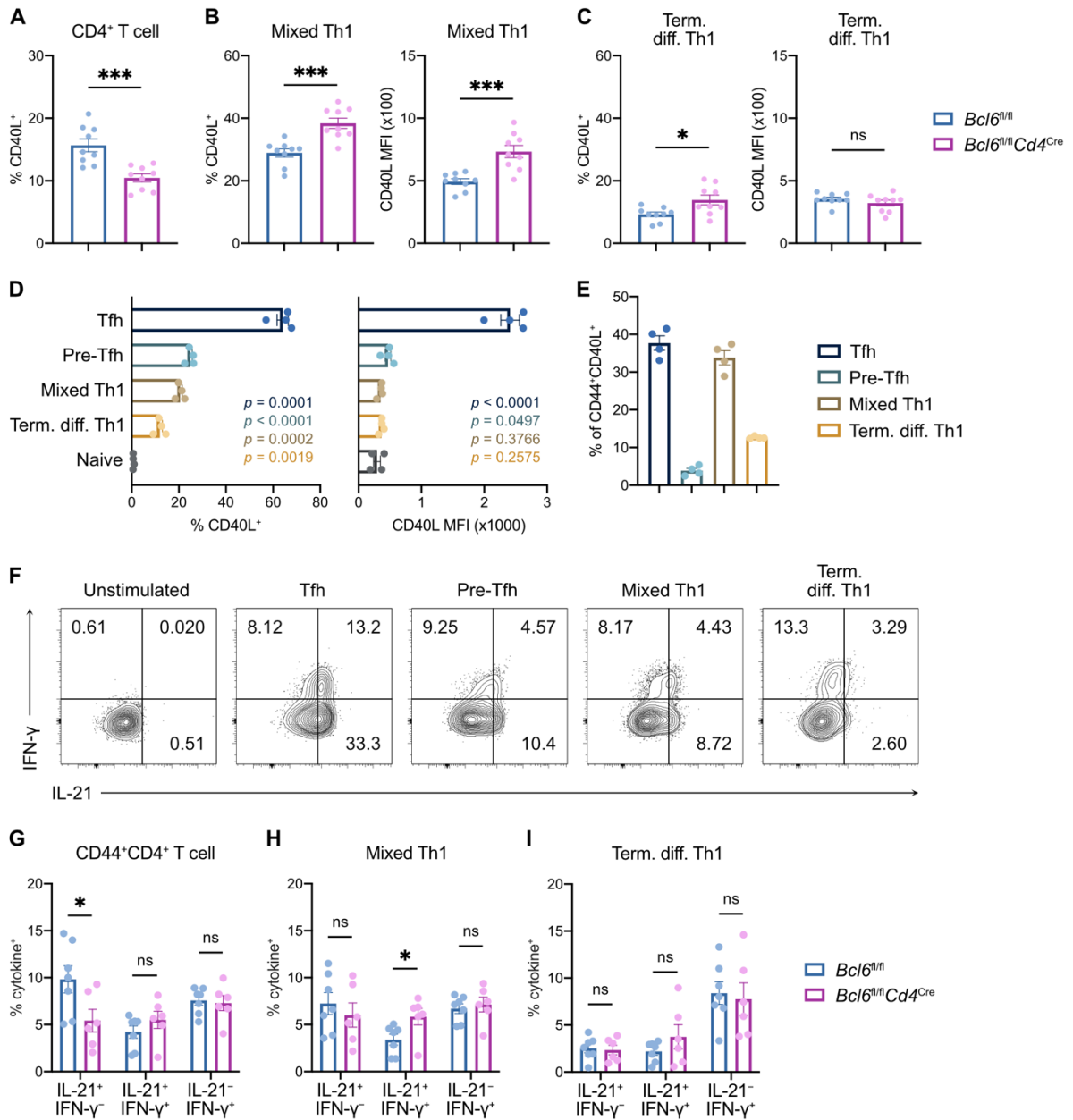


Figure S8: CD40L and cytokine expression in CD4⁺ T cell subsets after viral infection

(A to C) Flow cytometric analysis of medLN from $Bcl6^{fl/fl}$ (blue) or $Bcl6^{fl/fl}Cd4^{Cre}$ (magenta) mice at 7 dpi with SARS-CoV-2.

(A) Frequency of CD44⁺CD40L⁺ cells among CD4⁺ T cells.

(B and C) Frequency (left) and MFI (right) of CD40L expression among mixed Th1 cells (B) and terminally differentiated Th1 cells (C).

(D and E) Flow cytometric analysis of medLN from *Bcl6^{fl/fl}* mice at 7 dpi with PR8.
(D) Frequency (left) and MFI (right) of CD40L expression among CD4⁺ T cell subsets. *P* values for each subset relative to naive CD4⁺ T cells are color-coded.
(E) Relative proportions of CD4⁺ T cell subsets among CD44⁺CD40L⁺ cells.
(F) Representative flow cytometric analysis of IL-21 and IFN- γ protein expression in distinct CD4⁺ T cell subsets from medLN of SARS-CoV-2-infected mice at 7 dpi.
(G to I) Flow cytometric analysis of medLN from *Bcl6^{fl/fl}* (blue) or *Bcl6^{fl/fl}Cd4^{Cre}* (magenta) mice at 7 dpi with SARS-CoV-2. Frequencies of IL-21⁺IFN- γ ⁻, IL-21⁺IFN- γ ⁺, and IL-21⁻IFN- γ ⁺ expression among CD44⁺CD4⁺ T cells (G), mixed Th1 cells (H) and terminally differentiated Th1 cells (I).
Statistical significance was assessed by either two-tailed unpaired t-test or Welch's t-test, based on the F test for unequal variance. **P* < 0.05; ****P* < 0.001. ns, not significant. Data are expressed as mean \pm SEM. Each symbol represents an individual mouse. Data in (A to C and G to I) are aggregated from at least two independent experiments.

and constituted a large percentage of CD40L-expressing CD4⁺ T cells (Fig. S8, D and E). Therefore, mixed Th1 cells are a significant source of CD40L in the medLN of virally infected *Bcl6^{fl/fl}* and *Bcl6^{fl/fl}Cd4^{Cre}* mice, suggesting that they may provide contact-dependent help to B cells both in the presence and in the absence of Tfh cells.

In SARS-CoV-2 infection, Tfh cells also produced the highest levels of IL-21 (Fig. 8D and S8F). A portion of Tfh cells produced IL-21 together with IFN- γ , which is important for IgG2c class switching (43, 84). Pre-Tfh cells and mixed Th1 cells consisted of IL-21 single producers, IFN- γ single producers, and IL-21/IFN- γ double producers (Fig. 8, E and F). Terminally differentiated Th1 cells were predominantly IFN- γ single producers (Fig. 8G), suggesting that they likely migrate to peripheral tissues to exert their effector function (79). As with CD40L expression, Tfh cells and mixed Th1 cells comprised the majority of IL-21 single-producing and IL-21/IFN- γ double-producing CD4⁺ T cells in *Bcl6^{fl/fl}* mice (Fig. 8, H and I). In *Bcl6^{fl/fl}Cd4^{Cre}* mice, the frequency of IL-21 single producers was decreased, potentially due to the loss of Tfh cells, and mixed Th1 cells became the dominant cytokine-producing population (Fig. S8G and Fig. 8, H and I). Mixed Th1 and terminally differentiated Th1 cells displayed similar cytokine profiles between *Bcl6^{fl/fl}* and *Bcl6^{fl/fl}Cd4^{Cre}* mice (Fig. S8, H and I).

As mixed Th1 cells express IL-21 in addition to CD40L, they could support an alternative pathway of antibody production to that driven by Tfh cells. We therefore assessed whether mixed Th1 cells are sub-anatomically positioned to provide help to B cells. PSGL-1 mediates chemotaxis to CCL21 and CCL19, therefore helping naïve CD4⁺ T cells home to secondary lymphoid organs (85). During their differentiation, Tfh cells downregulate PSGL-1 and upregulate CXCR5 to enable their migration into B cell follicles (23, 82). However, as mixed Th1 cells continue to express PSGL-1 and do not upregulate CXCR5, it is unclear whether they can migrate to sites of

B cell help. Immunofluorescence of medLN following PR8 infection showed that Th1 cells (PSGL-1⁺CD4⁺T-bet⁺) co-localized with IgG2c⁺ B cells at the T cell-B cell (T-B) border (Fig. 8J). This was true in both *Bcl6*^{fl/fl} and *Bcl6*^{fl/fl}*Cd4*^{Cre} mice, suggesting that Th1 cells may promote antibody production in parallel with Tfh cells as well as in their absence. Taken together, we found that a subset of mixed Th1 cells expressed CD40L and IL-21 and were positioned at the T-B border to help B cells during viral infection.

Discussion

While protective antibodies are generally thought to originate from Tfh/GC-dependent pathways, it is unclear what happens to the antibody response when these structures are disrupted, as has been observed in patients with severe SARS-CoV-2 infection (46, 47). We found that certain class-switched antibodies were reduced but still present in Tfh-deficient mice following SARS-CoV-2 or influenza A virus infection, as well as SARS-CoV-2 vaccination. Though BCR analysis demonstrated impairment of SHM and mutation selection, Tfh-independent antibodies to SARS-CoV-2 were still high-affinity. They were also durable and demonstrated more diverse epitope reactivity compared to Tfh-dependent antibodies. Importantly, Tfh-independent antibody responses neutralized both homologous SARS-CoV-2 (USA-WA1/2020) and the B.1.351 variant of concern and were functional *in vitro* and *in vivo* (Fig. 9).

Our findings raise the question of which CD4⁺ T cell subset promotes protective class-switched antibodies in the absence of Tfh cells. Our preliminary results indicate that a subset of mixed Th1 cells may be responsible, given that they express CD40L and IL-21 and are also positioned to interact with B cells at the T-B border. Furthermore, it has previously been shown in the setting of influenza vaccination that Th1 cells make IFN- γ along with IL-21 to induce IgG2c

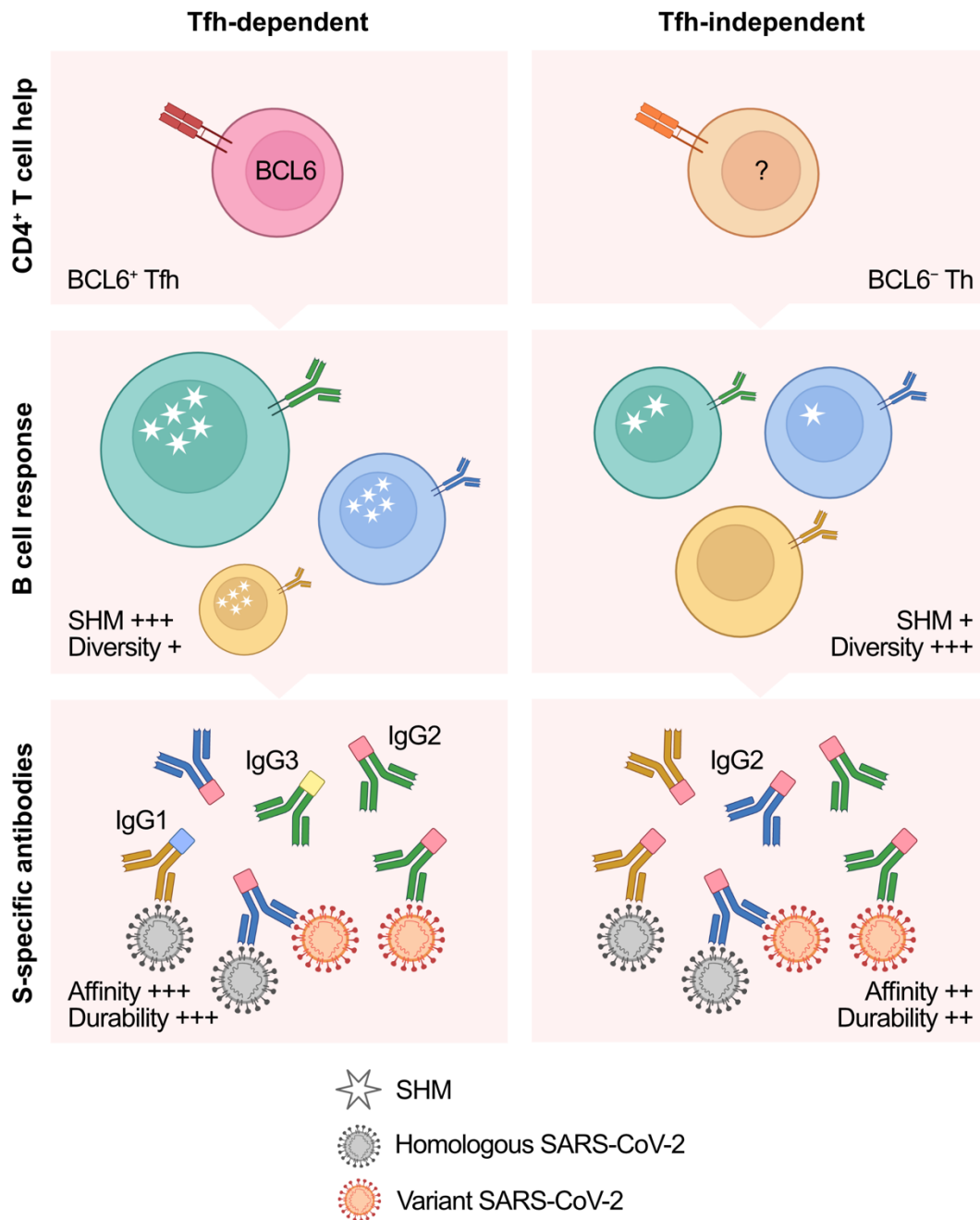


Figure 9: Complementary T cell-dependent pathways of antibody production mediate neutralizing responses to SARS-CoV-2

Tfh cells promote high levels of somatic hypermutation in S-specific B cells and select for particular mutated B cells clones, thus focusing the antibody repertoire. Non-Tfh CD4⁺ T cells support low levels of somatic hypermutation but without selection, leading to a more diverse repertoire of antibody epitope reactivity. S-specific antibodies that arise through Tfh-dependent

and -independent pathways are high-affinity and durable and also similarly neutralize both homologous and variant SARS-CoV-2.

B cell colors represent different clones. Size of B cells represents size of clones. Number of stars represents mutation burden. Antibody colors of Fab and Fc regions represent different epitope specificity and IgG subclass. Homologous and variant SARS-CoV-2 are indicated in gray and orange, respectively.

antibodies (36). Though less mutated and of lower avidity, these Th1-driven antibodies still neutralize influenza virus *in vitro* and protect from lethal challenge *in vivo* (36). Additionally, a recent study proposed a division of labor between Th1 cells and Tfh cells in promoting IgG2c class switching and supporting GC growth, respectively, during influenza virus infection (86). Therefore, it is possible that lymph node-resident Th1 cells are also responsible for the IgG2c antibodies we observed to SARS-CoV-2 infection and vaccination (51).

Contrary to the consistent Tfh-independent induction of IgG2c, IgG1 demonstrated a divergent requirement for Tfh cell help between SARS-CoV-2 infection and vaccination. These findings align with prior literature (26, 37, 50), suggesting that there may be different cellular requirements for IgG1 in the setting of diverse immune stimuli. Similarly, CD4⁺ T cells are dispensable for IgG3 in response to influenza virus infection (87), but we observed that IgG3 to SARS-CoV-2 was completely dependent on Tfh cell help. Thus, the same subclass may be produced by disparate mechanisms even during different viral infections. Finally, it is important to consider whether incomplete deletion of Tfh cells could contribute to antibody responses in *Bcl6^{fl/fl}Cd4^{Cre}* mice. This same mouse model demonstrates complete abrogation of IgE and IgG1 to allergens (41), and our characterization of cells and structures in the medLN support a lack of T cell-infiltrated, organized GCs in *Bcl6^{fl/fl}Cd4^{Cre}* mice; therefore, we conclude that highly specific and long-lived antibodies can be produced through Tfh-independent mechanisms likely dependent on the nature of infection or vaccination.

A surprising finding from our work was that SARS-CoV-2, but not influenza A virus, induced high-affinity Tfh-independent antibodies. As a possible mechanism for this finding, S-specific BCRs from Tfh-deficient mice used V genes highly homologous to human V genes that generate potent S-specific antibodies with minimal SHM (61–65). Furthermore, S-specific BCRs

still experienced low levels of SHM in the absence of Tfh cell help. Though SHM conventionally occurs in GCs (19), it has also been shown to occur at extrafollicular sites during bacterial infection and chronic autoimmunity (66–68). However, in the absence of Tfh cell help, mutated B cell clones did not experience positive selection, differentiating this process from classical affinity maturation. In this non-canonical pathway of high-affinity antibody production, non-Tfh CD4⁺ T cells may help by selecting naïve B cells that already express potent S-specific BCRs as well as supporting plasmablast differentiation of lowly mutated B cell clones. Our findings also suggest that long-lived plasma cells can emerge from this pathway, providing a durable source of humoral immunity.

Epitope profiling revealed that Tfh cells focus the antibody repertoire against S2-derived epitopes that are highly conserved across human coronaviruses as well as the emerging variants of concern. These same epitopes have been repeatedly identified in studies profiling the antibody repertoire of COVID-19 patients (75, 76), suggesting that the immunodominance of these epitopes in humans is mediated by Tfh cells. It has also been proposed that S2-reactive antibodies in people are primed by prior infections with endemic human coronaviruses (75). Given our findings in mice, which were not exposed to other coronaviruses prior to SARS-CoV-2 infection, it is likely that the intrinsic qualities of these S2-derived epitopes also contribute to their immunodominance. In addition, broadly neutralizing betacoronavirus antibodies with S2 specificity have recently been described, suggesting the use of S2-derived epitopes as targets for a pan-coronavirus vaccine (88). However, S2-specific antibodies are generally less potent neutralizers than RBD-specific antibodies and may even demonstrate little neutralization *in vitro* despite providing protection *in vivo* (88, 89). This provides a possible explanation for why we observed slightly lower neutralization potency indices of Tfh-dependent antibodies enriched for S2 epitope reactivity compared to more diverse Tfh-independent antibodies. Alternatively, the less focused antibody

repertoire of Tfh-deficient mice may better neutralize SARS-CoV-2 by targeting multiple sites of vulnerability, similar to previous findings of GC inhibition promoting a broader antibody response and enhanced heterosubtypic immunity to influenza virus infection (90).

While long-lived, high-affinity, neutralizing antibody responses conventionally depend on Tfh cells, we found that antibodies of similar quality, though not quantity, could be generated with the help of non-Tfh CD4⁺ T cells. Therefore, multiple pathways involving different CD4⁺ T cell subsets likely exist to promote protective antiviral humoral immunity (51). Tfh-independent responses may serve as a parallel mechanism for producing protective antibodies in settings of Tfh/GC impairment, such as COVID-19-induced inflammation and advanced age (46, 48). Understanding this additional axis of antiviral antibody production may therefore inform more effective vaccine design and help establish a new paradigm for how T cell-dependent humoral immunity is generated.

Future directions

Our work demonstrated that non-Tfh CD4⁺ T cells can promote antiviral antibodies in the setting of Tfh cell deficiency, providing an alternative mechanism for generating humoral immunity when the conventional pathway for doing so is disrupted. However, an outstanding question is whether this Tfh-independent pathway of antibody generation still exists when Tfh cells are intact. While our preliminary findings indicate that Th1 cells co-localize with IgG2c⁺ B cells at the T-B border in both Tfh-sufficient and -deficient mice, additional experiments are required to demonstrate that the Tfh-independent pathway is functional in the presence of Tfh cells.

First, to delineate the non-Tfh CD4⁺ T cells that interact with B cells during SARS-CoV-2 infection, we can leverage the LIPSTIC method developed by the Victora lab (91). LIPSTIC, also

known as “Labelling Immune Partnerships by SorTagging Intercellular Contacts,” uses bacterial sortase A (SrtA)-mediated cell-labeling to identify immune cells that engage in CD40-CD40L interactions (91). In the method originally described, CD40L-fused SrtA catalyzes the transfer of its substrate, a biotinylated LPETG peptide, onto CD40 tagged with five N-terminal glycine residues (G5). The result is that a CD40-G5-expressing B cell or dendritic cell that interacts with a CD40L-SrtA-expressing T cell will be labeled with biotin, which can then stained and identified by flow cytometry (91).

For our experiment, we will instead utilize mice with CD40-SrtA-expressing B cells and CD40L-G5-expressing T cells, so that the T cells that engage in CD40-CD40L interactions with B cells will be labeled with biotin. After infecting the mice with SARS-CoV-2, we will administer biotinylated LPETG peptide intranasally to enable T cell labeling. To specifically label T cells that interact with SARS-CoV-2 S-specific B cells, we will conjugate the biotinylated LPETG peptide to S protein, enabling S-specific B cells to preferentially bind the SrtA substrate and catalyze its transfer onto CD40L-G5 of the interacting T cell. We can then sort out the biotinylated CD4⁺ T cells and comprehensively characterize them by single-cell RNA sequencing or mass cytometry to identify surface markers, chemokine receptors, and transcription factors that distinguish the non-Tfh cell population from Tfh cells.

Using these markers, we can then disrupt the function of B cell-helping non-Tfh cells by inhibiting their migration, deleting a transcription factor required for their development, or depleting them with antibodies that recognize a unique surface marker. For example, if non-Tfh cells indeed interact with B cells at the T-B border, then it is plausible that they express the chemokine receptor CXCR3 to migrate to this area (86). Blocking interactions between CXCR3 and its ligands CXCL9 and CXCL10 could therefore disrupt positioning of non-Tfh cells, prevent

them from providing help to B cells, and reveal whether this Tfh-independent pathway of antibody generation is functional in a Tfh-sufficient setting. However, CXCR3 is likely expressed by Tfh cells as well during viral infection (53), so other markers that are uniquely expressed by non-Tfh cells will be required for these studies.

We can also test the function of these non-Tfh cells through adoptive transfer studies. We would sort Tfh cells and non-Tfh cells from SARS-CoV-2-infected WT mice and then transfer the T cell populations separately or together into T cell-deficient recipients. By comparing the antibody response in mice that receive both Tfh cells and non-Tfh cells to those that receive Tfh cells only, we can assess whether non-Tfh cells induce additional antibody production or generate a complementary antibody response that is, for example, more diverse. Furthermore, the mice that receive only non-Tfh cells should also produce antibodies, confirming our results from Tfh-deficient mice.

In addition to testing whether the Tfh-independent pathway operates in the setting of intact Tfh cells, it is also important to assess whether this pathway functions in physiological models of Tfh/GC impairment. Our studies utilized a well-established genetic mouse model to cleanly delete Tfh cells, but the initial motivation for our work came from reports of Tfh/GC impairment due to COVID-19-induced inflammation (46). Therefore, using a mouse model that recapitulates the disrupted Tfh/GC structures seen in severe COVID-19 patients would better demonstrate the function of the Tfh-independent pathway. While the AAV-hACE2 and K18-hACE2 mouse models we used led to robust Tfh and GC induction, it is possible that other models, for example, using mouse-adapted SARS-CoV-2 (92, 93), may disrupt Tfh cells and GCs in wildtype mice. Alternatively, other infection models such as *Salmonella enterica* serovar Typhimurium, *Ehrlichia muris*, and *Borrelia burgdorferi* are known to induce GC suppression in mice and could be used

to interrogate the role of the Tfh-independent pathway (45). As advanced age is another setting in which Tfh cells and GCs are suppressed (48), it will also be interesting to study whether the Tfh-independent pathway mediates antibody production in aged mice.

Furthermore, one interesting finding from our work was that high-affinity antibodies could be made in a Tfh-independent manner to SARS-CoV-2 but not influenza A virus. To dissect whether this difference is due to the antigenic target or the nature of the viral infection, we could infect Tfh-deficient mice with HA-expressing SARS-CoV-2 or S protein-expressing PR8. If HA-specific antibodies induced by SARS-CoV-2 infection are still low-affinity and S-specific antibodies induced by PR8 infection are still high-affinity, this would indicate that the antigenic target is a more important determinant of Tfh-independent high-affinity antibody production. These results could be validated in the setting of vaccination by immunizing Tfh-deficient mice with HA or S protein with the same adjuvant. Finding that only Tfh-independent S-specific antibodies retain high affinity would suggest that the ability of the Tfh-independent pathway to generate high-affinity antibodies likely depends on whether germline-encoded BCRs already possess high affinity for a given antigen.

These proposed studies will: (1) identify the responsible non-Tfh CD4⁺ T cell population that provides help to B cells during SARS-CoV-2 infection, (2) elucidate whether this Tfh-independent pathway of antibody production operates in the setting of intact Tfh cells or only in their absence, and (3) delineate limitations of the Tfh-independent pathway in promoting high-affinity antibodies depending on the antigenic target. Such insight will be critical for determining the utility of this alternative pathway of antibody production and developing vaccination strategies that best leverage this pathway for protective immune responses.

§ CHAPTER 3: IL-4 regulation in T follicular helper cells dictates appropriate antibody class switching during type 1 versus type 2 immune responses

IL-4 is necessary and sufficient for high-affinity IgE production *in vivo*

To confirm the essential role of IL-4 for IgE production, we immunized WT and *Ii4*^{-/-} mice intranasally with allergen *Alternaria alternata* together with haptened protein antigen (4-hydroxy-3-nitrophenyl)-acetyl-ovalbumin (NP₁₉OVA). We have previously demonstrated that this allergic airway inflammation model leads to the generation of high-affinity NP₇-specific IgE antibodies (44). Consistent with past studies (39, 95), loss of IL-4 ablated IgE production (Fig. 10A).

We next assessed whether IL-4 is sufficient for IgE production by testing whether IL-4 overexpression could lead to aberrant induction of IgE antibodies during a type 1 immune response. As IL-4 from Tfh cells is required for IgE induction (39), we overexpressed IL-4 in OVA-specific CD4⁺ T cells (OT-II cells) and transferred them into recipients immunized intranasally with lipopolysaccharide (LPS) and NP₁₉OVA. OT-II Tfh cells transduced with the IL-4 overexpression construct produced IL-4 protein, while OT-II Tfh cells transduced with a GFP control vector did not (Fig. 10B). Mice that received GFP-expressing OT-II cells did not produce IgE antibodies, consistent with a normal type 1 immune response to LPS/NP₁₉OVA (Fig. 10C). In contrast, mice that received IL-4-overexpressing OT-II cells produced high-affinity NP₇-specific IgE antibodies. This suggests that uncontrolled IL-4 production by Tfh cells during a type 1 immune response is sufficient to induce aberrant IgE antibodies. Taken together, IL-4 is both necessary and sufficient for IgE production *in vivo*. Understanding how IL-4 production is regulated in Tfh cells is therefore

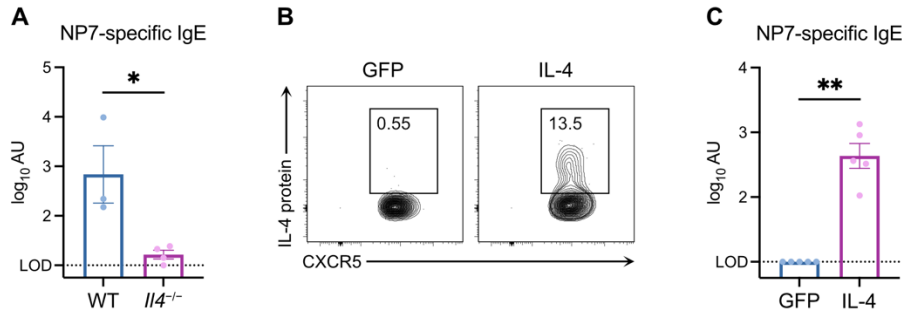


Figure 10: IL-4 is necessary and sufficient for high-affinity IgE production *in vivo*

(A) C57BL/6N WT and *Il4*^{-/-} mice were immunized intranasally (i.n.) with *Alternaria*/NP₁₉OVA followed by 2 boosts with NP₁₉OVA only. High-affinity NP₇-specific IgE antibody titers 8 days after the last boost.

(B and C) OT-II cells were retrovirally transduced with a GFP control (GFP) or IL-4 overexpression (IL-4) construct and then transferred into C57BL/6N WT recipients. The following day, mice were immunized i.n. with lipopolysaccharide (LPS)/NP₁₉OVA followed by 1 boost with NP₁₉OVA only.

(B) Representative flow plots of IL-4 protein production in OT-II T follicular helper (Tfh) cells 7 days after primary immunization.

(C) High-affinity NP₇-specific IgE antibody titers 7 days after boost.

LOD, limit of detection of the assay. Statistical significance was assessed by two-tailed Welch's t-test. **P* < 0.05; ***P* < 0.01. Data are expressed as mean ± standard error of mean (SEM) log₁₀ arbitrary units (AU). Each symbol represents an individual mouse. Data are from one experiment.

important for gaining insight into the appropriate induction of antibody isotypes during type 1 vs type 2 immune responses.

IL-4 from Tfh cells is required for IgG1 switching but not germinal center formation or plasmablast differentiation during type 1 immune responses

In addition to its role in IgE induction, IL-4 is considered a canonical Tfh cell cytokine, produced even during microbial immunizations that do not elicit IgE (96, 97). In these responses, IL-4-producing Tfh cells are thought to support GC B cell proliferation, survival, and differentiation, given that IL-4 is also a B cell growth factor (98). While it has been demonstrated *in vitro* that IL-4 blockade prevents optimal IgG production in Tfh cell-B cell co-cultures (96), no study has directly tested the role of Tfh cell-derived IL-4 *in vivo* during a type 1 immune response.

To this end, we generated mixed bone marrow chimeric mice (BMCM) lacking IL-4 specifically in the Tfh cell compartment. Mixed BMCM were generated by transferring an 80:20 mixture of *Bcl6^{fl/fl}Cd4^{Cre}:Il4^{WT}* (Tfh-WT) or *Bcl6^{fl/fl}Cd4^{Cre}:Il4^{-/-}* (Tfh-*Il4^{-/-}*) bone marrow into irradiated *Bcl6^{fl/fl}Cd4^{Cre}* recipients (Fig. 11A). After 12 weeks, control Tfh-WT and Tfh-*Il4^{-/-}* mice were administered LPS/NP₁₉OVA or mouse-adapted influenza A virus (PR8) intranasally, and cellular responses in the mediastinal lymph node were evaluated 9 days later. Tfh-WT and Tfh-*Il4^{-/-}* mice demonstrated similar levels of Tfh cell induction (Fig. 11B), indicating similar reconstitution of the Tfh cell compartment by *Il4^{WT}* and *Il4^{-/-}* bone marrow. GC B cell formation and plasmablast differentiation were also comparable between Tfh-WT and Tfh-*Il4^{-/-}* mice (Fig. 11, C and D), suggesting that Tfh cell-derived IL-4 is not required for B cell proliferation, survival, and differentiation in GC reactions as has previously been proposed.

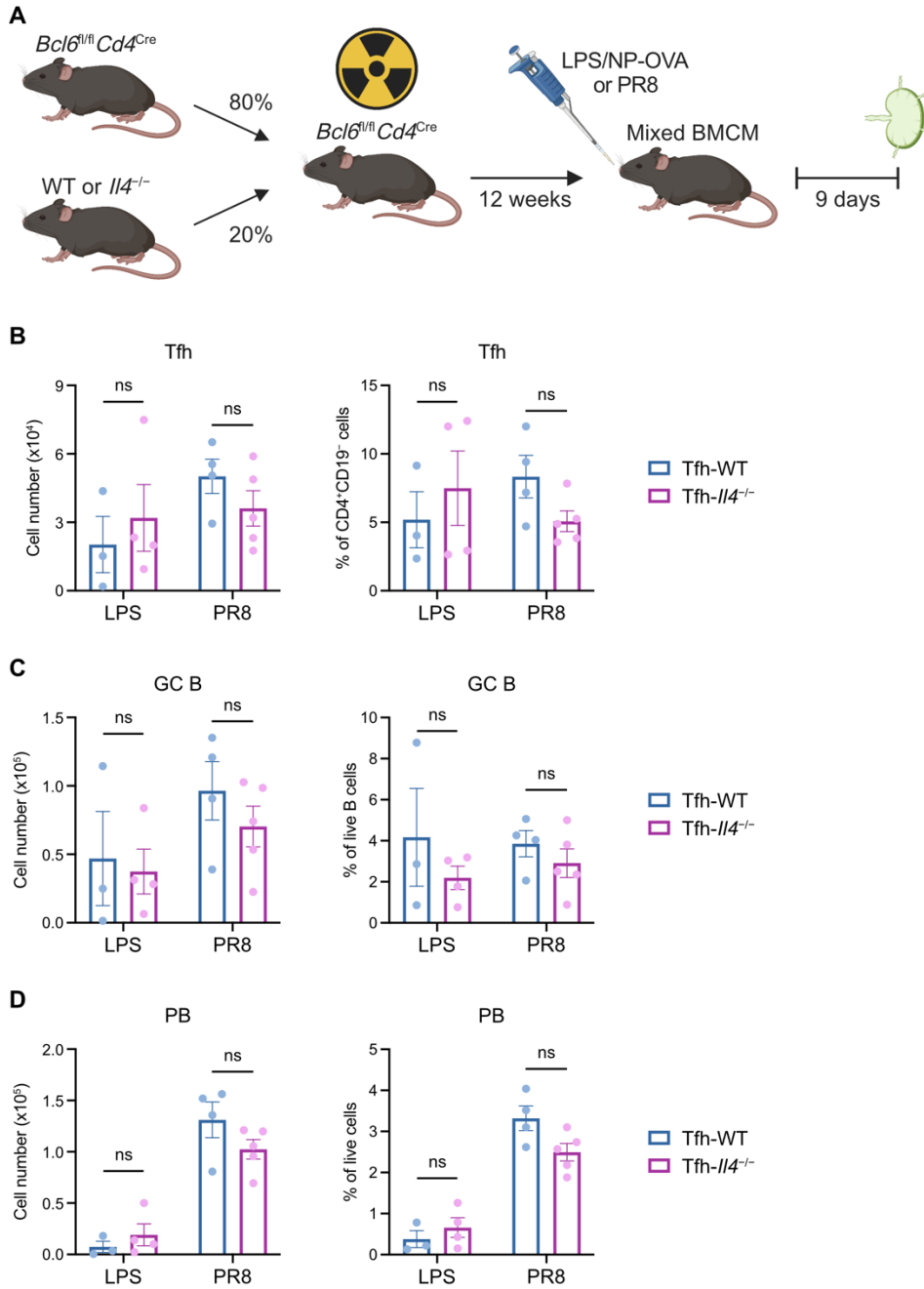


Figure 11: IL-4 from Tfh cells is not required for germinal center formation or plasmablast differentiation during type 1 immune responses

(A) Schematic of experimental design for generating mixed bone marrow chimeric mice (BMCM) and assessing cellular response to LPS/NP₁₉OVA immunization or mouse-adapted influenza A virus (PR8) infection. Mixed BMCM were generated by transferring an 80:20 mixture of

Bcl6^{fl/fl}Cd4^{Cre}:Il4^{WT} (Tfh-WT) or *Bcl6^{fl/fl}Cd4^{Cre}:Il4^{-/-}* (Tfh-*Il4^{-/-}*) bone marrow into irradiated *Bcl6^{fl/fl}Cd4^{Cre}* recipients. After 12 weeks, mice were administered LPS/NP₁₉OVA or PR8 i.n.

(**B to D**) Mediastinal lymph nodes (medLN) were analyzed 9 days post LPS/NP₁₉OVA immunization (LPS) or PR8 infection for Tfh cell (B), germinal center B (GC B) cell (C), and plasmablast (PB) responses (D).

Statistical significance was assessed by two-tailed unpaired t-test. ns, not significant. Data are expressed as mean ± SEM. Each symbol represents an individual mouse. Data are representative of two independent experiments with three to five mice per group.

We next assessed the effect of Tfh cell-specific IL-4 deficiency on class switching. IL-4 is known to be an immunoglobulin switch factor for IgG1 in addition to IgE (99). Accordingly, GC B cells and plasmablasts in *Tfh-Il4^{-/-}* mice displayed impaired class switching to IgG1 but not IgG2c in response to both LPS/NP₁₉OVA and PR8 (Fig. 12, A and B). Using two *in vivo* models of type 1 immune responses, we therefore demonstrated that Tfh cell-derived IL-4 is actually not required for supporting overall GC B cell formation and plasmablast formation but is critical for IgG1 switching.

Transcriptional and post-transcriptional regulation limit IL-4 protein production by Tfh cells during type 1 immune responses

Our results thus far indicated that, during type 1 immune responses, Tfh cells need to make enough IL-4 to induce IgG1 switching but not so much that IgE antibodies are aberrantly generated. We therefore hypothesized that Tfh cells fine-tune the levels of IL-4 they produce to induce the antibody isotypes appropriate for a given immune response. Indeed, we observed by intracellular cytokine staining that Tfh cells generated minimal IL-4 protein in response to LPS/NP₁₉OVA and PR8 (Fig. 13, A to C). In contrast, immunization with *Alternaria*/NP₁₉OVA led to high-levels of IL-4 protein production in Tfh cells (Fig. 13, A and C), consistent with the strong IgE response of this type 2 model.

Given the importance of tightly regulating IL-4, we predicted that Tfh cells would employ multiple mechanisms to constrain IL-4 production during type 1 immune responses. We first assessed the degree to which Tfh cells activate *Il4* transcription in type 1 versus type 2 immune responses, using the 4get (*Il4-IRES-eGFP*) reporter mouse (100). Tfh cells demonstrated lower 4get reporter expression in response to LPS/NP₁₉OVA and PR8 compared to *Alternaria*/NP₁₉OVA

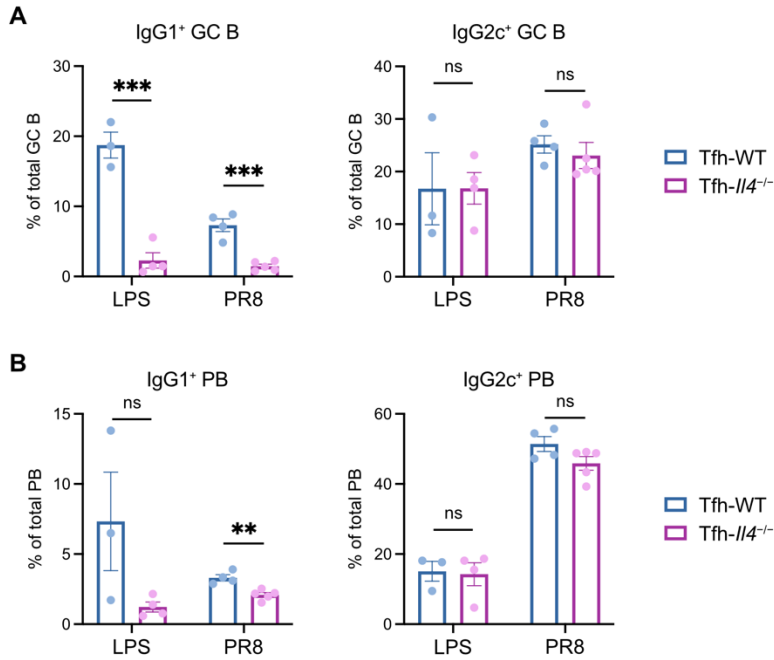


Figure 12: IL-4 from Tfh cells is required for IgG1 switching during type 1 immune responses

(A and B) Mixed BMCM were generated by transferring an 80:20 mixture of *Bcl6*^{fl/fl}*Cd4*^{Cre}:*Il4*^{WT} (Tfh-WT) or *Bcl6*^{fl/fl}*Cd4*^{Cre}:*Il4*^{-/-} (Tfh-*Il4*^{-/-}) bone marrow into irradiated *Bcl6*^{fl/fl}*Cd4*^{Cre} recipients. After 12 weeks, mice were administered LPS/NP₁₉OVA (LPS) or PR8 i.n. MedLN were analyzed 9 days later for IgG1 and IgG2c expression among GC B cells (A) and PB (B). Statistical significance was assessed by two-tailed unpaired t-test. ***P* < 0.01; ****P* < 0.001. ns, not significant. Data are expressed as mean ± SEM. Each symbol represents an individual mouse. Data are representative of two independent experiments with three to five mice per group.

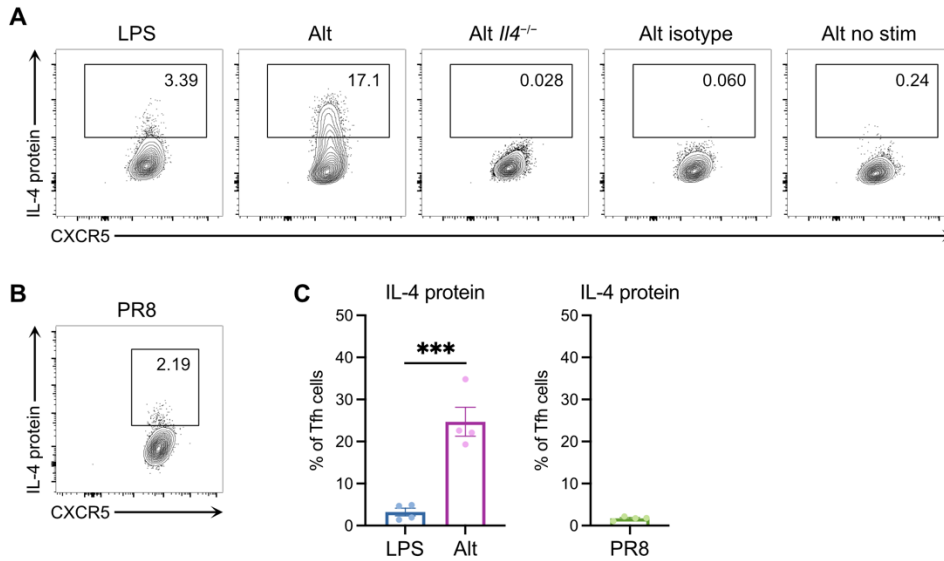


Figure 13: Tfh cells produce minimal levels of IL-4 protein during type 1 immune responses
(A) C57BL/6N WT and *Il4*^{-/-} mice were immunized i.n. with LPS/NP₁₉OVA (LPS) or *Alternaria*/NP₁₉OVA (Alt), and medLN were analyzed 7 days later. Representative flow plots of IL-4 protein production in Tfh cells in the following conditions from left to right: 1) WT mice immunized with LPS/NP₁₉OVA, 2) WT mice immunized with *Alternaria*/NP₁₉OVA, 3) *Il4*^{-/-} mice immunized with *Alternaria*/NP₁₉OVA, 4) WT mice immunized with *Alternaria*/NP₁₉OVA and stained with an anti-IL-4 isotype control antibody, 5) WT mice immunized with *Alternaria*/NP₁₉OVA and stained with an anti-IL-4 antibody without PMA/ionomycin stimulation.
(B) C57BL/6N WT were infected i.n. with PR8, and medLN were analyzed 7 days later. Representative flow plot of IL-4 protein production in Tfh cells.
(C) Frequency of IL-4 protein production in Tfh cells 7 days following i.n. administration of LPS/NP₁₉OVA (LPS), *Alternaria*/NP₁₉OVA (Alt), or PR8.
 Statistical significance was assessed by two-tailed unpaired t-test. ****P* < 0.001. Data are expressed as mean ± SEM. Each symbol represents an individual mouse. Data in (A, B, and C [right]) are from one experiment. Data in (C [left]) are representative of three independent experiments with three to four mice per group.

(Fig. 14, A and B), suggesting that transcriptional activation is one mechanism by which Tfh cells limit IL-4 protein production during type 1 immune responses. Corroborating the 4get reporter results, *Il4* transcript levels were reduced in Tfh cells sorted from mice immunized with LPS/NP₁₉OVA compared to *Alternaria*/NP₁₉OVA (Fig. 14C). Tfh cells were the only CD4⁺ T cell subset in LPS/NP₁₉OVA-immunized mice that expressed *Il4*, whereas both Tfh and non-Tfh CD4⁺ T cells expressed *Il4* in response to *Alternaria*/NP₁₉OVA.

We next tested whether Tfh cells also leverage post-transcriptional regulatory mechanisms to limit IL-4 protein production during type 1 immune responses. To this end, we performed an *Il4* mRNA degradation assay on Tfh cells sorted from LPS/NP₁₉OVA- and *Alternaria*/NP₁₉OVA-immunized mice. *Il4* transcripts experienced significant degradation in Tfh cells from both conditions without stimulation (Fig. 14D), indicating that *Il4* mRNA is highly unstable when Tfh cells are not making IL-4 protein, regardless of the type of immune response. However, upon stimulation to induce IL-4 protein, *Il4* transcripts displayed less degradation in Tfh cells from *Alternaria*/NP₁₉OVA compared to LPS/NP₁₉OVA immunization (Fig. 14D). Decreased *Il4* mRNA stability is therefore another mechanism that constrains IL-4 protein production in Tfh cells during type 1 immune responses. Taken together, these results implicate both transcriptional and post-transcriptional mechanisms in limiting IL-4 protein, thus ensuring IgG1 but not IgE generation in response to microbial stimuli.

Subcellular localization and ribosomal association of *Il4* mRNA may provide further insight into mechanisms of post-transcriptional regulation

Stress granules (SGs) and processing bodies are membrane-less compartments that regulate mRNA stability and translation (*101*). These structures are composed of translationally inactive

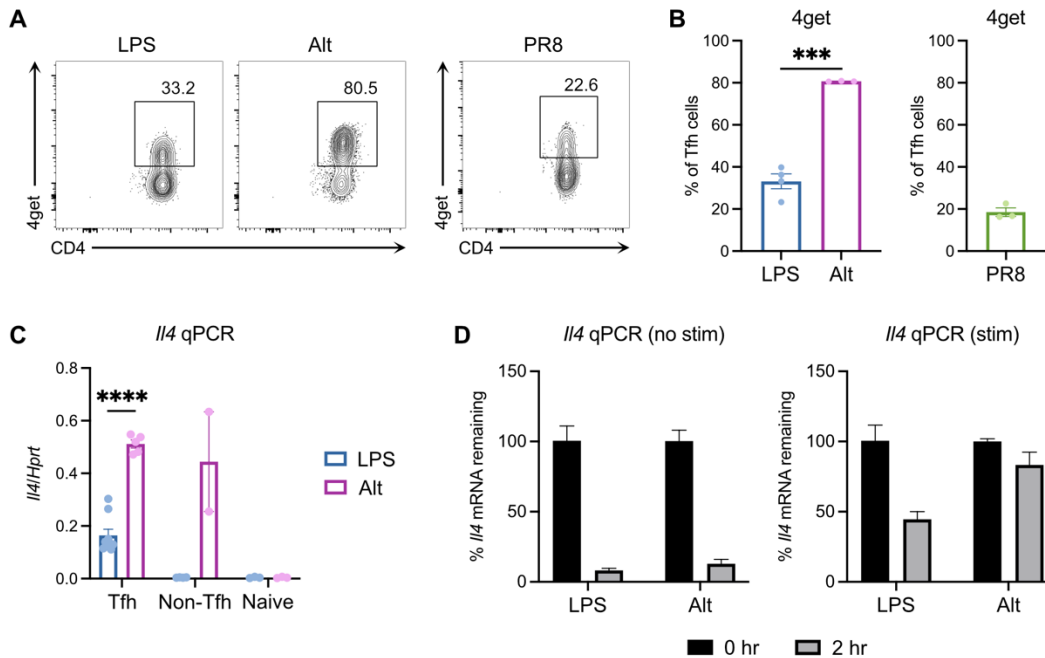


Figure 14: Transcriptional and post-transcriptional regulation limit IL-4 protein production by Tfh cells during type 1 immune responses

(A and B) 4get reporter mice were administered LPS/NP₁₉OVA (LPS), *Alternaria*/NP₁₉OVA (Alt), or PR8 i.n., and medLN were analyzed 7 days later. (A) Representative flow plots of 4get reporter expression in Tfh cells. (B) Frequency of 4get reporter expression in Tfh cells.

(C) Tfh, non-Tfh, and naïve CD4⁺ T cells were sorted from medLN of C57BL/6N WT mice 7 days following i.n. immunization with LPS/NP₁₉OVA (LPS) on *Alternaria*/NP₁₉OVA (Alt). *Il4* transcripts were quantified by qPCR, normalized to *Hprt*.

(D) Tfh cells were sorted from medLN of C57BL/6N WT mice 7 days following i.n. immunization with LPS/NP₁₉OVA (LPS) on *Alternaria*/NP₁₉OVA (Alt). Tfh cells were left unstimulated (left) or stimulated with PMA/ionomycin for 40 min (right) before the mRNA degradation assay. Cells were collected 0 hr and 2 hr after initiation of Actinomycin D treatment, and *Il4* transcripts were quantified by qPCR.

Statistical significance was assessed by either two-tailed unpaired t-test or Welch's t-test, based on the F test for unequal variance. ****P* < 0.001; *****P* < 0.0001. Data are expressed as mean ± SEM. Each symbol represents an individual mouse. Data in (B [left]) are representative of three independent experiments with three to four mice per group. Data in (B [right] and D) are from one experiment. Data in (C [Tfh]) are aggregated from two independent experiments with two to four mice per group.

complexes of mRNA and RNA-binding proteins (RBPs), including the translational repressor TIA1. In *in vitro*-cultured Th2 cells, TIA1 has been shown to prevent *Il4* translation in primed Th2 cells before they are re-stimulated (102). In human osteoarthritis chondrocytes, translational suppression of *Cox2* mRNA has been visualized by mRNA co-localization with TIA1 and additional SG RBPs, TIAR and G3BP1 (103). To first establish the feasibility of visualizing *Il4* mRNA localization, we performed *Il4* mRNA fluorescence *in situ* hybridization (FISH) on *in vitro*-cultured Th2 cells. *Il4* mRNA was detectable by FISH in WT Th2 cells but not in *Il4*^{-/-} Th2 cells, demonstrating the specificity of this technique (Fig. 15A). Furthermore, we performed *Il4* mRNA FISH on Tfh cells sorted from mice immunized with LPS/NP₁₉OVA or *Alternaria*/NP₁₉OVA (Fig. 15B). This demonstrated increased levels of *Il4* mRNA in *Alternaria*-induced Tfh cells compared to LPS-induced Tfh cells, consistent with prior *Il4* qPCR results (Fig. 14C). We are currently optimizing the protocol for co-staining RBPs, which will allow us to evaluate whether *Il4* mRNA is co-localized with SGs and/or processing bodies in Tfh cells sorted from type 1 versus type 2 immune responses.

We also sought to investigate whether IL-4 protein production in Tfh cells is regulated by differential association of *Il4* mRNA with ribosomes. To study this, we used the RiboTag mouse crossed with a *Cd4*^{Cre} mouse (104). In RiboTag^{fl/fl}*Cd4*^{Cre} mice, expression of Cre recombinase in CD4⁺ cells mediates the incorporation of a hemagglutinin (HA) tag onto the ribosomal protein subunit RPL22 (104). The HA tag can then be used to immunoprecipitate polysomes and their associated mRNA transcripts. Performing *Il4* qPCR on total RNA and immunoprecipitated RNA quantifies the percentage of *Il4* mRNA transcripts that are polysome-associated, which serves as an indication of translational efficiency (104). This method works with inputs as low as 50,000 cells (105), making it well-suited for studying sorted Tfh cells. We first validated HA expression

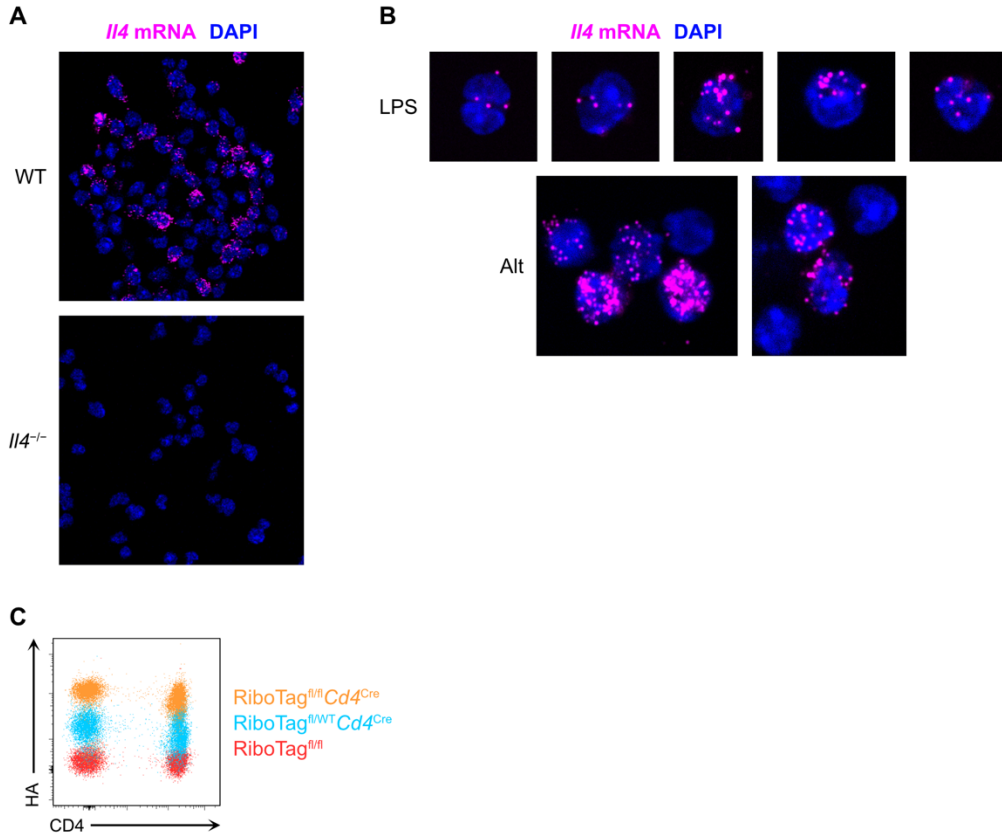


Figure 15: Subcellular localization and ribosomal association of *Il4* mRNA may provide further insight into mechanisms of post-transcriptional regulation

(A) CD4⁺ T cells from C57BL/6N WT and *Il4*^{-/-} mice were cultured *in vitro* with a Th2-polarizing cocktail. After 5 days of culture, Th2 cells were restimulated with PMA/ionomycin, and *Il4* mRNA FISH was performed. Images were acquired on a Leica TCS SP5 confocal microscope (60X).

(B) Tfh cells were sorted from medLN of C57BL/6N WT mice 7 days following i.n. immunization with LPS/NP₁₉OVA (LPS) on *Alternaria*/NP₁₉OVA (Alt). After PMA/ionomycin stimulation, *Il4* mRNA FISH was performed. Images were acquired on a Nikon TiE spinning disk confocal microscope (100X).

(C) Circulating T cells from RiboTag^{fl/fl}*Cd4*^{Cre}, RiboTag^{fl/WT}*Cd4*^{Cre}, and RiboTag^{fl/fl} mice were stained intracellularly for HA.

Data are from one experiment.

in T cells from RiboTag^{fl/fl}Cd4^{Cre} mice and also successfully performed immunoprecipitation of ribosome-associated *Il4* mRNA using *in vitro*-cultured RiboTag^{fl/fl}Cd4^{Cre} Th2 cells (Fig. 15C and data not shown). We are currently optimizing the RiboTag procedure to perform on Tfh cells sorted from RiboTag^{fl/fl}Cd4^{Cre} mice immunized with type 1 versus type 2 adjuvants.

Discussion and future directions

Antibody isotype is a critical determinant of the effector response to a given immune stimulus. Type 1 immune responses to microbial stimuli are typified by the production of IgG2 and IgG1 antibodies. Type 2 immune responses to allergens and helminths involve the generation of IgE and IgG1 antibodies. Our work demonstrates the role of Tfh cell-derived IL-4 as a rheostat for the appropriate induction of IgG1 versus IgE antibodies during type 1 and type 2 immune responses. Tfh cells in type 1 immune responses produced minimal amounts of IL-4 to stimulate IgG1 class switching but not induce IgE. Tfh cells in type 2 immune responses produced high levels of IL-4, which was required for IgE. We also found that reduced *Il4* transcriptional activation and mRNA stability help constrain IL-4 protein production, with potentially additional contribution from other post-transcriptional regulatory mechanisms.

Our findings that IL-4 levels modulate the induction of IgG1 versus IgE are consistent with prior literature. In *in vitro* cultures of LPS-stimulated murine B cells, IgE production increases proportionally with the concentration of IL-4 added (106). Furthermore, *Il4*-hemizygous mice immunized with OVA/aluminum hydroxide demonstrate drastic impairment of OVA-specific IgE antibodies, while OVA-specific IgG1 is minimally affected (107). As CD4⁺ T cells in *Il4*-hemizygous mice produce at least two-fold less IL-4 protein compared to controls (107), these results suggest that there is a threshold requirement of IL-4 for IgE production. Below the threshold,

IgE production is abrogated, but IgG1 can still be made. Our work adds to these studies by implicating Tfh cells as the source of IL-4 that dictates IgG1 versus IgE *in vivo*, as well as relating this regulation to the appropriate induction of antibody isotypes in type 1 versus type 2 immune responses.

Our work also showed that Tfh cell-derived IL-4 is dispensable for GC B cell formation and plasmablast differentiation during type 1 immune responses. Tfh cell-derived IL-4 has been thought to support GC B cells due to its potent effects on B cell proliferation and differentiation *in vitro* (108). However, *in vivo* studies have reached conflicting conclusions about the requirement of IL-4 or STAT6 signaling for GC formation (109–112). Later observations that type 2 but not type 1 immune responses rely on IL-4 for GC formation help to reconcile these conflicting findings, and our results further confirm that IL-4 from Tfh cells is not required for GCs during type 1 immune responses (110, 112, 113). The absence of IL-4 *in vivo* may also be compensated by IL-21, another canonical Tfh cell cytokine that promotes B cell proliferation and differentiation and is highly expressed during type 1 immune responses (19, 110). It has further been argued that other sources of IL-4, such as NKT cells, support GC B cells, but the actual effect of IL-4 deficiency or blockade on GC B cell induction in that study was minimal (97).

To fine-tune the levels of IL-4 protein they produce, Tfh cells likely leverage multiple transcriptional and post-transcriptional regulatory mechanisms. We identified reduced *Il4* transcriptional activation and mRNA stability as two mechanisms operating in Tfh cells during type 1 immune responses, with ongoing experiments to investigate the roles of *Il4* mRNA subcellular localization and ribosomal association in further regulating IL-4 protein production. As differences in *Il4* transcriptional activation are likely a major driver of the divergent patterns

of IL-4 protein production, future work will investigate mechanisms of *Il4* transcriptional activation in Tfh cells from type 1 versus type 2 immune responses.

Prior studies have reported divergent mechanisms of *Il4* transcriptional activation between Th2 cells and Tfh cells involving different *Il4* enhancers and transcription factors. While Th2 cells utilize hypersensitivity site 2 (HS2) and Rad50 hypersensitive site 6 (RHS6) for *Il4* expression, Tfh cells instead require hypersensitivity site V (HS V), also known as conserved noncoding sequence 2 (CNS2) (114–117). In turn, the enhancers active in Th2 cells are bound by GATA3, whereas those active in Tfh cells are bound by BATF (114, 118, 119). It was previously thought that Tfh cells do not express GATA3 due to suppression by Tfh transcription factor BCL6 (21, 22, 120). In addition, studies using viral or helminth infection found no *Gata3* induction in Tfh cells (96, 121). However, multiple studies have since shown that Tfh cells can co-express BCL6 and GATA3 during particular type 2 immune responses, including *Alternaria* immunization (44, 122). Thus, it is possible that GATA3, HS2, and RHS6 cooperate to drive high *Il4* expression in Tfh cells from type 2 allergic responses, whereas BATF and HS V/CNS2 promote a lower level of *Il4* transcriptional activation in Tfh cells from type 1 immune responses.

To test this, we could identify *Il4* enhancers with open chromatin and permissive chromatin modifications by performing ATAC-seq as well as CUT&RUN for H3K9ac, H3K14ac, H3K4me2, and H3K4me3 on Tfh cells from type 1 versus type 2 immune responses (123, 124). After identifying the active enhancers for each condition, we could then use mice that lack each of these enhancers to assess the effect on IL-4 production and thus functionally validate the role of each enhancer. We could also map BATF and GATA3 binding in Tfh cells using CUT&RUN, which would show whether these two transcription factors work cooperatively in Tfh cells from type 2

immune responses to boost *Il4* transcriptional activation, and whether BATF demonstrates different binding patterns in type 1 versus type 2 Tfh cells.

In addition, we could further investigate post-transcriptional regulatory mechanisms using unbiased approaches. Our ongoing experiments to test whether *Il4* mRNA is co-localized with SGs and processing bodies rely on staining RBPs with known inhibitory function in non-Tfh cell types. To complement this approach, we could use biotinylated DNA oligonucleotides to capture *Il4* mRNA and any associated proteins from Tfh cells (125). We could then profile the proteins by mass spectrometry, which may reveal new RBPs that regulate *Il4* mRNA stability and translation specifically in Tfh cells.

After identifying the transcriptional and post-transcriptional mechanisms that regulate IL-4 production, we can perturb them to study the effects on IgE induction. For instance, deleting GATA3-bound *Il4* enhancers may dramatically reduce IL-4 production by Tfh cells and abrogate IgE induction during type 2 responses, highlighting the importance of strong *Il4* transcriptional activation for this antibody isotype. Or, disrupting co-localization of *Il4* mRNA with inhibitory RBPs may lead to dysregulated IL-4 production and aberrant IgE induction during a type 1 immune response, indicating a crucial role for post-transcriptional control as well. These insights into the molecular checkpoints that govern antibody isotype switching may help inform strategies to mitigate IgE production in pathological conditions such as allergy.

§ CHAPTER 4: Nonsteroidal anti-inflammatory drugs dampen the cytokine and antibody response to SARS-CoV-2 infection

We began this study shortly after the World Health Organization declared COVID-19 a pandemic. As public health officials had raised concerns about the use of nonsteroidal anti-inflammatory drugs (NSAIDs) for treating symptoms of COVID-19 (*126, 127*), we wanted to determine whether and how NSAIDs could affect COVID-19 pathogenesis. While NSAIDs had no effect on *ACE2* expression, viral entry, or viral replication, we found that they impaired the production of proinflammatory cytokines and neutralizing antibodies in a mouse model of SARS-CoV-2 infection.

We measured antibody titers at 6 dpi due to the rapid lethality of this model. At this early timepoint, antibodies are likely produced by short-lived plasmablasts that may or may not require T cell help (*128*). B cells upregulate cyclooxygenase-2 (COX-2), a target of NSAIDs, following activation, and COX-2 inhibition has been found to reduce expression of BLIMP-1 and XBP-1, transcription factors required for plasmablast differentiation (*129–131*). Therefore, it is plausible that NSAIDs impair the production of antibodies by B cells by directly interfering with activation and/or differentiation.

Our findings also raise the possibility that NSAIDs may alter the immune response to SARS-CoV-2 vaccination. We are currently using mouse models of chronic NSAID treatment and samples from patients chronically taking NSAIDs for rheumatological conditions to evaluate the potential effect of NSAIDs on the antibody response to SARS-CoV-2 mRNA vaccination.



Nonsteroidal Anti-inflammatory Drugs Dampen the Cytokine and Antibody Response to SARS-CoV-2 Infection

Jennifer S. Chen,^{a,b} Mia Madel Alfajaro,^{a,b} Ryan D. Chow,^c Jin Wei,^{a,b} Renata B. Filler,^{a,b} Stephanie C. Eisenbarth,^{a,b} Craig B. Wilen^{a,b}

^aDepartment of Laboratory Medicine, Yale University School of Medicine, New Haven, Connecticut, USA

^bDepartment of Immunobiology, Yale University School of Medicine, New Haven, Connecticut, USA

^cDepartment of Genetics, Yale University School of Medicine, New Haven, Connecticut, USA

ABSTRACT Identifying drugs that regulate severe acute respiratory syndrome coronavirus 2 (SARS-CoV-2) infection and its symptoms has been a pressing area of investigation during the coronavirus disease 2019 (COVID-19) pandemic. Nonsteroidal anti-inflammatory drugs (NSAIDs), which are frequently used for the relief of pain and inflammation, could modulate both SARS-CoV-2 infection and the host response to the virus. NSAIDs inhibit the enzymes cyclooxygenase-1 (COX-1) and cyclooxygenase-2 (COX-2), which mediate the production of prostaglandins (PGs). Since PGs play diverse biological roles in homeostasis and inflammatory responses, inhibiting PG production with NSAIDs could affect COVID-19 pathogenesis in multiple ways, including (i) altering susceptibility to infection by modifying expression of angiotensin-converting enzyme 2 (ACE2), the cell entry receptor for SARS-CoV-2; (ii) regulating replication of SARS-CoV-2 in host cells; and (iii) modulating the immune response to SARS-CoV-2. Here, we investigate these potential roles. We demonstrate that SARS-CoV-2 infection upregulates COX-2 in diverse human cell culture and mouse systems. However, suppression of COX-2 by two commonly used NSAIDs, ibuprofen and meloxicam, had no effect on ACE2 expression, viral entry, or viral replication. In contrast, in a mouse model of SARS-CoV-2 infection, NSAID treatment reduced production of proinflammatory cytokines and impaired the humoral immune response to SARS-CoV-2, as demonstrated by reduced neutralizing antibody titers. Our findings indicate that NSAID treatment may influence COVID-19 outcomes by dampening the inflammatory response and production of protective antibodies rather than modifying susceptibility to infection or viral replication.

IMPORTANCE Public health officials have raised concerns about the use of nonsteroidal anti-inflammatory drugs (NSAIDs) for treating symptoms of coronavirus disease 2019 (COVID-19). NSAIDs inhibit the enzymes cyclooxygenase-1 (COX-1) and cyclooxygenase-2 (COX-2), which are critical for the generation of prostaglandins—lipid molecules with diverse roles in homeostasis and inflammation. Inhibition of prostaglandin production by NSAIDs could therefore have multiple effects on COVID-19 pathogenesis. Here, we demonstrate that NSAID treatment reduced both the antibody and proinflammatory cytokine response to SARS-CoV-2 infection. The ability of NSAIDs to modulate the immune response to SARS-CoV-2 infection has important implications for COVID-19 pathogenesis in patients. Whether this occurs in humans and whether it is beneficial or detrimental to the host remains an important area of future investigation. This also raises the possibility that NSAIDs may alter the immune response to SARS-CoV-2 vaccination.

KEYWORDS SARS-CoV-2, COVID-19, NSAIDs, antibody response

During the ongoing coronavirus disease 2019 (COVID-19) pandemic, a common concern has been whether widely used anti-inflammatory medications affect the risk of infection by severe acute respiratory syndrome coronavirus 2 (SARS-CoV-2), the

Citation Chen JS, Alfajaro MM, Chow RD, Wei J, Filler RB, Eisenbarth SC, Wilen CB. 2021.

Nonsteroidal anti-inflammatory drugs dampen the cytokine and antibody response to SARS-CoV-2 infection. *J Virol* 95:e00014-21. <https://doi.org/10.1128/JVI.00014-21>.

Editor Tom Gallagher, Loyola University Chicago

Copyright © 2021, American Society for Microbiology. All Rights Reserved.

Address correspondence to Craig B. Wilen, craig.wilen@yale.edu.

Received 5 January 2021

Accepted 11 January 2021

Accepted manuscript posted online

13 January 2021

Published 10 March 2021

causative agent of COVID-19, or disease severity. Used ubiquitously for the relief of pain and inflammation, nonsteroidal anti-inflammatory drugs (NSAIDs) have been one such target of concern, with the health minister of France and the medical director of the National Health Service of England recommending the use of acetaminophen over NSAIDs for treating COVID-19 symptoms (1, 2).

NSAIDs function by inhibiting the cyclooxygenase (COX) isoforms COX-1 and COX-2. COX-1 is constitutively expressed in most cells, while COX-2 expression is induced by inflammatory stimuli (3). COX-1 and COX-2 metabolize arachidonic acid into prostaglandin H_2 , which can then be converted to several different bioactive prostaglandins (PGs), including PGD_2 , PGE_2 , $PGF_{2\alpha}$, and PGI_2 (3). PGs signal through specific receptors to perform diverse roles, such as regulating immune responses and gastrointestinal barrier integrity (3). Several potential hypotheses have linked NSAID use and COVID-19 pathogenesis. First, it has been suggested that NSAID use may upregulate angiotensin-converting enzyme 2 (ACE2), the cell entry receptor for SARS-CoV-2, and increase the risk of infection (4, 5). Second, NSAIDs may directly affect SARS-CoV-2 replication, since COX signaling has been shown to regulate replication of other viruses, including mouse coronavirus (6). Third, given their anti-inflammatory properties, NSAIDs may impair the immune response to SARS-CoV-2 and delay disease resolution or, alternatively, dampen the cytokine storm associated with severe disease (1). Therefore, given the widespread use of NSAIDs, evaluation of the interaction between NSAIDs and SARS-CoV-2 is warranted.

NSAIDs may modulate multiple stages of the SARS-CoV-2 life cycle. As described above, one potential mechanism is that NSAIDs could lead to ACE2 upregulation and thus increase susceptibility to SARS-CoV-2. Ibuprofen treatment of diabetic rats was found to increase ACE2 expression in the heart (7). In addition, inhibition of the PGE_2 receptor EP4 in human and mouse intestinal organoids increases ACE2 expression (8), suggesting that NSAID inhibition of COX/ PGE_2 signaling could similarly lead to ACE2 upregulation. NSAIDs could also affect a later stage of the SARS-CoV-2 life cycle. For porcine sapovirus, feline calicivirus, murine norovirus, and mouse coronavirus, COX inhibition impairs viral replication (6, 9, 10). COX inhibition was found to impair mouse coronavirus infection at a postbinding step early in the replication cycle, potentially entry or initial genome replication (6). Furthermore, SARS-CoV, the closest relative of SARS-CoV-2 among human coronaviruses and cause of the 2002-2003 epidemic (11), stimulates COX-2 expression via its spike and nucleocapsid proteins (12, 13), indicating the potential relevance of this pathway for SARS-CoV-2.

NSAIDs could also regulate the immune response to SARS-CoV-2 in multiple ways that ameliorate or exacerbate COVID-19. While mounting an immune response is necessary for clearing SARS-CoV-2 infection and establishing immunological memory to combat reinfection, it has also been appreciated that hyperinflammatory responses underlie the pathology of severe COVID-19 (14). Studies using immunomodulatory agents to treat COVID-19 suggest that immunostimulation is helpful early in the disease course, whereas immunosuppression may be more beneficial later (14). For example, dexamethasone treatment decreases mortality in COVID-19 patients on respiratory support but is potentially harmful for those with milder disease, suggesting that late-stage disease is mediated by hyperinflammation and therefore benefits from immunosuppression (15). Disease severity and mortality in COVID-19 patients is associated with elevated levels of proinflammatory cytokines, including interleukin- 1β (IL- 1β), IL-6, interferon gamma (IFN- γ), and tumor necrosis factor alpha (TNF- α), as well as chemokines such as CCL2, CCL4, CXCL9, and CXCL10 (16, 17). Since PGs can regulate and amplify the production of these cytokines (18, 19), NSAIDs could potentially mitigate the hyperinflammatory pathology of COVID-19. However, PGs can also be immunosuppressive in certain contexts, such that NSAIDs may instead promote immune responses. For instance, PGD_2 and PGE_2 have been shown to impair both innate and adaptive immunity to influenza A virus, with PGD_2 having a similar impact on SARS-CoV (20, 21). In addition, PGD_2 signaling prevents excessive inflammasome activation

during murine coronavirus-induced encephalitis (22). Therefore, reducing PGD_2 and PGE_2 levels with NSAID treatment could improve the induction of antiviral immunity and yet also promote hyperinflammatory responses. Conversely, NSAID treatment could have detrimental effects on resolution of infection by inhibiting production of PGI_2 , which is antiviral in respiratory syncytial virus infection (23). Furthermore, NSAIDs may inhibit antibody production to SARS-CoV-2, which has been observed for other viruses, but the effect of this on disease severity is unclear as antibodies can be protective or pathogenic (24, 25). Altogether, given the complex and sometimes conflicting roles of PGs, it is difficult to predict the overall effect of NSAIDs on the immune response to SARS-CoV-2 and, ultimately, disease outcome.

We therefore systematically assessed the effect of NSAIDs on SARS-CoV-2 infection and the immune response to SARS-CoV-2. We found that SARS-CoV-2 infection induced COX-2 expression in human cells and mice. However, suppression of COX-2 by two commonly used NSAIDs, ibuprofen and meloxicam, had no effect on ACE2 expression, viral entry, or viral replication. In a mouse model of SARS-CoV-2 infection, NSAID treatment impaired the production of proinflammatory cytokines and neutralizing antibodies but did not affect weight loss, viral burden, or activation of innate and adaptive immune cells in the lung. These results indicate that NSAID use in humans may affect COVID-19 pathogenesis by mitigating the inflammatory response and the production of protective antibodies rather than by directly influencing viral replication.

RESULTS

SARS-CoV-2 infection induces *PTGS2* expression in human cells and mice. To determine the role of the COX-2 pathway in SARS-CoV-2 infection, we evaluated induction of *PTGS2* (encoding COX-2) in human cells and mice. We found that SARS-CoV-2 infection of human lung cancer cell line Calu-3 led to significant upregulation of *PTGS2* (Fig. 1A). This is consistent with RNA sequencing (RNA-seq) data sets of SARS-CoV-2-infected Calu-3 cells and ACE2-overexpressing A549 cells, another lung cancer cell line (Fig. 1B and C) (26). However, infection of human liver cancer cell line Huh7.5 did not lead to significant *PTGS2* induction, demonstrating cell type specificity of *PTGS2* induction by SARS-CoV-2 (Fig. 1D).

We next assessed whether SARS-CoV-2 induces *PTGS2* in a more physiologically relevant cell culture system. We cultured primary human bronchial epithelial cells (HBECs) for 28 days at an air-liquid interface, which supports pseudostratified mucociliated differentiation providing an *in vitro* model of airway epithelium (27). We infected HBECs with SARS-CoV-2 at the apical surface of the culture and then performed single-cell RNA sequencing at 1, 2, and 3 days postinfection (dpi) (28). As we previously reported that ciliated cells in air-liquid interface cultures are the major target of infection (28), we looked for *PTGS2* induction in this cell type. Aggregating ciliated cells across the three time points, we found that infected ciliated cells expressed higher levels of *PTGS2* compared to uninfected bystander ciliated cells (Fig. 1E), indicating that *PTGS2* is also induced by SARS-CoV-2 in a cell-intrinsic manner in ciliated cells, a physiologically relevant target cell.

To determine the relevance of these findings *in vivo*, we utilized transgenic mice expressing human ACE2 driven by the epithelial cell keratin 18 promoter (K18-hACE2) (29). As SARS-CoV-2 does not efficiently interact with mouse ACE2 (4), human ACE2-expressing mice are required to support SARS-CoV-2 infection (30–35). K18-hACE2 mice were initially developed as a model of SARS-CoV infection and have recently been demonstrated as a model of severe SARS-CoV-2 infection in the lung (29, 36). We found that intranasal infection of K18-hACE2 mice with SARS-CoV-2 led to significant upregulation of *Ptgs2* in the lung at multiple time points postinfection (Fig. 1F), consistent with recent SARS-CoV-2-infected K18-hACE2 lung RNA-seq data (Fig. 1G) (36). Taken together, these results demonstrate that SARS-CoV-2 infection induces *PTGS2* in diverse *in vitro* and *in vivo* airway and lung systems, across multiple independent

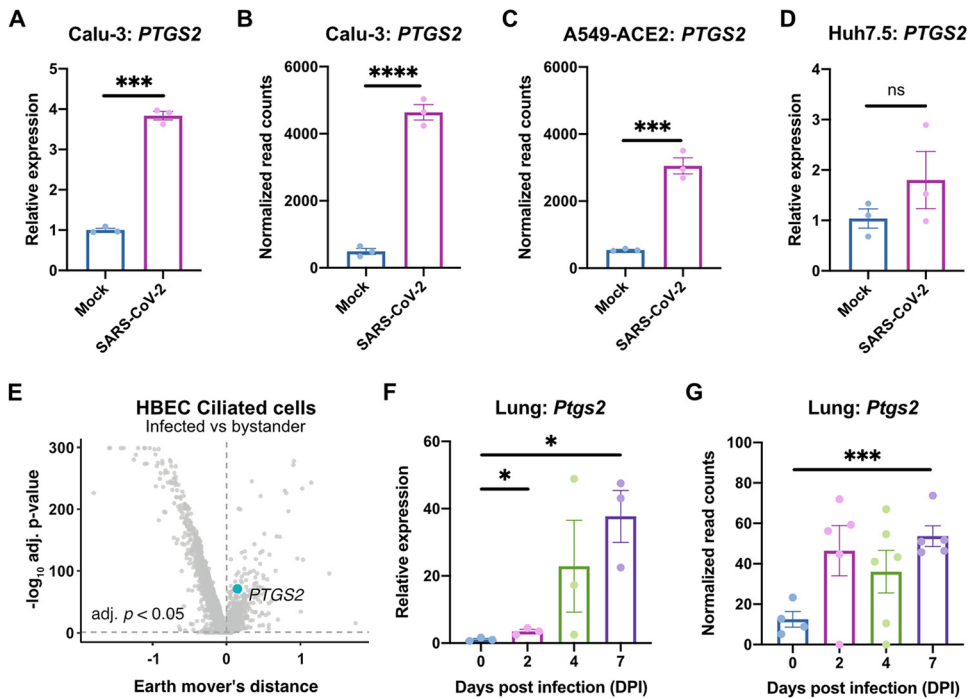


FIG 1 SARS-CoV-2 infection induces *PTGS2* expression in human cells and mice. (A) Calu-3 cells were infected with SARS-CoV-2 at an MOI of 0.05. *PTGS2* expression was measured at 2 dpi, normalized to *ACTB*. (B and C) *PTGS2* expression in Calu-3 (B) and ACE2-overexpressing A549 (A549-ACE2) (C) cells following SARS-CoV-2 infection. The data are from [GSE147507](#) (26). (D) Huh7.5 cells were infected with SARS-CoV-2 at an MOI of 0.05. *PTGS2* expression was measured at 2 dpi, normalized to *ACTB*. (E) HBECs were cultured at an air-liquid interface and then infected at the apical surface with 10^4 PFU of SARS-CoV-2. Cells were collected at 1, 2, and 3 dpi for single-cell RNA sequencing (scRNA-seq) (28). A volcano plot of differentially expressed genes in infected versus bystander ciliated cells pooled from all time points is shown. *PTGS2* is highlighted. (F) K18-hACE2 mice were infected intranasally with 1.2×10^6 PFU of SARS-CoV-2. *Ptgs2* expression in the lung was measured at 0, 2, 4, and 7 dpi. (G) *Ptgs2* expression in the lung of K18-hACE2 mice following intranasal SARS-CoV-2 infection. The data are from [GSE154104](#) (36). All data points in this figure are presented as means \pm the standard errors of the mean (SEM). Data were analyzed by Welch's two-tailed, unpaired *t* test (A, D, and F); Student two-tailed, unpaired *t* test (B, C, and G); and two-sided Mann-Whitney U test with continuity and Benjamini-Hochberg correction (E). *, $P < 0.05$; ***, $P < 0.001$; ****, $P < 0.0001$. Data in panels A and D are representative of two independent experiments with three replicates per condition.

studies. These findings therefore suggest that COX-2 signaling may be a relevant pathway for regulating SARS-CoV-2 infection or the immune response to the virus.

NSAID treatment does not affect ACE2 expression in human cells and mice. We next explored whether inhibition of COX-2 could affect viral infection by regulating *ACE2* expression, as has been reported in studies of diabetic rats and intestinal organoids (7, 8). We utilized two NSAIDs, the nonselective COX-1/COX-2 inhibitor ibuprofen and the selective COX-2 inhibitor meloxicam, which are commonly used clinically. We determined the maximum nontoxic doses of ibuprofen and meloxicam on Calu-3 and Huh7.5 cells (Fig. 2A and B) and demonstrated that both drugs are bioactive in Calu-3 cells, as measured by reduced PGE₂ levels (Fig. 2C). Treatment of Calu-3 or Huh7.5 cells with ibuprofen or meloxicam did not significantly affect *ACE2* expression (Fig. 2D and E). To test whether NSAID treatment affects *Ace2* expression in diverse tissues *in vivo*, we treated C57BL/6 mice with therapeutic doses of ibuprofen and meloxicam (37–40), which did not lead to changes in *Ace2* expression in the lung, heart, kidney, or ileum (Fig. 2F to I). These data indicate that inhibition of the COX-2 pathway by NSAIDs does not affect *ACE2* expression in multiple cell and tissue types *in vitro* or *in vivo*.

NSAID treatment does not affect SARS-CoV-2 entry or replication *in vitro*. To assess whether NSAID treatment functionally affects SARS-CoV-2 entry, we used a vesicular stomatitis virus (VSV) core expressing *Renilla* luciferase pseudotyped with the SARS-CoV-2 spike protein (SARS2-VSVpp). We used VSV glycoprotein (G) pseudovirus (G-VSVpp) as a control (41, 42). Quantification of luciferase activity showed that

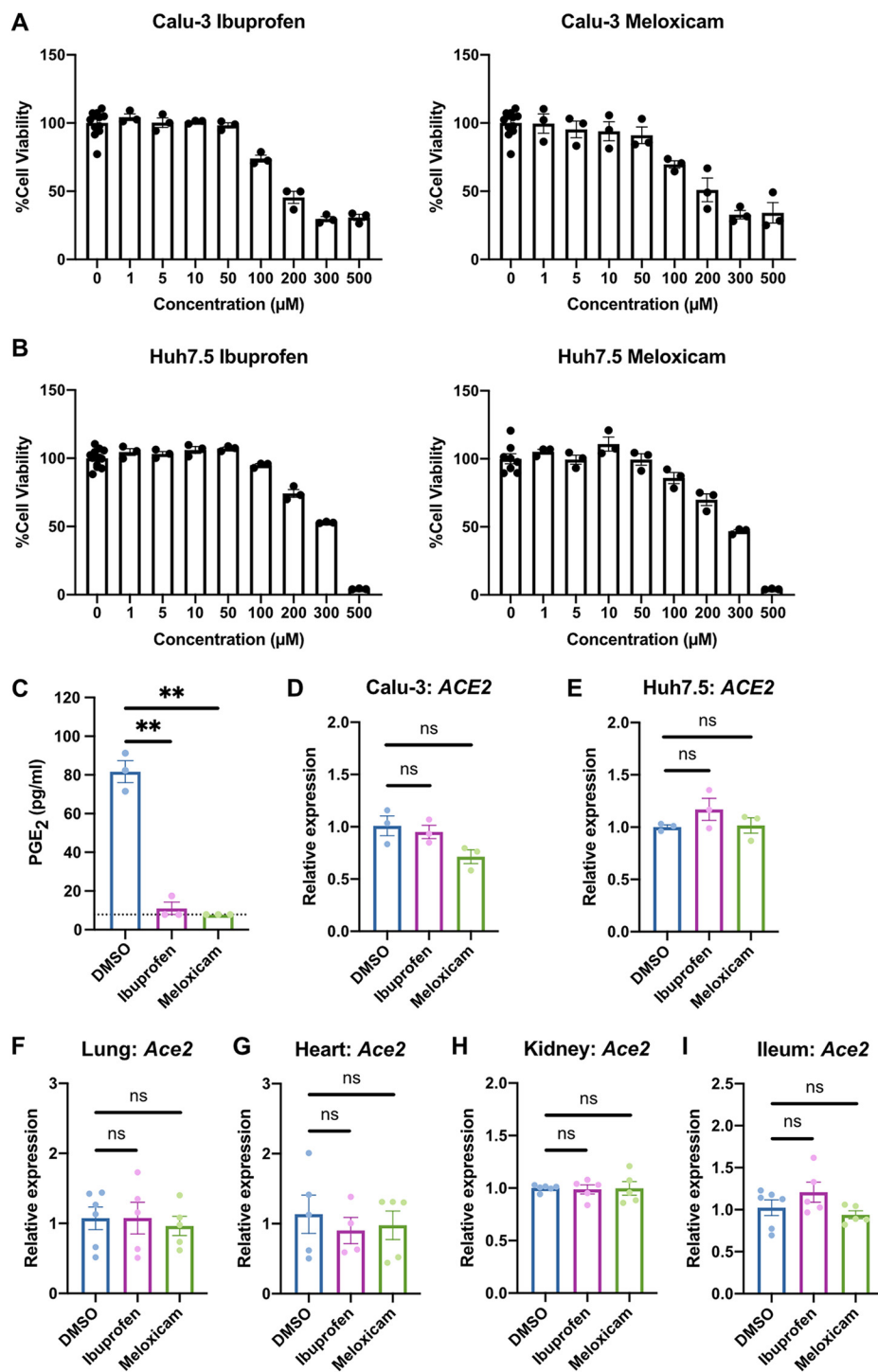


FIG 2 NSAID treatment does not affect *ACE2* expression in human cells and mice. (A and B) Calu-3 (A) and Huh7.5 (B) cells were treated with different concentrations of ibuprofen or meloxicam for 48 h. Cell viability was measured and calculated as a percentage of no treatment. (C) Calu-3 cells were treated with DMSO, 50 μM ibuprofen, or 50 μM meloxicam for 48 h. The levels of prostaglandin E₂ (PGE₂) were measured in the supernatant. The dotted line represents the limit of detection. (D and E) Calu-3 (D) and Huh7.5 (E) cells were treated with DMSO, 50 μM ibuprofen, or 50 μM meloxicam for 24 h. *ACE2* expression was measured and normalized to *ACTB*. (F to I) C57BL/6 mice were treated intraperitoneally with DMSO, 30 mg/kg ibuprofen, or 1 mg/kg meloxicam daily for 4 days. *Ace2* expression was measured in the lung (F), heart (G), kidney (H), and ileum (I), normalized to *Actb*. All data points in this figure are presented as means ± the SEM. Data were analyzed by Welch's two-tailed, unpaired *t* test (C to I). **, *P* < 0.01; ns, not significant. Data in panels A to E are representative of two independent experiments with three replicates per condition; data in panels F to I are pooled from two independent experiments with a total of four to six mice per condition.

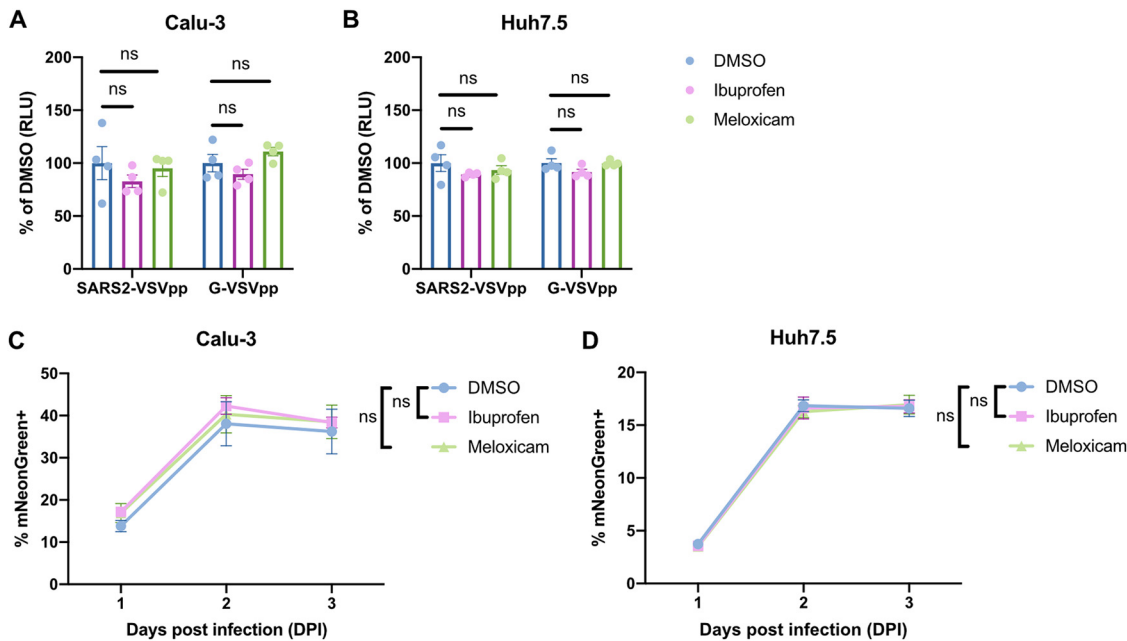


FIG 3 NSAID treatment does not affect SARS-CoV-2 entry or replication *in vitro*. (A and B) Calu-3 (A) and Huh7.5 (B) cells were pretreated with DMSO, 50 μ M ibuprofen, or 50 μ M meloxicam for 24 h and then infected with SARS2-VSVpp or G-VSVpp expressing *Renilla* luciferase. Luminescence was measured at 24 h postinfection (hpi) and normalized to DMSO for each infection. (C and D) Calu-3 (C) and Huh7.5 (D) cells were pretreated with DMSO, 50 μ M ibuprofen, or 50 μ M meloxicam for 24 h and then infected with mNeonGreen reporter replication-competent SARS-CoV-2 (icSARS-CoV-2-mNG) at an MOI of 1. The frequency of infected cells was measured by mNeonGreen expression at 1, 2, and 3 dpi. All data points in this figure are presented as means \pm the SEM. Data were analyzed by Student two-tailed, unpaired *t* test (A and B) and two-way ANOVA (C and D). ns, not significant. Data in panels A and B are representative of two independent experiments with four replicates per condition; data in panels C and D are representative of two independent experiments with five replicates per condition.

pretreatment of Calu-3 or Huh7.5 cells with ibuprofen or meloxicam did not significantly affect SARS2-VSVpp or G-VSVpp entry (Fig. 3A and B), confirming that NSAID inhibition of COX-2 does not impact susceptibility to infection.

Next, we studied whether COX-2 inhibition affects SARS-CoV-2 replication. Viruses from several different families have been shown to induce COX-2 signaling in host cells, which can have either proviral or antiviral functions (9, 43, 44). To this end, we utilized a replication-competent SARS-CoV-2 expressing a mNeonGreen reporter (icSARS-CoV-2-mNG) to study the effect of COX-2 inhibition by NSAIDs on viral replication (45). We assessed icSARS-CoV-2-mNG replication in Calu-3 cells, which upregulate *PTGS2* in response to SARS-CoV-2 infection (Fig. 1A and B), and Huh7.5 cells, which do not (Fig. 1D). By quantifying the percentage of mNeonGreen-expressing cells, we found that treatment of Calu-3 or Huh7.5 cells with ibuprofen or meloxicam did not impact icSARS-CoV-2-mNG replication (Fig. 3C and D). These results indicate that SARS-CoV-2 induction of the COX-2 pathway in Calu-3 human lung cells does not regulate viral replication.

NSAID treatment does not affect SARS-CoV-2-induced weight loss or lung viral burden in mice. Since NSAIDs do not directly affect SARS-CoV-2 entry or replication *in vitro*, we next investigated whether they regulate SARS-CoV-2 replication and immunity *in vivo*. We treated K18-hACE2 mice with meloxicam 1 day prior to SARS-CoV-2 infection and continued daily meloxicam treatment throughout the course of the infection. Dimethyl sulfoxide (DMSO) control- and meloxicam-treated K18-hACE2 mice experienced similar weight loss beginning at 5 dpi (Fig. 4A). In addition, viral lung burden at 6 dpi was similar between infected DMSO- and meloxicam-treated mice (Fig. 4B), suggesting that meloxicam does not affect viral replication *in vitro* or *in vivo*.

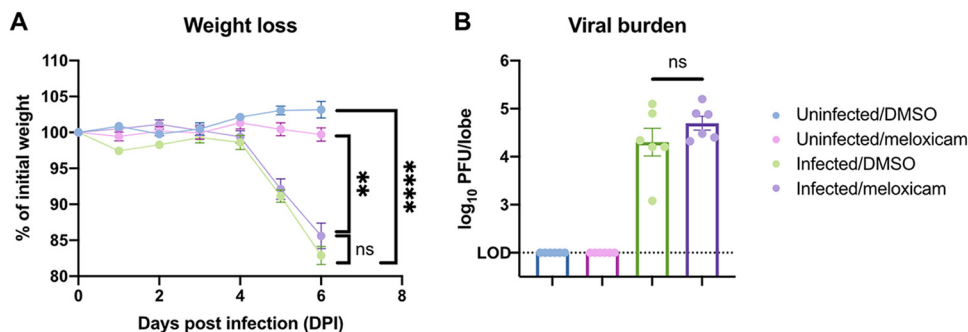


FIG 4 NSAID treatment does not affect SARS-CoV-2-induced weight loss or lung viral burden in mice. (A and B) K18-hACE2 mice were treated intraperitoneally with DMSO or 1 mg/kg meloxicam daily for 7 days starting 1 day prior to infection. K18-hACE2 mice were infected intranasally with 10^3 PFU of SARS-CoV-2 or left uninfected and monitored daily. (A) Weight change expressed as a percentage of initial weight. (B) Viral burden in the lungs at 6 dpi measured by plaque assay. All data points in this figure are presented as means \pm the SEM. Data were analyzed by two-way ANOVA (A) and Student two-tailed, unpaired *t* test (B). **, $P < 0.01$; ****, $P < 0.0001$; ns, not significant. Data in panels A and B are pooled from two independent experiments with a total of six mice per condition.

NSAID treatment does not affect innate or adaptive immune cell activation in the lungs of SARS-CoV-2-infected mice.

As NSAIDs regulate inflammation, we next assessed whether NSAIDs perturb the host immune response to SARS-CoV-2 in mice. First, we characterized the abundance and activation status of innate and adaptive immune cell types in the lung at 6 dpi (gating strategy is shown in Fig. S1A and B in the supplemental material). SARS-CoV-2 infection led to a slight decrease in alveolar macrophage abundance and upregulation of activation marker CD86. However, this was not modified by meloxicam treatment (Fig. 5A and B). Neutrophil counts were not significantly altered by infection or meloxicam treatment at this time point (Fig. 5C). Activated CD69⁺ NK cells increased with infection in both DMSO and meloxicam-treated mice (Fig. 5D). Ly6C⁺ monocyte/macrophage numbers and expression of activation markers CD86, MHCII, and CD64 all increased following SARS-CoV-2 infection but were not affected by meloxicam treatment (Fig. 5E to H). Furthermore, activated (CD44⁺ CD69⁺) T cell populations, including CD4⁺ T cells, CD8⁺ T cells, and $\gamma\delta$ T cells, increased with infection but were not significantly affected by concomitant meloxicam treatment (Fig. 6A to C). In contrast, B cells were decreased in the lungs of infected mice, independent of meloxicam treatment (Fig. 6D). Together, these results indicate that meloxicam treatment does not affect the overall numbers and activation status of innate or adaptive immune cells in the lung during SARS-CoV-2 infection.

NSAID treatment impairs systemic neutralizing antibody responses to SARS-CoV-2. While meloxicam did not alter the abundance of immune cell populations in the lung, NSAID treatment might regulate the function of these cell types. To assess the effect of meloxicam treatment on antibody production in infected mice, we measured the serum levels of spike-specific IgM and IgG antibodies at 6 dpi. DMSO-treated mice demonstrated detectable levels of both spike-specific IgM and IgG antibodies, which were significantly reduced in meloxicam-treated mice (Fig. 6E and F). Corroborating the difference in antibody titers, serum from DMSO-treated mice exhibited greater neutralization capacity compared to serum from meloxicam-treated mice (Fig. 6G).

NSAID treatment dampens the induction of proinflammatory cytokines that are upregulated by SARS-CoV-2 infection in mice. Finally, we studied whether NSAID treatment modulates the cytokine response to SARS-CoV-2 infection. SARS-CoV-2 infection led to increased production of proinflammatory cytokines (IL-1 β , IL-6, IFN- γ , TNF- α , and granulocyte-macrophage colony-stimulating factor [GM-CSF]); T cell growth factors (IL-2); and chemokines (CCL2, CCL4, CXCL9, and CXCL10) that have been associated with disease severity and mortality in COVID-19 patients (Fig. 7A) (16, 17). Among uninfected mice, meloxicam treatment led to minimal changes in cytokine

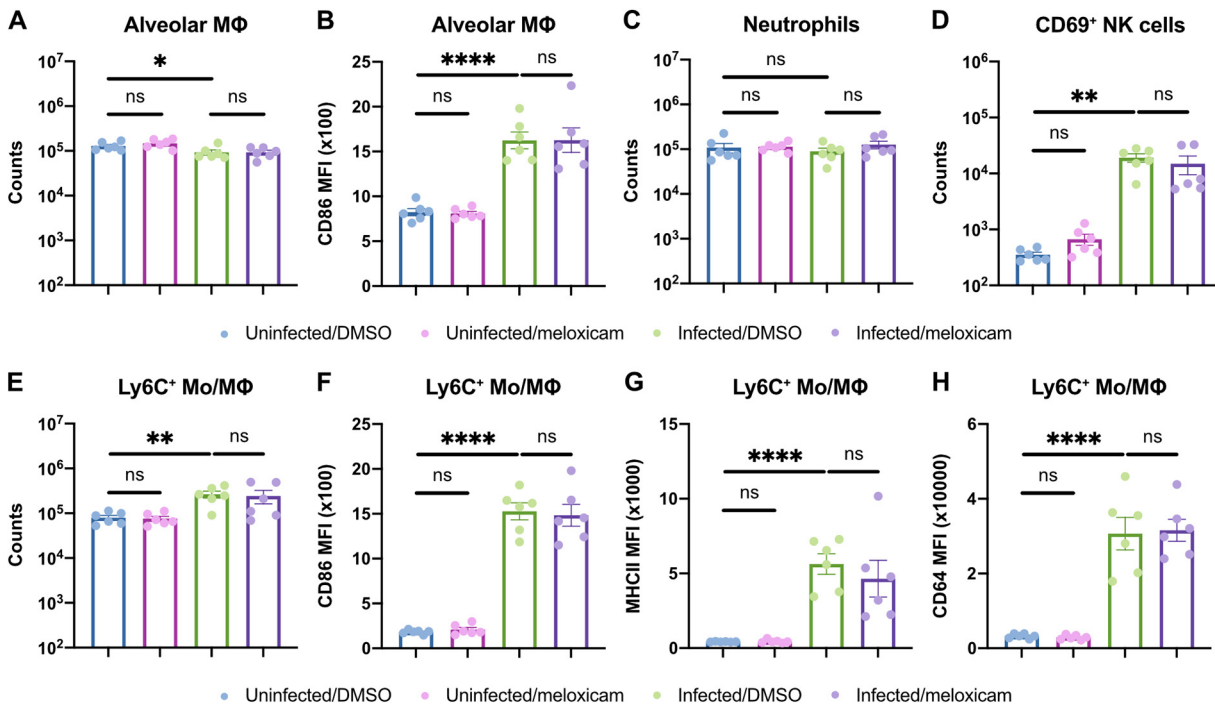


FIG 5 NSAID treatment does not affect innate immune cell activation in the lungs of SARS-CoV-2-infected mice. (A to H) K18-hACE2 mice were treated intraperitoneally with DMSO or 1 mg/kg meloxicam daily for 7 days starting 1 day prior to infection. K18-hACE2 mice were infected intranasally with 10^3 PFU of SARS-CoV-2 or left uninfected. Flow cytometric analysis of the lungs at 6 dpi for alveolar macrophage (MΦ) counts (A) and expression of CD86 (B), neutrophil counts (C), activated CD69⁺ natural killer (NK) cell counts (D), and Ly6C⁺ monocyte/macrophage (Mo/MΦ) counts (E) and expression of CD86 (F), MHCII (G), and CD64 (H) results are shown. All data points in this figure are presented as means \pm the SEM. Data were analyzed by two-tailed Mann-Whitney test (A to H). *, $P < 0.05$; **, $P < 0.01$; ***, $P < 0.0001$; ns, not significant. Data in panels A to H are pooled from two independent experiments with a total of six mice per condition.

production (Fig. 7B; see also Fig. S2 in the supplemental material). Among infected mice, meloxicam treatment decreased the production of a subset of cytokines upregulated by infection, including IL-6, CCL2, GM-CSF, CXCL10, IL-2, and TNF- α , while others were unaffected (Fig. 7C and D; see also Fig. S2). Together, these results demonstrate that NSAID treatment partially dampens the cytokine response to SARS-CoV-2 infection.

DISCUSSION

Given the concerns about NSAID use in patients with COVID-19, we studied whether NSAIDs affect SARS-CoV-2 infection and the immune response to the virus. We found that SARS-CoV-2 infection induced *PTGS2* upregulation in diverse systems, including Calu-3 and A549 lung cancer cell lines, primary HBEC air-liquid interface cultures, and the lungs of K18-hACE2 mice. Inhibition of COX-2 with the commonly used NSAIDs ibuprofen and meloxicam did not affect *ACE2* expression in multiple cell and tissue types *in vitro* or *in vivo*, nor did it affect SARS-CoV-2 entry or replication. In K18-hACE2 mice infected with SARS-CoV-2, NSAID treatment impaired the production of neutralizing antibodies and proinflammatory cytokines but did not influence weight loss, viral burden, or activation state of innate and adaptive immune cells in the lung. Our findings therefore rule out a direct effect of NSAIDs on SARS-CoV-2 infection but indicate that NSAIDs could modulate COVID-19 severity by dampening production of neutralizing antibodies and inflammatory cytokines.

An important question arising from our findings is how SARS-CoV-2 infection induces COX-2 expression. One possibility is that the pattern recognition receptor retinoic acid inducible gene-I (RIG-I), which can recognize double-stranded RNA generated during viral genome replication and transcription (46), may drive this response. Indeed,

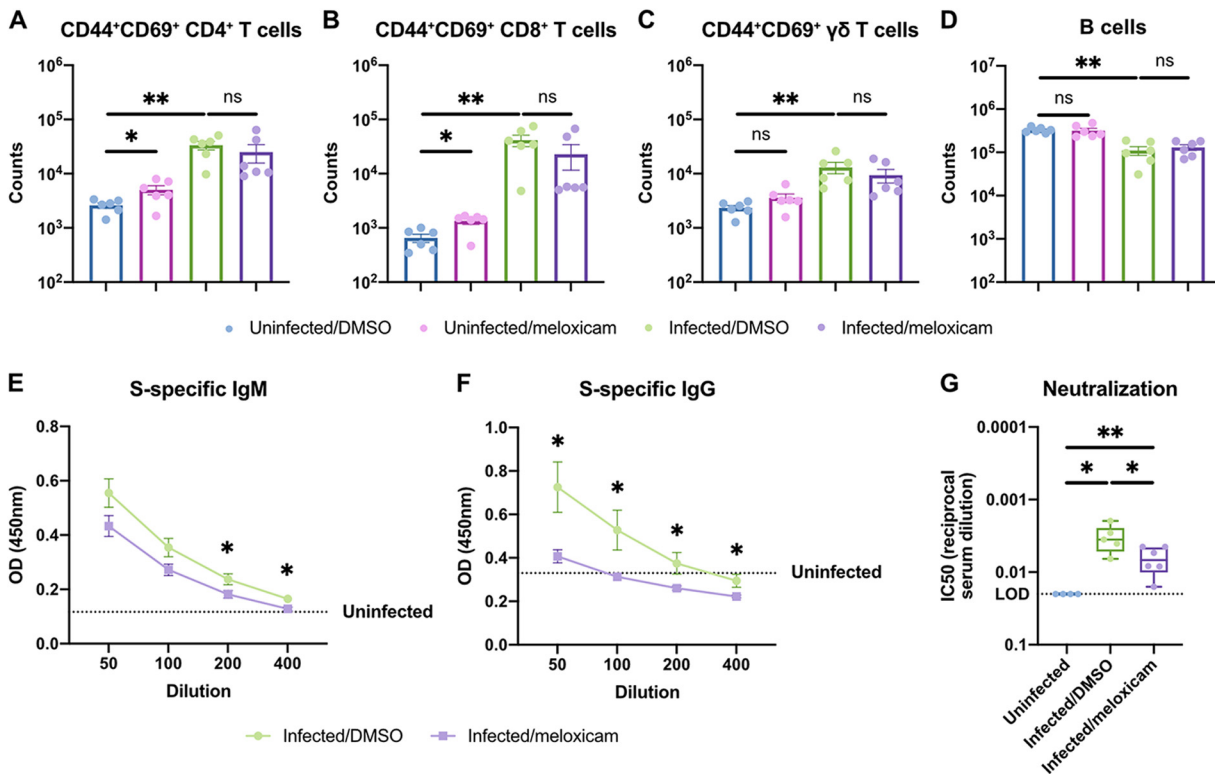


FIG 6 NSAID treatment impairs systemic neutralizing antibody responses but not adaptive immune cell activation in the lungs of SARS-CoV-2-infected mice. (A to G) K18-hACE2 mice were treated intraperitoneally with DMSO or 1 mg/kg meloxicam daily for 7 days starting 1 day prior to infection. K18-hACE2 mice were infected intranasally with 10³ PFU of SARS-CoV-2 or left uninfected. Flow cytometric analysis of the lungs at 6 dpi for activated CD44⁺CD69⁺ CD4⁺ T cells (A), CD44⁺ CD69⁺ CD8⁺ T cells (B), CD44⁺ CD69⁺ $\gamma\delta$ T cells (C), and B cells (D) was performed. (E and F) Spike (S)-specific IgM (E) and IgG (F) titers in the serum at 6 dpi. (G) Neutralizing antibody titers in the serum at 6 dpi measured by SARS2-VSVpp pseudovirus neutralization assay. Data points in panels A to F are presented as means \pm the SEM. Data points in panel G are presented as boxplots. Data were analyzed by two-tailed Mann-Whitney test (A to D, G) and Student two-tailed, unpaired t test (E and F). *, $P < 0.05$; **, $P < 0.01$; ns, not significant. Data in panels A to G are pooled from two independent experiments with a total of four to six mice per condition.

COX-2 induction by influenza A virus is RIG-I-dependent (47), and we showed here that Huh7.5 cells, which are defective in RIG-I signaling (48), do not upregulate *PTGS2* in response to SARS-CoV-2. Alternatively, SARS-CoV-2 proteins may mediate the induction of COX-2 through their complex effects on host cells. In the case of SARS-CoV, transfection of plasmids encoding either the spike or the nucleocapsid genes is sufficient to stimulate COX-2 expression (12, 13). SARS-CoV spike protein induces COX-2 expression through both calcium-dependent PKC α /ERK/NF- κ B and calcium-independent PI3K/PKC ϵ /JNK/CREB pathways (13), while the nucleocapsid protein directly binds to the COX-2 promoter to regulate its expression (12). Any of these potential mechanisms are consistent with our HBEC scRNA-seq results demonstrating that SARS-CoV-2 increases *PTGS2* expression in a cell-intrinsic manner.

One of the effects of NSAID treatment on the immune response to SARS-CoV-2 was impairment of early, neutralizing spike-specific antibodies. These early humoral responses are mediated by short-lived plasmablasts, and their requirement for T cell help is unclear (49). NSAID treatment could therefore act by inhibiting activation (T cell-dependent or T cell-independent), proliferation, differentiation, or antibody-secreting capacity of spike-specific B cells and plasmablasts. B cells have been found to upregulate COX-2 expression following activation with T cell-dependent and T cell-independent stimuli (50, 51), and treatment of purified B cell cultures with NSAIDs reduces IgM and IgG production (52). COX-2 inhibition reduces expression of BLIMP-1 and XBP-1 (53), which are essential transcription factors for plasmablast differentiation,

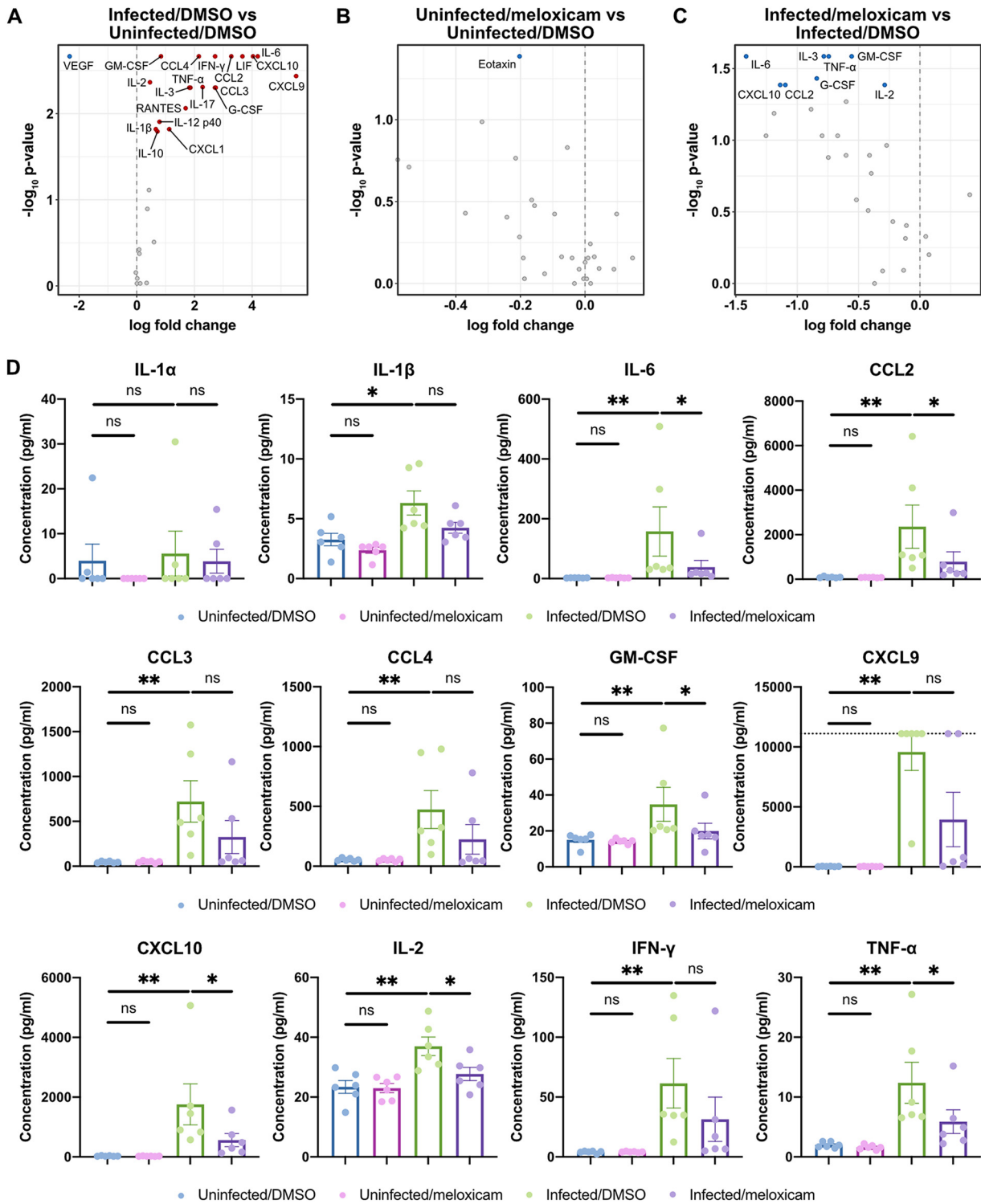


FIG 7 NSAID treatment dampens the induction of proinflammatory cytokines that are upregulated by SARS-CoV-2 infection in mice. (A to D) K18-hACE2 mice were treated intraperitoneally with DMSO or 1 mg/kg meloxicam daily for 7 days starting 1 day prior to infection. K18-hACE2 mice were infected intranasally with 10^3 PFU of SARS-CoV-2 or left uninfected. Cytokine levels were measured in lung homogenates at 6 dpi. (A to C) Volcano plots detailing the differential abundance of cytokines in lung homogenates from infected versus uninfected mice treated with DMSO (A), uninfected mice treated with meloxicam versus DMSO (B), and infected mice treated with meloxicam versus DMSO (C). Significantly upregulated (red) and downregulated (blue) cytokines are labeled. (D) Levels of proinflammatory cytokines in lung homogenates from uninfected mice treated with DMSO, uninfected mice treated with meloxicam, infected mice treated with DMSO, and infected mice treated with meloxicam. The dotted line represents the upper limit of quantification. Data points in panel D are presented as means \pm the SEM. Data were analyzed by two-tailed Mann-Whitney test (A to D). *, $P < 0.05$; **, $P < 0.01$; ns, not significant. Data in panels A to D are pooled from two independent experiments with a total of six mice per condition. Additional cytokine data are shown in Fig. S2 in the supplemental material.

providing a potential mechanism by which NSAIDs impair antibody production. In addition, in mice infected with vaccinia virus, antiviral antibody production is impaired by chronic but not acute COX-2 inhibition (24), indicating that the duration of NSAID treatment may regulate the impact on antibody production. Given that K18-hACE2 mice succumb to lethal SARS-CoV-2 disease within 7 days (36, 54), we could not assess the effect of NSAID treatment on long-term antibody production. This could be explored in nonlethal models of SARS-CoV-2 infection, as well as in the setting of vaccination.

Understanding the effect of NSAID treatment on cytokine production is also critical, as cytokines may be protective early in COVID-19 but potentially pathological at later stages, thus informing the timing of immunomodulatory drugs like NSAIDs. We observed that NSAID treatment decreased the production of a subset of cytokines that were induced by infection, including IL-6, CCL2, GM-CSF, CXCL10, IL-2, and TNF- α . This is consistent with prior reports of COX-2 inhibitors decreasing the production of these cytokines in various inflammatory settings (55–59). Mechanistically, NSAIDs may reduce production of these cytokines through inhibition of the PGE₂/NF- κ B positive-feedback loop, in which NF- κ B and COX-2 can reciprocally activate their respective signaling pathways and amplify inflammatory responses (18, 19, 60).

However, it is less clear whether this dampened cytokine response is beneficial, detrimental, or neutral in the setting of COVID-19 given the many roles that cytokines can play in controlling infection or driving immunopathology. GM-CSF is a myelopoietic growth factor, as well as proinflammatory cytokine, with pathogenic GM-CSF-producing Th1 cells being reported in patients with severe COVID-19 (61). Reduction of GM-CSF production by meloxicam could therefore indicate a beneficial effect of NSAIDs on restraining hyperinflammatory responses. IL-2, IFN- γ , TNF- α can be coproduced by polyfunctional T cells, which play important roles in the control of viral infections, and yet these cytokines can also promote lethal cytokine shock and tissue damage (62–64). In addition, while IL-6 is correlated with disease severity in COVID-19, clinical trials blocking IL-6 signaling have not shown clear evidence of benefit for patients (65). While we observed decreased cytokine responses with NSAID treatment in K18-hACE2 mice, these changes did not translate into differences in weight loss or viral burden, suggesting that these features of the disease may involve other cytokines or pathology at other sites (e.g., the brain) not affected by NSAID treatment (36, 54). The timing, duration, and dosing of NSAID treatment may also matter for COVID-19 pathogenesis, potentially with early treatment impacting the initiation of antiviral immune responses and later treatment suppressing immune-driven pathology (14). In the present study, we treated K18-hACE2 mice continuously throughout the course of infection, but it would be interesting to explore in future work whether limiting NSAID treatment to particular phases of disease has differential effects on pathogenesis.

Here, we demonstrated that SARS-CoV-2 infection induces COX-2 expression in cell lines, primary airway epithelial cells, and mice. Inhibition of COX-2 by NSAIDs did not affect viral entry or replication *in vitro* or *in vivo*. However, NSAID treatment impaired the production of proinflammatory cytokines and neutralizing antibodies in response to SARS-CoV-2 infection in mice. NSAIDs could therefore have complex effects on the host response to SARS-CoV-2. While studies thus far have not observed worse clinical outcomes in COVID-19 patients taking NSAIDs (66–71), evaluation of the breadth, potency, and durability of the humoral immune response is warranted in patients on NSAIDs in response to both natural infection and vaccination.

MATERIALS AND METHODS

Cell lines. Calu-3 and Huh7.5 were from ATCC. Calu-3 cells were cultured in Eagle minimum essential medium with 10% heat-inactivated fetal bovine serum (FBS), 1% GlutaMAX (Gibco), and 1% penicillin/streptomycin. Huh7.5 cells were cultured in Dulbecco modified Eagle medium (DMEM) with 10% heat-inactivated FBS and 1% penicillin/streptomycin. All cell lines tested negative for *Mycoplasma* spp.

Generation of SARS-CoV-2 stocks. As previously described (42), SARS-CoV-2 P1 stock was generated by inoculating Huh7.5 cells with SARS-CoV-2 isolate USA-WA1/2020 (BEI Resources, NR-52281) at a multiplicity of infection (MOI) of 0.01 for 3 days. The P1 stock was then used to inoculate Vero-E6 cells,

and after 3 days, the supernatant was harvested and clarified by centrifugation ($450 \times g$ for 5 min), filtered through a $0.45\text{-}\mu\text{m}$ filter, and stored in aliquots at -80°C . Virus titer was determined by plaque assay using Vero-E6 cells (42).

To generate icSARS-CoV-2-mNG stocks (45), lyophilized icSARS-CoV-2-mNG was reconstituted in 0.5 ml of deionized water. Then, $50\ \mu\text{l}$ of virus was diluted in 5 ml of medium and added to 10^7 Vero-E6 cells. After 3 days, the supernatant was harvested and clarified by centrifugation ($450 \times g$ for 5 min), filtered through a $0.45\text{-}\mu\text{m}$ filter, and stored in aliquots at -80°C .

All work with SARS-CoV-2 or icSARS-CoV-2-mNG was performed in a biosafety level 3 facility with approval from the office of Environmental Health and Safety and the Institutional Animal Care and Use Committee at Yale University.

Preparation of NSAIDs. Ibuprofen (I4883) and meloxicam (M3935) were purchased from Sigma-Aldrich. For cell culture experiments, ibuprofen and meloxicam were solubilized in DMSO at a stock concentration of 10 mM and then diluted in medium to make working solutions. For mouse experiments, stock solutions of ibuprofen (300 mg/ml) and meloxicam (10 mg/ml) were prepared in DMSO and then diluted 100-fold in phosphate-buffered saline (PBS) to make working solutions. To determine the maximum nontoxic dose of NSAIDs to use for cell culture experiments, cells were treated with different concentrations of ibuprofen or meloxicam for 48 h, and cell viability was measured by a CellTiter-Glo luminescent cell viability assay (Promega) according to the manufacturer's instructions.

Mice. C57BL/6J and K18-hACE2 [B6.Cg-Tg(K18-ACE2)2Prln/J (29)] were purchased from Jackson Laboratory. Mice were bred in-house using mating trios to enable utilization of littermates for experiments. Mice of both sexes between 6 and 8 weeks old were used for this study. C57BL/6J and K18-hACE2 mice were anesthetized using 30% (vol/vol) isoflurane diluted in propylene glycol (30% isoflurane) and administered 30 mg/kg ibuprofen, 1 mg/kg meloxicam, or an equivalent amount of DMSO intraperitoneally in a volume of 10 ml/kg daily for 4 or 7 days as indicated in the figure legends. K18-hACE2 mice were anesthetized using 30% isoflurane and administered 1.2×10^6 PFU or 10^3 PFU of SARS-CoV-2 intranasally as indicated in the figure legends. Mice were monitored daily for weight and survival. Animal use and care was approved in agreement with the Yale Animal Resource Center and Institutional Animal Care and Use Committee (no. 2018-20198) according to the standards set by the Animal Welfare Act.

Analysis of RNA-seq data. We utilized RNA-seq data from recent published studies to assess the impact of SARS-CoV-2 infection on *PTGS2* expression. From GSE147507 (26), we reanalyzed the raw count data from Calu-3 and A549-ACE2 cells, comparing SARS-CoV-2 infection to matched mock-treated controls. We performed differential expression analysis using the Wald test from DESeq2 (72), using a Benjamini-Hochberg adjusted $P < 0.05$ as the cutoff for statistical significance. For visualization of *PTGS2* expression, the DESeq2-normalized counts were exported and plotted in GraphPad Prism. Statistical significance was assessed using a Student two-tailed, unpaired t test.

For analysis of HBEC air-liquid interface cultures infected with SARS-CoV-2, we utilized a previously generated catalog of differentially expressed genes that our group recently described in a preprint study (28). The differential expression table is publicly available (https://github.com/vandijklab/HBEC_SARS-CoV-2_scrNA-seq). Here, we specifically investigated *PTGS2* expression in ciliated cells, comparing infected cells to bystander cells (cells aggregated across the 1, 2, and 3 dpi time points). The cutoff for statistical significance was set at adjusted $P < 0.05$, and the results were visualized as a volcano plot in R.

From GSE154104 (36), we reanalyzed the raw count data from the lungs of K18-hACE2 mice infected with SARS-CoV-2, performing pairwise comparisons of mice at 2 dpi, 4 dpi, and 7 to 0 dpi controls (prior to infection). For visualization of *Ptgs2* expression, the DESeq2-normalized counts were exported and plotted in GraphPad Prism. Statistical significance was assessed using a Student two-tailed, unpaired t test.

PGE₂ ELISA. Levels of PGE₂ in cell culture supernatants were measured using the Prostaglandin E₂ enzyme-linked immunosorbent assay (ELISA) kit (Cayman Chemical) according to the manufacturer's instructions. Absorbance was measured at 410 nm on a microplate reader (Molecular Devices), and PGE₂ concentrations were calculated using a standard curve.

Quantitative PCR. Cells or tissues were lysed in TRIzol (Life Technologies), and total RNA was extracted using the Direct-zol RNA Miniprep Plus kit (Zymo Research) according to the manufacturer's instructions. cDNA synthesis was performed using random hexamers and ImProm-II reverse transcriptase (Promega). qPCR was performed with Power SYBR Green (Thermo Fisher) and run on the QuantStudio3 (Applied Biosystems). Target mRNA levels were normalized to those of *ACTB* or *Actb*. The qPCR primer sequences were as follows: *ACTB* (human), GAGCACAGAGCCTCGCCTTT (forward) and ATCATCATCCATGGTGAGCTGG (reverse); *PTGS2* (human), AGAAAAGTCTCAACACCGGAA (forward) and GCACTGTGTTGGAGTGGGT (reverse); *ACE2* (human), GGGATCAGATCCGGAAGAAGAAA (forward) and AAGGAGGTCTGAACA TCATCAGTG (reverse); *Actb* (mouse), ACTGTCTGAGTCGCGTCCA (forward) and ATCCATGGCGAACTG GTGG (reverse); *Ptgs2* (mouse), CTCCCATGGGTGTGAAGGGAAA (forward) and TGGGGTTCAGGGATG AACTC (reverse); and *Ace2* (mouse), ACCTTCGAGAGATCAAGCC (forward) and CCAGTGGGGCTGATG AGGA (reverse).

Pseudovirus production. VSV-based pseudotyped viruses were produced as previously described (41, 42). Vector pCAGGS containing the SARS-related coronavirus 2, Wuhan-Hu-1 Spike glycoprotein gene, NR-52310, was produced under HHSN272201400008C and obtained through BEI Resources, NIAID, NIH. 293T cells were transfected with the pCAGGS vector expressing the SARS-CoV-2 spike glycoprotein and then incubated with replication-deficient VSV expressing *Renilla* luciferase for 1 h at 37°C (41). The virus inoculum was then removed, and the cells were washed with PBS before adding media with anti-

VSV-G clone I4 to neutralize residual inoculum. No antibody was added to cells expressing VSV-G. Supernatant containing pseudoviruses was collected 24 h postinoculation, clarified by centrifugation, and stored in aliquots at -80°C .

Pseudovirus entry and neutralization assays. We plated 3×10^4 Calu-3 or 1×10^4 Huh7.5 cells in a $100\text{-}\mu\text{l}$ volume in each well of a 96-well plate. The following day, the medium was replaced with $50\text{ }\mu\text{M}$ ibuprofen, $50\text{ }\mu\text{M}$ meloxicam, or an equivalent amount of DMSO. One day later, $10\text{ }\mu\text{l}$ of SARS-CoV-2 spike protein-pseudotyped (SARS2-VSVpp) or VSV glycoprotein-typed virus was added. The luciferase activity was measured at 24 hpi using the *Renilla* luciferase assay system (Promega). Each well of cells was lysed with $50\text{ }\mu\text{l}$ of lysis buffer, and $15\text{ }\mu\text{l}$ of cell lysate was then mixed with $15\text{ }\mu\text{l}$ of luciferase assay reagent. The luminescence was measured on a microplate reader (BioTek Synergy).

For neutralization assays, 2×10^4 Huh7.5 cells were plated in a $100\text{-}\mu\text{l}$ volume in each well of a 96-well plate. The following day, serial dilutions of serum were incubated with SARS2-VSVpp pseudovirus for 1 h at 37°C . The growth medium was then aspirated from the cells and replaced with $50\text{ }\mu\text{l}$ of the serum/virus mixture. Luciferase activity was measured at 24 hpi as detailed above. Half-maximal inhibitory concentrations (IC_{50} s) were calculated as previously described (73).

icSARS-CoV-2-mNG assay. We plated 6.5×10^3 Calu-3 or 2.5×10^3 Huh7.5 cells in $20\text{ }\mu\text{l}$ of phenol red-free medium containing $50\text{ }\mu\text{M}$ ibuprofen, $50\text{ }\mu\text{M}$ meloxicam, or an equivalent amount of DMSO in each well of a black-walled, clear-bottom 384-well plate. The following day, icSARS-CoV-2-mNG was added at an MOI of 1 in a $5\text{-}\mu\text{l}$ volume. The frequency of infected cells was measured by mNeonGreen expression at 1, 2, and 3 dpi by high content imaging (BioTek Cytation 5) configured with brightfield and GFP cubes. The total cell numbers were quantified by Gen5 software for brightfield images. Object analysis was used to determine the number of mNeonGreen-positive cells. The percentage of infection was calculated as the ratio of the number of mNeonGreen-positive cells to the total number of cells in brightfield.

Measurement of lung viral burden and cytokines. Lungs were perfused with 3 ml of sterile PBS. The left lobe was collected and homogenized in 1 ml of DMEM supplemented with 2% heat-inactivated FBS and 1% antibiotic-antimycotic. The viral burden was measured in lung homogenates by plaque assay on Vero-E6 cells as previously described (42). To measure cytokines, lung homogenates were incubated with a final concentration of 1% Triton X-100 for 1 h at room temperature to inactivate SARS-CoV-2. Cytokine analysis was performed by Eve Technologies using their Mouse Cytokine Array/Chemokine Array 31-Plex (MD31) platform.

Flow cytometry analysis of lung immune cells. Lungs were perfused with 3 ml of sterile PBS. The right inferior lobe was collected and digested with 0.5 mg/ml collagenase IV (Sigma-Aldrich) and 100 U/ml DNase I (Sigma-Aldrich) in complete RPMI for 45 min at 37°C . Single-cell suspensions of digested lung tissue were preincubated with Fc block (clone 2.4G2) for 5 min at room temperature before staining. The cells were stained with the following antibodies or viability dyes for 30 min at 4°C : PE anti-CD64 (clone X54-5/7.1), PE/Cy7 anti-Ly6C (clone HK1.4), PerCP/Cy5.5 anti-CD45.2 (clone 104), APC anti-CD86 (clone GL1), AF700 anti-CD19 (clone 6D5), DAPI (4',6'-diamidino-2-phenylindole; Thermo Fisher), BV510 anti-I-A/I-E (clone M5/114.15.2), BV605 anti-CD11c (clone N418), Live/Dead Fixable Green (Thermo Fisher), PE anti-TCR γ/δ (clone GL3), PE/Cy7 anti-CD69 (clone H1.2F3), PerCP/Cy5.5 anti-CD8 (clone 53.6-7), APC anti-CD45.2 (clone 104), APC/Cy7 anti-TCR β (clone H57-597), AF700 anti-CD4 (clone RM4-5), PB anti-Ly6G (clone 1A8), BV510 anti-NK1.1 (clone PK136), and BV605 anti-CD44 (clone IM7). After being washed, the cells were fixed with 4% paraformaldehyde for 30 min at room temperature to inactivate SARS-CoV-2. Samples were acquired on a CytoFLEX S (Beckman Coulter) and analyzed using FlowJo software (BD).

Spike-specific ELISAs. Serum was incubated with a final concentration of 0.5% Triton X-100 and 0.5 mg/ml RNase A to inactivate any potential SARS-CoV-2. SARS-CoV-2 stabilized spike glycoprotein (BEI Resources, NR-53524) was coated at a concentration of $2\text{ }\mu\text{g/ml}$ in carbonate buffer on 96-well MaxiSorp plates (Thermo Fisher) overnight at 4°C . Plates were blocked with 1% BSA in PBS for 1 h at room temperature. Serum samples were serially diluted in 1% BSA in PBS and incubated in plates for 2 h at room temperature. Antibody isotypes were detected with anti-mouse IgM-HRP or anti-mouse IgG Fc-HRP (Southern Biotech) by incubation for 1 h at room temperature. The plates were developed with TMB stabilized chromogen (Thermo Fisher), stopped with 3 N hydrochloric acid, and read at 450 nm on a microplate reader.

Statistical analysis. Data analysis was performed using GraphPad Prism 8 unless otherwise indicated. Data were analyzed using Welch's two-tailed, unpaired *t* test; Student two-tailed, unpaired *t* test; two-tailed Mann-Whitney test; or two-way ANOVA, as indicated. $P < 0.05$ was considered statistically significant.

Data availability. All previously published data are available as described above. Cytokine data generated in this study are available in Table S1 in the supplemental material.

SUPPLEMENTAL MATERIAL

Supplemental material is available online only.

SUPPLEMENTAL FILE 1, XLSX file, 0.02 MB.

SUPPLEMENTAL FILE 2, PDF file, 0.3 MB.

ACKNOWLEDGMENTS

We acknowledge Benhur Lee, Pei-Yong Shi, the World Reference Center for Emerging Viruses and Arboviruses (WRCEVA), Paulina Pawlica, Joan Steitz, Michael

Diamond, Adam Bailey, Emma Winkler, and BEI Resources for providing critical reagents and expertise. We thank all members of the Wilen and Eisenbarth labs for helpful discussions. We thank Yale Environmental Health and Safety for providing necessary training and support for SARS-CoV-2 research.

This study was supported by NIH Medical Scientist Training Program Training Grant T32GM007205 (J.S.C., R.D.C.), NIH/NHLBI F30HL149151 (J.S.C.), NIH/NCI F30CA250249 (R.D.C.), NIH/NIAID K08 AI128043 (C.B.W.), a Burroughs Wellcome Fund Career Award for Medical Scientists (C.B.W.), the Mathers Charitable Foundation (C.B.W.), the Ludwig Family Foundation (C.B.W.), and an Emergent Ventures Fast Grant (C.B.W.).

Jennifer S. Chen: Conceptualization, Formal Analysis, Investigation, Validation, Visualization, Writing – Original Draft; Mia Madel Alfajaro: Methodology, Investigation; Jin Wei: Methodology, Investigation; Ryan D. Chow: Formal Analysis, Visualization; Renata B. Filler: Investigation; Stephanie C. Eisenbarth: Supervision; Craig B. Wilen: Conceptualization, Formal Analysis, Funding Acquisition, Resources, Supervision, Writing – Original Draft. All authors reviewed and edited the manuscript.

Yale University (C.B.W.) has a patent pending related to this work entitled “Compounds and Compositions for Treating, Ameliorating, and/or Preventing SARS-CoV-2 Infection and/or Complications Thereof.” Yale University has committed to rapidly executable nonexclusive royalty-free licenses to intellectual property rights for the purpose of making and distributing products to prevent, diagnose, and treat COVID-19 infection during the pandemic and for a short period thereafter.

REFERENCES

- Day M. 2020. Covid-19: ibuprofen should not be used for managing symptoms, say doctors and scientists. *BMJ* 368:m1086.
- Powis S. 2020. Novel coronavirus: anti-inflammatory medications. Medicines and Healthcare Products Regulatory Agency, London, United Kingdom.
- Ricciotti E, FitzGerald GA. 2011. Prostaglandins and inflammation. *Arterioscler Thromb Vasc Biol* 31:986–1000. <https://doi.org/10.1161/ATVBAHA.110.207449>.
- Zhou P, Yang X-L, Wang X-G, Hu B, Zhang L, Zhang W, Si H-R, Zhu Y, Li B, Huang C-L, Chen H-D, Chen J, Luo Y, Guo H, Jiang R-D, Liu M-Q, Chen Y, Shen X-R, Wang X, Zheng X-S, Zhao K, Chen Q-J, Deng F, Liu L-L, Yan B, Zhan F-X, Wang Y-Y, Xiao G-F, Shi Z-L. 2020. A pneumonia outbreak associated with a new coronavirus of probable bat origin. *Nature* 579:270–273. <https://doi.org/10.1038/s41586-020-2012-7>.
- Fang L, Karakiulakis G, Roth M. 2020. Are patients with hypertension and diabetes mellitus at increased risk for COVID-19 infection? *Lancet Respir Med* 8:e21. [https://doi.org/10.1016/S2213-2600\(20\)30116-8](https://doi.org/10.1016/S2213-2600(20)30116-8).
- Raaben M, Einerhand AW, Taminiau LJ, van Houdt M, Bouma J, Raatgeep RH, Büller HA, de Haan CA, Rossen JW. 2007. Cyclooxygenase activity is important for efficient replication of mouse hepatitis virus at an early stage of infection. *Virology* 355:455–455. <https://doi.org/10.1016/j.virus.2006.11.011>.
- Qiao W, Wang C, Chen B, Zhang F, Liu Y, Lu Q, Guo H, Yan C, Sun H, Hu G, Yin X. 2015. Ibuprofen attenuates cardiac fibrosis in streptozotocin-induced diabetic rats. *Cardiology* 131:97–106. <https://doi.org/10.1159/000375362>.
- Miyoshi H, VanDussen KL, Malvin NP, Ryu SH, Wang Y, Sonnek NM, Lai C-W, Stappenbeck TS. 2017. Prostaglandin E₂ promotes intestinal repair through an adaptive cellular response of the epithelium. *EMBO J* 36:5–24. <https://doi.org/10.15252/embj.201694660>.
- Alfajaro MM, Choi J-S, Kim D-S, Seo J-Y, Kim J-Y, Park J-G, Soliman M, Baek Y-B, Cho E-H, Kwon J, Kwon H-J, Park S-J, Lee WS, Kang M-I, Hosmillo M, Goodfellow I, Cho K-O. 2017. Activation of COX-2/PGE2 promotes sapovirus replication via the inhibition of nitric oxide production. *J Virol* 91:e01656-16. <https://doi.org/10.1128/JVI.01656-16>.
- Alfajaro MM, Cho E-H, Park J-G, Kim J-Y, Soliman M, Baek Y-B, Kang M-I, Park S-J, Cho K-O. 2018. Feline calicivirus- and murine norovirus-induced COX-2/PGE₂ signaling pathway has proinfectious effects. *PLoS One* 13:e0200726. <https://doi.org/10.1371/journal.pone.0200726>.
- Lu R, Zhao X, Li J, Niu P, Yang B, Wu H, Wang W, Song H, Huang B, Zhu N, Bi Y, Ma X, Zhan F, Wang L, Hu T, Zhou H, Hu Z, Zhou W, Zhao L, Chen J, Meng Y, Wang J, Lin Y, Yuan J, Xie Z, Ma J, Liu WJ, Wang D, Xu W, Holmes EC, Gao GF, Wu G, Chen W, Shi W, Tan W. 2020. Genomic characterization and epidemiology of 2019 novel coronavirus: implications for virus origins and receptor binding. *Lancet* 395:565–574. [https://doi.org/10.1016/S0140-6736\(20\)30251-8](https://doi.org/10.1016/S0140-6736(20)30251-8).
- Yan X, Hao Q, Mu Y, Timani KA, Ye L, Zhu Y, Wu J. 2006. Nucleocapsid protein of SARS-CoV activates the expression of cyclooxygenase-2 by binding directly to regulatory elements for nuclear factor- κ B and CCAAT/enhancer binding protein. *Int J Biochem Cell Biol* 38:1417–1428. <https://doi.org/10.1016/j.biocel.2006.02.003>.
- Liu M, Yang Y, Gu C, Yue Y, Wu KK, Wu J, Zhu Y. 2007. Spike protein of SARS-CoV stimulates cyclooxygenase-2 expression via both calcium-dependent and calcium-independent protein kinase C pathways. *FASEB J* 21:1586–1596. <https://doi.org/10.1096/fj.06-6589com>.
- Fajgenbaum DC, June CH. 2020. Cytokine storm. *N Engl J Med* 383:2255–2273. <https://doi.org/10.1056/NEJMr2026131>.
- Horby P, Lim WS, Emberson JR, Mafham M, Bell JL, Linsell L, Staplin N, Brightling C, Ustianowski A, Elmahi E, Prudon B, Green C, Felton T, Chadwick D, Rege K, Fegan C, Chappell LC, Faust SN, Jaki T, Jeffery K, Montgomery A, Rowan K, Juszczak E, Baillie JK, Haynes R, Landray MJ, RECOVERY Collaborative Group. 2020. Dexamethasone in hospitalized patients with Covid-19: preliminary report. *N Engl J Med* <https://doi.org/10.1056/NEJMoa2021436>.
- Lucas C, Wong P, Klein J, Castro TBR, Silva J, Sundaram M, Ellingson MK, Mao T, Oh JE, Israelow B, Takahashi T, Tokuyama M, Lu P, Venkataraman A, Park A, Mohanty S, Wang H, Wyllie AL, Vogels CBF, Earnest R, Lapidus S, Ott IM, Moore AJ, Muenker MC, Fournier JB, Campbell M, Odio CD, Casanovas-Massana A, Herbst R, Shaw AC, Medzhitov R, Schulz WL, Grubaugh ND, Cruz CD, Farhadian S, Ko AI, Omer SB, Iwasaki A, Yale IMPACT Team. 2020. Longitudinal analyses reveal immunological misfiring in severe COVID-19. *Nature* 584:463–469. <https://doi.org/10.1038/s41586-020-2588-y>.
- Mann ER, Menon M, Knight SB, Konkel JE, Jagger C, Shaw TN, Krishnan S, Rattray M, Ustianowski A, Bakerly ND, Dark P, Lord GM, Simpson A, Felton T, Ho L-P, Trc NR, Feldmann M, CIRCO, Grainger JR, Hussell T. 2020. Longitudinal immune profiling reveals key myeloid signatures associated with COVID-19. *Sci Immunol* 5:eabd6197. <https://doi.org/10.1126/sciimmunol.abd6197>.
- Robb CT, Goepf M, Rossi AG, Yao C. 2020. Non-steroidal anti-inflammatory drugs, prostaglandins, and COVID-19. *Br J Pharmacol* 177:4899–4920. <https://doi.org/10.1111/bph.15206>.
- Yao C, Narumiya S. 2019. Prostaglandin-cytokine crosstalk in chronic inflammation. *Br J Pharmacol* 176:337–354. <https://doi.org/10.1111/bph.14530>.
- Zhao J, Zhao J, Legge K, Perlman S. 2011. Age-related increases in PGD₂

- expression impair respiratory DC migration, resulting in diminished T cell responses upon respiratory virus infection in mice. *J Clin Invest* 121:4921–4930. <https://doi.org/10.1172/JCI59777>.
21. Coulombe F, Jaworska J, Verway M, Tzelepis F, Massoud A, Gillard J, Wong G, Kobinger G, Xing Z, Couture C, Joubert P, Fritz JH, Powell WS, Divangahi M. 2014. Targeted prostaglandin E2 inhibition enhances antiviral immunity through induction of type I interferon and apoptosis in macrophages. *Immunity* 40:554–568. <https://doi.org/10.1016/j.immuni.2014.02.013>.
 22. Vijay R, Fehr AR, Janowski AM, Athmer J, Wheeler DL, Grunewald M, Sompallae R, Kurup SP, Meyerholz DK, Sutterwala FS, Narumiya S, Perlman S. 2017. Virus-induced inflammasome activation is suppressed by prostaglandin D2/DP1 signaling. *Proc Natl Acad Sci U S A* 114:E5444–E5453. <https://doi.org/10.1073/pnas.1704099114>.
 23. Hashimoto K, Graham BS, Geraci MW, FitzGerald GA, Egan K, Zhou W, Goleniewska K, O'Neal JF, Morrow JD, Wurbin RK, Wright PF, Collins RD, Suzutani T, Peebles RS. 2004. Signaling through the prostaglandin I2 receptor IP protects against respiratory syncytial virus-induced illness. *J Virol* 78:10303–10309. <https://doi.org/10.1128/JVI.78.19.10303-10309.2004>.
 24. Bernard MP, Bancos S, Chapman TJ, Ryan EP, Treanor JJ, Rose RC, Topham DJ, Phipps RP. 2010. Chronic inhibition of cyclooxygenase-2 attenuates antibody responses against vaccinia infection. *Vaccine* 28:1363–1372. <https://doi.org/10.1016/j.vaccine.2009.11.005>.
 25. Arvin AM, Fink K, Schmid MA, Cathcart A, Spreafico R, Havenar-Daughton C, Lanzavecchia A, Corti D, Virgin HW. 2020. A perspective on potential antibody-dependent enhancement of SARS-CoV-2. 7821. *Nature* 584:353–363. <https://doi.org/10.1038/s41586-020-2538-8>.
 26. Blanco-Melo D, Nilsson-Payant BE, Liu W-C, Uhl S, Hoagland D, Møller R, Jordan TX, Oishi K, Panis M, Sachs D, Wang TT, Schwartz RE, Lim JK, Albrecht RA, tenOever BR. 2020. Imbalanced host response to SARS-CoV-2 drives development of COVID-19. *Cell* 181:1036–1045. <https://doi.org/10.1016/j.cell.2020.04.026>.
 27. Leung C, Wadsworth SJ, Yang SJ, Dorscheid DR. 2020. Structural and functional variations in human bronchial epithelial cells cultured in air-liquid interface using different growth media. *Am J Physiol Lung Cell Mol Physiol* 318:L1063–L1073. <https://doi.org/10.1152/ajplung.00190.2019>.
 28. Ravindra NG, Alfajaro MM, Gasque V, Habet V, Wei J, Filler RB, Huston NC, Wan H, Sziget-Buck K, Wang B, Wang G, Montgomery RR, Eisenbarth SC, Williams A, Pyle AM, Iwasaki A, Horvath TL, Foxman EF, Pierce RW, van Dijk D, Wilen CB. 2020. Single-cell longitudinal analysis of SARS-CoV-2 infection in human airway epithelium. *bioRxiv* <https://doi.org/10.1101/2020.05.06.081695>.
 29. McCray PB, Pewe L, Wohlford-Lenane C, Hickey M, Manzel L, Shi L, Netland J, Jia HP, Halabi C, Sigmund CD, Meyerholz DK, Kirby P, Look DC, Perlman S. 2007. Lethal infection of K18-hACE2 mice infected with severe acute respiratory syndrome coronavirus. *J Virol* 81:813–821. <https://doi.org/10.1128/JVI.02012-06>.
 30. Bao L, Deng W, Huang B, Gao H, Liu J, Ren L, Wei Q, Yu P, Xu Y, Qi F, Qu Y, Li F, Lv Q, Wang W, Xue J, Gong S, Liu M, Wang G, Wang S, Song Z, Zhao L, Liu P, Zhao L, Ye F, Wang H, Zhou W, Zhu N, Zhen W, Yu H, Zhang X, Guo L, Chen L, Wang C, Wang Y, Wang X, Xiao Y, Sun Q, Liu H, Zhu F, Ma C, Yan L, Yang M, Han J, Xu W, Tan W, Peng X, Jin Q, Wu G, Qin C. 2020. The pathogenicity of SARS-CoV-2 in hACE2 transgenic mice. *Nature* 583:830–833. <https://doi.org/10.1038/s41586-020-2312-y>.
 31. Jiang R-D, Liu M-Q, Chen Y, Shan C, Zhou Y-W, Shen X-R, Li Q, Zhang L, Zhu Y, Si H-R, Wang Q, Min J, Wang X, Zhang W, Li B, Zhang H-J, Baric RS, Zhou P, Yang X-L, Shi Z-L. 2020. Pathogenesis of SARS-CoV-2 in transgenic mice expressing human angiotensin-converting enzyme 2. *Cell* 182:50–58. <https://doi.org/10.1016/j.cell.2020.05.027>.
 32. Hassan AO, Case JB, Winkler ES, Thackeray LB, Kafai NM, Bailey AL, McCune BT, Fox JM, Chen RE, Alsoussi WB, Turner JS, Schmitz AJ, Lei T, Shrihari S, Keeler SP, Fremont DH, Greco S, McCray PB, Perlman S, Holtzman MJ, Ellebedy AH, Diamond MS. 2020. A SARS-CoV-2 infection model in mice demonstrates protection by neutralizing antibodies. *Cell* 182:744–753. <https://doi.org/10.1016/j.cell.2020.06.011>.
 33. Sun J, Zhuang Z, Zheng J, Li K, Wong RL-Y, Liu D, Huang J, He J, Zhu A, Zhao J, Li X, Xi Y, Chen R, Alshukairi AN, Chen Z, Zhang Z, Chen C, Huang X, Li F, Lai X, Chen D, Wen L, Zhuo J, Zhang Y, Wang Y, Huang S, Dai J, Shi Y, Zheng K, Leidinger MR, Chen J, Li Y, Zhong N, Meyerholz DK, McCray PB, Perlman S, Zhao J. 2020. Generation of a broadly useful model for COVID-19 pathogenesis, vaccination, and treatment. *Cell* 182:734–743. <https://doi.org/10.1016/j.cell.2020.06.010>.
 34. Israelow B, Song E, Mao T, Lu P, Meir A, Liu F, Alfajaro MM, Wei J, Dong H, Homer RJ, Ring A, Wilen CB, Iwasaki A. 2020. Mouse model of SARS-CoV-2 reveals inflammatory role of type I interferon signaling. *J Exp Med* 217:e20201241. <https://doi.org/10.1084/jem.20201241>.
 35. Sun S-H, Chen Q, Gu H-J, Yang G, Wang Y-X, Huang X-Y, Liu S-S, Zhang N-N, Li X-F, Xiong R, Guo Y, Deng Y-Q, Huang W-J, Liu Q, Liu Q-M, Shen Y-L, Zhou Y, Yang X, Zhao T-Y, Fan C-F, Zhou Y-S, Qin C-F, Wang Y-C. 2020. A mouse model of SARS-CoV-2 infection and pathogenesis. *Cell Host Microbe* 28:124–133. <https://doi.org/10.1016/j.chom.2020.05.020>.
 36. Winkler ES, Bailey AL, Kafai NM, Nair S, McCune BT, Yu J, Fox JM, Chen RE, Earnest JT, Keeler SP, Ritter JH, Kang L-I, Dort S, Robichaud A, Head R, Holtzman MJ, Diamond MS. 2020. SARS-CoV-2 infection of human ACE2-transgenic mice causes severe lung inflammation and impaired function. *Nat Immunol* 21:1470–1479. <https://doi.org/10.1038/s41590-020-0794-2>.
 37. Park MK, Kang SH, Son JY, Lee MK, Ju JS, Bae YC, Ahn DK. 2019. Co-administered low doses of ibuprofen and dexamethasone produce synergistic antinociceptive effects on neuropathic mechanical allodynia in rats. *J Pain Res* 12:2959–2968. <https://doi.org/10.2147/JPR.S222095>.
 38. Tubbs JT, Kissling GE, Travlos GS, Goulding DR, Clark JA, King-Herbert AP, Blankenship-Paris TL. 2011. Effects of buprenorphine, meloxicam, and flunixin meglumine as postoperative analgesia in mice. *J Am Assoc Lab Anim Sci* 50:185–191.
 39. Santos ARS, Vedana EMA, De Freitas GAG. 1998. Antinociceptive effect of meloxicam, in neurogenic and inflammatory nociceptive models in mice. *Inflammation Res* 47:302–307. <https://doi.org/10.1007/s000110050333>.
 40. Laird JMA, Herrero JF, Garcia de la Rubia P, Cervero F. 1997. Analgesic activity of the novel COX-2 preferring NSAID, meloxicam in mono-arthritic rats: central and peripheral components. *Inflamm Res* 46:203–210. <https://doi.org/10.1007/s000110050174>.
 41. Avanzato VA, Oguntuyo KY, Escalera-Zamudio M, Gutierrez B, Golden M, Pond SLK, Pryce R, Walter TS, Seow J, Doores KJ, Pybus OG, Munster VJ, Lee B, Bowden TA. 2019. A structural basis for antibody-mediated neutralization of Nipah virus reveals a site of vulnerability at the fusion glycoprotein apex. *Proc Natl Acad Sci U S A* 116:25057–25067. <https://doi.org/10.1073/pnas.1912503116>.
 42. Wei J, Alfajaro MM, DeWeirdt PC, Hanna RE, Lu-Culligan WJ, Cai WL, Strine MS, Zhang S-M, Graziano VR, Schmitz CO, Chen JS, Mankowski MC, Filler RB, Ravindra NG, Gasque V, de Miguel FJ, Patil A, Chen H, Oguntuyo KY, Abriola L, Surovtseva YV, Orchard RC, Lee B, Lindenbach BD, Politi K, van Dijk D, Kadoch C, Simon MD, Yan Q, Doench JG, Wilen CB. 2021. Genome-wide CRISPR screens reveal host factors critical for SARS-CoV-2 infection. *Cell* 184:76–91. <https://doi.org/10.1016/j.cell.2020.10.028>.
 43. Sander WJ, O'Neill HG, Pohl CH. 2017. Prostaglandin E2 as a modulator of viral infections. *Front Physiol* 8:89. <https://doi.org/10.3389/fphys.2017.00089>.
 44. Luczak M, Gumulka W, Szmigielski S, Korbecki M. 1975. Inhibition of multiplication of parainfluenza 3 virus in prostaglandin-treated WISH cells. *Arch Virol* 49:377–380. <https://doi.org/10.1007/BF01318248>.
 45. Xie X, Muruato A, Lokugamage KG, Narayanan K, Zhang X, Zou J, Liu J, Schindewolf C, Bopp NE, Aguilar PV, Plante KS, Weaver SC, Makino S, LeDuc JW, Menachery VD, Shi P-Y. 2020. An infectious cDNA clone of SARS-CoV-2. *Cell Host Microbe* 27:841–848. <https://doi.org/10.1016/j.chom.2020.04.004>.
 46. Kindler E, Thiel V, Weber F. 2016. Interaction of SARS and MERS coronaviruses with the antiviral interferon response. *Adv Virus Res* 96:219–243.
 47. Dudek SE, Nitzsche K, Ludwig S, Ehrhardt C. 2016. Influenza A viruses suppress cyclooxygenase-2 expression by affecting its mRNA stability. 1. *Sci Rep* 6:27275. <https://doi.org/10.1038/srep27275>.
 48. Sumpter R, Loo Y-M, Foy E, Li K, Yoneyama M, Fujita T, Lemon SM, Gale M. 2005. Regulating intracellular antiviral defense and permissiveness to hepatitis C virus RNA replication through a cellular RNA helicase, RIG-I. *J Virol* 79:2689–2699. <https://doi.org/10.1128/JVI.79.5.2689-2699.2005>.
 49. Fink K. 2012. Origin and function of circulating plasmablasts during acute viral infections. *Front Immunol* 3:78. <https://doi.org/10.3389/fimmu.2012.00078>.
 50. Ryan EP, Pollock SJ, Pollack SJ, Murant TI, Bernstein SH, Felgar RE, Phipps RP. 2005. Activated human B lymphocytes express cyclooxygenase-2 and cyclooxygenase inhibitors attenuate antibody production. *J Immunol* 174:2619–2626. <https://doi.org/10.4049/jimmunol.174.5.2619>.
 51. Bernard MP, Phipps RP. 2007. CpG oligodeoxynucleotides induce cyclooxygenase-2 in human B lymphocytes: implications for adjuvant activity and antibody production. *Clin Immunol* 125:138–148. <https://doi.org/10.1016/j.clim.2007.07.006>.
 52. Bancos S, Bernard MP, Topham DJ, Phipps RP. 2009. Ibuprofen and other widely used non-steroidal anti-inflammatory drugs inhibit antibody

- production in human cells. *Cell Immunol* 258:18–28. <https://doi.org/10.1016/j.cellimm.2009.03.007>.
53. Bernard MP, Phipps RP. 2010. Inhibition of cyclooxygenase-2 impairs the expression of essential plasma cell transcription factors and human B-lymphocyte differentiation. *Immunology* 129:87–96. <https://doi.org/10.1111/j.1365-2567.2009.03152.x>.
 54. Zheng J, Wong L-YR, Li K, Verma AK, Ortiz M, Wohlford-Lenane C, Leidinger MR, Knudson CM, Meyerholz DK, McCray PB, Perlman S. 2020. COVID-19 treatments and pathogenesis including anosmia in K18-hACE2 mice. *Nature* <https://doi.org/10.1038/s41586-020-2943-z>.
 55. Tipton DA, Flynn JC, Stein SH, Dabbous MK. 2003. Cyclooxygenase-2 inhibitors decrease interleukin-1 β -stimulated prostaglandin E2 and IL-6 production by human gingival fibroblasts. *J Periodontol* 74:1754–1763. <https://doi.org/10.1902/jop.2003.74.12.1754>.
 56. Cheng Q, Li N, Chen M, Zheng J, Qian Z, Wang X, Huang C, Xu S, Shi G. 2013. Cyclooxygenase-2 promotes hepatocellular apoptosis by interacting with TNF- α and IL-6 in the pathogenesis of nonalcoholic steatohepatitis in rats. *Dig Dis Sci* 58:2895–2902. <https://doi.org/10.1007/s10620-013-2823-6>.
 57. Kaur J, Sanyal SN. 2011. Diclofenac, a selective COX-2 inhibitor, inhibits DMH-induced colon tumorigenesis through suppression of MCP-1, MIP-1 α , and VEGF. *Mol Carcinog* 50:707–718. <https://doi.org/10.1002/mc.20736>.
 58. Lisboa FA, Bradley MJ, Hueman MT, Schobel SA, Gaucher BJ, Styrmisdottir EL, Potter BK, Forsberg JA, Elster EA. 2017. Nonsteroidal anti-inflammatory drugs may affect cytokine response and benefit healing of combat-related extremity wounds. *Surgery* 161:1164–1173. <https://doi.org/10.1016/j.surg.2016.10.011>.
 59. Anderson GD, Hauser SD, McGarity KL, Bremer ME, Isakson PC, Gregory SA. 1996. Selective inhibition of cyclooxygenase (COX)-2 reverses inflammation and expression of COX-2 and interleukin 6 in rat adjuvant arthritis. *J Clin Invest* 97:2672–2679. <https://doi.org/10.1172/JCI118717>.
 60. Aoki T, Frösen J, Fukuda M, Bando K, Shioi G, Tsuji K, Ollikainen E, Nozaki K, Laakkonen J, Narumiya S. 2017. Prostaglandin E2–EP2–NF- κ B signaling in macrophages as a potential therapeutic target for intracranial aneurysms. *Sci Signal* 10:eaah6037. <https://doi.org/10.1126/scisignal.aah6037>.
 61. Zhou Y, Fu B, Zheng X, Wang D, Zhao C, Qi Y, Sun R, Tian Z, Xu X, Wei H. 2020. Pathogenic T cells and inflammatory monocytes incite inflammatory storms in severe COVID-19 patients. *Nat Sci Rev* 7:998–1002. <https://doi.org/10.1093/nsr/nwaa041>.
 62. Lam JKP, Hui KF, Ning RJ, Xu XQ, Chan KH, Chiang AKS. 2018. Emergence of CD4⁺ and CD8⁺ polyfunctional T cell responses against immunodominant lytic and latent EBV antigens in children with primary EBV infection. *Front Microbiol* 9:416. <https://doi.org/10.3389/fmicb.2018.00416>.
 63. Seo SH, Webster RG. 2002. Tumor necrosis factor alpha exerts powerful anti-influenza virus effects in lung epithelial cells. *J Virol* 76:1071–1076. <https://doi.org/10.1128/jvi.76.3.1071-1076.2002>.
 64. Karki R, Sharma BR, Tuladhar S, Williams EP, Zalduondo L, Samir P, Zheng M, Sundaram B, Banoth B, Malireddi RKS, Schreiner P, Neale G, Vogel P, Webby R, Jonsson CB, Kanneganti T-D. 2021. Synergism of TNF- α and IFN- γ triggers inflammatory cell death, tissue damage, and mortality in SARS-CoV-2 infection and cytokine shock syndromes. *Cell* 184:149–168. <https://doi.org/10.1016/j.cell.2020.11.025>.
 65. Huang E, Jordan SC. 2020. Tocilizumab for Covid-19: the ongoing search for effective therapies. *N Engl J Med* 383:2387–2388. <https://doi.org/10.1056/NEJMe2032071>.
 66. Imam Z, Odish F, Gill I, O'Connor D, Armstrong J, Vanood A, Ibironke O, Hanna A, Ranski A, Halalau A. 2020. Older age and comorbidity are independent mortality predictors in a large cohort of 1305 COVID-19 patients in Michigan, United States. *J Intern Med* 288:469–476. <https://doi.org/10.1111/joim.13119>.
 67. Rinott E, Kozer E, Shapira Y, Bar-Haim A, Youngster I. 2020. Ibuprofen use and clinical outcomes in COVID-19 patients. *Clin Microbiol Infect* 26:1259.e5–1259.e7. <https://doi.org/10.1016/j.cmi.2020.06.003>.
 68. Wong AY, MacKenna B, Morton C, Schultze A, Walker AJ, Bhaskaran K, Brown J, Rentsch CT, Williamson E, Drysdale H, Croker R, Bacon S, Hulme W, Bates C, Curtis HJ, Mehrkar A, Evans D, Inglesby P, Cockburn J, McDonald H, Tomlinson L, Mathur R, Wing K, Forbes H, Parry J, Hester F, Harper S, Evans S, Smeeth L, Douglas I, Goldacre B. 2020. OpenSAFELY: do adults prescribed Non-steroidal anti-inflammatory drugs have an increased risk of death from COVID-19? medRxiv <https://doi.org/10.1101/2020.08.12.20171405>.
 69. Abu Esba LC, Alqahtani RA, Thomas A, Shamas N, Alswaidan L, Mardawi G. 2020. Ibuprofen and NSAID use in COVID-19 infected patients is not associated with worse outcomes: a prospective cohort study. *Infect Dis Ther* <https://doi.org/10.1007/s40121-020-00363-w>.
 70. Bruce E, Barlow-Pay F, Short R, Vilches-Moraga A, Price A, McGovern A, Braude P, Stechman MJ, Moug S, McCarthy K, Hewitt J, Carter B, Myint PK. 2020. Prior routine use of non-steroidal anti-inflammatory drugs (NSAIDs) and important outcomes in hospitalized patients with COVID-19. *J Clin Med* 9:2586. <https://doi.org/10.3390/jcm9082586>.
 71. Lund LC, Kristensen KB, Reilev M, Christensen S, Thomsen RW, Christiansen CF, Støvring H, Johansen NB, Brun NC, Hallas J, Pottegård A. 2020. Adverse outcomes and mortality in users of non-steroidal anti-inflammatory drugs who tested positive for SARS-CoV-2: a Danish nationwide cohort study. *PLoS Med* 17:e1003308. <https://doi.org/10.1371/journal.pmed.1003308>.
 72. Love MI, Huber W, Anders S. 2014. Moderated estimation of fold change and dispersion for RNA-seq data with DESeq2. *Genome Biol* 15:550. <https://doi.org/10.1186/s13059-014-0550-8>.
 73. Decker JM, Bibollet-Ruche F, Wei X, Wang S, Levy DN, Wang W, Delaporte E, Peeters M, Derdeyn CA, Allen S, Hunter E, Saag MS, Hoxie JA, Hahn BH, Kwong PD, Robinson JE, Shaw GM. 2005. Antigenic conservation and immunogenicity of the HIV coreceptor binding site. *J Exp Med* 201:1407–1419. <https://doi.org/10.1084/jem.20042510>.

§ CHAPTER 5: Conclusion and Implications

Though Tfh cells are considered the conventional drivers of protective antibody responses, our work in Chapter 2 demonstrated that non-Tfh CD4⁺ T cells can promote antibodies in the absence of Tfh cells to diverse immune stimuli, from infection to vaccination. However, it remains to be seen whether this Tfh-independent pathway of antibody production still exists when the conventional Tfh-dependent pathway is intact. Future work will therefore focus on delineating the settings in which non-Tfh CD4⁺ T cells promote antibody production. In addition to the compensatory role of non-Tfh CD4⁺ T cells that we described, in other settings these cells may work collaboratively with Tfh cells to promote robust antibody responses. Or, non-Tfh CD4⁺ T cells and Tfh cells may even promote entirely different antibody responses depending on the antigen. For example, prior work from our lab has shown that the serum IgE and gut IgA responses to food develop through divergent T-dependent pathways, with IgE being completely Tfh-dependent and IgA being completely Tfh-independent (132).

Thus, perhaps the most exciting question arising from these studies is why particular T cell subsets are endowed with the ability to induce certain antibody isotypes during a given immune response. For instance, we observed that Tfh cells have the unique ability to induce IgG1 during SARS-CoV-2 and influenza A virus infection. As a consequence, IgG1 arises more slowly than other IgG subclasses in mice with Tfh cells, and mice without Tfh cells cannot generate any IgG1 at all while other IgG subclasses are still made. The molecular mechanism for this, shown by our work in Chapter 3, is that Tfh cell-derived IL-4 is required for IgG1 switching during type 1 immune responses. But the teleological basis for Tfh cell-restricted IgG1 induction is less clear.

One hypothesis is that the role of IgG1 may actually be to limit the inflammatory potential of the humoral response (133). While IgG2 antibodies bind activating Fc receptors such as FcγRI

and Fc γ RIV, IgG1 tends to bind Fc receptors like Fc γ RIIB with more inhibitory function (6). Furthermore, it has been shown that IgG1 is necessary and sufficient to prevent IgG3 immune complex-mediated immunopathology (134). In the setting of viral infection, IgG1 may therefore serve to limit the degree of IgG2-driven inflammation. The slower kinetics of IgG1 production may ensure that IgG2-mediated viral clearance can initially proceed unfettered and then later be balanced by less inflammatory IgG1 function if the infection persists. In the setting of disrupted Tfh cells, IgG2 antibodies are still produced but at lower levels, perhaps obviating the need for IgG1 to constrain antibody-mediated inflammation.

Allergen-specific IgE is another antibody isotype that is completely dependent on Tfh cell help (41, 42, 44, 132). In contrast to the Tfh-independent pathway of IgG2 production during viral infection, it is unclear why non-Tfh CD4⁺ T cells are not allowed to promote IgE antibodies to allergens. In fact, non-Tfh CD4⁺ T cells, namely Th2 cells, in the lymph node do express *Il4*, but they only make IL-4 protein after reaching their site of effector function in the peripheral tissues (102, 121, 122). Why is there a post-transcriptional checkpoint in place to prevent IL-4 protein production by Th2 cells in the lymph node, thus eliminating the possibility of a Tfh-independent pathway of IgE generation? This is another interesting question that, if answered, may reveal important insight into the rules and restraint of humoral immunity.

Furthermore, while we found that Tfh-independent antibodies to SARS-CoV-2 maintained many of the same qualities as Tfh-dependent antibodies, the Tfh-independent antibody response did demonstrate two important distinctions: 1) inability to undergo classical affinity maturation, and 2) increased diversity of epitope reactivity. The unique ability of Tfh cells to promote affinity maturation and focus the antibody repertoire has important implications for developing vaccines that induce broadly neutralizing antibodies (bnAbs) against pathogens. In the case of HIV

infection, the development of rare bnAbs relies on strong Tfh cell help to support the accumulation of multiple mutations conferring high-affinity, neutralizing capability (135). In contrast, during influenza vaccination, GC inhibition enables the development of cross-reactive antibodies that bind the conserved stem region of the HA protein, thus providing protection against different influenza virus subtypes (90). This suggests that GCs and, by extension, Tfh cells focus the antibody response against the highly variable globular head of the HA protein, to the detriment of developing bnAbs (90). For SARS-CoV-2, we found that Tfh cells focused the antibody response against S2-derived epitopes, which are broadly conserved across betacoronaviruses but tend to be less potent targets for neutralization compared to the RBD (88). However, affinity maturation of anti-SARS-CoV-2 antibodies has been shown to enhance neutralization breadth (136), suggesting that vaccine strategies that induce both Tfh-dependent and -independent antibodies may be most effective for providing protection against the SARS-CoV-2 variants of concern.

In Chapter 3, we found that IL-4 functions as a rheostat for class switching, with multiple transcriptional and post-transcriptional regulatory mechanisms likely working together to fine-tune levels of IL-4 production. While our work demonstrated the importance of IL-4 levels for appropriately inducing antibody isotypes during type 1 and type 2 responses, it is also possible that the role of IL-4 as a rheostat may enable flexibility of the humoral response against pathogens that cannot be sufficiently countered with only type 1 or type 2 immunity. For instance, as a bacterium, *Staphylococcus aureus* is presumably best kept at bay by type 1 immune responses. However, recent work has demonstrated that IgE antibodies and mast cell effector responses directed against *S. aureus* toxins contribute to anti-*S. aureus* immunity (138), providing insight into the nuanced immune responses that may leverage components of both type 1 and type 2 immunity to best protect against diverse pathogens.

Finally, in Chapter 4, we explored the effect of NSAIDs, one of the most commonly used medications, on the immune response to SARS-CoV-2 infection. While NSAID treatment led to an expected reduction in proinflammatory cytokine production, we also observed an unanticipated dampening of neutralizing antibody titers. NSAIDs function by inhibiting the enzymes cyclooxygenase-1 (COX-1) and cyclooxygenase-2 (COX-2), which mediate the production of prostaglandins (PGs) (*139*). Given the diverse functions of PGs throughout the immune system, NSAID treatment may act at multiple steps to impair the development of antibody responses. However, prior literature has shown that COX-2 inhibition in B cells reduces expression of BLIMP-1 and XBP-1, transcription factors required for plasmablast differentiation (*129–131*), indicating that NSAIDs may interfere with antibody production in a B cell-intrinsic manner. Given that people often take NSAIDs after vaccination to mitigate side effects (*140*), it is important to determine whether NSAIDs similarly dampen the antibody response to vaccination.

Together, our findings provide insight into the diverse mechanisms that regulate humoral immunity. By leveraging our understanding of the cells, cytokines, and drugs that affect antibody responses, we may be able to develop more effective strategies to protect us from pathogens.

MATERIALS AND METHODS

Mice

C57BL/6N WT mice were purchased from Charles River Laboratories. *Bcl6^{fl/fl}* [B6.129S(FVB)-*Bcl6^{tm1.1Dent}/J* (25)], *Cd4^{Cre}* [B6.Cg-Tg(Cd4-cre)1Cwi/BfluJ (141)], *Ciita^{-/-}* [B6.129S2-*Ciita^{tm1Ccum}/J* (56)], K18-hACE2 [B6.Cg-Tg(K18-ACE2)2PrImn/J (59)], OT-II [B6.Cg-Tg(TcraTcrb)425Cbn/J (142)], 4get reporter [C.129-*Il4^{tm1Lky}/J* (100)], and RiboTag [B6N.129-*Rpl22^{tm1.1Psam}/J* (104)] mice were purchased from Jackson Laboratory. *Il4^{-/-}* (KN2/KN2) mice were a gift from Markus Mohrs (143). *Bcl6^{fl/fl}* and RiboTag mice were crossed with *Cd4^{Cre}* mice to generate *Bcl6^{fl/fl}Cd4^{Cre}* and RiboTag^{fl/fl}*Cd4^{Cre}* mice. K18-hACE2 mice were crossed with *Bcl6^{fl/fl}Cd4^{Cre}* mice to generate K18-hACE2 *Bcl6^{fl/fl}* and *Bcl6^{fl/fl}Cd4^{Cre}* mice. Mice were bred in-house using mating trios to enable utilization of littermates for experiments. Mice of both sexes between 6 and 10 weeks old were used for this study. Animal use and care was approved in agreement with the Yale Animal Resource Center and Institutional Animal Care and Use Committee according to the standards set by the Animal Welfare Act.

Cell lines

Huh7.5 (CVCL-7927), Vero-E6 (CRL-1586), and 293T (CRL-3216) cells were from ATCC. Cell lines were cultured in Dulbecco's Modified Eagle Medium (DMEM) with 10% heat-inactivated fetal bovine serum (FBS) and 1% Penicillin/Streptomycin. All cell lines tested negative for *Mycoplasma* spp.

AAV-hACE2 transduction

Adeno-associated virus 9 expressing hACE2 from a CMV promoter (AAV-hACE2) was purchased from Vector Biolabs (SKU AAV-200183). Mice were anesthetized by intraperitoneal injection of ketamine (50 mg/kg) and xylazine (5 mg/kg). The rostral neck was shaved and disinfected with povidone-iodine. After a 5-mm incision was made, the salivary glands were retracted and the trachea visualized. Using a 31G insulin syringe, 10^{11} genomic copies of AAV-hACE2 in 50 μ l PBS were injected into the trachea. The incision was closed with 3M Vetbond tissue adhesive, and mice were monitored until full recovery.

Viruses

SARS-CoV-2 P1 stock was generated by inoculating Huh7.5 cells with SARS-CoV-2 isolate USA-WA1/2020 (BEI Resources, NR-52281) at a MOI of 0.01 for three days. The P1 stock was then used to inoculate Vero-E6 cells, and the supernatant was harvested after three days at 50% cytopathic effect. The supernatant was clarified by centrifugation ($450 \times g$ for 5 min), filtered through a 0.45-micron filter, and stored in aliquots at -80°C . For infection of AAV-hACE2 mice, virus was concentrated by mixing one volume of cold 4X PEG-it Virus Precipitation Solution (40% wt/vol PEG-8000 and 1.2 M NaCl) with three volumes of viral supernatant. The mixture was incubated overnight at 4°C and then centrifuged at $1500 \times g$ for 60 min at 4°C . The pelleted virus was resuspended in PBS and stored in aliquots at -80°C . Virus titer was determined by plaque assay using Vero-E6 cells (144).

Influenza virus A/PR/8/34 H1N1 (PR8) expressing the ovalbumin OT-II peptide was grown for 2.5 days at 37°C in the allantoic cavities of 10-day-old specific-pathogen-free fertilized chicken eggs. Harvested virus was centrifuged at $3000 \times g$ for 20 min at 4°C to remove debris and

stored in aliquots at -80°C. Virus titer was determined by plaque assay on Madin-Darby canine kidney cells (145).

For all infections, mice were anesthetized using 30% vol/vol isoflurane diluted in propylene glycol (30% isoflurane) and administered SARS-CoV-2 or PR8 intranasally in 50 µl PBS. AAV-hACE2 *Bcl6^{fl/fl}*, *Bcl6^{fl/fl}Cd4^{Cre}*, and *Ciita^{-/-}* mice were infected with 1.2×10⁶ PFU of SARS-CoV-2. K18-hACE2 *Bcl6^{fl/fl}* and *Bcl6^{fl/fl}Cd4^{Cre}* mice were infected with 20 PFU of SARS-CoV-2. K18-hACE2 mice in serum transfer experiments were infected with 100 PFU of SARS-CoV-2. Mice for influenza virus infection experiments were infected with 70 PFU of PR8. All work with SARS-CoV-2 was performed in a biosafety level 3 (BSL3) facility with approval from the office of Environmental Health and Safety and the Institutional Animal Care and Use Committee at Yale University.

mRNA vaccination

Used vials of Moderna mRNA-1273 and Pfizer-BioNTech BNT162b2 mRNA vaccine were obtained from Yale Health within 6 hours of opening. All vials contained less than one full dose per vial, and no vaccines were diverted for the purpose of this study. Mice were anesthetized using 30% isoflurane and administered 1 µg of either Moderna or Pfizer-BioNTech vaccine intramuscularly in 50 µl PBS. Vaccine was injected into the right hamstring muscles with a 31G insulin syringe.

Intranasal immunizations

For all intranasal immunizations, mice were anesthetized using methoxyflurane and administered LPS/NP₁₉OVA or *Alternaria*/NP₁₉OVA in 50 µl PBS. For LPS/NP₁₉OVA immunization, mice

were administered 2 µg LPS (Sigma) with 25 µg NP₁₉OVA (LGC, Biosearch Technologies) for the primary immunization and 25 µg NP₁₉OVA only for day 8 boost. For *Alternaria*/NP₁₉OVA immunization, mice were administered 10 µg *Alternaria alternata* (Greer, Lot #322776) with 25 µg NP₁₉OVA for the primary immunization and 25 µg NP₁₉OVA only for boosts on days 10 and 18. Serum antibody titers were measured 7-8 days after the final boost.

Enzyme-linked immunosorbent assay (ELISA)

Sera from SARS-CoV-2-infected mice were incubated with a final concentration of 0.5% Triton X-100 and 0.5 mg/ml RNase A for 30 min at room temperature to inactivate potential virus. SARS-CoV-2 stabilized spike glycoprotein (BEI Resources, NR-53257) (146), SARS-CoV-2 spike glycoprotein receptor-binding domain (RBD) (BEI Resources, NR-52946), and influenza virus A/PR/8/34 H1N1 hemagglutinin (HA) protein (Sino Biological, 11684-V08H) were coated at a concentration of 2 µg/ml in carbonate buffer on 96-well MaxiSorp plates (Thermo Fisher) overnight at 4°C. PR8 was inactivated with 1% Triton X-100 for 1 hr at 37°C and coated at a concentration of 20 µg/ml in carbonate buffer. NP₇BSA (LGC, Biosearch Technologies) was coated at a concentration of 20 µg/ml in carbonate buffer.

Plates were blocked with 1% BSA in PBS for 1 hr at room temperature. Serum samples were serially diluted in 1% BSA in PBS and incubated in plates for 2 hr at room temperature or 37°C (for IgE ELISA). Antibody isotypes were detected with anti-mouse IgG-HRP (1013-05), anti-mouse IgG1-HRP (1073-05), anti-mouse IgG2b-HRP (1093-05), anti-mouse IgG2c-HRP (1077-05), anti-mouse IgG3-HRP (1103-05), or anti-mouse IgE-HRP (1110-05) from Southern Biotech or anti-mouse IgM-HRP (550588) from BD Biosciences by incubating for 1 hr at room temperature or 37°C (for IgE ELISA). Plates were developed with TMB Stabilized Chromogen

(Thermo Fisher), stopped with 3 N hydrochloric acid, and read at 450 nm on a microplate reader. Background was determined as twice the average OD value of blank wells. Pooled sera from mice infected with SARS-CoV-2 or PR8 or immunized with *Alternaria*/NP₁₉OVA were used as reference standards to calculate arbitrary units. To measure antibody affinity, serial dilutions of serum samples were plated in duplicate. After incubation of serum samples, a 10-min wash with 5.3 M urea was performed on one set of the samples. Percentage of IgG binding after urea wash was calculated by dividing the area under the curve for each sample with urea wash by that without urea wash.

Enzyme-linked immunosorbent spot (ELISpot)

SARS-CoV-2 stabilized spike glycoprotein (BEI Resources, NR-53257) (146) was coated at a concentration of 2 µg/ml in carbonate buffer on 96-well MultiScreen HTS IP Filter plates (Millipore) overnight at 4°C. Plates were blocked with complete RPMI (10% heat-inactivated FBS, 1% Penicillin/Streptomycin, 2 mM L-glutamine, 1 mM sodium pyruvate, 10 mM HEPES, 55 µM 2-mercaptoethanol) for 4 hr at 37°C. Bone marrow cells were isolated from the left femur + tibia of mice infected with SARS-CoV-2. Red blood cells were lysed with RBC Lysis Buffer (BioLegend) for 2 min. Cells were resuspended in complete RPMI and plated in duplicate at three dilutions (1/5, 1/10, and 1/20 of total bone marrow cells) for 20 hr at 37°C. Plates were washed six times with PBS-T (0.01% Tween-20), followed by incubation with anti-mouse IgG-Alkaline Phosphatase (Southern Biotech, 1030-04) in PBS with 0.5% BSA for 2 hr at room temperature. Plates were then washed three times with PBS-T and three times with PBS. Spots were developed with Vector® Blue Substrate Kit (Vector Laboratories, SK-5300) and imaged with an

ImmunoSpot analyzer (Cellular Technology Limited). Spots were counted manually by a blinded investigator.

Flow cytometry and cell sorting

Mediastinal lymph nodes (medLN) were homogenized with a syringe plunger and filtered through a 70- μ m cell strainer. Red blood cells were lysed with RBC Lysis Buffer (BioLegend) for 1 min. Single-cell preparations were resuspended in PBS with 2% FBS and 1 mM EDTA and pre-incubated with Fc block (2.4G2; BD Biosciences, 553141) for 5 min at room temperature before staining. Cells were stained with the following antibodies or viability dye for 30 min at 4°C: anti-CD4 (RM4-5; BioLegend, 100568), TCR β (H57-597; BioLegend, 109228), PD-1 (RMP1-30; BioLegend, 109110), CD44 (IM7; BioLegend, 103047), PSGL-1 (2PH1; BD Biosciences, 563448), Ly6C (HK1.4; BioLegend, 128005), B220 (RA3-6B2; BioLegend, 103260), Fas (Jo2; BD Biosciences, 563647), GL7 (GL7; BioLegend, 144610), CD138 (281-2; BioLegend, 142514), IgG1 (A85-1; BD Biosciences, 562107), IgG2c (5.7; BD Biosciences, 553504) and LIVE/DEAD™ Fixable Aqua (Thermo Fisher, L34966). CXCR5 (L138D7; BioLegend, 145510) was stained for 25 min at room temperature. Intracellular cytokine staining was performed as previously described (*147*) (PDF included at the end of the Materials and Methods). Samples from SARS-CoV-2-infected mice were fixed with 4% paraformaldehyde for 30 min at room temperature before removal from BSL3 facility. Samples were acquired on a CytoFLEX S (Beckman Coulter) and analyzed using FlowJo software (BD).

For spike-specific B cell sorting, medLN were stained with aforementioned B cell surface markers and viability dye, along with 2 μ g/ml FLAG-tagged SARS-CoV-2 spike protein (GenScript, Z03481) for 30 min at 4°C (*148*). Cells were then stained with both APC- and PE-

conjugated anti-FLAG antibodies (BioLegend, 637309 and 637307) to double-stain spike-specific B cells. Spike-specific plasmablasts (live CD138^{hi}Spike⁺) were sorted into 350 µl Buffer RLT Plus (Qiagen) with 1% β-mercaptoethanol. RLT lysate was vortexed for 1 min, frozen on dry ice, and then stored at -80°C. Cell sorting was performed on a FACS Aria II (BD Biosciences) in the BSL3 facility.

For T cell sorting, Tfh (CD4⁺TCRβ⁺CD44⁺PD-1⁺CXCR5⁺), non-Tfh (CD4⁺TCRβ⁺CD44⁺PD-1⁻CXCR5⁻), and naïve (CD4⁺TCRβ⁺CD44⁻) CD4⁺ T cells were sorted from medLN, spun down, and lysed with Buffer RLT containing 1% β-mercaptoethanol.

BCR library preparation

RNA from spike-specific B cells was isolated using the RNeasy Plus Micro Kit (Qiagen) following manufacturer's instructions. BCR libraries were prepared using the NEBNext® Single Cell/Low Input cDNA Synthesis & Amplification Module (NEB, E6421) and NEBNext® Immune Sequencing Kit (NEB, E6330), with additional reagents provided by NEB to integrate the two kits. 1-20 ng of high-quality RNA with RIN score ≥ 8 was used as input. Libraries were analyzed by Bioanalyzer High Sensitivity DNA assay, pooled in equal amounts with PhiX spike-in, and sequenced on an Illumina MiSeq using the V3 kit, with 325 bp for read 1 and 275 bp for read 2.

BCR repertoire analysis

UMI-barcoded paired-end sequencing reads were processed and analyzed with the Immcantation suite (Docker image v4.3.0). Read preprocessing was performed with the presto-abseq pipeline interface for pRESTO (v0.7.0) (69) with default settings, using mouse constant region primers, isotype-specific internal constant region sequences, and template switch sequences provided by

NEB. The preprocessed reads were aligned to the mouse germline V(D)J genes with the changeo-igblast pipeline interface for Change-O (v1.2.0) (149) and IgBLAST (v1.17.1). Productive sequences aligning to immunoglobulin heavy chains were retained for further analysis. Each sequence was annotated with the corresponding germline V(D)J sequence, masking N/P and D-segment regions. Spectral clustering was performed using SCOPer (v1.2.0) (150) to identify clonally-related sequences, based on the level of junction region homology and the mutation profiles in the V-J segments. Following clonal clustering, consensus germline sequences for each clone were reconstructed as above.

Sequences aligning to constant regions other than IgM, IgA, or IgG were filtered out from further analysis. Relative clonal proportions were calculated by tabulating the number of UMI-barcoded sequences belonging to each clonal family. Clonal proportions were visualized as pie charts, with the top 10 clones each represented individually and all other clones combined into one category. Given the wide variation in the number of clones across samples, in order to characterize the diversity of each BCR repertoire, 100 clones were randomly sampled from each repertoire to calculate Shannon entropy and Simpson's diversity index. This process was repeated 100 times for each sample, ultimately taking the average value across all repeats.

Downstream analysis was performed using Alakazam (v1.2.0) and SHazaM (v1.1.0) (70, 71). Heavy chain V gene usage frequencies were calculated on either the sequence-level or the clone-level. For the sequence-level analysis, the frequency of individual UMI-barcoded BCR sequences aligned to each V gene was calculated. For the clone-level analysis, the frequency of clones aligned to each V gene was determined, taking the consensus V gene assignment across all constituent UMI-barcoded sequences belonging to each clone. V genes that were present at ≥ 0.02 frequency in ≥ 2 repertoires were retained for visualization purposes. The most frequently used

human V genes in SARS-CoV-2 specific antibodies from patients were determined by mining the CoV-AbDab database (94). Out of the mouse V genes that were expressed at ≥ 0.02 clone-level frequency in ≥ 2 repertoires, those that are most similar to the top-ranked human V genes were identified with BLAST. For visualization, alignment of mouse and human V genes was performed using Clustal Omega and visualized using Jalview with the Clustal X color scheme. Lineage trees were constructed with dowser (151), building the maximum parsimony tree for all constituent BCRs in a clone. Branch lengths were scaled by the number of mutations between nodes. To facilitate qualitative comparisons, the pair of *Bcl6*^{fl/fl} and *Bcl6*^{fl/fl}*Cd4*^{Cre} mice with the greatest similarity in the total number of clones and the size of the largest clone were selected for visualization.

Sequences belonging to the same clone were then collapsed, taking the most common nucleotide at each position along the consensus sequence. Clones were annotated for antibody isotypes by majority vote. IgG isotype clones were retained for further analysis of somatic hypermutation. Nucleotide mutation frequencies of each collapsed clone were calculated across the entire heavy chain sequence (with N/P and D-segment regions masked), normalizing by the length of the input sequence. To evaluate somatic hypermutation propensity, the percentage of clones with 1+ or 2+ mutations was determined in each sample and compared across experimental groups. To estimate selection pressure, the collapsed clone sequences from each experimental group (*Bcl6*^{fl/fl} or *Bcl6*^{fl/fl}*Cd4*^{Cre}) were analyzed using BASELINE (70, 71), a method that compares the observed vs expected ratios of replacement to synonymous mutations. Specifically, the observed substitution frequencies in each V segment (excluding CDR3), grouped by CDR or FWR, were compared to the expected frequencies of a reference somatic hypermutation targeting model using the “focused” test statistic. As a reference model for somatic hypermutation in murine heavy

chains is not currently available, the HH_S5F human heavy chain 5-mer targeting model was used for analysis, since it has been previously been shown that human heavy vs light chains have considerably different mutational patterns (152). Larger BASELINE values (corresponding to an increased ratio of replacement mutations) are consistent with positive selection.

Immunofluorescence

MedLN were fixed with 4% paraformaldehyde in PBS for 4 hr at 4°C, followed by cryopreservation with 20% sucrose in PBS for 2 hr at 4°C. MedLN were snap-frozen in optimal cutting temperature compound and stored at -80°C. Tissues were cut into 7- μ m sections and blocked with 10% rat serum in staining solution (PBS with 1% BSA and 0.1% Tween-20) for 1 hr at room temperature. Sections were stained with Fc block, BV421 anti-IgD (11-26c.2a; BioLegend, 405725), AF488 anti-TCR β (H57-597; BioLegend, 109215), biotinylated anti-CD35 (8C12; BD Biosciences, 553816), and AF647 anti-GL7 (GL7; BioLegend, 144606) overnight at 4°C. Secondary staining was performed with AF594 streptavidin (BioLegend, 405240) for 1 hr at room temperature. Images were acquired on a Nikon TiE Spinning Disk Confocal Microscope with the 20 \times objective. Tile scan images were taken with the 20 \times objective with 10% overlap. Image analysis was performed with ImageJ.

Pseudovirus production

Vesicular stomatitis virus (VSV)-based pseudotyped viruses were produced as previously described (144, 153). Vector pCAGGS containing the SARS-CoV-2 Wuhan-Hu-1 spike glycoprotein gene was produced under HHSN272201400008C and obtained through BEI Resources (NR-52310). The sequence of the Wuhan-Hu-1 isolate spike glycoprotein is identical

to that of the USA-WA1/2020 isolate. The spike sequence of the B.1.351 variant of concern was generated by introducing the following mutations: L18F, D80A, D215G, R246I, K417N, E484K, N501Y, and A701V. 293T cells were transfected with either spike plasmid, followed by inoculation with replication-deficient VSV expressing *Renilla* luciferase for 1 hour at 37°C (153). The virus inoculum was then removed, and cells were washed with PBS before adding media with anti-VSV-G (8G5F11) to neutralize residual inoculum. Supernatant containing pseudovirus was collected 24 hours post inoculation, clarified by centrifugation, concentrated with Amicon Ultra Centrifugal Filter Units (100 kDa), and stored in aliquots at -80°C. Pseudoviruses were titrated in Huh7.5 cells to achieve a relative light unit (RLU) signal of 600 times the cell-only control background.

Pseudovirus neutralization assay

Sera for neutralization assay were heat-inactivated for 30 min at 56°C. Sera were tested at a starting dilution of 1:50 for USA-WA1/2020 pseudovirus and 1:12.5 for B.1.351 pseudovirus, with up to eight two-fold serial dilutions. 2×10^4 Huh7.5 cells were plated in each well of a 96-well plate the day before. Serial dilutions of sera were incubated with pseudovirus for 1 hour at 37°C. Growth media was then aspirated from the cells and replaced with 50 µl of serum/virus mixture. Luciferase activity was measured at 24 hours post infection using the *Renilla* Luciferase Assay System (Promega). Each well of cells was lysed with 50 µl Lysis Buffer, and 15 µl cell lysate was then mixed with 15 µl Luciferase Assay reagent. Luminescence was measured on a microplate reader (BioTek Synergy). Half maximal inhibitory concentration (IC₅₀) was calculated as previously described (154). Neutralizing titer (NT₅₀) was defined as the inverse of IC₅₀.

Serum transfer

Sera from SARS-CoV-2-infected AAV-hACE2 *Bcl6^{fl/fl}* or *Bcl6^{fl/fl}Cd4^{Cre}* mice at 14 days post infection (dpi) were pooled, and the resulting levels of spike-specific IgG were measured by ELISA. *Bcl6^{fl/fl}* sera was left undiluted or diluted with naïve sera to match the spike-specific IgG titer of undiluted *Bcl6^{fl/fl}Cd4^{Cre}* sera. Serum samples were then mixed 1:1 with PBS, and 200 µl of serum/PBS mixture was transferred intravascularly by retro-orbital injection into K18-hACE2 mice under anesthesia with 30% isoflurane.

Measurement of lung viral burden

The left lobe of the lung was collected and homogenized in 1 ml DMEM supplemented with 2% heat-inactivated FBS and 1% Penicillin/Streptomycin. Lung homogenates were clarified by centrifugation at $3200 \times g$ for 10 min and stored in aliquots at -80°C . Viral burden was measured in lung homogenates by plaque assay on Vero-E6 cells as previously described (144). In addition, 250 µl of lung homogenate was mixed with 750 µl of TRIzol™ LS Reagent (Invitrogen), and RNA was extracted with the RNeasy Mini Kit (Qiagen) following manufacturer's instructions. cDNA synthesis was performed using random hexamers and ImProm-II™ Reverse Transcriptase (Promega). Quantitative PCR (qPCR) was performed in triplicate for samples and standards using SARS-CoV-2 nucleocapsid (N1)-specific oligonucleotides: Probe: 5' 6FAM-ACCCCGCATTACGTTTGGTGGACC-BHQ1 3'; Forward primer: 5' GACCCCAAATCAGCGAAAT-3'; Reverse primer: 5' TCTGGTTACTGCCAGTTGAATCTG 3'. The limit of detection was 100 SARS-CoV-2 genome copies/µl. Virus copy numbers were quantified using a control plasmid containing the complete nucleocapsid gene from SARS-CoV-2. SARS-CoV-2 genome copies were normalized to *Actb*

using *Actb*-specific oligonucleotides: Probe: 5' 6-JOEN-CACCAGTTC /ZEN/ GCCATGGATGACGA-IABkFQ 3'; Forward primer: 5' GCTCCTTCGTTGCCGGTCCA 3'; Reverse primer: 5' TTGCACATGCCGGAGCCGTT 3'. The limit of detection was 100 *Actb* copies/ μ l. Samples with undetectable SARS-CoV-2 genome copies were set at 0.01 relative to *Actb*.

Serum epitope repertoire analysis (SERA) with SARS-CoV-2 linear epitope library

Serum samples for epitope profiling were inactivated with UV light (250 mJ). The SERA platform for next-generation sequencing (NGS)-based analysis of antibody epitope repertoires has been previously described (155). In brief, *Escherichia coli* were engineered with a surface display vector carrying linear peptides derived from the SARS-CoV-2 proteome (GenBank MN908947.3), designed using oligonucleotides (Twist Bioscience) encoding peptides 12 amino acids in length and tiled with 8 amino acids overlapping. Serum samples (0.5 μ l each) were then diluted 1:200 in a suspension of PBS and bacteria carrying the surface display library (10^9 cells per sample with 3×10^5 fold library representation), and incubated so that antibodies contained in the serum would bind to the peptides on the surface of the bacteria. After incubating with protein A/G magnetic beads and magnetically isolating bacteria that were bound to antibodies contained in the serum, plasmid DNA was purified and PCR amplified for NGS. Unique molecular identifiers (UMIs) were applied during PCR to minimize amplification bias, designed as an 8 base pair semi-random sequence (NNNNNNHH). After preprocessing and read trimming the raw sequencing data, the resulting reads were filtered by utilizing the UMIs to remove PCR duplicates. The filtered UMI data (hereafter referred to as reads) were then aligned to the original reference of linear epitopes derived from SARS-CoV-2 and quantified.

From the raw mapped read counts for each of the 2410 linear epitopes represented in the library, we first calculated the Shannon entropy and Simpson's diversity index of each sample using the *diversity* function in the *diverse* R package. To calculate the "repertoire focusing index", we used the formula: $1-(H'/\log_2(R))$, where H' is Shannon entropy and R is richness (156), defined here as the number of unique epitopes recognized by a given sample (read count > 0). Statistical differences in these various metrics were assessed by two-tailed unpaired Welch's t-test, comparing $Bcl6^{fl/fl}$ and $Bcl6^{fl/fl}Cd4^{Cre}$ conditions.

For further analysis, we normalized the raw count data using the median ratio approach implemented in DESeq2 (72, 73). Differential enrichment analysis was performed using the Wald test in DESeq2, comparing $Bcl6^{fl/fl}$ vs $Bcl6^{fl/fl}Cd4^{Cre}$ samples. Multiple hypothesis correction was performed by the Benjamini-Hochberg method, setting a statistical significance threshold of adjusted $p < 0.05$. After identifying differentially enriched epitopes, the normalized counts were \log_2 transformed (hereafter referred to as \log_2 normalized counts) for downstream visualization and analysis.

For converting the \log_2 normalized counts into relative enrichment scores on a sample-by-sample basis, we scaled the \log_2 normalized counts within each sample to z -scores. In this manner, a z -score of 0 would correspond to epitopes that exhibited an average level of enrichment in a given sample; a positive z -score would indicate that an epitope is relatively enriched in a sample, while a negative z -score would denote a low-scoring epitope. Where applicable, statistical significance was assessed on the within-sample z -scores by two-tailed unpaired Welch's t-test. For visualization purposes, we also calculated the average z -scores in $Bcl6^{fl/fl}$ or $Bcl6^{fl/fl}Cd4^{Cre}$ groups.

Pan-human coronavirus (hCoV) conservation scores were calculated through multiple alignment of several hCoV spike sequences using Clustal Omega (157). The following hCoV spike

sequences were used: HKU1 (UniProt: Q0ZME7), OC43 (P36334), 229E (P15423), NL63 (Q6Q1S2), SARS-CoV (P59594), SARS-CoV-2 (P0DTC2), and MERS-CoV (K9N5Q8). Amino-acid level conservation scores for SARS-CoV-2 spike were extracted through JalView (158).

Retroviral transduction and cell transfer

293T cells were transfected with pMSCV-IL-4-P2A-eGFP or pMSCV-eGFP expression plasmid together with pCL-Eco retroviral packaging plasmid. The media was replaced 18 hours later, and virus was grown for another 32 hours. Supernatant containing retrovirus was then used to transduce OT-II splenocytes pre-activated with anti-CD3 (1 µg/ml) and anti-CD28 (1 µg/ml). Retroviral transduction was performed by spinfection at $1200 \times g$ for 90 min at 37°C in the presence of polybrene (10 µg/ml). CD4⁺ cells were then isolated from transduced splenocytes using the EasySep™ Mouse CD4 Positive Selection Kit II (STEMCELL Technologies), and 15,000 CD4⁺ cells were transferred into each recipient by retroorbital injection.

Mixed bone marrow chimeric mice

Bcl6^{fl/fl}Cd4^{Cre} recipients were irradiated with two doses of 600 rad 3 hours apart. One hour following the second irradiation, the recipients received 1.6×10^6 bone marrow cells from *Bcl6^{fl/fl}Cd4^{Cre}* mice mixed with 4×10^5 bone marrow cells from WT or *Il4^{-/-}* mice by retroorbital injection. Ten days later, mice were administered 150 µg anti-CD4 depleting antibodies (GK1.5; BioXCell, BE0003-1) intravenously. Experiments with bone marrow chimeric mice were performed 14 weeks after bone marrow transplant.

mRNA degradation assay

Sorted Tfh cells were left unstimulated or stimulated for 40 min with phorbol 12-myristate 13-acetate (PMA) (50 ng/ml) and ionomycin (1 µg/ml) in complete IMDM (10% heat-inactivated FBS, 1% Penicillin/Streptomycin, 2 mM L-glutamine, 1 mM sodium pyruvate, 55 µM 2-mercaptoethanol). Actinomycin D (5 µg/ml) was then added to the cells to inhibit new transcription, and cells were collected at 0 and 2 hours after initiation of Actinomycin D for measurement of mRNA degradation.

Quantitative PCR (qPCR)

RNA from sorted Tfh cells was isolated using the RNeasy Micro Kit (Qiagen) following the manufacturer's protocol. cDNA was prepared using the Power SYBR Green Cells-to-CT Kit (Invitrogen) in accordance with the manufacturer's protocol. qPCR was performed using KAPA SYBR Fast Master Mix (Kapa Biosystems) and Low ROX (Kapa Biosystems) and run on the QuantStudio3 (Applied Biosystems). cDNA expression was analyzed by the ΔC_t (change in cycle threshold) method normalized to values of *Hprt* obtained in parallel reactions during each cycle. The following primers were used: *Il4*: forward 5'-AGATCATCGGCATTTTGAACG-3', reverse 5'-TTTGGCACATCCATCTCCG-3'; *Hprt*: forward 5'-CTGGTGAAAAGGACCTCTCG-3', reverse 5'-TGAAGTACTCATTATAGTCAAGGGCA-3'.

Th2 culture

CD4⁺ T cells were isolated from splenocytes using the EasySep™ Mouse CD4⁺ T Cell Isolation Kit (STEMCELL Technologies). Isolated cells were cultured for 3 days with plate-bound anti-CD3 (2 µg/ml), soluble anti-CD28 (2 µg/ml), human IL-2 (12.5 ng/ml), murine IL-4 (25 ng/ml),

anti-IFN- γ (5 $\mu\text{g/ml}$), and anti-IL-12 (2 $\mu\text{g/ml}$) in complete RPMI. Cells were then re-plated on day 3 without anti-CD3 and rested for 2 days prior to analysis.

*I*14 mRNA fluorescence in situ hybridization (FISH)

Cultured Th2 cells or sorted Tfh cells were stimulated with PMA (50 ng/ml) and ionomycin (1 $\mu\text{g/ml}$) in complete IMDM for 40 min. *I*14 mRNA FISH was then performed using the ViewRNA™ Cell Plus Assay Kit (Invitrogen) following manufacturer's guidelines. Images were acquired on a Leica TCS SP5 or Nikon TiE spinning disk confocal microscope.

RiboTag immunoprecipitation

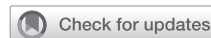
The RiboTag procedure was performed as previously described (104, 159). *In vitro*-cultured RiboTag^{fl/fl}Cd4^{Cre} Th2 cells were stimulated with PMA (50 ng/ml) and ionomycin (1 $\mu\text{g/ml}$) in complete IMDM for 2 hours. Prior to harvesting, cycloheximide (50 $\mu\text{g/ml}$) was added to the cells for 2 min. Cells were then washed with ice-cold PBS containing cycloheximide (50 $\mu\text{g/ml}$) and lysed with freshly prepared Supplemented Homogenization buffer (10% NP-40, 100 mM KCl, 50 mM Tris pH 7.4, 12 mM MgCl₂, 0.1% Tween-20, 100 $\mu\text{g/ml}$ cycloheximide, 1% Protease Inhibitor Cocktail, 1 mg/ml heparin, 1 U/ μl SUPERase•In™ RNase Inhibitor). Lysates were homogenized by passing through a 26-g needle 10 times, incubated on ice for 30 min, and then spun down at 12,000 $\times g$ for 10 min at 4°C to remove debris. Pre-washed Pierce anti-HA magnetic beads were added to the ribosome-containing supernatants and incubated overnight with rotation at 4°C. Beads were washed 4 times with High Salt Buffer (10% NP-40, 300 mM KCl, 50 mM Tris pH 7.4, 12 mM MgCl₂, 0.1% Tween-20, 100 $\mu\text{g/ml}$ cycloheximide), and RNA was eluted from beads with

Buffer RLT Plus containing 1% β -mercaptoethanol and DX Reagent (Qiagen). RNA was then purified using the RNeasy Plus Micro Kit (Qiagen) following manufacturer's instructions.

Statistical analysis

Data analysis was performed using GraphPad Prism 9 unless otherwise indicated. Data were analyzed using one-way ANOVA with Tukey's test or Dunnett's test; Welch's t-test with Bonferroni multiple hypothesis correction; Student's two-tailed, unpaired t-test; Welch's two-tailed, unpaired t-test; two-tailed Mann–Whitney test; or two-tailed Wilcoxon signed-rank test, as indicated. $P < 0.05$ was considered statistically significant.

Flow cytometric identification of T_{FH}13 cells in mouse and human



Jennifer S. Chen, AB,^{a,b*} Jessica D. S. Grassmann, MS,^{c*} Uthaman Gowthaman, PhD,^{a,b*} Sam J. Olyha, MSc,^{a,b} Tregony Simoneau, MD,^{d,e} M. Cecilia Berin, PhD,^f Stephanie C. Eisenbarth, MD, PhD,^{a,b} and Adam Williams, PhD^{c,g}
New Haven and Farmington, Conn, Boston, Mass, and New York, NY

Anaphylaxis is a life-threatening allergic reaction caused by cross-linking of high-affinity IgE antibodies on the surface of mast cells and basophils. Understanding the cellular mechanisms that lead to high-affinity IgE production is required to develop better therapeutics for preventing this severe reaction. A recently discovered population of T follicular helper T_{FH}13 cells regulates the production of high-affinity IgE in mouse models of allergy and can also be found in patients with allergies with IgE antibodies against food or aeroallergens. Here we describe optimized protocols for identifying T_{FH}13 cells in both mice and humans. (J Allergy Clin Immunol 2021;147:470-83.)

Key words: T follicular helper cells, T_{FH}13 cells, intracellular cytokine staining, IL-4, IL-5, IL-13, allergy, IgE

1. INTRODUCTION

Cross-linking of high-affinity IgE on the surface of mast cells and basophils leads to the release of chemical mediators that precipitate anaphylaxis, a potentially life-threatening allergic

From ^athe Department of Laboratory Medicine, and ^bthe Department of Immunobiology, Yale University School of Medicine, New Haven; ^cThe Jackson Laboratory for Genomic Medicine, Farmington; ^dthe Department of Pediatrics, Harvard Medical School, Boston; ^ethe Division of Respiratory Diseases, Boston Children's Hospital; ^fthe Jaffe Food Allergy Institute/Immunology Institute, Icahn School of Medicine at Mount Sinai, New York; and ^gthe Department of Genetics and Genome Sciences, University of Connecticut Health Center, Farmington.

*These authors contributed equally to this work.

This work was supported by National Institutes of Health (NIH) grant T32GM007205 (to J.S.C. and S.J.O.), Gershon/Trudeau Fellowship from Immunobiology at Yale University (to U.G.), Robert E. Leet and Clara Guthrie Patterson Trust Mentored Research Award (to T.S.), NIH U24AI118644 (to M.C.B.), Food Allergy Research and Education (to S.C.E.), Ira and Diana Riklis Family Research Award in Food Allergy (to S.C.E.), NIH R01 AI136942 (to S.C.E.), NIH R01 AI108829 (to S.C.E.), NIH R21 AI135221 (to A.W.), NIH R21 AI133440 (to A.W.), and NIH R01 AI141609 (to A.W.).

Disclosure of potential conflict of interest: M.C. Berin serves on the scientific advisory board of Prota Therapeutics. The rest of the authors declare that they have no relevant conflicts of interest.

Received for publication December 17, 2019; revised March 25, 2020; accepted for publication April 21, 2020.

Available online July 21, 2020.

Corresponding author: Adam Williams, PhD, The Jackson Laboratory for Genomic Medicine, Department of Genetics and Genome Sciences, University of Connecticut Health Center, 10 Discovery Drive, Farmington, CT 06032. E-mail: adam.williams@jax.org.

The CrossMark symbol notifies online readers when updates have been made to the article such as errata or minor corrections

0091-6749/\$36.00

© 2020 American Academy of Allergy, Asthma & Immunology

<https://doi.org/10.1016/j.jaci.2020.04.063>

Abbreviations used

BCL-6: B cell lymphoma 6
cIMDM: Complete Iscove modified Dulbecco media
CPE: Crude peanut extract
CXCR: C-X-C chemokine receptor
FACS: Fluorescence-activated cell sorting
FcR: Fc receptor
FMO: Fluorescence minus one
IMDM: Iscove modified Dulbecco media
LN: Lymph node
medLN: Mediastinal lymph node
NP-OVA: 4-hydroxy-3-nitrophenylacetyl conjugated to ovalbumin
PD-1: Programmed cell death protein 1
PMA: Phorbol 12-myristate 13-acetate
RBC: Red blood cell
RT: Room temperature
TC: Tissue culture
T_{FH}: T follicular helper

reaction.¹ The increasing incidence of anaphylaxis-related hospital admissions signals an urgent need to understand the mechanisms underlying anaphylaxis and to develop better therapeutics to prevent this severe reaction.^{2,3} The induction of IgE relies on T follicular helper (T_{FH}) cells, a specialized subset of CD4⁺ T cells that provides help to B cells in the germinal center, rather than T_H2 cells.⁴⁻⁶ T_{FH} cells instruct the antibody isotypes produced during a given immune response through the cytokines they secrete.⁷ While T_{FH} cell-derived IL-4 is required for IgE production, it is not sufficient to induce the high-affinity, anaphylactic IgE antibodies present in allergic conditions.^{8,9} IL-13 is required as well, which is produced by a recently identified T_{FH}13 cell population.⁹ T_{FH}13 cells regulate the induction of anaphylactic IgE in mouse models of allergy and are also found in patients who are allergic to food or aeroallergens. In addition to expressing the canonical T_{FH} cell markers programmed cell death protein 1 (PD-1), C-X-C chemokine receptor 5 (CXCR5), and transcription factor B cell lymphoma 6 (BCL-6), T_{FH}13 cells are distinguished by their coproduction of the cytokines IL-4, IL-5, and IL-13 and expression of T_H2 transcription factor GATA3.

The identification of T_{FH}13 cells by flow cytometry relies on optimized stimulation and staining conditions. Traditionally, CXCR5 has been difficult to stain on T_{FH} cells after the stimulation required to induce *ex vivo* cytokine production.¹⁰ We addressed this issue by performing CXCR5 staining postfixation with a particular antibody clone. Additionally, the increased concentration of Ca²⁺ in Iscove modified Dulbecco media (IMDM) as

compared to RPMI media has been shown to enhance cytokine production by phorbol 12-myristate 13-acetate (PMA)/ionomycin-restimulated T_H cells.¹¹ While this has previously been shown to enhance production of IL-17A, IFN- γ , TNF- α , IL-10, and IL-22,¹¹ we also found IMDM to boost IL-4 and IL-13 production by T_{FH13} cells, allowing for clearer identification of this rare population. Furthermore, BCL-6 is ideally stained after fixation and permeabilization with the eBioscience FoxP3/Transcription Factor Staining Buffer Set (Thermo Fisher Scientific, Waltham, Mass); however, this method results in poor resolution of cytokine-producing cells.¹² Therefore, our optimized T_{FH13} cell staining protocol employs the BD Biosciences Fixation/Permeabilization Solution Kit (Franklin Lakes, NJ) to preserve cytokine staining, and overnight staining of cytokines and BCL-6 improve detection of these targets without compromising specificity. We also describe protocols for identifying T_{FH13} cells by more physiologic methods of stimulation: anti-CD3/CD28 and antigen stimulation.

Analysis of peripheral blood provides the least invasive method of studying the human immune system. Although T_{FH} cells are predominantly located in the secondary lymphoid organs, circulating T_{FH} cells can be identified in the blood.^{13,14} Circulating T_{FH13} cells can either be identified using nonspecific activation with PMA/ionomycin or specific activation with allergen.^{9,15} While the latter has the advantage of resolving numbers of antigen-specific T_{FH13} cells, this is only possible when the antigen is known. Protocols for both approaches are described below. Given that T_{FH13} cells are a rare population in the blood, we found that isolation of CD4⁺ T cells from PBMCs before PMA/ionomycin activation improved their detection.

2. IDENTIFICATION OF POLYCLONAL AND ANTIGEN-SPECIFIC MURINE T_{FH13} CELLS

Murine T_{FH13} cells can be identified at multiple sites following the administration of a relevant allergen. For instance, intranasal administration of aeroallergen *Alternaria alternata* induces T_{FH13} cells in the mediastinal lymph nodes (medLN), while intragastric administration of food allergen peanut with cholera toxin leads to T_{FH13} cell induction in mesenteric LNs.⁹ Coadministration of allergen and the model antigen 4-hydroxy-3-nitrophenylacetyl conjugated to ovalbumin (NP-OVA) allows for measurement of high-affinity NP-specific IgE antibodies as a complementary readout to T_{FH13} cell induction. Polyclonal T_{FH13} cells can be identified by stimulation with PMA/ionomycin or anti-CD3/CD28, while antigen-specific T_{FH13} cells can be identified by NP-OVA stimulation. When performing antigen stimulation, staining for the activation marker CD154 (CD40 ligand) helps enrich for T_{FH13} cells during analysis.

2A. Materials

Equipment and consumables

- Feeding tubes for oral gavage
- 1-mL syringes
- 5-mL round bottom polystyrene tubes
- 100- μ m nylon mesh filter
- 60-mm \times 15-mm petri dishes

- Frosted microscope slides
- Hemocytometer
- 96-well round bottom tissue culture (TC)-treated plate

Reagents

- Allergens
 - *A alternata* extract (lot 322776; Greer Laboratories, Lenoir, NC)
 - NP-OVA (Biosearch Technologies, LGC Group, Petaluma, Calif)
 - Peanut (Western Mixers Produce & Nuts, Los Angeles, Calif)
 - Cholera toxin (lots 10165A1 and 10167A2; List Biological Laboratories, Omaha, Neb)
- Anesthesia
 - Methoxyflurane
 - 30% isoflurane
- Sodium bicarbonate (AmericanBio, Canton, Mass)
- Milli-Q Ultrapure water (Millipore Sigma, Burlington, Mass)
- PBS (Gibco, Thermo Fisher Scientific)
- Heat-inactivated FBS (Sigma-Aldrich, St Louis, Mo)
- EDTA solution, pH 8.0 (AmericanBio)
- RBC (red blood cell) Lysis Buffer (10 \times) (BioLegend, San Diego, Calif)
- Distilled water
- Trypan blue 0.4% (Gibco)
- IMDM (Gibco)
- Penicillin-streptomycin (Gibco)
- L-glutamine (Gibco)
- Sodium pyruvate (Gibco)
- 2-mercaptoethanol (Gibco)
- PMA (Sigma)
- Ionomycin (Sigma)
- Ultra-LEAF Purified anti-mouse CD3 ϵ Antibody (clone 145-2C11; BioLegend)
- Ultra-LEAF Purified anti-mouse CD28 Antibody (clone 37.51; BioLegend)
- Fixation/Permeabilization Solution Kit with BD GolgiPlug (BD Biosciences)
- Mouse BD Fc Block (BD Biosciences)
- LIVE/DEAD Fixable Aqua Dead Cell Stain (Life Technologies, Thermo Fisher Scientific)
- Antibodies (see [Tables I-III](#))

Reagent setup

- 0.2 mol/L sodium bicarbonate: Prepare a solution of 8.4 g sodium bicarbonate in 500 mL Milli-Q Ultrapure water.
- Fluorescence-activated cell sorting (FACS) buffer: Prepare a solution of 2% (vol/vol) FBS and 1 mmol/L EDTA in PBS.
- RBC Lysis Buffer (1 \times): Dilute RBC Lysis Buffer (10 \times) 1:10 in distilled water.
- Complete IMDM (cIMDM): Supplement IMDM with 10% (vol/vol) heat-inactivated FBS, 100 U/mL penicillin-streptomycin, 2 mmol/L L-glutamine, 1 mmol/L sodium pyruvate, and 55 μ mol/L 2-mercaptoethanol.
- BD Perm/Wash buffer (1 \times): Dilute BD Perm/Wash buffer (10 \times) 1:10 in distilled water.

TABLE I. Antibody panel for polyclonal murine T_H13 cells, without IL-5

Step	Antigen (clone)	Fluorophore	Dilution*	Source
Surface	LIVE/DEAD Fixable Aqua Dead Cell Stain	(AmCyan channel)	1:1000 (1:500)	Life Technologies
	PD-1 (RMP1-30)	Alexa Fluor 647	1:200 (1:100)	BioLegend
Postfixation 1°	CD4 (RM4-5)	APC-Fire 750	1:400	BioLegend
	CD44 (IM7)	Brilliant Violet 605	1:600	BioLegend
	TCRβ (H57-597)	PerCP/Cyanine5.5	1:300	BioLegend
	IL-4 (11B11)	PE	1:100	BioLegend
	IL-13 (eBio13A)	PE-Cyanine7	1:100	eBioscience
	BCL-6 (K112-91)	FITC	1:50	BD Biosciences
Post-fixation 2°	CXCR5 (L138D7)	Biotin	1:300	BioLegend
	Streptavidin	BD Horizon BV421	1:400	BD Biosciences

FITC, Fluorescein isothiocyanate; PE, phycoerythrin.

*All dilutions, except those in parentheses, represent final concentrations for staining. In the steps that require serial dilution of the antibodies, the dilutions for preparing the antibody cocktail are listed in parentheses.

2B. Methods

2B.1. Immunization and LN collection (see note 1).

- Immunize mice with allergen (eg, intranasal *A alternata* NP-OVA, intragastric peanut/cholera toxin).⁹
 - Intranasal immunization: For each mouse, prepare 10 μg *A alternata* extract and 25 μg NP-OVA in 50 μL PBS. Anesthetize mice with methoxyflurane using the open-drop method. Once the mice are under anesthesia and their breathing is slow and steady, administer 50 μL of antigen diluted in PBS through the nares using a pipette.
 - Intragastric immunization: For each mouse, prepare 5 mg ground peanut and 10 μg cholera toxin in 200 μL 0.2 mol/L sodium bicarbonate. Anesthetize mice with 30% isoflurane using the open-drop method. Once the mice are under anesthesia, gently gavage 200 μL of antigen diluted in 0.2 mol/L sodium bicarbonate using a feeding tube connected to a 1-mL syringe.
- Seven or 8 days later, harvest draining LNs (eg, medLN for intranasal immunization, mesenteric LN for intragastric immunization). Also harvest a nondraining LN (eg, inguinal LN) as a staining control.

2B.2. Cell preparation.

- For each LN, prepare a 5-mL round bottom polystyrene tube covered with 100-μm nylon mesh filter.
- In a 60-mm × 15-mm petri dish containing 1 mL FACS buffer, grind LN between 2 frosted microscope slides.
- Rinse microscope slides and petri dish with additional 3 mL FACS buffer, and filter cell suspension into polystyrene tube.
- Centrifuge the tubes for 5 minutes at 500g.
- Decant the supernatant. If LN cell preparation contains RBCs, resuspend the pellet in 500 μL 1× RBC lysis buffer. Otherwise, proceed to step 7.
- Incubate the cells in RBC lysis buffer for 1 minute. Neutralize with 2 mL FACS buffer and centrifuge for 5 minutes at 500g.
- Decant the supernatant and resuspend cells in FACS buffer (400 μL for medLN and inguinal LN, 1200 μL for mesenteric LN).

- To count cells, take 10 μL of cells and dilute 1:10 with PBS. Then mix 10 μL of diluted cells with 10 μL of Trypan blue (1:2). Count cells using a hemocytometer and light microscope.
- Adjust the concentration of cells to 16 × 10⁶ cells/mL in FACS buffer.

2B.3. Stimulation (see notes 2 and 3).

- Using 100-μm nylon mesh, filter 250 μL (4 × 10⁶ cells) of each sample into a well of a 96-well round bottom plate. Leave adjacent wells empty to prevent cross-contamination of samples.
- Centrifuge the plate for 3 minutes at 600g. Decant the supernatant.
- Perform one of the following methods of stimulation:
 - PMA/ionomycin
 - Resuspend cells in 90 μL cIMDM containing PMA (50 ng/mL) and ionomycin (1 μg/mL). Incubate the cells at 37°C with 5% CO₂.
 - After 1 hour, add to each well 10 μL cIMDM containing BD GolgiPlug (1:100), to achieve a final concentration of 1:1000 BD GolgiPlug. Mix samples thoroughly and incubate for additional 3 hours (total stimulation time 4 hours).
 - Anti-CD3/CD28
 - Resuspend cells in 90 μL cIMDM containing soluble anti-CD3e (1 μg/mL) and anti-CD28 (2 μg/mL). Incubate the cells at 37°C with 5% CO₂.
 - After 2 hours, add to each well 10 μL cIMDM containing BD GolgiPlug (1:100), to achieve a final concentration of 1:1000 BD GolgiPlug. Mix samples thoroughly and incubate for additional 4 hours (total stimulation time 6 hours).
- Antigen
 - Resuspend cells in 90 μL cIMDM containing antigen (20 μg/mL). Incubate the cells at 37°C with 5% CO₂.
 - After 2 hours, add to each well 10 μL cIMDM containing BD GolgiPlug (1:100), to achieve a final concentration of 1:1000 BD GolgiPlug. Mix samples thoroughly and incubate for additional 10 hours (total stimulation time 12 hours).

TABLE II. Antibody panel for polyclonal murine T_H13 cells, with IL-5

Step	Antigen (clone)	Fluorophore	Dilution*	Source
Surface	LIVE/DEAD Fixable Aqua Dead Cell Stain	(AmCyan channel)	1:1000 (1:500)	Life Technologies
	PD-1 (29F.1A12)	APC-Fire 750	1:200 (1:100)	BioLegend
Postfixation 1°	CD4 (RM4-5)	PE/Dazzle 594	1:400	BioLegend
	CD44 (IM7)	Brilliant Violet 605	1:600	BioLegend
	TCRβ (H57-597)	PerCP/Cyanine5.5	1:300	BioLegend
	IL-4 (11B11)	PE	1:100	BioLegend
	IL-5 (TRFK5)	APC	1:150	BioLegend
	IL-13 (eBio13A)	PE-Cyanine7	1:100	eBioscience
	BCL-6 (K112-91)	FITC	1:50	BD Biosciences
Postfixation 2°	CXCR5 (L138D7)	Biotin	1:300	BioLegend
	Streptavidin	BD Horizon BV421	1:400	BD Biosciences

APC, Allophycocyanin.

*All dilutions, except those in parentheses, represent final concentrations for staining. In the steps that require serial dilution of the antibodies, the dilutions for preparing the antibody cocktail are listed in parentheses.

TABLE III. Antibody panel for antigen-specific murine T_H13 cells

Step	Antigen (clone)	Fluorophore	Dilution*	Source
Surface	LIVE/DEAD Fixable Aqua Dead Cell Stain	(AmCyan channel)	1:1000 (1:500)	Life Technologies
	PD-1 (RMP1-30)	Alexa Fluor 647	1:200 (1:100)	BioLegend
Postfixation 1°	CD4 (RM4-5)	APC-Fire 750	1:400	BioLegend
	CD44 (IM7)	Brilliant Violet 605	1:600	BioLegend
	TCRβ (H57-597)	PerCP/Cyanine5.5	1:300	BioLegend
	IL-4 (11B11)	Brilliant Violet 421	1:100	BioLegend
	IL-13 (eBio13A)	PE	1:100	eBioscience
	CD154 (MR1)	PE-Cyanine7	1:100	BioLegend
Postfixation 2°	CXCR5 (L138D7)	Biotin	1:300	BioLegend
	Streptavidin	FITC	1:400	BD Biosciences

*All dilutions, except those in parentheses, represent final concentrations for staining. In the steps that require serial dilution of the antibodies, the dilutions for preparing the antibody cocktail are listed in parentheses.

4. Wash cells by adding 200 μL cold FACS buffer to each well, then centrifuge for 3 minutes at 600g. Decant supernatant and repeat washing step. Decant supernatant.

2B.4. Surface staining.

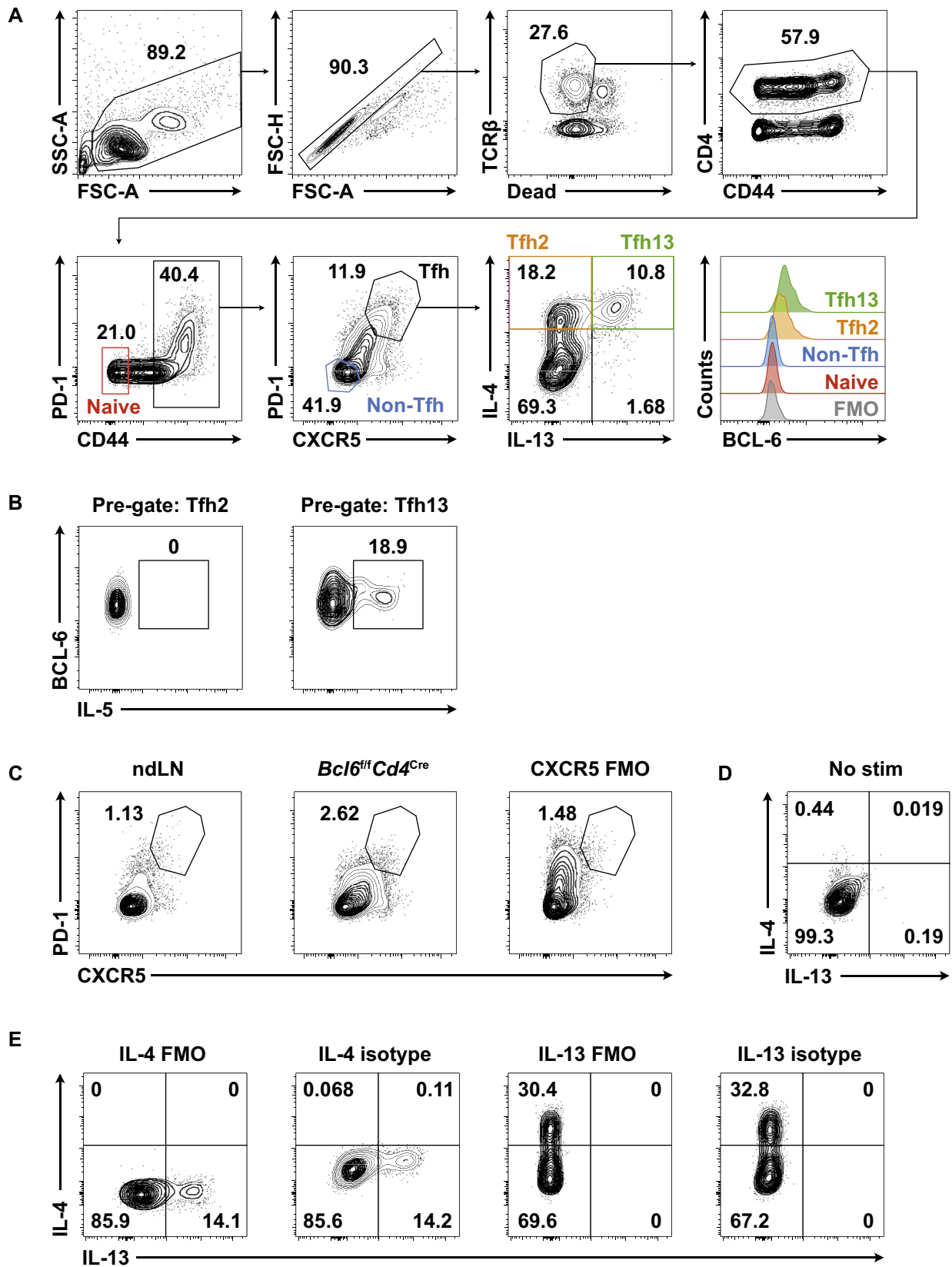
1. Resuspend cells in 25 μL diluted Fc block (1:200 in cold FACS buffer). Incubate for 5 minutes at 4°C.
2. Dilute the surface antibodies in 25 μL cold FACS buffer/well at the concentration listed in [Table I](#) or [II](#) (for PMA/ionomycin– or anti-CD3/CD8–stimulated cells) or [Table III](#) (for antigen-stimulated cells).
3. Add 25 μL diluted surface antibodies mix to each well on top of the existing 25 μL diluted Fc block. Incubate for 25 minutes at 4°C in the dark.
4. Wash cells with 200 μL cold FACS buffer and centrifuge for 3 minutes at 600g. Decant supernatant and repeat washing step. Decant supernatant.

2B.5. Fixation and permeabilization.

1. Resuspend cells in 70 μL cold Fixation/Permeabilization solution. Incubate for 20 minutes at 4°C in the dark.
2. Wash cells with 200 μL cold 1× Perm/Wash buffer and centrifuge for 3 minutes at 900g. Decant supernatant and repeat washing step. Decant supernatant.

2B.6. Postfixation and intracellular staining (see notes 4-8).

1. Resuspend cells in 50 μL cold 1X Perm/Wash buffer containing postfixation primary (1°) antibodies at the concentration listed in [Table I](#) or [II](#) (for PMA/ionomycin– or anti-CD3/CD8–stimulated cells) or [Table III](#) (for antigen-stimulated cells). Incubate overnight (<16 hours) at 4°C in the dark.
2. The next morning, wash cells with 200 μL cold 1× Perm/Wash buffer and centrifuge for 3 minutes at 900g. Decant supernatant and repeat washing step. Decant supernatant.
3. Resuspend cells in 50 μL cold 1× Perm/Wash buffer containing streptavidin fluorochrome conjugate (postfixation 2°) at the concentration listed in [Table I](#) or [II](#) (for PMA/ionomycin– or anti-CD3/CD8–stimulated cells) or [Table III](#) (for antigen-stimulated cells). Incubate for 20 minutes on ice in the dark.
4. Wash cells with 200 μL cold 1× Perm/Wash buffer and centrifuge for 3 minutes at 900g. Decant supernatant and repeat washing step with 200 μL cold FACS buffer. Decant supernatant.
5. Resuspend samples in 200 μL cold FACS buffer. Keep on ice in the dark prior to flow cytometric analysis. Perform flow cytometric analysis within 2 hours.
6. Gating strategy is shown in [Figs 1, A and B](#), and [2](#).



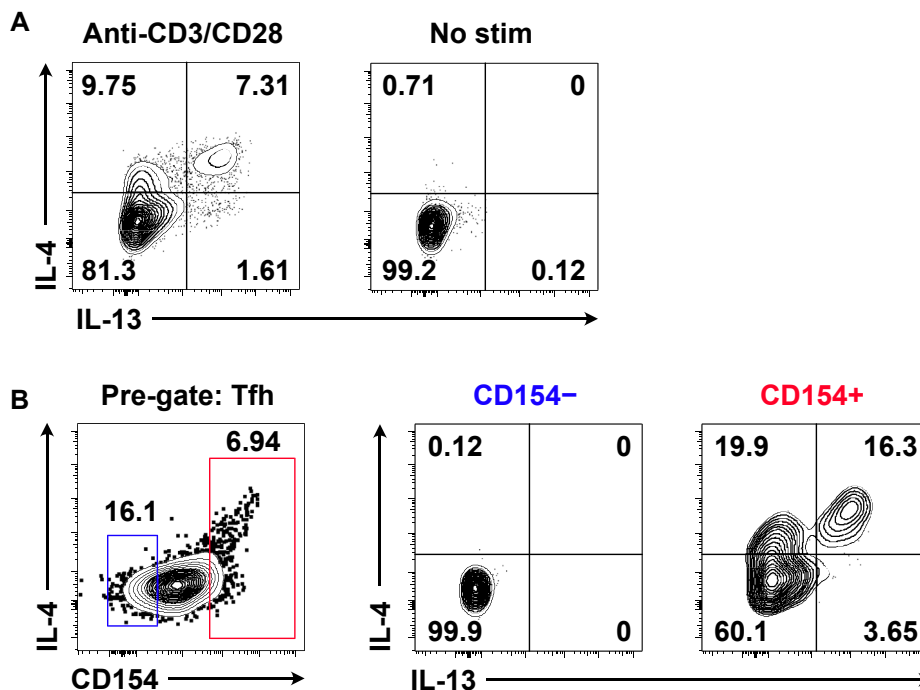


FIG 2. Identification of polyclonal murine $T_{FH}13$ cells by anti-CD3/CD28 stimulation and antigen-specific $T_{FH}13$ cells by NP-OVA stimulation. Day 7 medLN from intranasal immunization with *A alternata* and NP-OVA following (A) anti-CD3/CD28 or (B) NP-OVA stimulation. A, IL-4 and IL-13 intracellular staining in anti-CD3/CD28-stimulated or nonstimulated cells. Pregated on T_{FH} cells. B, IL-4 and IL-13 intracellular staining in CD154⁻ versus CD154⁺ NP-OVA-stimulated cells. Pregated on T_{FH} cells. CD154 helps enrich for antigen-specific $T_{FH}13$ cells during analysis. Samples were acquired on a CytoFLEX (Beckman Coulter, Pasadena, Calif).

2C. Notes

1. Readers should use a method of anesthesia that is approved by their local Institutional Animal Care and Use Committee. An alternative to using the open-drop method is to use a precision vaporizer.
2. Though the current protocol only describes cytokine staining for IL-4, IL-5, and IL-13, these stimulation conditions are also compatible with staining for other T_{FH} cell cytokines, such as IL-21, IL-17A, and IFN- γ .
3. Stimulation in IMDM rather than RPMI media improves detection of IL-4 and IL-13, allowing for enhanced identification of $T_{FH}13$ cells (Fig 3).
4. Note the particular antibody clone used for CXCR5 staining (L138D7) during this step. While clone 2G8 is more frequently used in the literature for CXCR5 staining in unstimulated cells, resolution is poor with stimulated cells.
5. The recommended clone for CD4 staining postfixation is RM4-5. The other commonly used clone GK1.5 does not stain well after fixing cells. If using GK1.5, then include it in the surface staining panel.
6. An ideal cytokine staining control is from a parallel sample (ie, treated in an identical manner) but genetically deficient

- in a particular cytokine (ie, from an IL-13 knockout mouse). However, this is often not readily available, and so acceptable alternative controls for $T_{FH}13$ staining include cells from a nonimmunized/nondraining LN or cells from an immunized T_{FH} cell-deficient mouse line (eg, *Cd4^{Cre}Bcl6^{fl/fl}*) to help with T_{FH} cell gating (Fig 1, C). Fluorescence minus one (FMO) and isotype control antibody staining as well as unstimulated cells from an immunized LN help with cytokine gating (Fig 1, D and E).
7. Overnight staining of cytokines and BCL-6 improves detection of these targets without compromising specificity (Fig 1, A and E).
8. For secondary staining, do not exceed 20 minutes of staining to prevent overstaining of CXCR5 and loss of resolution. Staining on ice further helps to reduce overstaining.

3. IDENTIFICATION OF POLYCLONAL HUMAN $T_{FH}13$ CELLS

When the inciting allergen is not known, human $T_{FH}13$ cells can be identified using nonspecific activation with PMA/ionomycin. However, these activation conditions result in significant

C, PD-1 and CXCR5 staining in nonimmunized nondraining LN (*ndLN*), immunized T_{FH} cell-deficient medLN (*Bcl6^{fl/fl}Cd4^{Cre}*), and FMO control for CXCR5 in immunized wild-type (*WT*) medLN (CXCR5 FMO). D, IL-4 and IL-13 intracellular staining in immunized WT medLN without stimulation. Pregated on T_{FH} cells (live CD4⁺ TCR β ⁺ CD44⁺ PD-1⁺ CXCR5⁺). E, IL-4 and IL-13 FMO and isotype control staining in immunized WT medLN with stimulation. Pregated on T_{FH} cells. Samples were acquired on a BD LSR II (BD Biosciences). A, Area; FSC, forward scatter; H, height; SSC, side scatter.

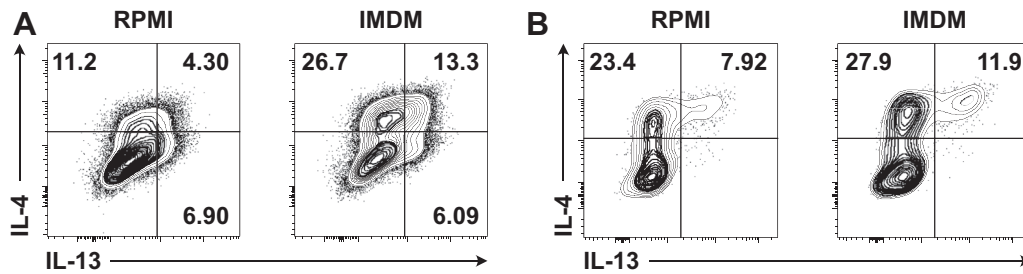


FIG 3. Enhanced cytokine production with stimulation in IMDM compared with RPMI. **A**, T_H2 cells were cultured *in vitro* for 3 days with plate-bound anti-CD3 (2 μ g/mL), soluble anti-CD28 (2 μ g/mL), human IL-2 (12.5 ng/mL), murine IL-4 (25 ng/mL), anti-IFN- γ (5 μ g/mL), and anti-IL-12 (2 μ g/mL). T_H2 cells were replated on day 3 without anti-CD3 and rested for 2 additional days. On day 5 of the culture, T_H2 cells were stimulated with PMA/ionomycin in complete RPMI versus IMDM. IL-4 and IL-13 intracellular staining is shown. Pregated on live CD4 $^+$ cells. **B**, IL-4 and IL-13 intracellular staining in day 7 medLN cells from intranasal immunization with *A alternata* and NP-OVA. Cells were stimulated with PMA/ionomycin in complete RPMI versus IMDM. Pregated on T_H cells (live CD4 $^+$ TCR β^+ CD44 $^+$ PD-1 $^+$ CXCR5 $^+$). Samples were acquired on a BD LSR II (BD Biosciences).

downregulation of surface CD4, making it difficult to identify CD4 $^+$ T cells within a bulk PBMC population. To overcome this limitation, CD4 $^+$ T cells are first purified by negative selection using magnetic bead isolation. In contrast to antigen-specific activation, PMA/ionomycin activation can be performed on previously frozen PBMCs, allowing samples to be banked and later processed together to minimize batch effects.

3A. Materials

Equipment and consumables

- Acid Citrate Dextrose Solution A Whole Blood Tubes (#364606; BD Biosciences)
- 15- and 50-mL conical tubes
- Hemocytometer
- EasySep Magnet (Stemcell Technologies, Vancouver, British Columbia, Canada)
- 5-mL polystyrene tubes (12 \times 75 mm)
- 24- or 12-well TC-treated plate
- 96-well V bottom plate
- Mr. Frosty Freezing Container (Thermo Fisher Scientific)
- PolarSafe Cryogenic Storage Vials, 1 mL (Argos Technologies, Cole-Parmer North America, Vernon Hills, Ill)

Reagents

- PBS (1 \times) (Gibco)
- IMDM (Gibco)
- Penicillin-streptomycin (Gibco)
- L-glutamine (Gibco)
- HEPES (Gibco)
- Minimum Essential Medium non-essential amino acids solution (Gibco)
- Sodium pyruvate (Gibco)
- Heat-inactivated FBS (VWR International, Radnor, Penn)
- EDTA solution, pH 8.0 (Gibco)
- Lymphoprep (Stemcell Technologies)
- RBC Lysis Buffer (10 \times) (Tonbo Biosciences, San Diego, Calif)
- Distilled water
- Trypan blue 0.4% (Gibco)

- Dimethyl sulfoxide (Sigma-Aldrich)
- EasySep Human CD4 $^+$ T Cell Enrichment Kit (Stemcell Technologies)
- PMA (Sigma-Aldrich)
- Ionomycin (Sigma-Aldrich)
- Fixation/Permeabilization Solution Kit with BD GolgiPlug (BD Biosciences)
- FcR (Fc receptor) Blocking Reagent Human (Miltenyi Biotec, Bergisch Gladbach, Germany)
- Ghost Dye Violet 510 (Tonbo Biosciences)
- Antibodies (see Table IV)

Reagent setup

- FACS buffer: Prepare a solution of 2% (vol/vol) FBS and 4 mmol/L EDTA in PBS.
- RBC Lysis Buffer (1 \times): Dilute RBC Lysis Buffer (10 \times) 1:10 in distilled water.
- Freezing medium: Prepare a solution of 10% dimethyl sulfoxide (vol/vol) in FBS. Store at 4 $^{\circ}$ C.
- Complete IMDM: Supplement IMDM with 10% (vol/vol) heat-inactivated FBS, 100 U/mL penicillin-streptomycin, 2 mmol/L L-glutamine, 10 mmol/L HEPES, 0.1 mmol/L nonessential amino acids, and 1 mmol/L sodium pyruvate.
- BD Perm/Wash buffer (1 \times): Dilute BD Perm/Wash buffer (10 \times) 1:10 in distilled water.

3B. Methods

3B.1. PBMC isolation (see note 1).

1. Make sure all the reagents are at room temperature (RT) before starting. Adjust centrifuge to 20 $^{\circ}$ C. If freezing PBMCs at the end of harvest, place the freezing container at 4 $^{\circ}$ C to cool it down.
2. Dilute 10 mL blood 1:3 in PBS + 4 mmol/L EDTA (total volume 30 mL diluted blood).
3. Add 15 mL Lymphoprep to each empty 50-mL tube (use one 50-mL tube for each 10 mL undiluted blood).
4. Mix the diluted blood by pipetting (slow speed). Very slowly, disperse the 30 mL diluted blood on top of the Lymphoprep.

TABLE IV. Antibody panel for polyclonal human T_H13 cells

Step	Antigen (clone)	Fluorophore	Dilution*	Source
Live/Dead	Ghost Dye Violet 510	(AmCyan channel)	1:1000	Tonbo Biosciences
Surface	CD3 (UCHT1)	PerCP/Cyanine5.5	1:23.5 (1:11.75)	
	CD4 (RPA-T4)	APC-Cyanine7	1:33.3 (1:16.65)	
	CD45RA (HI100)	VioletFluor 450	1:36.3 (1:18.15)	
Postfixation	CXCR5 (RF8B2)	BD Horizon BB515	1:20 (1:10)	BD Biosciences
	IL-4 (MP4-25D2)	PE-Cyanine7	1:20	BioLegend
	IL-13 (JES10-5A2)	APC	1:20	
	IFN- γ (4S.B3)	Alexa Fluor 700	1:50	

*All dilutions, except those in parentheses, represent final concentrations for staining. In the steps that require serial dilution of the antibodies, the dilutions for preparing the antibody cocktail are listed in parentheses.

- Centrifuge at 850g for 25 minutes at RT with slow brake. Keep the brakes on in all the remaining centrifugation steps.
- Aspirate 15 mL of supernatant to remove platelets.
- Harvest the PBMCs (white layer between the plasma and the RBCs) using a short 10-mL serological pipette.
- Transfer the PBMCs to a new 50-mL tube and fill up to 50 mL with FACS buffer.
- Centrifuge at 500g for 10 minutes at RT. Aspirate supernatant.
- Resuspend and mix all the pellets from a single donor in 1 mL RBC Lysis Buffer (1 \times), then add an additional 29 mL RBC Lysis Buffer. Mix by inverting the tube 3 times and incubate at RT for 5 minutes.
- Fill up to 50 mL with FACS buffer.
- Centrifuge at 500g for 8 minutes at RT. Aspirate the supernatant.
- Resuspend the pellet in 30 mL FACS buffer to wash.
- Centrifuge at 300g for 8 minutes at RT. Aspirate the supernatant.
- Repeat the washing step. Aspirate the supernatant.
- Resuspend the cells in the same volume of starting material (eg, if starting with 20 mL undiluted blood, resuspend in 20 mL FACS buffer).
- To count cells, mix 10 μ L cells with 10 μ L Trypan blue (1:2). Count cells in duplicate using a hemocytometer and a light microscope. The expected yield is $>1 \times 10^6$ cells/mL.
- Centrifuge at 300g for 8 minutes at RT. Aspirate the supernatant.
- If using samples immediately, proceed to 3B.4. If not, continue to 3B.2.

3B.2. PBMC freezing.

- Resuspend cells at 5 to 10 $\times 10^6$ /mL in freezing medium.
- Aliquot 1 mL cells per cryogenic storage vial, then transfer the vials to the prechilled freezing container.
- Store the freezing container at -80°C overnight.
- The next day, transfer the vials to freezer boxes in liquid nitrogen vapor phase for long-term storage.

3B.3. PBMC defrosting.

- Warm up cIMDM at 37°C .
- Thaw frozen vials of PBMCs in a 37°C water bath. Remove the vials when the freezing medium starts to turn liquid (~ 2 minutes).

- With a disposable Pasteur pipette, add a few drops of warm cIMDM into the vial to thaw it completely.
- Slowly transfer the cell suspension to a 15-mL tube and fill up with warm cIMDM.
- Centrifuge at 300g for 8 minutes at RT.
- Aspirate the supernatant and resuspend the pellet in 5 mL FACS buffer.
- Count cells as described above.
- Centrifuge at 300g for 8 minutes at RT. Aspirate the supernatant.

3B.4. CD4⁺ T cell isolation (see note 2).

- Prepare a suspension of cells at 5×10^7 /mL in FACS buffer and place cells in a 5-mL polystyrene tube.
- Add the EasySep Human CD4⁺ T cell Enrichment Cocktail at 50 μ L/mL to the cell suspension and mix well.
- Incubate for 10 minutes at RT.
- Vortex the EasySep D Magnetic Particles for 30 seconds.
- Add the magnetic particles at 100 μ L/mL to the cell suspension and mix well.
- Incubate for 5 minutes at RT.
- Bring the cell suspension to a total volume of 2.5 mL total with FACS buffer.
- Mix the cells by pipetting up and down 3 times. Place the tube without cap into the EasySep Magnet.
- Incubate for 5 minutes at RT.
- Pick up the magnet with the tube inside and, in a continuous motion, invert to pour the desired fraction into a new 15-mL tube. Leave the magnet inverted for no more than 3 seconds, then return to the upright position.
- Centrifuge at 300g for 8 minutes at RT. Aspirate the supernatant.

3B.5. Cell resting (see note 3).

- Resuspend the cells to 1×10^6 in 950 μ L of cIMDM. Transfer to a well of a 24- or 12-well plate.
- Rest the cells by leaving the plate in the incubator at 37°C overnight.

3B.6. Stimulation (see notes 4-9).

- For each well, prepare 50 μ L cIMDM containing PMA (1 μ g/mL) and ionomycin (20 μ g/mL).
- Add 50 μ L of the stimulation mix to each well on top of the existing 950 μ L cIMDM, to achieve a final concentration of 50 ng/mL PMA and 1 μ g/mL ionomycin. Incubate the cells at 37°C with 5% CO₂.

3. After 1 hour, add to each well 10 μL cIMDM containing BD GolgiPlug (1:10), to achieve a final concentration of 1:1000 BD GolgiPlug.
4. Mix samples thoroughly and incubate the cells at 37°C for an additional 5 hours (total stimulation time 6 hours).

3B.7. Surface staining (see note 10).

1. Transfer the cells to 1.5-mL tubes.
2. Centrifuge at 300g for 8 minutes at RT. Aspirate the supernatant.
3. Resuspend the cells in 150 μL PBS and transfer to a 96-well V bottom plate.
4. Centrifuge at 850g for 4 minutes at RT. Decant the supernatant.
5. Add 100 μL diluted Ghost Dye Violet 510 (1:1000 in PBS) to each well. Incubate for 10 minutes at RT in the dark.
6. Add 50 μL FACS buffer to each well.
7. Centrifuge at 850g for 4 minutes at RT. Decant the supernatant.
8. Resuspend the cells in 100 μL FACS buffer to wash.
9. Centrifuge at 850g for 4 minutes at RT. Decant the supernatant.
10. Add 25 μL diluted FcR block (1:5 in FACS buffer) to each well.
11. Incubate for 5 minutes at RT in the dark.
12. Dilute the surface antibodies in 25 μL FACS buffer/well at the concentration listed in Table IV.
13. Add 25 μL diluted surface antibodies mix to each well on top of the existing 25 μL diluted FcR block.
14. Incubate for 15 minutes at RT in the dark.
15. Add 100 μL FACS buffer to each well.
16. Centrifuge at 850g for 4 minutes at RT. Decant the supernatant and repeat washing step. Decant the supernatant.

3B.8. Fixation and permeabilization.

1. Resuspend the cells in 100 μL Fixation/Permeabilization solution. Incubate for 20 minutes at 4°C in the dark.
2. Centrifuge at 850g for 4 minutes at RT. Decant the supernatant.
3. Resuspend the cells in 100 μL 1 \times Perm/Wash buffer to wash.
4. Centrifuge at 850g for 4 minutes at RT. Decant the supernatant and repeat washing step. Decant the supernatant.
5. Resuspend the cells in 100 μL 1 \times Perm/Wash buffer. Incubate overnight at 4°C in the dark.

3B.9. Postfixation and intracellular staining (note 11).

1. Centrifuge at 850g for 4 minutes at RT. Decant the supernatant.
2. Resuspend cells in 50 μL 1 \times Perm/Wash buffer containing postfixation antibodies at the concentration listed in Table IV.
3. Incubate for 30 minutes at 4°C in the dark.
4. Add 100 μL 1 \times Perm/Wash buffer to each well.
5. Centrifuge at 850g for 4 minutes at RT. Decant the supernatant.

6. Resuspend the cells in 100 μL 1 \times Perm/Wash buffer to wash.
7. Centrifuge at 850g for 4 minutes at RT. Decant the supernatant.
8. Repeat washing step. Decant the supernatant.
9. Resuspend the cells in 150 μL FACS buffer. Keep on ice in the dark prior to flow cytometric analysis. Perform flow cytometric analysis within 2 hours.
10. Gating strategy is shown in Fig 4, A.

3C. Notes

1. PBMC isolation can also be performed using Ficoll-Paque PLUS (GE Healthcare, Princeton, NJ). Instead of Trypan blue, Türk solution (Ricca Chemical, Arlington, Tex) can be used to count cells.
2. Isolation of CD4⁺ T cells improves the ease of detecting T_{FH}13 cells.
3. Resting the cells overnight before activation increases the number of cytokine-positive cells.
4. FMO and isotype control antibody staining as well as unstimulated cells can be used to help with gating (Fig 4, B and C).
5. We have found that GolgiPlug gives better cytokine staining than GolgiStop.
6. PD-1 can be included in the gating strategy; however, compared with T_{FH} cells in lymphoid tissues, blood-circulating T_{FH} cells express lower levels of PD-1, so this marker can be difficult to stain.
7. After PMA/ionomycin stimulation, CD4 is downregulated.
8. Stimulation for 6 hours promotes more cytokine-positive cells than 12 hours of stimulation does, due to significant cell death with prolonged stimulation.
9. Stimulation with PMA/ionomycin induces increased cytokine-positive cells compared with stimulation with anti-CD3/CD28 beads.
10. Staining the surface markers CD3, CD4, and CXCR5 before permeabilization improves their detection.
11. IFN- γ can be used as a control marker for the stimulation. T_{FH}13 cells do not produce IFN- γ (Fig 4, D).

4. IDENTIFICATION OF PEANUT-SPECIFIC HUMAN T_{FH}13 CELLS

When the inciting allergen is known, it is preferable to identify human T_{FH}13 cells by activating samples with antigen. In this system, antigen-specific cells can be identified by the upregulation of the activation marker CD154 (CD40L). For optimal staining, this protocol should be performed on freshly isolated PBMCs.

4A. Materials

Equipment and consumables

- Sodium heparin tubes for blood collection (#367874; BD Biosciences)
- Food-grade coffee grinder
- Glass funnel

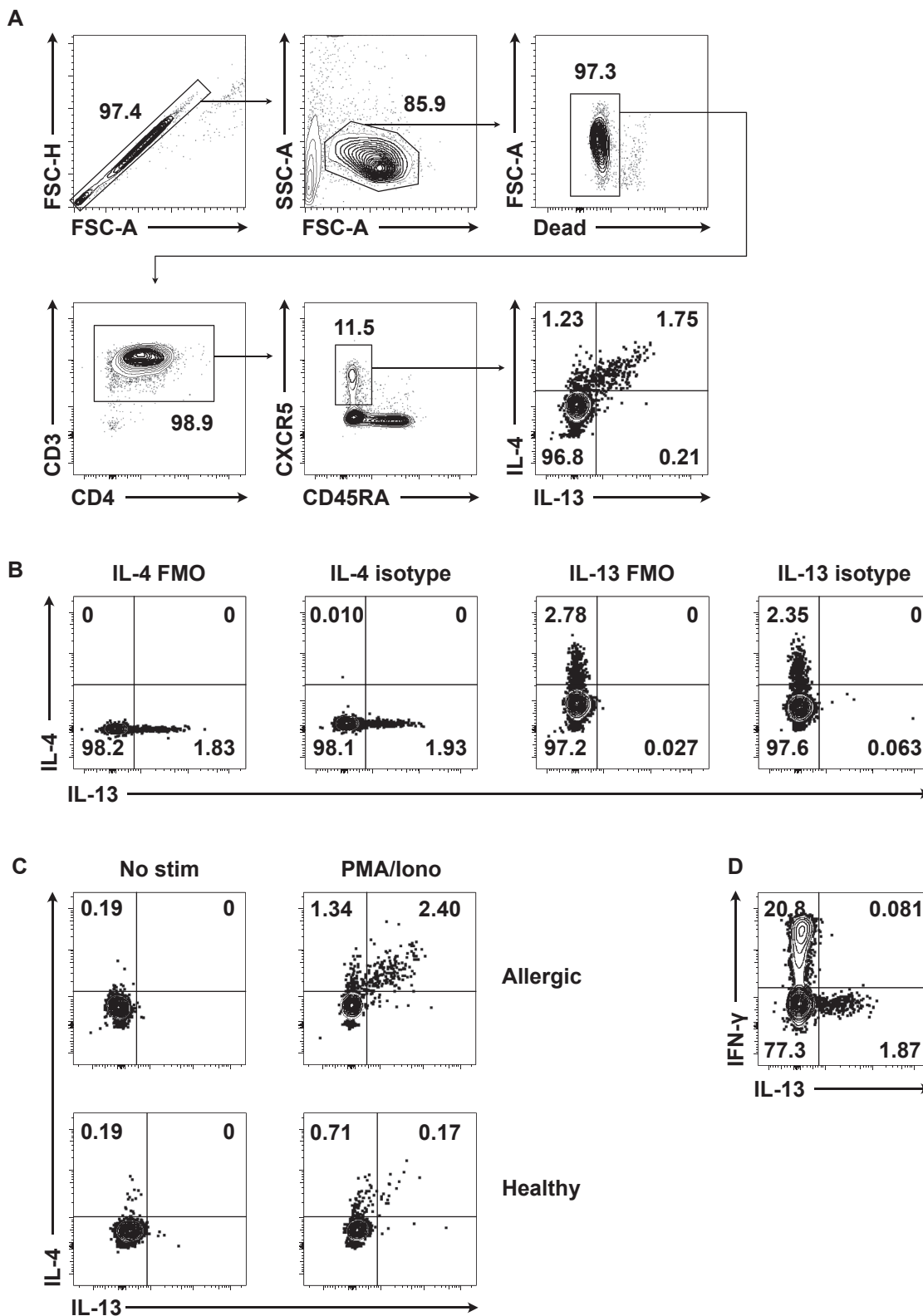


FIG 4. Identification of polyclonal human T_{FH13} cells. **A**, Gating strategy for polyclonal human T_{FH13} cells from an aeroallergen-sensitized patient after PMA/ionomycin stimulation. **B**, IL-4 and IL-13 FMO and isotype control staining in cells from a patient with allergies with stimulation. Pregated on circulating T_{FH} cells (live $CD4^+ CD3^+ CD45RA^- CXCR5^+$). **C**, IL-4 and IL-13 intracellular staining in a patient with allergies and a healthy control following no stimulation or PMA/ionomycin stimulation. Pregated on circulating T_{FH} cells. **D**, IFN- γ and IL-13 intracellular staining in a patient with allergies following PMA/ionomycin stimulation. Pregated on circulating T_{FH} cells. Samples were acquired on a BD FACSymphony A5 (BD Biosciences).

TABLE V. Antibody panel for peanut-specific human T_H13 cells

Step	Antigen (clone)	Fluorophore	Dilution*	Source
Live/dead	LIVE/DEAD Fixable Aqua Dead Cell Stain	(AmCyan channel)	1:1000	Life Technologies
Surface	CD3 (SK7)	APC-eFluor 780	1:100 (1:50)	eBioscience
	CD4 (OKT4)	Brilliant Violet 605	1:100 (1:50)	BioLegend
	CXCR5 (RF8B2)	Alexa Fluor 488	1:40 (1:20)	BD Biosciences
Postfixation	CD154 (24-31)	PE	1:209 (1:9)	eBioscience
	IL-4 (MP4-25D2)	Alexa Fluor 647	1:104.5 (1:4.5)	BioLegend
	IL-13 (JES10-5A2)	BD Horizon V450	1:104.5 (1:4.5)	BD Biosciences

*All dilutions, except those in parentheses, represent final concentrations for staining. In the steps that require serial dilution of the antibodies, the dilutions for preparing the antibody cocktail are listed in parentheses.

- Glass beaker
- Grade 1 filter paper (Whatman, GE Healthcare, Buckinghamshire, UK)
- Magnetic stir bar
- Magnetic stirrer
- Sorvall centrifuge tubes
- 15- and 50-mL tubes
- Kimwipes (Kimberly-Clark Professional, Roswell, Ga)
- Hemocytometer
- 24-well TC-treated plate
- 4.5-mL Sarstedt polystyrene tubes
- 5-mL polystyrene tubes

Reagents

- Peanut (food-grade, roasted in shell)
- Acetone (Sigma-Aldrich)
- cOmplete Protease Inhibitor Cocktail (Roche, Merck, Darmstadt, Germany)
- PBS (1×)
- Detoxi-Gel Endotoxin Removing Gel (Thermo Fisher Scientific)
- LAL (limulus amoebocyte lysate) Chromogenic Endotoxin Quantitation Kit (Thermo Fisher Scientific)
- Pierce Coomassie (Bradford) Protein Assay Kit (Thermo Fisher Scientific)
- AIM V Medium (Gibco)
- Heat-inactivated FBS (ATCC, Manassas, Va)
- BD GolgiPlug (BD Biosciences)
- 4% paraformaldehyde (Electron Microscopy Services, Hatfield, Penn)
- Permeabilization Buffer (10×) (eBioscience, Thermo Fisher Scientific)
- Distilled water
- BSA (Sigma-Aldrich)
- EDTA
- FcR Blocking Reagent Human (Miltenyi Biotec)
- LIVE/DEAD Fixable Aqua Dead Cell Stain (Life Technologies)
- Antibodies (see Table V)

Reagent setup

- Complete AIM V media: Supplement AIM V medium with 2.5% (vol/vol) autologous plasma.
- FACS buffer: Prepare a solution of 1% BSA and 2 mmol/L EDTA in PBS.
- Permeabilization Buffer (1×): Dilute Permeabilization Buffer (10×) 1:10 in distilled water.

4B. Methods

4B.1. CPE preparation (see note 1).

1. Shell approximately 70 g peanut. Grind to a paste using food-grade coffee grinder.
2. Dissolve the paste with 200 mL cold acetone and mix well.
3. In a chemical hood, set up 2 funnels each with 2 layers of grade 1 filter paper.
4. Pour the peanut paste/acetone mix into the funnels. Run an additional ~1.4 L (20× the volume of peanut used) cold acetone through the funnels. Discard the flow-through containing peanut fat dissolved in acetone. Dry the remaining peanut paste in the funnels overnight.
5. The next day, unfold the filters and collect the dry peanut powder into a clean, autoclaved beaker. Avoid the peripheral areas of yellow fat. The yield from 70 g shelled peanuts should be ~30 g dry powder.
6. Dissolve 2 protease inhibitor tablets in 100 mL PBS.
7. Slowly add the PBS with protease inhibitor to the peanut powder until the mixture is a viscous solution (not completely liquid). This will take 50 to 70 mL PBS with protease inhibitor given a starting amount of 70 g shelled peanuts.
8. Add a magnetic stir bar into the mixture and place the beaker containing the mixture on a magnetic stirrer at RT on high spin. The mixture should be homogenized in ~2 hours.
9. Centrifuge the mixture in Sorvall tubes (4 tubes for ~100 mL) at 20,000g for 20 minutes at RT. Collect the supernatant.
10. Cover the opening of a 50-mL tube with a Kimwipe. Gently filter the supernatant through the Kimwipe into the tube. This should yield ~40 mL final volume.
11. Determine crude peanut extract (CPE) protein concentration using the Coomassie (Bradford) Protein Assay Kit.
12. Perform serial removals of endotoxin from the filtered supernatant using Detoxi-Gel Endotoxin Removing Gel until the endotoxin contamination in a working concentration is below 0.5 EU/mL (EU = endotoxin units) as measured by the LAL Chromogenic Endotoxin Quantitation Kit.
13. Repeat measurement of CPE protein concentration using the Coomassie (Bradford) Protein Assay Kit, as endotoxin removal may lead to loss of protein.
14. Run SDS-PAGE to verify the presence of major allergens. Major allergens include Ara h 1 (65 kDa), Ara h 2 (17 kDa), and Ara h 3 (14 kDa).¹⁶
15. Aliquot CPE and store at -80°C.

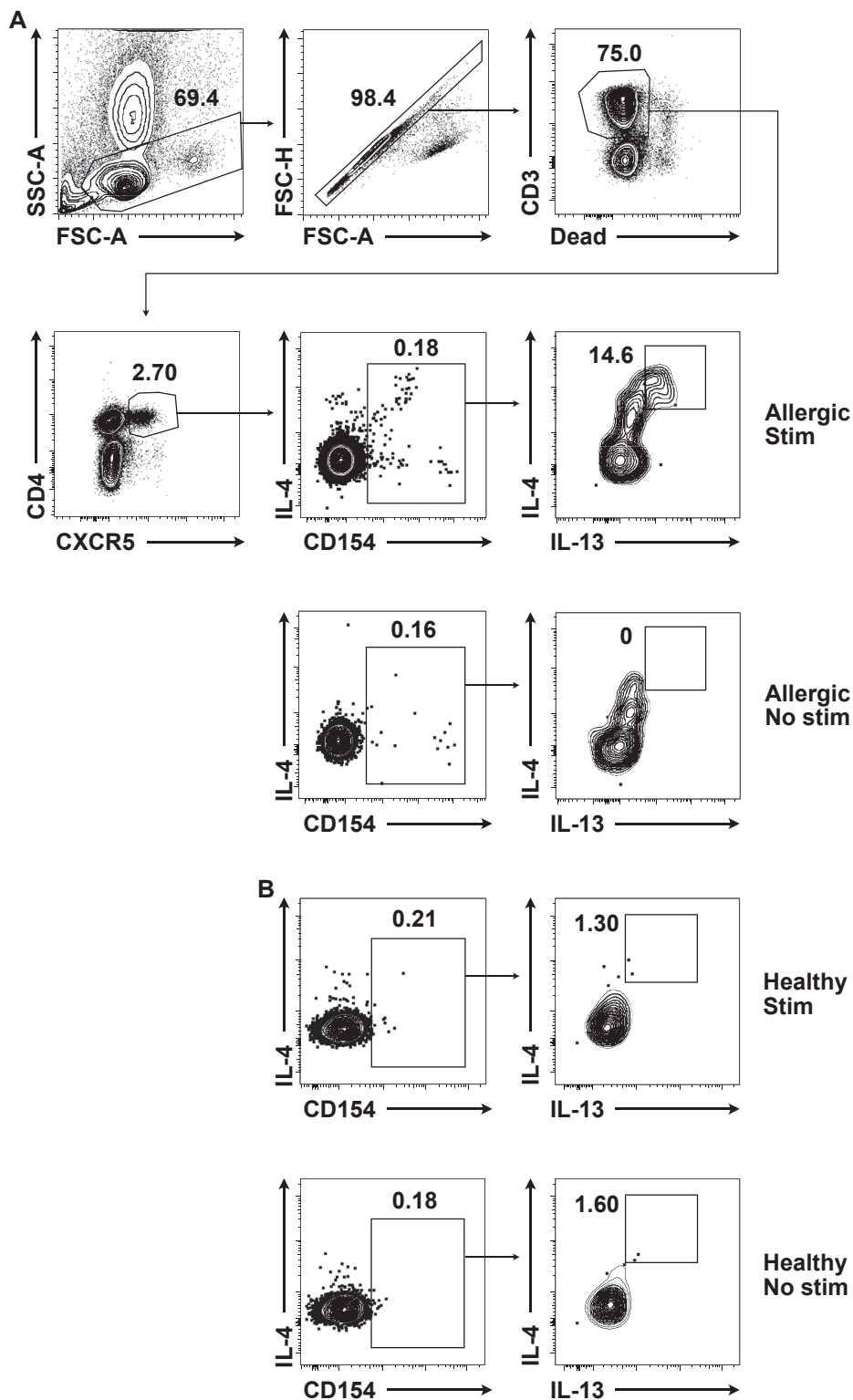


FIG 5. Identification of peanut-specific human T_{H13} cells. **A**, Gating strategy for peanut-specific human T_{H13} cells from a patient with allergies, with peanut stimulation or no stimulation. **B**, IL-4 and IL-13 production by a healthy control, with peanut stimulation or no stimulation. Pregated on circulating T_{H13} cells (live $CD4^+ CD3^+ CXCR5^+$). Samples were acquired on a BD LSRFortessa (BD Biosciences).

4B.2. Plasma isolation.

1. Centrifuge blood tubes at 450g for 15 minutes at 22°C with no acceleration and no brake.
2. In a TC hood, remove plasma layer and transfer to 15-mL conical tube. Use this to prepare complete AIM V media for each donor sample.
3. Transfer remaining blood into a 50-mL conical tube (1 50-mL tube per blood tube).
4. Replace plasma volume removed with equivalent volume of PBS + 2% FBS.

4B.3. PBMC isolation.

1. Perform PBMC isolation as described in section 3B.1, steps 1 to 9.
2. Use 1 mL complete AIM V media to resuspend and mix all the pellets from 1 donor. Transfer the cells to a 15-mL conical tube. Use 10 mL complete AIM V media to rinse the 50-mL tubes for 1 donor and then transfer to the same 15-mL tube, which should ultimately contain cells in 11 mL media.
3. Centrifuge at 400g for 10 minutes at 22°C. Resuspend in 10 mL complete AIM V media.
4. Count cells as described in section 3B.1, step 17. Resuspend cells at 4×10^6 cells/mL in complete AIM V media.
5. Plate 1 mL cells/well in a 24-well plate. Plate 5 wells each for CPE stimulation. Rest cells in incubator overnight.

4B.4. Stimulation (see notes 2-4).

1. Add 100 μ g CPE to each well and place in the incubator for 2 hours.
2. For each well, add 10 μ L BD GolgiPlug diluted 1:10 in complete AIM V media, to achieve a final concentration of 1:1000 BD GolgiPlug. Place in the incubator for an additional 4 hours (total stimulation time 6 hours).

4B.5. Surface staining.

1. Transfer each well of cells into a 4.5-mL conical-bottom Sarstedt polystyrene tube. Rinse each well with 2 mL PBS and transfer to tube, leading to a final volume of 3 mL per tube. Centrifuge at 500g for 5 minutes at 4°C and aspirate supernatant.
2. Resuspend cells in 1 mL LIVE/DEAD Fixable Aqua Dead Cell Stain (diluted 1:1000 in PBS). Incubate for 30 minutes on ice in the dark.
3. Add 2 mL PBS and centrifuge at 500g for 5 minutes at 4°C. Aspirate supernatant.
4. Resuspend cells in 50 μ L diluted FcR block (1:5 in FACS buffer). Incubate for 5 minutes at RT in the dark.
5. Dilute the surface antibodies in 50 μ L FACS buffer/sample at the concentration listed in Table V.
6. Add 50 μ L diluted surface antibodies mix to each tube on top of the existing 50 μ L diluted FcR block. Incubate for 30 minutes on ice in the dark.
7. Add 2 mL PBS and centrifuge at 500g for 5 minutes at 4°C. Aspirate supernatant.

4B.6. Fixation and permeabilization.

1. Resuspend cells in 500 μ L 4% paraformaldehyde. Incubate for 5 minutes at RT in the dark. Vortex briefly at 1, 3, and 5 minutes to mix.

2. Add 1 mL ice-cold FACS buffer and centrifuge at 500g for 5 minutes at 4°C. Aspirate supernatant.
3. Wash with 1 mL 1 \times Permeabilization Buffer and centrifuge at 1400g for 10 minutes at 4°C. Aspirate supernatant.
4. Resuspend cells in 500 μ L 1 \times Permeabilization Buffer. Incubate for 20 minutes at RT in the dark.

4B.7. Postfixation and intracellular staining (see note 5).

1. Add postfixation staining cocktail directly to the tubes containing 500 μ L of 1 \times Permeabilization Buffer (22.5 μ L/sample) (Table V). Incubate for 45 minutes on ice in the dark.
2. Add 2 mL 1 \times Permeabilization Buffer and centrifuge at 1400g for 10 minutes at 4°C. Aspirate supernatant. Repeat washing step and aspirate supernatant.
3. Resuspend cells in 300 to 500 μ L FACS buffer. Keep on ice in the dark prior to flow cytometric analysis. Perform flow cytometric analysis within 1 day. Before running samples, combine duplicate samples into a 5-mL polystyrene tube.
4. Gating strategy is shown in Fig 5, A.

4C. Notes

1. Using this protocol, a large amount of CPE can be prepared. Alternatively, a number of peanut preparations are commercially available. For readers who do not want to perform endotoxin removal and validation, they can use LoTox Peanut Flour Protein with Defined Allergen Content (Indoor Biotechnologies, Charlottesville, Va). Staller-genes Greer (London, UK) sells a peanut preparation, but this formulation still requires endotoxin removal. If possible, a single batch of peanut preparation should be used for a series of experiments.
2. It is important to include FMO and isotype control antibody staining as well as unstimulated cells for setting gates (Fig 5, A and B).
3. We have only performed this assay with peanut; however, other allergens/antigens may also work in this assay.
4. Do not include GolgiPlug on initial activation as it may affect *in vitro* activation of T cells by interfering with antigen processing and presentation.¹⁷
5. Given that circulating antigen-specific T_H13 cells are a relatively rare population, it is important to acquire at least 8×10^6 events if using total PBMCs. Alternatively, fewer events can be acquired if CD4⁺ T cells are enriched prior to staining.

REFERENCES

1. Gowthaman U, Chen JS, Eisenbarth SC. Regulation of IgE by T follicular helper cells. *J Leukoc Biol* 2020;107:409-18.
2. Ma L, Danoff TM, Borish L. Case fatality and population mortality associated with anaphylaxis in the United States. *J Allergy Clin Immunol* 2014;133:1075-83.
3. Mullins RJ, Wainstein BK, Barnes EH, Liew WK, Campbell DE. Increases in anaphylaxis fatalities in Australia from 1997 to 2013. *Clin Exp Allergy* 2016;46:1099-110.
4. Noble A, Zhao J. Follicular helper T cells are responsible for IgE responses to Der p 1 following house dust mite sensitization in mice. *Clin Exp Allergy* 2016;46:1075-82.

5. Kobayashi T, Iijima K, Dent AL, Kita H. Follicular helper T cells mediate IgE antibody response to airborne allergens. *J Allergy Clin Immunol* 2017;139:300-13.e7.
6. Dolence JJ, Kobayashi T, Iijima K, Krempski J, Drake LY, Dent AL, et al. Airway exposure initiates peanut allergy by involving the IL-1 pathway and T follicular helper cells in mice. *J Allergy Clin Immunol* 2018;142:1144-58.e8.
7. Reinhardt RL, Liang H-E, Locksley RM. Cytokine-secreting follicular T cells shape the antibody repertoire. *Nat Immunol* 2009;10:385-93.
8. Meli AP, Fontés G, Leung Soo C, King IL. T follicular helper cell-derived IL-4 is required for IgE production during intestinal helminth infection. *J Immunol* 2017;199:244-52.
9. Gowthaman U, Chen JS, Zhang B, Flynn WF, Lu Y, Song W, et al. Identification of a T follicular helper cell subset that drives anaphylactic IgE. *Science* 2019;365:eaaw6433.
10. Wu H, Xu L-L, Teuscher P, Liu H, Kaplan MH, Dent AL. An inhibitory role for the transcription factor Stat3 in controlling IL-4 and Bcl6 expression in follicular helper T cells. *J Immunol* 2015;195:2080-9.
11. Zimmermann J, Radbruch A, Chang H-D. A Ca²⁺ concentration of 1.5 mM, as present in IMDM but not in RPMI, is critical for maximal response of Th cells to PMA/ionomycin. *Eur J Immunol* 2015;45:1270-3.
12. Jandl C, Loetsch C, King C. Cytokine expression by T follicular helper cells. In: Calado DP, editor. *Germinal centers: methods and protocols*. New York, NY: Springer; 2017. pp. 95-103, Available at: https://doi.org/10.1007/978-1-4939-7095-7_8. Accessed November 21, 2019.
13. Morita R, Schmitt N, Bentebibel S-E, Ranganathan R, Bourdery L, Zurawski G, et al. Human blood CXCR5+CD4+ T cells are counterparts of T follicular cells and contain specific subsets that differentially support antibody secretion. *Immunity* 2011;34:108-21.
14. Byford E, Carr M, Piñon L, Ahearne MJ, Wagner SD. Isolation of CD4+ T-cells and analysis of circulating T-follicular helper (cTfh) cell subsets from peripheral blood using 6-color flow cytometry. *J Vis Exp* 2019;143:e58431.
15. Chiang D, Chen X, Jones SM, Wood RA, Sicherer SH, Burks AW, et al. Single-cell profiling of peanut-responsive T cells in patients with peanut allergy reveals heterogeneous effector TH2 subsets. *J Allergy Clin Immunol* 2018;141:2107-20.
16. Beyer K, Morrow E, Li X-M, Bardina L, Bannon GA, Burks AW, et al. Effects of cooking methods on peanut allergenicity. *J Allergy Clin Immunol* 2001;107:1077-81.
17. Adorini L, Ullrich SJ, Appella E, Fuchs S. Inhibition by brefeldin A of presentation of exogenous protein antigens to MHC class II-restricted T cells. *Nature* 1990;346:63-6.

REFERENCES

1. F. Annunziato, C. Romagnani, S. Romagnani, The 3 major types of innate and adaptive cell-mediated effector immunity. *Journal of Allergy and Clinical Immunology*. **135**, 626–635 (2015).
2. A. Iwasaki, R. Medzhitov, Control of adaptive immunity by the innate immune system. *Nature Immunology*. **16**, 343–353 (2015).
3. L. L. Lu, T. J. Suscovich, S. M. Fortune, G. Alter, Beyond binding: antibody effector functions in infectious diseases. *Nat Rev Immunol*. **18**, 46–61 (2018).
4. J. Charles A Janeway, P. Travers, M. Walport, M. J. Shlomchik, The structure of a typical antibody molecule. *Immunobiology: The Immune System in Health and Disease. 5th edition* (2001) (available at <https://www.ncbi.nlm.nih.gov/books/NBK27144/>).
5. J. Charles A Janeway, P. Travers, M. Walport, M. J. Shlomchik, The generation of diversity in immunoglobulins. *Immunobiology: The Immune System in Health and Disease. 5th edition* (2001) (available at <https://www.ncbi.nlm.nih.gov/books/NBK27140/>).
6. P. Bruhns, F. Jönsson, Mouse and human FcR effector functions. *Immunological Reviews*. **268**, 25–51 (2015).
7. A. Ioan-Facsinay, S. J. de Kimpe, S. M. M. Hellwig, P. L. van Lent, F. M. A. Hofhuis, H. H. van Ojik, C. Sedlik, S. A. da Silveira, J. Gerber, Y. F. de Jong, R. Roozendaal, L. A. Aarden, W. B. van den Berg, T. Saito, D. Mosser, S. Amigorena, S. Izui, G.-J. B. van Ommen, M. van Vugt, J. G. J. van de Winkel, J. S. Verbeek, Fc γ RI (CD64) Contributes Substantially to Severity of Arthritis, Hypersensitivity Responses, and Protection from Bacterial Infection. *Immunity*. **16**, 391–402 (2002).
8. A. Schäfer, F. Muecksch, J. C. C. Lorenzi, S. R. Leist, M. Cipolla, S. Bournazos, F. Schmidt, R. M. Maison, A. Gazumyan, D. R. Martinez, R. S. Baric, D. F. Robbiani, T. Hatzioannou, J. V. Ravetch, P. D. Bieniasz, R. A. Bowen, M. C. Nussenzweig, T. P. Sheahan, Antibody potency, effector function, and combinations in protection and therapy for SARS-CoV-2 infection in vivo. *J Exp Med*. **218** (2021), doi:10.1084/jem.20201993.
9. E. S. Winkler, P. Gilchuk, J. Yu, A. L. Bailey, R. E. Chen, Z. Chong, S. J. Zost, H. Jang, Y. Huang, J. D. Allen, J. B. Case, R. E. Sutton, R. H. Carnahan, T. L. Darling, A. C. M. Boon, M. Mack, R. D. Head, T. M. Ross, J. E. Crowe, M. S. Diamond, Human neutralizing antibodies against SARS-CoV-2 require intact Fc effector functions for optimal therapeutic protection. *Cell*. **184**, 1804-1820.e16 (2021).
10. I. Ullah, J. Prévost, M. S. Ladinsky, H. Stone, M. Lu, S. P. Anand, G. Beaudoin-Bussièrès, K. Symmes, M. Benlarbi, S. Ding, R. Gasser, C. Fink, Y. Chen, A. Tauzin, G. Goyette, C. Bourassa, H. Medjahed, M. Mack, K. Chung, C. B. Wilen, G. A. Dekaban, J. D. Dikeakos, E. A. Bruce, D. E. Kaufmann, L. Stamatatos, A. T. McGuire, J. Richard, M. Pazgier, P. J. Bjorkman, W. Mothes, A. Finzi, P. Kumar, P. D. Uchil, Live imaging of SARS-CoV-2

- infection in mice reveals that neutralizing antibodies require Fc function for optimal efficacy. *Immunity*. **0** (2021), doi:10.1016/j.immuni.2021.08.015.
11. S. J. Galli, M. Tsai, IgE and mast cells in allergic disease. *Nat Med*. **18**, 693–704 (2012).
 12. M. Reth, Matching cellular dimensions with molecular sizes. *Nat Immunol*. **14**, 765–767 (2013).
 13. P. C. Taylor, A. C. Adams, M. M. Hufford, I. de la Torre, K. Winthrop, R. L. Gottlieb, Neutralizing monoclonal antibodies for treatment of COVID-19. *Nat Rev Immunol*. **21**, 382–393 (2021).
 14. C. Mohan, C. Putterman, Genetics and pathogenesis of systemic lupus erythematosus and lupus nephritis. *Nat Rev Nephrol*. **11**, 329–341 (2015).
 15. J. Charles A Janeway, P. Travers, M. Walport, M. J. Shlomchik, B-cell activation by armed helper T cells. *Immunobiology: The Immune System in Health and Disease. 5th edition* (2001) (available at <https://www.ncbi.nlm.nih.gov/books/NBK27142/>).
 16. R. J. Armitage, W. C. Fanslow, L. Strockbine, T. A. Sato, K. N. Clifford, B. M. Macduff, D. M. Anderson, S. D. Gimpel, T. Davis-Smith, C. R. Maliszewski, E. A. Clark, C. A. Smith, K. H. Grabstein, D. Cosman, M. K. Spriggs, Molecular and biological characterization of a murine ligand for CD40. *Nature*. **357**, 80–82 (1992).
 17. S. Kuchen, R. Robbins, G. P. Sims, C. Sheng, T. M. Phillips, P. E. Lipsky, R. Ettinger, Essential Role of IL-21 in B Cell Activation, Expansion, and Plasma Cell Generation during CD4+ T Cell-B Cell Collaboration. *The Journal of Immunology*. **179**, 5886–5896 (2007).
 18. S. Crotty, A brief history of T cell help to B cells. *Nat Rev Immunol*. **15**, 185–189 (2015).
 19. S. Crotty, T Follicular Helper Cell Biology: A Decade of Discovery and Diseases. *Immunity*. **50**, 1132–1148 (2019).
 20. R. J. Johnston, A. C. Poholek, D. DiToro, I. Yusuf, D. Eto, B. Barnett, A. L. Dent, J. Craft, S. Crotty, Bcl6 and Blimp-1 Are Reciprocal and Antagonistic Regulators of T Follicular Helper Cell Differentiation. *Science*. **325**, 1006–1010 (2009).
 21. R. I. Nurieva, Y. Chung, G. J. Martinez, X. O. Yang, S. Tanaka, T. D. Matskevitch, Y.-H. Wang, C. Dong, Bcl6 Mediates the Development of T Follicular Helper Cells. *Science*. **325**, 1001–1005 (2009).
 22. D. Yu, S. Rao, L. M. Tsai, S. K. Lee, Y. He, E. L. Sutcliffe, M. Srivastava, M. Linterman, L. Zheng, N. Simpson, J. I. Ellyard, I. A. Parish, C. S. Ma, Q.-J. Li, C. R. Parish, C. R. Mackay, C. G. Vinuesa, The Transcriptional Repressor Bcl-6 Directs T Follicular Helper Cell Lineage Commitment. *Immunity*. **31**, 457–468 (2009).

23. N. M. Haynes, C. D. C. Allen, R. Lesley, K. M. Ansel, N. Killeen, J. G. Cyster, Role of CXCR5 and CCR7 in Follicular Th Cell Positioning and Appearance of a Programmed Cell Death Gene-1^{High} Germinal Center-Associated Subpopulation. *The Journal of Immunology*. **179**, 5099–5108 (2007).
24. J. Shi, S. Hou, Q. Fang, X. Liu, X. Liu, H. Qi, PD-1 Controls Follicular T Helper Cell Positioning and Function. *Immunity* (2018), doi:10.1016/j.immuni.2018.06.012.
25. K. Hollister, S. Kusam, H. Wu, N. Clegg, A. Mondal, D. V. Sawant, A. L. Dent, Insights into the role of Bcl6 in follicular Th cells using a new conditional mutant mouse model. *J. Immunol.* **191**, 3705–3711 (2013).
26. H. Liang, J. Tang, Z. Liu, Y. Liu, Y. Huang, Y. Xu, P. Hao, Z. Yin, J. Zhong, L. Ye, X. Jin, H. Wang, ZIKV infection induces robust Th1-like Tfh cell and long-term protective antibody responses in immunocompetent mice. *Nature Communications*. **10**, 3859 (2019).
27. J. P. Ray, H. D. Marshall, B. J. Laidlaw, M. M. Staron, S. M. Kaech, J. Craft, Transcription factor STAT3 and type I interferons are corepressive insulators for differentiation of follicular helper and T helper 1 cells. *Immunity*. **40**, 367–377 (2014).
28. X. Liu, X. Chen, B. Zhong, A. Wang, X. Wang, F. Chu, R. I. Nurieva, X. Yan, P. Chen, L. G. van der Flier, H. Nakatsukasa, S. S. Neelapu, W. Chen, H. Clevers, Q. Tian, H. Qi, L. Wei, C. Dong, Transcription factor achaete-scute homologue 2 initiates follicular T-helper-cell development. *Nature*. **507**, 513–518 (2014).
29. L. M. Fahey, E. B. Wilson, H. Elsaesser, C. D. Fistonich, D. B. McGavern, D. G. Brooks, Viral persistence redirects CD4 T cell differentiation toward T follicular helper cells. *Journal of Experimental Medicine*. **208**, 987–999 (2011).
30. U. Greczmiel, N. J. Kräutler, A. Pedrioli, I. Bartsch, P. Agnellini, G. Bedenikovic, J. Harker, K. Richter, A. Oxenius, Sustained T follicular helper cell response is essential for control of chronic viral infection. *Science Immunology*. **2**, eaam8686 (2017).
31. H. Qi, J. L. Cannons, F. Klauschen, P. L. Schwartzberg, R. N. Germain, SAP-controlled T–B cell interactions underlie germinal centre formation. *Nature*. **455**, 764–769 (2008).
32. S. Crotty, E. N. Kersh, J. Cannons, P. L. Schwartzberg, R. Ahmed, SAP is required for generating long-term humoral immunity. *Nature*. **421**, 282–287 (2003).
33. C. Kamperschroer, J. P. Dibble, D. L. Meents, P. L. Schwartzberg, S. L. Swain, SAP Is Required for Th Cell Function and for Immunity to Influenza. *The Journal of Immunology*. **177**, 5317–5327 (2006).
34. S. K. Lee, R. J. Rigby, D. Zotos, L. M. Tsai, S. Kawamoto, J. L. Marshall, R. R. Ramiscal, T. D. Chan, D. Gatto, R. Brink, D. Yu, S. Fagarasan, D. M. Tarlinton, A. F. Cunningham, C. G. Vinuesa, B cell priming for extrafollicular antibody responses requires Bcl-6 expression by T cells. *Journal of Experimental Medicine*. **208**, 1377–1388 (2011).

35. X. Bai, X. Chi, Q. Qiao, S. Xie, S. Wan, L. Ni, P. Wang, W. Jin, C. Dong, T Follicular Helper Cells Regulate Humoral Response for Host Protection against Intestinal *Citrobacter rodentium* Infection. *J.I.* **204**, 2754–2761 (2020).
36. K. Miyauchi, A. Sugimoto-Ishige, Y. Harada, Y. Adachi, Y. Usami, T. Kaji, K. Inoue, H. Hasegawa, T. Watanabe, A. Hijikata, S. Fukuyama, T. Maemura, M. Okada-Hatakeyama, O. Ohara, Y. Kawaoka, Y. Takahashi, T. Takemori, M. Kubo, Protective neutralizing influenza antibody response in the absence of T follicular helper cells. *Nature Immunology.* **17**, 1447–1458 (2016).
37. H. Toyama, S. Okada, M. Hatano, Y. Takahashi, N. Takeda, H. Ichii, T. Takemori, Y. Kuroda, T. Tokuhisa, Memory B Cells without Somatic Hypermutation Are Generated from Bcl6-Deficient B Cells. *Immunity.* **17**, 329–339 (2002).
38. J. S. Weinstein, E. I. Herman, B. Lainez, P. Licona-Limón, E. Esplugues, R. Flavell, J. Craft, TFH cells progressively differentiate to regulate the germinal center response. *Nature Immunology.* **17**, 1197–1205 (2016).
39. A. P. Meli, G. Fontés, C. Leung Soo, I. L. King, T Follicular Helper Cell–Derived IL-4 Is Required for IgE Production during Intestinal Helminth Infection. *The Journal of Immunology.* **199**, 244–252 (2017).
40. A. Noble, J. Zhao, Follicular helper T cells are responsible for IgE responses to Der p 1 following house dust mite sensitization in mice. *Clinical & Experimental Allergy.* **46**, 1075–1082 (2016).
41. T. Kobayashi, K. Iijima, A. L. Dent, H. Kita, Follicular helper T cells mediate IgE antibody response to airborne allergens. *Journal of Allergy and Clinical Immunology.* **139**, 300-313.e7 (2017).
42. J. J. Dolence, T. Kobayashi, K. Iijima, J. Krempski, L. Y. Drake, A. L. Dent, H. Kita, Airway exposure initiates peanut allergy by involving the IL-1 pathway and T follicular helper cells in mice. *J. Allergy Clin. Immunol.* (2017), doi:10.1016/j.jaci.2017.11.020.
43. R. L. Reinhardt, H.-E. Liang, R. M. Locksley, Cytokine-secreting follicular T cells shape the antibody repertoire. *Nature Immunology.* **10**, 385–393 (2009).
44. U. Gowthaman, J. S. Chen, B. Zhang, W. F. Flynn, Y. Lu, W. Song, J. Joseph, J. A. Gertie, L. Xu, M. A. Collet, J. D. S. Grassmann, T. Simoneau, D. Chiang, M. C. Berin, J. E. Craft, J. S. Weinstein, A. Williams, S. C. Eisenbarth, Identification of a T follicular helper cell subset that drives anaphylactic IgE. *Science.* **365**, eaaw6433 (2019).
45. R. A. Elsner, M. J. Shlomchik, Germinal Center and Extrafollicular B Cell Responses in Vaccination, Immunity, and Autoimmunity. *Immunity.* **53**, 1136–1150 (2020).
46. N. Kaneko, H.-H. Kuo, J. Boucau, J. R. Farmer, H. Allard-Chamard, V. S. Mahajan, A. Piechocka-Trocha, K. Lefteri, M. Osborn, J. Bals, Y. C. Bartsch, N. Bonheur, T. M. Caradonna, J. Chevalier, F. Chowdhury, T. J. Diefenbach, K. Einkauf, J. Fallon, J.

- Feldman, K. K. Finn, P. Garcia-Broncano, C. A. Hartana, B. M. Hauser, C. Jiang, P. Kaplonek, M. Karpell, E. C. Koscher, X. Lian, H. Liu, J. Liu, N. L. Ly, A. R. Michell, Y. Rassadkina, K. Seiger, L. Sessa, S. Shin, N. Singh, W. Sun, X. Sun, H. J. Ticheli, M. T. Waring, A. L. Zhu, G. Alter, J. Z. Li, D. Lingwood, A. G. Schmidt, M. Lichterfeld, B. D. Walker, X. G. Yu, R. F. Padera, S. Pillai, Loss of Bcl-6-Expressing T Follicular Helper Cells and Germinal Centers in COVID-19. *Cell*, S0092867420310679 (2020).
47. Y. Duan, M. Xia, L. Ren, Y. Zhang, Q. Ao, S. Xu, D. Kuang, Q. Liu, B. Yan, Y. Zhou, Q. Chu, L. Liu, X.-P. Yang, G. Wang, Deficiency of Tfh Cells and Germinal Center in Deceased COVID-19 Patients. *CURR MED SCI*. **40**, 618–624 (2020).
 48. M. A. Linterman, How T follicular helper cells and the germinal centre response change with age. *Immunology & Cell Biology*. **92**, 72–79 (2014).
 49. M. C. Woodruff, R. P. Ramonell, D. C. Nguyen, K. S. Cashman, A. S. Saini, N. S. Haddad, A. M. Ley, S. Kyu, J. C. Howell, T. Ozturk, S. Lee, N. Suryadevara, J. B. Case, R. Bugrovsky, W. Chen, J. Estrada, A. Morrison-Porter, A. Derrico, F. A. Anam, M. Sharma, H. M. Wu, S. N. Le, S. A. Jenks, C. M. Tipton, B. Staitieh, J. L. Daiss, E. Ghosn, M. S. Diamond, R. H. Carnahan, J. E. Crowe, W. T. Hu, F. E.-H. Lee, I. Sanz, Extrafollicular B cell responses correlate with neutralizing antibodies and morbidity in COVID-19. *Nature Immunology*. **21**, 1506–1516 (2020).
 50. J. A. Kotov, M. K. Jenkins, Cutting Edge: T Cell–Dependent Plasmablasts Form in the Absence of Single Differentiated CD4⁺ T Cell Subsets. *J.I.* **202**, 401–405 (2019).
 51. S. C. Eisenbarth, D. Baumjohann, J. Craft, N. Fazilleau, C. S. Ma, S. G. Tangye, C. G. Vinuesa, M. A. Linterman, CD4⁺ T cells that help B cells – a proposal for uniform nomenclature. *Trends in Immunology*. **42**, 658–669 (2021).
 52. T. Junt, K. Fink, R. Förster, B. Senn, M. Lipp, M. Muramatsu, R. M. Zinkernagel, B. Ludewig, H. Hengartner, CXCR5-Dependent Seeding of Follicular Niches by B and Th Cells Augments Antiviral B Cell Responses. *The Journal of Immunology*. **175**, 7109–7116 (2005).
 53. S.-E. Bentebibel, S. Lopez, G. Obermoser, N. Schmitt, C. Mueller, C. Harrod, E. Flano, A. Mejias, R. A. Albrecht, D. Blankenship, H. Xu, V. Pascual, J. Banchereau, A. Garcia-Sastre, A. K. Palucka, O. Ramilo, H. Ueno, Induction of ICOS⁺CXCR3⁺CXCR5⁺ TH Cells Correlates with Antibody Responses to Influenza Vaccination. *Science Translational Medicine*. **5**, 176ra32-176ra32 (2013).
 54. F. Spensieri, E. Borgogni, L. Zedda, M. Bardelli, F. Buricchi, G. Volpini, E. Fragapane, S. Tavarini, O. Finco, R. Rappuoli, G. Del Giudice, G. Galli, F. Castellino, Human circulating influenza-CD4⁺ ICOS⁺IL-21⁺ T cells expand after vaccination, exert helper function, and predict antibody responses. *Proc Natl Acad Sci U S A*. **110**, 14330–14335 (2013).
 55. R. S. Herati, M. A. Reuter, D. V. Dolfi, K. D. Mansfield, H. Aung, O. Z. Badwan, R. K. Kurupati, S. Kannan, H. Ertl, K. E. Schmader, M. R. Betts, D. H. Canaday, E. J. Wherry,

- Circulating CXCR5⁺ PD-1⁺ Response Predicts Influenza Vaccine Antibody Responses in Young Adults but not Elderly Adults. *J.I.* **193**, 3528–3537 (2014).
56. C.-H. Chang, S. Guerder, S.-C. Hong, W. van Ewijk, R. A. Flavell, Mice Lacking the MHC Class II Transactivator (CIITA) Show Tissue-Specific Impairment of MHC Class II Expression. *Immunity*. **4**, 167–178 (1996).
 57. P. Zhou, X.-L. Yang, X.-G. Wang, B. Hu, L. Zhang, W. Zhang, H.-R. Si, Y. Zhu, B. Li, C.-L. Huang, H.-D. Chen, J. Chen, Y. Luo, H. Guo, R.-D. Jiang, M.-Q. Liu, Y. Chen, X.-R. Shen, X. Wang, X.-S. Zheng, K. Zhao, Q.-J. Chen, F. Deng, L.-L. Liu, B. Yan, F.-X. Zhan, Y.-Y. Wang, G.-F. Xiao, Z.-L. Shi, A pneumonia outbreak associated with a new coronavirus of probable bat origin. *Nature*. **579**, 270–273 (2020).
 58. B. Israelow, E. Song, T. Mao, P. Lu, A. Meir, F. Liu, M. M. Alfajaro, J. Wei, H. Dong, R. J. Homer, A. Ring, C. B. Wilen, A. Iwasaki, Mouse model of SARS-CoV-2 reveals inflammatory role of type I interferon signaling. *J Exp Med*. **217** (2020), doi:10.1084/jem.20201241.
 59. P. B. McCray, L. Pewe, C. Wohlford-Lenane, M. Hickey, L. Manzel, L. Shi, J. Netland, H. P. Jia, C. Halabi, C. D. Sigmund, D. K. Meyerholz, P. Kirby, D. C. Look, S. Perlman, Lethal Infection of K18-hACE2 Mice Infected with Severe Acute Respiratory Syndrome Coronavirus. *Journal of Virology*. **81**, 813–821 (2007).
 60. W. Dejnirattisai, D. Zhou, H. M. Ginn, H. M. E. Duyvesteyn, P. Supasa, J. B. Case, Y. Zhao, T. S. Walter, A. J. Mentzer, C. Liu, B. Wang, G. C. Paesen, J. Slon-Campos, C. López-Camacho, N. M. Kafai, A. L. Bailey, R. E. Chen, B. Ying, C. Thompson, J. Bolton, A. Fyfe, S. Gupta, T. K. Tan, J. Gilbert-Jaramillo, W. James, M. Knight, M. W. Carroll, D. Skelly, C. Dold, Y. Peng, R. Levin, T. Dong, A. J. Pollard, J. C. Knight, P. Klenerman, N. Temperton, D. R. Hall, M. A. Williams, N. G. Paterson, F. K. R. Bertram, C. A. Siebert, D. K. Clare, A. Howe, J. Radecke, Y. Song, A. R. Townsend, K.-Y. A. Huang, E. E. Fry, J. Mongkolsapaya, M. S. Diamond, J. Ren, D. I. Stuart, G. R. Screaton, The antigenic anatomy of SARS-CoV-2 receptor binding domain. *Cell*. **184**, 2183-2200.e22 (2021).
 61. P. J. M. Brouwer, T. G. Caniels, K. van der Straten, J. L. Snitselaar, Y. Aldon, S. Bangaru, J. L. Torres, N. M. A. Okba, M. Claireaux, G. Kerster, A. E. H. Benthage, M. M. van Haaren, D. Guerra, J. A. Burger, E. E. Schermer, K. D. Verheul, N. van der Velde, A. van der Kooi, J. van Schooten, M. J. van Breemen, T. P. L. Bijl, K. Sliepen, A. Aartse, R. Derking, I. Bontjer, N. A. Kootstra, W. J. Wiersinga, G. Vidarsson, B. L. Haagmans, A. B. Ward, G. J. de Bree, R. W. Sanders, M. J. van Gils, Potent neutralizing antibodies from COVID-19 patients define multiple targets of vulnerability. *Science*. **369**, 643–650 (2020).
 62. D. F. Robbiani, C. Gaebler, F. Muecksch, J. C. C. Lorenzi, Z. Wang, A. Cho, M. Agudelo, C. O. Barnes, A. Gazumyan, S. Finkin, T. Hägglöf, T. Y. Oliveira, C. Viant, A. Hurley, H.-H. Hoffmann, K. G. Millard, R. G. Kost, M. Cipolla, K. Gordon, F. Bianchini, S. T. Chen, V. Ramos, R. Patel, J. Dizon, I. Shimeliovich, P. Mendoza, H. Hartwegler, L. Nogueira, M. Pack, J. Horowitz, F. Schmidt, Y. Weisblum, E. Michailidis, A. W.

- Ashbrook, E. Waltari, J. E. Pak, K. E. Huey-Tubman, N. Koranda, P. R. Hoffman, A. P. West, C. M. Rice, T. Hatziioannou, P. J. Bjorkman, P. D. Bieniasz, M. Caskey, M. C. Nussenzweig, Convergent antibody responses to SARS-CoV-2 in convalescent individuals. *Nature*. **584**, 437–442 (2020).
63. M. Yuan, H. Liu, N. C. Wu, C.-C. D. Lee, X. Zhu, F. Zhao, D. Huang, W. Yu, Y. Hua, H. Tien, T. F. Rogers, E. Landais, D. Sok, J. G. Jardine, D. R. Burton, I. A. Wilson, Structural basis of a shared antibody response to SARS-CoV-2. *Science*. **369**, 1119–1123 (2020).
64. L. Wang, T. Zhou, Y. Zhang, E. S. Yang, C. A. Schramm, W. Shi, A. Pegu, O. K. Oloniniyi, A. R. Henry, S. Darko, S. R. Narpala, C. Hatcher, D. R. Martinez, Y. Tsybovsky, E. Phung, O. M. Abiona, A. Antia, E. M. Cale, L. A. Chang, M. Choe, K. S. Corbett, R. L. Davis, A. T. DiPiazza, I. J. Gordon, S. H. Hait, T. Hermanus, P. Kgagudi, F. Laboune, K. Leung, T. Liu, R. D. Mason, A. F. Nazzari, L. Novik, S. O’Connell, S. O’Dell, A. S. Olia, S. D. Schmidt, T. Stephens, C. D. Stringham, C. A. Talana, I.-T. Teng, D. A. Wagner, A. T. Widge, B. Zhang, M. Roederer, J. E. Ledgerwood, T. J. Ruckwardt, M. R. Gaudinski, P. L. Moore, N. A. Doria-Rose, R. S. Baric, B. S. Graham, A. B. McDermott, D. C. Douek, P. D. Kwong, J. R. Mascola, N. J. Sullivan, J. Misasi, Ultrapotent antibodies against diverse and highly transmissible SARS-CoV-2 variants. *Science*. **373**, eabh1766 (2021).
65. J. Feldman, J. Bals, C. G. Altomare, K. St Denis, E. C. Lam, B. M. Hauser, L. Ronsard, M. Sangesland, T. Bracamonte Moreno, V. Okonkwo, N. Hartojo, A. B. Balazs, G. Bajic, D. Lingwood, A. G. Schmidt, Naive human B cells engage the receptor binding domain of SARS-CoV-2, variants of concern, and related sarbecoviruses. *Sci Immunol*, eabl5842 (2021).
66. R. Di Niro, S.-J. Lee, J. A. Vander Heiden, R. A. Elsner, N. Trivedi, J. M. Bannock, N. T. Gupta, S. H. Kleinstein, F. Vigneault, T. J. Gilbert, E. Meffre, S. J. McSorley, M. J. Shlomchik, Salmonella Infection Drives Promiscuous B Cell Activation Followed by Extrafollicular Affinity Maturation. *Immunity*. **43**, 120–131 (2015).
67. N. Trivedi, F. Weisel, S. Smita, S. Joachim, M. Kader, A. Radhakrishnan, C. Clouser, A. M. Rosenfeld, M. Chikina, F. Vigneault, U. Hershberg, N. Ismail, M. J. Shlomchik, Liver Is a Generative Site for the B Cell Response to *Ehrlichia muris*. *Immunity*. **51**, 1088–1101.e5 (2019).
68. J. William, C. Euler, S. Christensen, M. J. Shlomchik, Evolution of Autoantibody Responses via Somatic Hypermutation Outside of Germinal Centers. *Science*. **297**, 2066–2070 (2002).
69. J. A. Vander Heiden, G. Yaari, M. Uduman, J. N. H. Stern, K. C. O’Connor, D. A. Hafler, F. Vigneault, S. H. Kleinstein, pRESTO: a toolkit for processing high-throughput sequencing raw reads of lymphocyte receptor repertoires. *Bioinformatics*. **30**, 1930–1932 (2014).

70. G. Yaari, M. Uduman, S. H. Kleinstejn, Quantifying selection in high-throughput Immunoglobulin sequencing data sets. *Nucleic Acids Res.* **40**, e134 (2012).
71. G. Yaari, J. A. Vander Heiden, M. Uduman, D. Gadala-Maria, N. Gupta, J. N. H. Stern, K. C. O'Connor, D. A. Hafler, U. Laserson, F. Vigneault, S. H. Kleinstejn, Models of somatic hypermutation targeting and substitution based on synonymous mutations from high-throughput immunoglobulin sequencing data. *Front Immunol.* **4**, 358 (2013).
72. S. Anders, W. Huber, Differential expression analysis for sequence count data. *Genome Biology.* **11**, R106 (2010).
73. M. I. Love, W. Huber, S. Anders, Moderated estimation of fold change and dispersion for RNA-seq data with DESeq2. *Genome Biology.* **15**, 550 (2014).
74. M. A. Tortorici, D. Veessler, in *Advances in Virus Research*, F. A. Rey, Ed. (Academic Press, 2019; <https://www.sciencedirect.com/science/article/pii/S0065352719300284>), vol. 105 of *Complementary Strategies to Understand Virus Structure and Function*, pp. 93–116.
75. J. T. Ladner, S. N. Henson, A. S. Boyle, A. L. Engelbrektson, Z. W. Fink, F. Rahee, J. D'ambrozio, K. E. Schaecher, M. Stone, W. Dong, S. Dadwal, J. Yu, M. A. Caligiuri, P. Cieplak, M. Bjørås, M. H. Fenstad, S. A. Nordbø, D. E. Kainov, N. Muranaka, M. S. Chee, S. A. Shiryayev, J. A. Altin, Epitope-resolved profiling of the SARS-CoV-2 antibody response identifies cross-reactivity with endemic human coronaviruses. *CR Med.* **2** (2021), doi:10.1016/j.xcrm.2020.100189.
76. Y. Li, M. Ma, Q. Lei, F. Wang, W. Hong, D. Lai, H. Hou, Z. Xu, B. Zhang, H. Chen, C. Yu, J. Xue, Y. Zheng, X. Wang, H. Jiang, H. Zhang, H. Qi, S. Guo, Y. Zhang, X. Lin, Z. Yao, J. Wu, H. Sheng, Y. Zhang, H. Wei, Z. Sun, X. Fan, S. Tao, Linear epitope landscape of the SARS-CoV-2 Spike protein constructed from 1,051 COVID-19 patients. *Cell Reports.* **34** (2021), doi:10.1016/j.celrep.2021.108915.
77. M. Hoffmann, P. Arora, R. Groß, A. Seidel, B. F. Hörnich, A. S. Hahn, N. Krüger, L. Graichen, H. Hofmann-Winkler, A. Kempf, M. S. Winkler, S. Schulz, H.-M. Jäck, B. Jahrsdörfer, H. Schrezenmeier, M. Müller, A. Kleger, J. Münch, S. Pöhlmann, SARS-CoV-2 variants B.1.351 and P.1 escape from neutralizing antibodies. *Cell.* **184**, 2384-2393.e12 (2021).
78. D. Zhou, W. Dejnirattisai, P. Supasa, C. Liu, A. J. Mentzer, H. M. Ginn, Y. Zhao, H. M. E. Duyvesteyn, A. Tuekprakhon, R. Nutalai, B. Wang, G. C. Paesen, C. Lopez-Camacho, J. Slon-Campos, B. Hallis, N. Coombes, K. Bewley, S. Charlton, T. S. Walter, D. Skelly, S. F. Lumley, C. Dold, R. Levin, T. Dong, A. J. Pollard, J. C. Knight, D. Crook, T. Lambe, E. Clutterbuck, S. Bibi, A. Flaxman, M. Bittaye, S. Belij-Rammerstorfer, S. Gilbert, W. James, M. W. Carroll, P. Klenerman, E. Barnes, S. J. Dunachie, E. E. Fry, J. Mongkolsapaya, J. Ren, D. I. Stuart, G. R. Screaton, Evidence of escape of SARS-CoV-2 variant B.1.351 from natural and vaccine-induced sera. *Cell.* **184**, 2348-2361.e6 (2021).

79. H. D. Marshall, A. Chandele, Y. W. Jung, H. Meng, A. C. Poholek, I. A. Parish, R. Rutishauser, W. Cui, S. H. Kleinstein, J. Craft, S. M. Kaech, Differential Expression of Ly6C and T-bet Distinguish Effector and Memory Th1 CD4+ Cell Properties during Viral Infection. *Immunity*. **35**, 633–646 (2011).
80. H. D. Marshall, J. P. Ray, B. J. Laidlaw, N. Zhang, D. Gawande, M. M. Staron, J. Craft, S. M. Kaech, The transforming growth factor beta signaling pathway is critical for the formation of CD4 T follicular helper cells and isotype-switched antibody responses in the lung mucosa. *eLife*. **4**, e04851 (2015).
81. M. Pepper, A. J. Pagán, B. Z. Igyártó, J. J. Taylor, M. K. Jenkins, Opposing Signals from the Bcl6 Transcription Factor and the Interleukin-2 Receptor Generate T Helper 1 Central and Effector Memory Cells. *Immunity*. **35**, 583–595 (2011).
82. A. C. Poholek, K. Hansen, S. G. Hernandez, D. Eto, A. Chandele, J. S. Weinstein, X. Dong, J. M. Odegard, S. M. Kaech, A. L. Dent, S. Crotty, J. Craft, In Vivo Regulation of Bcl6 and T Follicular Helper Cell Development. *The Journal of Immunology*. **185**, 313–326 (2010).
83. A. I. Jaiswal, C. Dubey, S. L. Swain, M. Croft, Regulation of CD40 ligand expression on naive CD4 T cells: a role for TCR but not co-stimulatory signals. *International Immunology*. **8**, 275–285 (1996).
84. C. M. Snapper, W. E. Paul, Interferon-gamma and B cell stimulatory factor-1 reciprocally regulate Ig isotype production. *Science*. **236**, 944–947 (1987).
85. K. M. Veerman, M. J. Williams, K. Uchimura, M. S. Singer, J. S. Merzaban, S. Naus, D. A. Carlow, P. Owen, J. Rivera-Nieves, S. D. Rosen, H. J. Ziltener, Interaction of the selectin ligand PSGL-1 with chemokines CCL21 and CCL19 facilitates efficient homing of T cells to secondary lymphoid organs. *Nature Immunology*. **8**, 532–539 (2007).
86. A. Mendoza, W. T. Yewdell, B. Hoyos, M. Schizas, R. Bou-Puerto, A. J. Michaels, C. C. Brown, J. Chaudhuri, A. Y. Rudensky, Assembly of a spatial circuit of T-bet-expressing T and B lymphocytes is required for antiviral humoral immunity. *Science Immunology*. **6** (2021), doi:10.1126/sciimmunol.abi4710.
87. B. O. Lee, J. Rangel-Moreno, J. E. Moyron-Quiroz, L. Hartson, M. Makris, F. Sprague, F. E. Lund, T. D. Randall, CD4 T Cell-Independent Antibody Response Promotes Resolution of Primary Influenza Infection and Helps to Prevent Reinfection. *The Journal of Immunology*. **175**, 5827–5838 (2005).
88. D. Pinto, M. M. Sauer, N. Czudnochowski, J. S. Low, M. A. Tortorici, M. P. Housley, J. Noack, A. C. Walls, J. E. Bowen, B. Guarino, L. E. Rosen, J. di Iulio, J. Jerak, H. Kaiser, S. Islam, S. Jaconi, N. Sprugasci, K. Culap, R. Abdelnabi, C. Foo, L. Coelmont, I. Bartha, S. Bianchi, C. Silacci-Fregni, J. Bassi, R. Marzi, E. Vetti, A. Cassotta, A. Ceschi, P. Ferrari, P. E. Cippà, O. Giannini, S. Ceruti, C. Garzoni, A. Riva, F. Benigni, E. Cameroni, L. Piccoli, M. S. Pizzuto, M. Smithey, D. Hong, A. Telenti, F. A. Lempp, J. Neyts, C. Havenar-Daughton, A. Lanzavecchia, F. Sallusto, G. Snell, H. W. Virgin, M. Beltramello,

- D. Corti, D. Veessler, Broad betacoronavirus neutralization by a stem helix-specific human antibody. *Science*. **373**, 1109–1116 (2021).
89. C.-L. Hsieh, A. P. Werner, S. R. Leist, L. J. Stevens, E. Falconer, J. A. Goldsmith, C.-W. Chou, O. M. Abiona, A. West, K. Westendorf, K. Muthuraman, E. J. Fritch, K. H. Dinnon, A. Schäfer, M. R. Denison, J. D. Chappell, R. S. Baric, B. S. Graham, K. S. Corbett, J. S. McLellan, Stabilized Coronavirus Spike Stem Elicits a Broadly Protective Antibody. *Cell Reports*, 109929 (2021).
 90. R. Keating, T. Hertz, M. Wehenkel, T. L. Harris, B. A. Edwards, J. L. McClaren, S. A. Brown, S. Surman, Z. S. Wilson, P. Bradley, J. Hurwitz, H. Chi, P. C. Doherty, P. G. Thomas, M. A. McGargill, The kinase mTOR modulates the antibody response to provide cross-protective immunity to lethal infection with influenza virus. *Nat Immunol*. **14**, 1266–1276 (2013).
 91. G. Pasqual, A. Chudnovskiy, J. M. J. Tas, M. Agudelo, L. D. Schweitzer, A. Cui, N. Hacohen, G. D. Victora, Monitoring T cell–dendritic cell interactions in vivo by intercellular enzymatic labelling. *Nature*. **553**, 496–500 (2018).
 92. K. H. Dinnon, S. R. Leist, A. Schäfer, C. E. Edwards, D. R. Martinez, S. A. Montgomery, A. West, B. L. Yount, Y. J. Hou, L. E. Adams, K. L. Gully, A. J. Brown, E. Huang, M. D. Bryant, I. C. Choong, J. S. Glenn, L. E. Gralinski, T. P. Sheahan, R. S. Baric, A mouse-adapted model of SARS-CoV-2 to test COVID-19 countermeasures. *Nature* (2020), doi:10.1038/s41586-020-2708-8.
 93. S. R. Leist, K. H. Dinnon, A. Schäfer, L. V. Tse, K. Okuda, Y. J. Hou, A. West, C. E. Edwards, W. Sanders, E. J. Fritch, K. L. Gully, T. Scobey, A. J. Brown, T. P. Sheahan, N. J. Moorman, R. C. Boucher, L. E. Gralinski, S. A. Montgomery, R. S. Baric, A Mouse-Adapted SARS-CoV-2 Induces Acute Lung Injury and Mortality in Standard Laboratory Mice. *Cell*. **183**, 1070-1085.e12 (2020).
 94. M. I. J. Raybould, A. Kovaltsuk, C. Marks, C. M. Deane, CoV-AbDab: the coronavirus antibody database. *Bioinformatics*. **37**, 734–735 (2021).
 95. F. D. Finkelman, I. M. Katona, J. F. Urban, J. Holmes, J. Ohara, A. S. Tung, J. V. Sample, W. E. Paul, IL-4 is required to generate and sustain in vivo IgE responses. *J. Immunol*. **141**, 2335–2341 (1988).
 96. I. Yusuf, R. Kageyama, L. Monticelli, R. J. Johnston, D. Ditoro, K. Hansen, B. Barnett, S. Crotty, Germinal center T follicular helper cell IL-4 production is dependent on signaling lymphocytic activation molecule receptor (CD150). *J. Immunol*. **185**, 190–202 (2010).
 97. M. Gaya, P. Barral, M. Burbage, S. Aggarwal, B. Montaner, A. Warren Navia, M. Aid, C. Tsui, P. Maldonado, U. Nair, K. Ghneim, P. G. Fallon, R.-P. Sekaly, D. H. Barouch, A. K. Shalek, A. Bruckbauer, J. Strid, F. D. Batista, Initiation of Antiviral B Cell Immunity Relies on Innate Signals from Spatially Positioned NKT Cells. *Cell*. **172**, 517-533.e20 (2018).

98. C. M. Snapper, W. E. Paul, B cell stimulatory factor-1 (interleukin 4) prepares resting murine B cells to secrete IgG1 upon subsequent stimulation with bacterial lipopolysaccharide. *J. Immunol.* **139**, 10–17 (1987).
99. R. L. Coffman, J. Carty, A T cell activity that enhances polyclonal IgE production and its inhibition by interferon-gamma. *The Journal of Immunology.* **136**, 949–954 (1986).
100. M. Mohrs, K. Shinkai, K. Mohrs, R. M. Locksley, Analysis of type 2 immunity in vivo with a bicistronic IL-4 reporter. *Immunity.* **15**, 303–311 (2001).
101. P. Ivanov, N. Kedersha, P. Anderson, Stress Granules and Processing Bodies in Translational Control. *Cold Spring Harb Perspect Biol.* **11**, a032813 (2019).
102. S. Scheu, D. B. Stetson, R. L. Reinhardt, J. H. Leber, M. Mohrs, R. M. Locksley, Activation of the integrated stress response during T helper cell differentiation. *Nature Immunology.* **7**, 644–651 (2006).
103. M. Y. Ansari, T. M. Haqqi, Interleukin-1 β induced Stress Granules Sequester COX-2 mRNA and Regulates its Stability and Translation in Human OA Chondrocytes. *Scientific Reports.* **6**, 27611 (2016).
104. E. Sanz, L. Yang, T. Su, D. R. Morris, G. S. McKnight, P. S. Amieux, Cell-type-specific isolation of ribosome-associated mRNA from complex tissues. *Proceedings of the National Academy of Sciences.* **106**, 13939–13944 (2009).
105. Z. Haimon, A. Volaski, J. Orthgiess, S. Boura-Halfon, D. Varol, A. Shemer, S. Yona, B. Zuckerman, E. David, L. Chappell-Maor, I. Bechmann, M. Gericke, I. Ulitsky, S. Jung, Re-evaluating microglia expression profiles using RiboTag and cell isolation strategies. *Nature Immunology.* **19**, 636–644 (2018).
106. C. M. Snapper, F. D. Finkelman, W. E. Paul, Differential regulation of IgG1 and IgE synthesis by interleukin 4. *Journal of Experimental Medicine.* **167**, 183–196 (1988).
107. M. J. Robinson, M. Prout, H. Mearns, R. Kyle, M. Camberis, E. E. Forbes-Blom, W. E. Paul, C. D. C. Allen, G. L. Gros, IL-4 Haploinsufficiency Specifically Impairs IgE Responses against Allergens in Mice. *The Journal of Immunology.* **198**, 1815–1822 (2017).
108. W. E. Paul, J. Ohara, B-cell stimulatory factor-1/interleukin 4. *Annu Rev Immunol.* **5**, 429–459 (1987).
109. R. Reiter, K. Pfeffer, Impaired germinal centre formation and humoral immune response in the absence of CD28 and interleukin-4. *Immunology.* **106**, 222–228 (2002).
110. K. Ozaki, R. Spolski, C. G. Feng, C.-F. Qi, J. Cheng, A. Sher, H. C. Morse, C. Liu, P. L. Schwartzberg, W. J. Leonard, A Critical Role for IL-21 in Regulating Immunoglobulin Production. *Science.* **298**, 1630–1634 (2002).

111. A. F. Cunningham, K. Serre, K.-M. Toellner, M. Khan, J. Alexander, F. Brombacher, I. C. M. MacLennan, Pinpointing IL-4-independent acquisition and IL-4-influenced maintenance of Th2 activity by CD4 T cells. *European Journal of Immunology*. **34**, 686–694 (2004).
112. R. I. Nurieva, Y. Chung, D. Hwang, X. O. Yang, H. S. Kang, L. Ma, Y. Wang, S. S. Watowich, A. M. Jetten, Q. Tian, C. Dong, Generation of T follicular helper cells is mediated by interleukin-21 but independent of T helper 1, 2, or 17 cell lineages. *Immunity*. **29**, 138–149 (2008).
113. A. Turqueti-Neves, M. Otte, O. Prazeres da Costa, U. E. Höpken, M. Lipp, T. Buch, D. Voehringer, B-cell-intrinsic STAT6 signaling controls germinal center formation. *Eur. J. Immunol.* **44**, 2130–2138 (2014).
114. S. Tanaka, Y. Motomura, Y. Suzuki, R. Yagi, H. Inoue, S. Miyatake, M. Kubo, The enhancer HS2 critically regulates GATA-3-mediated *Il4* transcription in T_H2 cells. *Nature Immunology*. **12**, 77–85 (2011).
115. A. Williams, G. R. Lee, C. G. Spilianakis, S. S. Hwang, S. C. Eisenbarth, R. A. Flavell, Hypersensitive site 6 of the Th2 locus control region is essential for Th2 cytokine expression. *PNAS*. **110**, 6955–6960 (2013).
116. Y. Harada, S. Tanaka, Y. Motomura, Y. Harada, S. Ohno, S. Ohno, Y. Yanagi, H. Inoue, M. Kubo, The 3' enhancer CNS2 is a critical regulator of interleukin-4-mediated humoral immunity in follicular helper T cells. *Immunity*. **36**, 188–200 (2012).
117. P. Vijayanand, G. Seumois, L. J. Simpson, S. Abdul-Wajid, D. Baumjohann, M. Panduro, X. Huang, J. Interlandi, I. M. Djuretic, D. R. Brown, A. H. Sharpe, A. Rao, K. M. Ansel, Interleukin-4 production by follicular helper T cells requires the conserved Il4 enhancer hypersensitivity site V. *Immunity*. **36**, 175–187 (2012).
118. A. Sahoo, A. Alekseev, K. Tanaka, L. Obertas, B. Lerman, C. Haymaker, K. Clise-Dwyer, J. S. McMurray, R. Nurieva, Batf is important for IL-4 expression in T follicular helper cells. *Nature Communications*. **6**, 7997 (2015).
119. A. Sahoo, S. Wali, R. Nurieva, T helper 2 and T follicular helper cells: Regulation and function of interleukin-4. *Cytokine Growth Factor Rev.* **30**, 29–37 (2016).
120. S. Kusam, L. M. Toney, H. Sato, A. L. Dent, Inhibition of Th2 Differentiation and GATA-3 Expression by BCL-6. *The Journal of Immunology*. **170**, 2435–2441 (2003).
121. H.-E. Liang, R. L. Reinhardt, J. K. Bando, B. M. Sullivan, I.-C. Ho, R. M. Locksley, Divergent expression patterns of IL-4 and IL-13 define unique functions in allergic immunity. *Nature Immunology*. **13**, 58–66 (2011).
122. A. G. Zaretsky, J. J. Taylor, I. L. King, F. A. Marshall, M. Mohrs, E. J. Pearce, T follicular helper cells differentiate from Th2 cells in response to helminth antigens. *The Journal of Experimental Medicine*. **206**, 991–999 (2009).

123. J. D. Buenrostro, P. G. Giresi, L. C. Zaba, H. Y. Chang, W. J. Greenleaf, Transposition of native chromatin for fast and sensitive epigenomic profiling of open chromatin, DNA-binding proteins and nucleosome position. *Nat Methods*. **10**, 1213–1218 (2013).
124. P. J. Skene, S. Henikoff, An efficient targeted nuclease strategy for high-resolution mapping of DNA binding sites. *eLife*. **6**, e21856 (2017).
125. B. T. Phillips, J. G. Williams, D. T. Atchley, X. Xu, J.-L. Li, A. L. Adams, K. L. Johnson, T. M. T. Hall, Mass spectrometric identification of candidate RNA-binding proteins associated with Transition Nuclear Protein mRNA in the mouse testis. *Sci Rep*. **9**, 13618 (2019).
126. M. Day, Covid-19: ibuprofen should not be used for managing symptoms, say doctors and scientists. *BMJ*. **368** (2020), doi:10.1136/bmj.m1086.
127. S. Powis, Novel Coronavirus - Anti-inflammatory medications. *Medicines and Healthcare products Regulatory Agency* (2020), (available at <https://www.cas.mhra.gov.uk/ViewandAcknowledgment/ViewAlert.aspx?AlertID=103001>).
128. K. Fink, Origin and Function of Circulating Plasmablasts during Acute Viral Infections. *Front. Immunol*. **3** (2012), doi:10.3389/fimmu.2012.00078.
129. E. P. Ryan, S. J. Pollack, T. I. Murant, S. H. Bernstein, R. E. Felgar, R. P. Phipps, Activated Human B Lymphocytes Express Cyclooxygenase-2 and Cyclooxygenase Inhibitors Attenuate Antibody Production. *The Journal of Immunology*. **174**, 2619–2626 (2005).
130. M. P. Bernard, R. P. Phipps, CpG oligodeoxynucleotides induce cyclooxygenase-2 in human B lymphocytes: Implications for adjuvant activity and antibody production. *Clinical Immunology*. **125**, 138–148 (2007).
131. M. P. Bernard, R. P. Phipps, Inhibition of cyclooxygenase-2 impairs the expression of essential plasma cell transcription factors and human B-lymphocyte differentiation. *Immunology*. **129**, 87–96 (2010).
132. B. Zhang, E. Liu, J. A. Gertie, J. Joseph, L. Xu, E. Y. Pinker, D. A. Waizman, J. Catanzaro, K. H. Hamza, K. Lahl, U. Gowthaman, S. C. Eisenbarth, Divergent T follicular helper cell requirement for IgA and IgE production to peanut during allergic sensitization. *Science Immunology*. **5** (2020), doi:10.1126/sciimmunol.aay2754.
133. A. M. Collins, IgG subclass co-expression brings harmony to the quartet model of murine IgG function. *Immunology & Cell Biology*. **94**, 949–954 (2016).
134. R. T. Strait, M. T. Posgai, A. Mahler, N. Barasa, C. O. Jacob, J. Köhl, M. Ehlers, K. Stringer, S. K. Shanmukhappa, D. Witte, M. M. Hossain, M. Khodoun, A. B. Herr, F. D. Finkelman, IgG1 protects against renal disease in a mouse model of cryoglobulinaemia. *Nature*. **517**, 501–504 (2015).

135. C. Havenar-Daughton, J. H. Lee, S. Crotty, Tfh cells and HIV bnAbs, an immunodominance model of the HIV neutralizing antibody generation problem. *Immunological Reviews*. **275**, 49–61 (2017).
136. F. Muecksch, Y. Weisblum, C. O. Barnes, F. Schmidt, D. Schaefer-Babajew, Z. Wang, J. C. C. Lorenzi, A. I. Flyak, A. T. DeLaitch, K. E. Huey-Tubman, S. Hou, C. A. Schiffer, C. Gaebler, J. D. Silva, D. Poston, S. Finkin, A. Cho, M. Cipolla, T. Y. Oliveira, K. G. Millard, V. Ramos, A. Gazumyan, M. Rutkowska, M. Caskey, M. C. Nussenzweig, P. J. Bjorkman, T. Hatziioannou, P. D. Bieniasz, Affinity maturation of SARS-CoV-2 neutralizing antibodies confers potency, breadth, and resilience to viral escape mutations. *Immunity*. **0** (2021), doi:10.1016/j.immuni.2021.07.008.
137. S. C. Eisenbarth, Dendritic cell subsets in T cell programming: location dictates function. *Nature Reviews Immunology*, 1 (2018).
138. P. Starkl, M. L. Watzenboeck, L. M. Popov, S. Zahalka, A. Hladik, K. Lakovits, M. Radhouani, A. Haschemi, T. Marichal, L. L. Reber, N. Gaudenzio, R. Sibilano, L. Stulik, F. Fontaine, A. C. Mueller, M. R. Amieva, S. J. Galli, S. Knapp, IgE Effector Mechanisms, in Concert with Mast Cells, Contribute to Acquired Host Defense against *Staphylococcus aureus*. *Immunity*. **53**, 793-804.e9 (2020).
139. Ricciotti Emanuela, FitzGerald Garret A., Prostaglandins and Inflammation. *Arteriosclerosis, Thrombosis, and Vascular Biology*. **31**, 986–1000 (2011).
140. E. Saleh, M. A. Moody, E. B. Walter, Effect of antipyretic analgesics on immune responses to vaccination. *Human Vaccines & Immunotherapeutics*. **12**, 2391–2402 (2016).
141. P. P. Lee, D. R. Fitzpatrick, C. Beard, H. K. Jessup, S. Lehar, K. W. Makar, M. Pérez-Melgosa, M. T. Sweetser, M. S. Schlissel, S. Nguyen, S. R. Cherry, J. H. Tsai, S. M. Tucker, W. M. Weaver, A. Kelso, R. Jaenisch, C. B. Wilson, A Critical Role for Dnmt1 and DNA Methylation in T Cell Development, Function, and Survival. *Immunity*. **15**, 763–774 (2001).
142. M. J. Barnden, J. Allison, W. R. Heath, F. R. Carbone, Defective TCR expression in transgenic mice constructed using cDNA-based α - and β -chain genes under the control of heterologous regulatory elements. *Immunology & Cell Biology*. **76**, 34–40 (1998).
143. K. Mohrs, A. E. Wakil, N. Killeen, R. M. Locksley, M. Mohrs, A Two-Step Process for Cytokine Production Revealed by IL-4 Dual-Reporter Mice. *Immunity*. **23**, 419–429 (2005).
144. J. Wei, M. M. Alfajaro, P. C. DeWeirdt, R. E. Hanna, W. J. Lu-Culligan, W. L. Cai, M. S. Strine, S.-M. Zhang, V. R. Graziano, C. O. Schmitz, J. S. Chen, M. C. Mankowski, R. B. Filler, N. G. Ravindra, V. Gasque, F. J. de Miguel, A. Patil, H. Chen, K. Y. Oguntuyo, L. Abriola, Y. V. Surovtseva, R. C. Orchard, B. Lee, B. D. Lindenbach, K. Politi, D. van Dijk, C. Kadoch, M. D. Simon, Q. Yan, J. G. Doench, C. B. Wilen, Genome-wide CRISPR Screens Reveal Host Factors Critical for SARS-CoV-2 Infection. *Cell* (2020), doi:10.1016/j.cell.2020.10.028.

145. P. S. Pillai, R. D. Molony, K. Martinod, H. Dong, I. K. Pang, M. C. Tal, A. G. Solis, P. Bielecki, S. Mohanty, M. Trentalange, R. J. Homer, R. A. Flavell, D. D. Wagner, R. R. Montgomery, A. C. Shaw, P. Staeheli, A. Iwasaki, Mx1 reveals innate pathways to antiviral resistance and lethal influenza disease. *Science*. **352**, 463–466 (2016).
146. A. C. Walls, Y.-J. Park, M. A. Tortorici, A. Wall, A. T. McGuire, D. Veessler, Structure, Function, and Antigenicity of the SARS-CoV-2 Spike Glycoprotein. *Cell*. **181**, 281-292.e6 (2020).
147. J. S. Chen, J. D. S. Grassmann, U. Gowthaman, S. J. Olyha, T. Simoneau, M. C. Berin, S. C. Eisenbarth, A. Williams, Flow cytometric identification of Tfh13 cells in mouse and human. *Journal of Allergy and Clinical Immunology*. **147**, 470–483 (2021).
148. Y. Chen, A. Zuiani, S. Fischinger, J. Mullur, C. Atyeo, M. Travers, F. J. N. Lelis, K. M. Pullen, H. Martin, P. Tong, A. Gautam, S. Habibi, J. Bensko, D. Gakpo, J. Feldman, B. M. Hauser, T. M. Caradonna, Y. Cai, J. S. Burke, J. Lin, J. A. Lederer, E. C. Lam, C. L. Lavine, M. S. Seaman, B. Chen, A. G. Schmidt, A. B. Balazs, D. A. Lauffenburger, G. Alter, D. R. Wesemann, Quick COVID-19 Healers Sustain Anti-SARS-CoV-2 Antibody Production. *Cell*. **183**, 1496-1507.e16 (2020).
149. N. T. Gupta, J. A. Vander Heiden, M. Uduman, D. Gadala-Maria, G. Yaari, S. H. Kleinstein, Change-O: a toolkit for analyzing large-scale B cell immunoglobulin repertoire sequencing data. *Bioinformatics*. **31**, 3356–3358 (2015).
150. N. Nouri, S. H. Kleinstein, Somatic hypermutation analysis for improved identification of B cell clonal families from next-generation sequencing data. *PLOS Computational Biology*. **16**, e1007977 (2020).
151. K. B. Hoehn, O. G. Pybus, S. H. Kleinstein, “Phylogenetic analysis of migration, differentiation, and class switching in B cells” (2020), p. 2020.05.30.124446, , doi:10.1101/2020.05.30.124446.
152. A. Cui, R. D. Niro, J. A. V. Heiden, A. W. Briggs, K. Adams, T. Gilbert, K. C. O’Connor, F. Vigneault, M. J. Shlomchik, S. H. Kleinstein, A Model of Somatic Hypermutation Targeting in Mice Based on High-Throughput Ig Sequencing Data. *The Journal of Immunology*. **197**, 3566–3574 (2016).
153. V. A. Avanzato, K. Y. Oguntuyo, M. Escalera-Zamudio, B. Gutierrez, M. Golden, S. L. K. Pond, R. Pryce, T. S. Walter, J. Seow, K. J. Doores, O. G. Pybus, V. J. Munster, B. Lee, T. A. Bowden, A structural basis for antibody-mediated neutralization of Nipah virus reveals a site of vulnerability at the fusion glycoprotein apex. *PNAS*. **116**, 25057–25067 (2019).
154. J. M. Decker, F. Bibollet-Ruche, X. Wei, S. Wang, D. N. Levy, W. Wang, E. Delaporte, M. Peeters, C. A. Derdeyn, S. Allen, E. Hunter, M. S. Saag, J. A. Hoxie, B. H. Hahn, P. D. Kwong, J. E. Robinson, G. M. Shaw, Antigenic conservation and immunogenicity of the HIV coreceptor binding site. *Journal of Experimental Medicine*. **201**, 1407–1419 (2005).

155. K. Kamath, J. Reifert, T. Johnston, C. Gable, R. J. Pantazes, H. N. Rivera, I. McAuliffe, S. Handali, P. S. Daugherty, Antibody epitope repertoire analysis enables rapid antigen discovery and multiplex serology. *Sci Rep.* **10** (2020), doi:10.1038/s41598-020-62256-9.
156. L. Paschold, D. Simnica, E. Willscher, M. J. G. T. Vehreschild, J. Dutzmann, D. G. Sedding, C. Schultheiß, M. Binder, SARS-CoV-2-specific antibody rearrangements in prepandemic immune repertoires of risk cohorts and patients with COVID-19. *J Clin Invest.* **131** (2021), doi:10.1172/JCI142966.
157. F. Madeira, Y. mi Park, J. Lee, N. Buso, T. Gur, N. Madhusoodanan, P. Basutkar, A. R. N. Tivey, S. C. Potter, R. D. Finn, R. Lopez, The EMBL-EBI search and sequence analysis tools APIs in 2019. *Nucleic Acids Research.* **47**, W636–W641 (2019).
158. A. M. Waterhouse, J. B. Procter, D. M. A. Martin, M. Clamp, G. J. Barton, Jalview Version 2—a multiple sequence alignment editor and analysis workbench. *Bioinformatics.* **25**, 1189–1191 (2009).
159. R. Jackson, L. Kroehling, A. Khitun, W. Bailis, A. Jarret, A. G. York, O. M. Khan, J. R. Brewer, M. H. Skadow, C. Duizer, C. C. D. Harman, L. Chang, P. Bielecki, A. G. Solis, H. R. Steach, S. Slavoff, R. A. Flavell, The translation of non-canonical open reading frames controls mucosal immunity. *Nature*, 1 (2018).